II. Physik-UniGö-Dipl-2011/01

R-Parity Violating Supersymmetric Models with a Selectron or Smuon as the Lightest Supersymmetric Particle and their Discovery Potential at the Tevatron and the LHC

Diplomarbeit

von

Tim Stefaniak

geboren in

Kappeln

angefertigt am

II. Physikalisches Institut
der Georg-August-Universität Göttingen

und dem

Physikalisches Institut
der Rheinischen Friedrich-Wilhelms-Universität Bonn

2010

Angenommen am:	16.12.2010
Referent:	Prof. Dr. Arnulf Quadt
Korreferent:	Prof. Herbert K. Dreiner, Ph.D.

GEORG-AUGUST-UNIVERSITÄT GÖTTINGEN

II. Physikalisches Institut

R-Parity Violating Supersymmetric Models with a Selectron or Smuon as the Lightest Supersymmetric Particle and their Discovery Potential at the Tevatron and the LHC

von

Tim Stefaniak

A phenomenological study of supersymmetric models with broken R-Parity is presented. Within the model of minimal supergravity with R-Parity violation, we discuss the renormalization group evolution of the mass of the right-handed first and second generation scalar lepton (slepton) and show, that these particles arise as natural candidates for the lightest supersymmetric particle (LSP). We then study the possible slepton LSP parameter space. We show that these models yield a striking multi-leptonic signature at hadron colliders and discuss constraints from recent three lepton searches at the Tevatron. A detailed Monte Carlo study is performed in order to study the prospects of a discovery at the Large Hadron Collider (LHC) with early data. Finally, we present an idea how to determine the masses of supersymmetric particles in these models.

Post address:
Friedrich-Hund-Platz 1
37077 Göttingen
Germany

Physik-UniGö-Dipl-2011/01
II. Physikalisches Institut
Georg-August-Universität Göttingen
December 2010

Contents

1. Introduction 1
  1.1. Notation and Conventions 3

2. The Standard Model 5
  2.1. Quantum Electrodynamics (QED) 5
  2.2. Non-Abelian gauge theories 6
  2.3. The Higgs mechanism 7
  2.4. Renormalization and the running of physical quantities 8
  2.5. Quantum Chromodynamics (QCD) 10
  2.6. Electroweak Theory 11
  2.7. Lepton- and Baryon-number conservation 14

3. Supersymmetry 17
  3.1. Motivation for Supersymmetry 17
  3.2. Global Supersymmetry 20
  3.3. The Supersymmetric Extension of the Standard Model 21
    3.3.1. Particle Content 21
    3.3.2. Superpotential and Proton Decay 23
    3.3.3. Discrete Symmetries 24
    3.3.4. Supersymmetry breaking 26
  3.4. Minimal Supergravity (mSUGRA) 27
    3.4.1. Phenomenological motivation 27
    3.4.2. The P_6 mSUGRA model and its mass spectrum 28
    3.4.3. The P_6 violating mSUGRA model 32

4. Selectron and Smuon as the lightest supersymmetric particle (LSP) 35
  4.1. Renormalization group evolution of the right-handed slepton mass 35
  4.2. A_0 dependence 37
  4.3. Selectron and Smuon LSP parameter space 38

5. Probing Selectron and Smuon LSP models at hadron colliders 43
  5.1. Selectron and Smuon LSP signatures at hadron colliders 43
  5.2. Constraints from SUSY searches at the Tevatron 46
    5.2.1. The DØ trilepton analysis 46
    5.2.2. DØ results and a test of two benchmark scenarios 48
    5.2.3. Excluded selectron and smuon LSP parameter space with existing data . 51
    5.2.4. Sensitive selectron and smuon LSP parameter space with future data . . . 55
  5.3. Discovery potential at the LHC 57
    5.3.1. Benchmark Scenarios 58
    5.3.2. Major Backgrounds 58
    5.3.3. MC Simulation and object selection 59

5.3.4. Kinematic Distributions and Event Selection 61
5.3.5. Discovery reach with early LHC data 67

6. Mass reconstruction at the LHC 73
6.1. The Basic Idea 73
6.2. Event selection 76
6.3. Results 77
6.3.1. Dilepton invariant mass 78
6.3.2. Dilepton-jet invariant mass 78
6.3.3. Lepton-jet invariant masses 80
6.4. Prospects and future plans 81

7. Summary and Conclusions 83

A. Properties of the benchmark models 85
A.1. Benchmark scenarios for the Tevatron 85
A.2. Benchmark scenarios for the LHC 86

B. Signal and Background at the LHC at $\sqrt{s} = 14$ TeV 93

C. Three-body slepton decays 95
C.1. Three-body slepton decay $\tilde{\ell}_R^- \to \ell^- \ell'^\pm \tilde{\ell}'^\mp_R$ 95
C.2. Three-body slepton decay $\tilde{\tau}_1^- \to \tau^- \ell^\pm \tilde{\ell}_R^\mp$ 97
C.3. Resulting branching ratios in the $\tilde{\ell}_R$ LSP parameter space 98

Bibliography 101

Acknowledgements 113

1. Introduction

We are standing on the edge of great discoveries in particle physics. In spring this year (2010), the Large Hadron Collider (LHC) at the European Organization for Nuclear Research (CERN) in Geneva started to collide highly accelerated protons at world record energies. These amount to a multiple of hitherto existing collision energies of recent particle accelerators, such as the Tevatron at the Fermi National Accelerator Laboratory (Fermilab) near Chicago. Particle collisions at such high energies have never been studied under controlled laboratory conditions before. They promise to open a window to unexplored territory in our understanding of particle physics.

The history of elementary particle physics arguably started with the discovery of the electron by Thomson in 1897 [1]. At that time, physicists believed that they had understood the fundamental principles of nature. However, there were some open questions concerning the spectrum of the black-body radiation and the photoelectric effect, which could not be explained with the current understanding of physics at that time. The solution to these problems lead Planck and Einstein around 1900 to postulate energy quantization, which was the first step to the theory of quantum physics. At the same time, both conceptual and empirical arguments guided Einstein to the theory of special relativity. Both theories revolutionized the understanding of the fundamental principles of nature and formed the pillars of modern particle physics.

In the following decades more and more new particles were discovered and postulated, so far ending up with the discovery of the top quark in 1996 [2] and the tau neutrino in 2000 [3, 4]. An effective interplay between theory and experiment lead to the current Standard Model (SM) of Particle Physics. Herein, the elementary particles fit into a pattern formed by the symmetries of nature. Due to its remarkable success in the description of particle physics phenomena, the Standard Model is so far the most precise model of modern physics. The only SM particle which is not yet discovered is the Higgs boson [5, 6, 7]. Its potential discovery is one major purpose of the LHC.

Despite its enormous success, particle physicists are convinced that the SM is not the complete theory of the fundamental forces of nature, since it does not incorporate gravity. While this weakness only becomes important at very high energies, a related issue commonly known as the *hierarchy problem* [8] engages the particle physics community. It asks why gravity is roughly 10^{32} times weaker than the weak force. This problem manifests in the fact, that the Higgs mass is unstable under quantum corrections. Within the SM, this problem can only be resolved by an unnatural fine-tuning of the model parameters, or by accepting the fact, that new physics will appear at the TeV energy scale, which render a new solution to this problem. Besides the hierarchy problem, there are other open issues which cannot be explained by the SM, such as the nature of cold dark matter in the universe [9], the origin of neutrino masses [10] or the CP asymmetry needed for baryogenesis [11].

Most of these problems can be solved by supersymmetry (SUSY), which is a space-time symmetry between fermions and bosons. It predicts the existence of a yet undiscovered superpartner for each SM particle, which differs in spin by 1/2, thus basically doubling the particle spectrum of the SM. Furthermore, it may provide a connection to string theory, which is a promising candidate for a fundamental theory of *all* fundamental interactions including gravity. If supersymmetry is realized in nature, it will most likely be discovered at the LHC.

The supersymmetric extension of the Standard Model (SSM) introduces new particle interactions and some of them lead to the rapid decay of the proton, which is not observed by experiment. In order to prohibit these dangerous interactions, a discrete symmetry has to be added, such as Proton-Hexality (or similarly R-Parity) or Baryon-Triality. With the first symmetry, Proton-Hexality, the lightest supersymmetric particle (LSP) is stable and therefore a cold dark matter candidate. Cosmological considerations then restrict the LSP to be color, flavor and charge neutral. The second symmetry, Baryon-Triality, allows lepton number violating (LNV) interactions and provides an elegant mechanism to generate light neutrino masses. Here, the LSP is unstable and thus not constrained by cosmology. Hence, in principle, every supersymmetric particle can be the LSP. In this thesis, we study supersymmetric models which preserve Baryon-Triality but violate Proton-Hexality (and R-Parity).

The SSM contains a large number of unknown parameters. A detailed phenomenological study is thus only feasible for constrained models, where additional assumptions reduce the number of free parameters to a few. In this thesis, we investigate the model of minimal supergravity (mSUGRA), where we account for the R-Parity violating interactions by one additional LNV coupling at the grand unification scale, $M_{\rm GUT}$.

It has been shown in Ref. [12], that in this model there are only a few LSP candidates, which naturally arise from the evolution of the renormalization group equations (RGEs). These are the lightest neutralino, $\tilde{\chi}_1^0$, the lightest scalar tau (stau), $\tilde{\tau}_1$, the left-handed scalar neutrinos (sneutrinos), $\tilde{\nu}_i$, and the right-handed scalar electron (selectron), $\tilde{e}_R$, and scalar muon (smuon), $\tilde{\mu}_R$. The typical collider signatures of supersymmetric models significantly depend on the nature of the LSP, since usually all supersymmetric particles rapidly cascade decay down into the LSP. It is therefore crucial to study all possible LSP candidates and their characteristic collider signatures in order to be prepared for what experimentalists may find in the LHC data.

Scenarios with a neutralino LSP have been studied extensively in the literature, see *e.g.* Ref. [13, 14, 15, 16]. Furthermore, the stau LSP [17, 18, 19, 20] and the sneutrino LSP [21] have been investigated. In this thesis, we focus on the remaining part, namely the case of a selectron or smuon LSP. We discuss in detail, how certain LNV couplings at $M_{\rm GUT}$ reduce the selectron or smuon mass via the RGE running, thus making them to possible LSP candidates. We then present the possible supersymmetric parameter regions with a selectron or a smuon LSP.

We will further show, that these models typically lead to multi-leptonic final states at hadron colliders. In general, these signatures are hard to achieve with the SM processes and should be easy to identify at collider experiments. Moreover, selectron and smuon LSP scenarios with a light mass spectrum could have been observed at the Tevatron experiments. Therefore, we discuss in detail how the parameter space is already constrained by the SUSY trilepton search performed by the DØ experiment at the Tevatron. We further provide an estimate of the parameter region, which may be excluded by the DØ search using a larger (future) dataset.

The main goal of this thesis is to provide a search strategy of how to discover (or exclude) these models at the LHC with early data. We therefore select three benchmark scenarios with a selectron LSP, representing certain regions of the parameter space. We then perform a detailed Monte Carlo (MC) study of the signal and SM background and design an inclusive search with three final state leptons in order to improve the signal to background ratio. The analysis is then extended to a larger supersymmetric parameter space. We present the discovery potential at the LHC for early data at both 7 TeV and 14 TeV center-of-mass energies.

Once a discovery has been accomplished, the task will be to prove that the new physics is really supersymmetry and to determine the model parameters, *i.e.* the supersymmetric particle masses and couplings. Therefore, we discuss how we can determine the masses of some supersymmetric particles within these models. Hereby, we adapt a method using kinematic endpoints of invariant mass distributions, which is widely used in R-Parity conserving scenarios. We demonstrate, that this method enables the mass reconstruction of the right-handed squarks, $\tilde{q}_R$, the lightest top squark, $\tilde{t}_1$, the lightest neutralino, $\tilde{\chi}_1^0$, and the $\tilde{e}_R$ (or $\tilde{\mu}_R$) LSP.

The thesis is organized as follows. After this introduction, we give an overview of the Standard Model and its underlying principles in Chapter 2. In Chapter 3 we present the supersymmetric extension of the Standard Model. Here, we discuss the possible discrete symmetries which prohibit rapid proton decay, and introduce the R-Parity violating mSUGRA model. In Chapter 4, we study the renormalization group evolution of the right-handed selectron and smuon mass and discuss the selectron and smuon LSP parameter space. The hadron collider phenomenology of these models is then presented in Chapter 5. Here, we first present the typical collider signatures. Then, we discuss in detail the constraints from the SUSY trilepton search performed by the DØ experiment at the Tevatron and provide an estimate of the sensitive parameter region for a larger (future) dataset. In the remaining part of the chapter, we study the prospects for a discovery at the LHC. In Chapter 6 we discuss our approach for the mass reconstruction. We summarize and conclude in Chapter 7.

In Appendix A we provide the SUSY particle mass spectra and branching ratios for the selected benchmark models. Appendix B contains a discussion of the performance of the designed event selection on the signal and SM background for the LHC at 14 TeV. For this work, some three-body slepton decays had to be taken into account which were not investigated before. In Appendix C we present the calculation of the squared matrix amplitude of these decays and discuss their rôle in the supersymmetric parameter space.

1.1. Notation and Conventions

We use natural units throughout this thesis, *i.e.* $\hbar = c = 1$. Also, the Einstein summation convention is used, so repeated indices are summed over unless explicitly stated otherwise. All other conventions are introduced when they are needed.

2. The Standard Model

The Standard Model (SM) of particle physics is a quantum field theory which describes all known fundamental forces of nature, except gravity. It was developed over the last decades by an effective interplay between theory [22, 23, 24] and experiment [25, 26]. Nearly all known particle physics phenomena[1] of the electromagnetic, weak and strong interaction are extremely well described[2] by the SM.

In the present view of particle physics the symmetries of the theory play a central rôle. In fact, the SM Lagrangian is usually obtained by specifying the particle content of the theory and the symmetries it obeys. Given the symmetries and the requirement of renormalizability[3], we can write down the most general Lagrangian for the particle interactions, as we will demonstrate in the following sections.

For the construction of the SM two types of symmetries have to be considered. Firstly, we require the theory to be *Lorentz invariant*, i.e. it obeys the laws of special relativity. Lorentz invariance is a space-time symmetry and all Lagrangians we will consider will obey this symmetry[4]. Secondly, we consider *gauge symmetries* which lead to gauge field theories. In these theories the forces between the fundamental particles are mediated by the exchange of spin-1 gauge bosons. In the SM, the electromagnetic force between charged particles is mediated by the photon, the weak force by the W and Z bosons, and the strong force between colored particles by the gluons.

2.1. Quantum Electrodynamics (QED)

A simple example of a gauge theory is Quantum Electrodynamics (QED). The Dirac Lagrangian for n free fermion fields is given by [39]

$$\mathcal{L}_{\text{Dirac}} = \sum_{i=1}^{n} \bar{\psi}_i (i\partial_\mu \gamma^\mu - m_i)\psi_i, \tag{2.1}$$

where ψ_i are the fermionic fields, γ^μ the Dirac matrices and m_i is the mass of the fermion i. This Lagrangian is invariant under a global $U(1)$ phase transformation

$$\psi_i \to e^{iq_i\alpha}\psi_i, \tag{2.2}$$

---

[1] In the SM neutrinos are taken to be massless. However, neutrino oscillations have been observed by experiment [27, 28, 29, 30, 31, 32, 33, 34], which means that at least two neutrino-types have to be massive.

[2] Probably the most important discrepancy between a SM prediction and electroweak precision measurements has been found for the anomalous magnetic moment of the muon [35, 36, 37, 38]. Here, a deviation of about 3σ has been established.

[3] A theory is renormalizable if the ultraviolet divergencies involved in calculations beyond tree-level can be absorbed into the bare parameters of the theory. Practically, this means that the Lagrangian of the theory involves only terms with mass dimension ≤ 4.

[4] Strictly speaking, the Lagrangian $\mathcal{L}$ has to be invariant up to the addition of a total derivative under the symmetry transformation. Actually, we are only interested in the invariance of the action, $S = \int d^4x\, \mathcal{L}$, and a total derivative in $\mathcal{L}$ will lead to a surface term which will vanish provided the fields go to zero as $x \to \infty$.

where α is the phase change and q_i is an a priori arbitrary fermion flavor-dependent parameter. This invariance means that the phase α has no physical meaning and can be chosen arbitrarily. But then it should also be possible to choose different values for α at different points in space-time without changing the physics. However, if we consider a local change of phase, $\alpha \to \alpha(x)$, the Dirac Lagrangian in Eq. (2.1) is no longer invariant under this transformation. The invariance of the Lagrangian under a local change of phase can be achieved by introducing a new vector field, A^μ, which has the kinetic term

$$\mathcal{L}_{\text{kinetic}} = -\frac{1}{4} F^{\mu\nu} F_{\mu\nu}, \tag{2.3}$$

where $F_{\mu\nu} = \partial_\mu A_\nu - \partial_\nu A_\mu$ is the field strength tensor. Now we have to substitute

$$\partial_\mu \to D_\mu = \partial_\mu + iQA_\mu, \tag{2.4}$$

where D_μ is the gauge covariant derivative and Q is the charge operator defined by $Q\psi_i = q_i\psi_i$. Eq. (2.4) introduces interactions between the vector field and the fermions with the formerly arbitrary constants q_i now reinterpreted as the couplings of these interactions. If the vector field transforms as

$$A_\mu \to A_\mu - \partial_\mu \alpha(x) \tag{2.5}$$

under a local change of phase, the Lagrangian

$$\mathcal{L}_{\text{QED}} = \sum_{i=1}^{n} \bar{\psi}_i (iD_\mu \gamma^\mu - m_i)\psi_i + \mathcal{L}_{\text{kinetic}} \tag{2.6}$$

is invariant under a local $U(1)$ phase transformation. This Lagrangian gives the interactions of the fermions, ψ_i, e.g. the electron, with the electromagnetic field, A_μ, and the couplings q_i are the electric charges of the fermions.

2.2. Non-Abelian gauge theories

The gauge theories of the SM are based on generalizations of the local gauge invariance shown in Sect. 2.1 to non-Abelian[5] gauge groups. The non-Abelian local gauge transformation for a fermion field is

$$\psi_a(x) \to \psi'_a(x) = \left[e^{i\theta_A(x)\mathbf{t}^A} \right]_{ab} \psi_b(x) \equiv \Omega_{ab}(x)\psi_b(x), \tag{2.7}$$

where $\theta_A(x)$ are the continuous parameters of the transformation and $\mathbf{t}^A$ are the generators of the non-Abelian gauge group in the adjoint representation. The generalized covariant derivative has the form

$$D^\mu_{ab} = \delta_{ab}\partial^\mu + ig\mathbf{t}^A_{ab} A^\mu_A, \tag{2.8}$$

---

[5] Non-Abelian means that the local gauge transformations do not commute. In particular, the generators $\mathbf{t}^A$ of the gauge group obey the Lie algebra $[\mathbf{t}^A, \mathbf{t}^B] = if^{ABC}\mathbf{t}^C$, where $f^{ABC} \in \mathbb{R}$ are the structure constants of the group and the upper case indices A, B, C run over the adjoint representation.

where A^μ_A are the spin-1 gauge fields in the adjoint representation of the gauge group and g is the coupling of the fermion to the gauge field. The non-Abelian gauge transformation for the gauge fields is

$$\mathbf{t}^A A^A_\mu \to \mathbf{t}^A A'^A_\mu = \Omega(x)\mathbf{t}^A A^A_\mu \Omega^{-1}(x) + \frac{i}{g}(\partial_\mu \Omega(x))\Omega^{-1}(x). \tag{2.9}$$

Now, the Lagrangian of the non-Abelian gauge theory can be constructed,

$$\mathcal{L} = \mathcal{L}_{\text{gauge}} + \mathcal{L}_{\text{fermion}}, \tag{2.10}$$

where

$$\mathcal{L}_{\text{gauge}} = -\frac{1}{4} F^A_{\mu\nu} F^{\mu\nu}_A, \tag{2.11}$$

$$\mathcal{L}_{\text{fermion}} = \bar{\psi}_a (iD_\mu \gamma^\mu - m)_{ab} \psi_b. \tag{2.12}$$

Here, the field strength tensor is generalized to

$$F^A_{\mu\nu} = \partial_\mu A^A_\nu - \partial_\nu A^A_\mu - g f^{ABC} A^B_\mu A^C_\nu. \tag{2.13}$$

The additional terms of the field strength tensor lead to self-interactions of the gauge bosons in the non-Abelian gauge theories of the SM. The weak and the strong force are both described by non-Abelian gauge theories.

2.3. The Higgs mechanism

The W and Z gauge bosons of the weak force were observed to be massive [25, 26]. This seems to be a problem because a mass term for a gauge boson,

$$\mathcal{L}^{\text{boson}}_{\text{mass}} = \frac{1}{2} m^2 A^\mu_A A^A_\mu, \tag{2.14}$$

is not gauge invariant and thus cannot be included in the Lagrangian. However, there is a way of implementing a mass for the gauge bosons in a gauge-invariant manner. This is called the *Higgs mechanism* [40, 41, 42, 43, 44]. We illustrate this mechanism by considering the simplest example, i.e. a $U(1)$ gauge field A_μ coupled to a complex scalar field ϕ with the Lagrangian

$$\mathcal{L} = \mathcal{L}^{\text{gauge}}_{\text{kinetic}} + \mathcal{L}^{\text{scalar}}_{\text{kinetic}} - V(\phi) = -\frac{1}{4} F^{\mu\nu} F_{\mu\nu} + (D^\mu \phi)^* (D_\mu \phi) - V(\phi), \tag{2.15}$$

where D^μ is given by Eq. (2.4). Here, the charge operator Q in D_μ acts on the scalar field, i.e. $Q\phi = q\phi$, where q is the coupling of the gauge field to the scalar field. The most general renormalizable, gauge-invariant potential is

$$V(\phi) = \mu^2 \phi^* \phi + \lambda (\phi^* \phi)^2. \tag{2.16}$$

The sign of μ^2 determines the shape of the potential:

1. if $\mu^2 > 0$ then the minimum of the potential is at $|\phi| = 0$;
2. if $\mu^2 < 0$ then the minimum of the potential is at $|\phi|^2 = -\frac{\mu^2}{2\lambda} \equiv \frac{v^2}{2}$, with $v \in \mathbb{R}$.

In the second case, $\mu^2 < 0$, the field ϕ acquires a non-zero vacuum expectation value (vev) $\langle\phi\rangle = v/\sqrt{2}$ and the $U(1)$ global symmetry will be spontaneously broken. In other words, while any point on the circle $|\phi| = v/\sqrt{2}$ is equally likely to be the ground state, only one point gets chosen. This breaks the symmetry.

Now we consider fluctuations around the ground state by rewriting the scalar field as

$$\phi = \frac{1}{\sqrt{2}}(v+\rho)e^{i(\xi/v+\theta)}, \tag{2.17}$$

where ρ and ξ are real scalar fields and $ve^{i\theta}/\sqrt{2}$ is the point on the circle $|\phi| = v/\sqrt{2}$ about which we are expanding the field. With this, the kinetic part of the Lagrangian for the scalar field turns into

$$\mathcal{L}^{\text{scalar}}_{\text{kinetic}} = \frac{1}{2}\left(\partial_\mu\rho - i(v+\rho)\left[qA_\mu + \frac{1}{v}\partial_\mu\xi\right]\right)\left(\partial^\mu\rho + i(v+\rho)\left[qA^\mu + \frac{1}{v}\partial^\mu\xi\right]\right). \tag{2.18}$$

By performing a gauge transformation on this Lagrangian,

$$A^\mu \to A^\mu - \frac{1}{qv}\partial^\mu\xi, \tag{2.19}$$

we can eliminate all dependence on the field ξ. This gauge choice is called the *unitary gauge*. With this gauge, the complete Lagrangian is

$$\begin{aligned}\mathcal{L} = &-\frac{1}{4}F^{\mu\nu}F_{\mu\nu} + \frac{1}{2}q^2v^2A_\mu A^\mu + \frac{1}{2}\partial_\mu\rho\partial^\mu\rho \\ &+\frac{1}{2}(2v\rho+\rho^2)q^2A_\mu A^\mu - \frac{1}{4}\mu^2v^2 + \mu^2\rho^2 - \lambda v\rho^3 - \frac{\lambda}{4}\rho^4.\end{aligned} \tag{2.20}$$

This Lagrangian now includes a mass term for the gauge boson with mass $M_A^2 = q^2v^2$, a mass term for a real scalar field with mass $m_\rho^2 = -2\mu^2$, self-interactions of the scalar field and interaction terms of the scalar field with the gauge boson. This mechanism introduces the gauge boson mass term in a manifestly gauge-invariant way. The initial complex scalar field ϕ possesses two degrees of freedom whereas the real scalar field ρ has only one degree of freedom. The second degree of freedom has been "eaten" to provide the longitudinal polarization of the massive gauge boson, which has three degrees of freedom rather than the two degrees of freedom of a massless gauge boson.

This example describes a massive $U(1)$ gauge boson, i.e. a massive photon. In the SM, the photon is massless. However, we need this mechanism in its generalized form to non-Abelian gauge theories to give masses the the W and Z gauge bosons of the weak force.

2.4. Renormalization and the running of physical quantities

Given the Lagrangian of a quantum field theory we can construct the Feynman rules for calculating elementary processes in pertubation theory. However, once we calculate diagrams containing loops, we often encounter infinities which render the calculation meaningless. The theory of renormalization is a prescription how to consistently isolate and remove all these infinities from the physically measurable quantities. A detailed description of this theory can be found e.g. in [45, 39, 46]. Here, we only want to review the idea and the main results that we will need in this work.

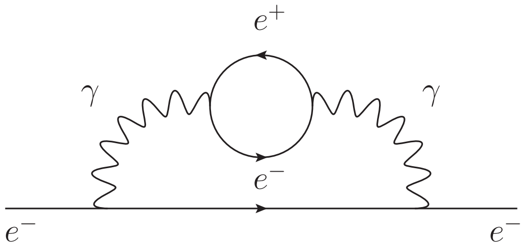

Figure 2.1.: Emission and absorption of a virtual photon from an electron. The photon polarizes the vacuum by creating a virtual electron-positron pair. Due to these kind of virtual corrections the initial electron is always surrounded by a cloud of virtual electron-positron pairs. Thus we will only be able to measure the effective charge of the electron and its electron-positron cloud.

The parameters which appear in the Lagrangian are *not* measurable. This can be illustrated within QED as follows: Given a free electron, it will always be surrounded by a cloud of virtual electron-positron-pairs due to the emission of virtual photons which polarize the vacuum, see Fig. 2.1. If we now try to measure the electron charge, we would in fact measure the charge of the complete system, i.e. of the electron and its surrounding electron-positron cloud. Since we cannot switch off these interactions, the *bare* charge of the electron, which appears in the Lagrangian in form of the coupling, *cf.* Eq. (2.6), is not measurable. Moreover, we also observe a screening effect: The further we move away from the "bare" electron the smaller its charge appears. Therefore, in QED the charge and thus the coupling decreases with distance, i.e. it increases with energy. Due to this energy dependence we speak of a *running* coupling.

The main idea of renormalization is to shuffle all divergences appearing in loop-corrections into the bare quantities such that we get finite *renormalized* quantities which we can measure. There exist several renormalization schemes which we will not further review here, see *e.g.* Ref. [45, 39, 46] for more details. There are basically two strategies:

1. The divergences arising from vertex-correction, self-energy and vacuum-polarization diagrams lead to the renormalization of the field strength, mass and charge, respectively (see e.g. Ref [39]). The resulting effective quantities depend on the energy scale Q^2 and on boundary conditions (see below).
2. In renormalized pertubation theory, we split the Lagrangian into two parts:

   $$\mathcal{L} = \mathcal{L}_0(\mu) + \Delta\mathcal{L}(\mu). \tag{2.21}$$

   $\mathcal{L}_0(\mu)$ has the same structure as the original Lagrangian $\mathcal{L}$ but contains only finite physical quantities, i.e. the renormalized parameters. The other part, $\Delta\mathcal{L}(\mu)$, contains *counterterms* which absorb the infinite but unobservable shifts between the bare parameters and the physical parameters. This new Lagrangian, Eq. (2.21), gives rise to new Feynman rules including those for the counterterms.

The precise relation between the renormalized and unrenormalized quantities depends on the choice of *renormalization conditions* μ. Different choices of this reference point lead to different definitions of the physical quantities. However, the physics should not depend on the choice of the renormalization conditions. This idea leads to the *renormalization group* which is the set of all transformations between renormalization conditions which leave the physical content of the theory invariant. In particle physics the *renormalization group equations* (RGEs) describe how the physical quantities, i.e. the couplings, masses and field strengths, change as one varies the energy at which the physical processes occur. For the simplest case of $\lambda\phi^4$-theory[6], the *Callan-Symanzik equation* has the form [46]

$$\left[\mu\frac{\partial}{\partial\mu}+\beta(\lambda)\frac{\partial}{\partial\lambda}-\gamma_m(\lambda)m^2\frac{\partial}{\partial m^2}-n\gamma(\lambda)\right]\Gamma^{(n)}(\mathbf{p},m^2,\lambda;\mu^2)=0, \tag{2.22}$$

and describes the evolution of the n-point correlation function $\Gamma^{(n)}(\mathbf{p},m^2,\lambda;\mu^2)$ under variation of the renormalization conditions μ. The finite dimensionless functions β, γ_m and γ are given by

$$\beta(\lambda)=\mu\frac{\partial}{\partial\mu}\lambda, \tag{2.23}$$

$$\gamma_m(\lambda)=-\mu\frac{\partial}{\partial\mu}\ln m^2, \tag{2.24}$$

$$\gamma(\lambda)=-\mu\frac{\partial}{\partial\mu}\ln\phi, \tag{2.25}$$

and describe the evolution of the coupling λ, mass m and field strength ϕ with μ, respectively. They are related to renormalization constants which can be calculated perturbatively, see Ref. [46] for more details. In $SU(N)$ non-Abelian gauge theories with fermions in the fundamental representation, the 1-loop β-function is given by [39]

$$\beta(g)=-\frac{g^3}{(4\pi)^2}\left(\frac{11}{3}N-\frac{2}{3}n_f\right), \tag{2.26}$$

where g is the gauge coupling and n_f the number of fermion species.

The renormalization group equations turn out to be of great importance. Once we know the physical quantities at one energy scale, e.g. measured by experiment, the RGEs predict the values of these parameters at any energy scale. The SM prediction for the running of the gauge couplings has been experimentally verified [47, 48] at accessible energies.

Now we can discuss the two theories which form the SM in slightly more detail, i.e. Quantum Chromodynamics which describes the strong force and the Glashow-Weinberg-Salam model which describes the electroweak force.

2.5. Quantum Chromodynamics (QCD)

Quantum Chromodynamics (QCD) describes the color force between the quarks which is mediated by the exchange of gluons. The Lagrangian is

$$\mathcal{L}_{\mathrm{QCD}}=-\frac{1}{4}F^A_{\mu\nu}F^{\mu\nu}_A+\sum_i\bar{q}^i_a(iD_\mu\gamma^\mu-m_i)_{ab}q^i_b, \tag{2.27}$$

where the non-Abelian field strength tensor $F^A_{\mu\nu}$ is given by Eq. (2.13), q^i are the quark fields with mass m_i and the covariant derivative D^μ_{ab} is given by Eq. (2.8). QCD is a $SU(3)$ non-

---

[6] The $\lambda\phi^4$-theory is given by the Lagrangian $\mathcal{L}=\frac{1}{2}(\partial_\mu\phi)^2-\frac{1}{2}m^2\phi^2-\frac{1}{8}\lambda(\phi^2)^2$, where $\phi\equiv(\phi_1,\phi_2,\ldots,\phi_N)$ are complex scalar fields with $\phi^2=\sum_{i=1}^N\phi_i^2$. Because of its simple structure, it is often used as a toy model to study the phenomena of quantum field theories.

Abelian gauge theory and is thus based on the general non-Abelian theory discussed in Sect. 2.2. The fermions, i.e. the quarks, are in the fundamental representation of $SU(3)$ and the gauge bosons, i.e. the gluons, in the adjoint representation. Note, that we have gluon self-interactions due to the different structure of the field strength tensor, Eq. (2.13).

This theory has two important features which are related to the running of the gauge coupling. As we have seen in Sect. 2.4 this is described by the β-function, Eq. (2.23). In QCD, the β-function in Eq. (2.26) is *negative* for $n_f < 17$ quark flavors. Six quark flavors have been observed, so even at energy scales above the top quark mass the β-function is negative. This has the following consequences:

1. **Asymptotic freedom**. The coupling decreases as the energy scale at which it is evaluated increases. Thus, in high energy processes, we can make use of perturbation theory due to the small coupling constant. In general, pertubation theory is only applicable if the quantity we are calculating is infra-red safe, i.e. it does not receive large corrections due to long-range physics.
2. **Confinement**. The coupling becomes large at low energies $Q^2 \lesssim \mathcal{O}(1\ \text{GeV}^2)$ and we can no longer use pertubation theory to perform calculations. At these energies, all quarks and gluons are strongly bound together in hadrons. Experimentally, no free quarks and gluons have been observed. Once free quarks or gluons are produced in high-energy-collisions they will form color-singlet bound states in the *hadronization process*. These bound states, which we then observe, either contain a valence quark-antiquark pair, a meson, or three valence quarks, a baryon. Moreover, these bound states contain gluons which bind the quarks together and a sea of virtual quark-antiquark pairs produced by gluon splitting.

2.6. Electroweak Theory

The unification of the electromagnetic and weak force into a single gauge theory is a major success in theoretical particle physics and was achieved by Glashow, Weinberg and Salam[7] in the 1960's [22, 23, 24]. It is based on the symmetry group $SU(2)_L \times U(1)_Y$. Via the Higgs mechanism, this symmetry is broken spontaneously into the $U(1)_{\text{em}}$ gauge symmetry of QED. The Lagrangian is given by

$$\mathcal{L}_{\text{electroweak}} = \mathcal{L}_{\text{Higgs}} + \mathcal{L}_{\text{gauge}} + \mathcal{L}_{\text{fermions}}, \tag{2.28}$$

where

$$\begin{aligned}
\mathcal{L}_{\text{Higgs}} &= (D_\mu \phi)^\dagger (D^\mu \phi) - \mu^2 \phi^\dagger \phi - \lambda (\phi^\dagger \phi)^2, && (2.29)\\
\mathcal{L}_{\text{gauge}} &= -\frac{1}{4} F^A_{\mu\nu} F^{\mu\nu}_A - \frac{1}{4} B_{\mu\nu} B^{\mu\nu}, && (2.30)\\
\mathcal{L}_{\text{fermions}} &= \bar{Q}_L i \not{D} Q_L + \bar{u}_R i \not{D} u_R + \bar{d}_R i \not{D} d_R + \bar{L}_L i \not{D} L_L + \bar{e}_R i \not{D} e_R \\
&\quad - g_e \bar{L}_L \phi e_R - g_u \bar{Q}_L \phi^c u_R - g_d \bar{Q}_L \phi d_R + \text{h.c.}, && (2.31)
\end{aligned}$$

are the Lagrangians for the Higgs field, the gauge fields and the fermions, respectively. Here, we have two type of gauge fields: The first is the $SU(2)_L$ field, A^A_μ, with the field strength tensor, $F^A_{\mu\nu}$. It lives in the adjoint of $SU(2)_L$, *i.e.* A^A_μ is a $SU(2)_L$ triplet with gauge coupling g. The associated charge is called *weak isospin* T^A. The second is the $U(1)$ field, B_μ, with field strength tensor $B_{\mu\nu}$ and gauge coupling g'. The associated $U(1)$ charge is called *hypercharge* Y. The fields

---

[7] For this work, Glashow, Weinberg and Salam were awarded with the Nobel prize in 1979.

Q_L, L_L (u_R, d_R, e_R) are the left-handed (right-handed) components of the up and down quark and lepton fields and are $SU(2)_L$ doublets (singlets). We distinguish between left- and right-handed fields because experimentally the W bosons only couple to the left-handed fermions. The Higgs field $\phi = (\phi^+ \; \phi^0)$ is a complex scalar isospin doublet with hypercharge $Y = 1/2$. The second row of Eqn. (2.31) contains Yukawa interaction terms of the Higgs fields with the leptons, up- and down-type quarks with Yukawa couplings g_e, g_u and g_d, respectively. Here, the up-type quarks couple to the charge conjugate Higgs field $\phi^c = -i\tau_2\phi^*$ with hypercharge $Y = -1/2$. We introduced a short notation, $\not{D} = D_\mu\gamma^\mu$, where the covariant derivative is given by

$$D_\mu = \partial_\mu + igT_A A_\mu^A + ig' Y B_\mu. \tag{2.32}$$

We shall first discuss the Higgs part of the Lagrangian, $\mathcal{L}_{\text{Higgs}}$, Eq. (2.29). The Higgs potential is similar to the $U(1)$ case, Eq. (2.16), however, here ϕ is a $SU(2)$ doublet. We expand the Higgs field about the ground state $\langle\phi\rangle = (0 \; v)/\sqrt{2}$ in terms of one real field and three phases in $SU(2)_L$ space to obtain the following mass terms for the gauge bosons:

$$\mathcal{L}_{\text{gauge}}^{\text{mass}} = \frac{1}{8} g^2 v^2 \left[g^2 (A_\mu^1)^2 + g^2 (A_\mu^2)^2 + (-gA_\mu^3 + g' B_\mu)^2 \right] \tag{2.33}$$

Thus, the interaction fields A_μ^A, B_μ mix to form the mass eigenstates

$$W_\mu^\pm \equiv \frac{1}{\sqrt{2}}(A_\mu^1 \mp iA_\mu^2) \quad \text{with mass} \quad M_W = \frac{gv}{2}, \tag{2.34}$$

$$Z_\mu^0 \equiv \cos\theta_W A_\mu^3 - \sin\theta_W B_\mu \quad \text{with mass} \quad M_Z = \frac{gv}{2\cos\theta_W}, \tag{2.35}$$

and the massless eigenstate

$$A_\mu \equiv \sin\theta_W A_\mu^3 + \cos\theta_W B_\mu \quad \text{with mass} \quad M_A = 0, \tag{2.36}$$

where the weak mixing angle is given by $\tan\theta_W = g'/g$. By using the Higgs mechanism, we obtain two massive charged vector bosons, $W^\pm$, and one massive neutral vector boson, Z^0, carrying the weak force, and a massless neutral vector boson, A, which is the photon of electromagnetism.

The second term in the Lagrangian, $\mathcal{L}_{\text{gauge}}$, Eq. (2.30), contains the kinetic terms of the gauge fields, which lead to interactions between the gauge bosons. Thus we obtain for example interactions of the photon with the $W^\pm$ bosons.

Finally, $\mathcal{L}_{\text{fermions}}$, Eq. (2.31), gives the interactions of the gauge and the Higgs boson with the Standard Model fermions. Using the expressions for the mass eigenstates, Eq. (2.34) - (2.36), we can express the couplings of the fermions to the photon and the Z boson in terms of their hypercharge and isospin:

$$\text{photon-coupling} = (T^3 + Y) g \sin\theta_W \equiv Qe, \tag{2.37}$$

$$\text{Z-coupling} = (T^3 \cos^2\theta_W - Y \sin^2\theta_W) \frac{g}{\cos\theta_W}. \tag{2.38}$$

Here, T^3 is the third component of the weak isospin T, and e is the magnitude of the electric charge of the electron, given by $e = g\cos\theta_W$. The electric charge, Q, of a fermion is related to

Fermion	Isospin T	T^3	Hypercharge Y	Charge Q
d_R	0	0	$-\frac{1}{3}$	$-\frac{1}{3}$
u_R	0	0	$+\frac{2}{3}$	$+\frac{2}{3}$
$Q_L = \begin{pmatrix} u \\ d \end{pmatrix}_L$	$\frac{1}{2}$	$+\frac{1}{2}$ $-\frac{1}{2}$	$+\frac{1}{6}$	$+\frac{2}{3}$ $-\frac{1}{3}$
e_R	0	0	-1	-1
$L_L = \begin{pmatrix} \nu_e \\ e \end{pmatrix}_L$	$\frac{1}{2}$	$+\frac{1}{2}$ $-\frac{1}{2}$	$-\frac{1}{2}$	0 -1

Table 2.1.: $SU(2)_L \times U(1)_Y$ gauge quantum numbers of the Standard Model fermions. All fermions come in three generations. Here, only the first generation is shown.

its weak isospin and hypercharge via

$$Q = T^3 + Y. \tag{2.39}$$

In Tab. 2.1 we give the gauge quantum numbers of the electroweak force for the Standard Model fermions.

The last three terms in $\mathcal{L}_{\text{fermions}}$, Eq. (2.31), couple the Higgs field and the fermions in a gauge-invariant manner. This is necessary because a Dirac mass term, as in Eq. (2.1), violates the $SU(2)$ gauge invariance. Given in terms of the left- and right-handed fields, a Dirac mass term would be

$$\mathcal{L}_{\text{Dirac}}^{\text{mass}} = -m\bar{\psi}\psi = -m(\bar{\psi}_L\psi_R + \bar{\psi}_R\psi_L). \tag{2.40}$$

Since the $SU(2)_L$ gauge transformation only acts upon the left-handed fields this term is not gauge invariant. However, after electroweak symmetry breaking (EWSB) the last three terms in $\mathcal{L}_{\text{fermions}}$ (and their hermitian conjugates) give fermion mass terms in a gauge invariant way,

$$\mathcal{L}_{\text{fermions}}^{\text{mass}} = -g_e v(\bar{e}_L e_R + \bar{e}_R e_L) - g_d v(\bar{d}_L d_R + \bar{d}_R d_L) - g_u v(\bar{u}_L u_R + \bar{u}_R u_L), \tag{2.41}$$

where the fermion mass is given by $m_f = g_f v$. Here, we have only considered one generation of fermions. Note that we had to use both the Higgs field ϕ and its charge conjugate ϕ^c to give masses to both the up- and down-type quarks.

In the Standard Model, the fermions given in Tab. 2.1 come in three generations. In general, the mass eigenstates of the fermions and their weak interaction states can be different. By writing down all possible terms in the Lagrangian which are renormalizable and invariant under the symmetries, the masses of the quark sector are given by

$$\begin{aligned}\mathcal{L}^{\text{mass}}_{\text{quarks}} &= -v \begin{pmatrix} \bar{d}_L & \bar{s}_L & \bar{b}_L \end{pmatrix} \begin{pmatrix} g_{dd} & g_{ds} & g_{db} \\ g_{sd} & g_{ss} & g_{sb} \\ g_{bd} & g_{bs} & g_{bb} \end{pmatrix} \begin{pmatrix} d_R \\ s_R \\ b_R \end{pmatrix} \\ &\quad -v \begin{pmatrix} \bar{u}_L & \bar{c}_L & \bar{t}_L \end{pmatrix} \begin{pmatrix} g_{uu} & g_{uc} & g_{ut} \\ g_{cu} & g_{cc} & g_{ct} \\ g_{tu} & g_{tc} & g_{tt} \end{pmatrix} \begin{pmatrix} u_R \\ c_R \\ t_R \end{pmatrix} + \text{h.c.} \qquad (2.42) \\ &\equiv -\bar{D}_L M_d D_R - \bar{U}_L M_u U_R + \text{h.c.}, \qquad (2.43)\end{aligned}$$

where $D_{L,R}$ is a vector containing the three (left-/right-handed) down-type quark fields and $U_{L,R}$ is a vector containing the three (left-/right-handed) up-type quark fields. M_u and M_d are the mass matrices for the up- and down-type quarks, respectively. We thus observe mixing between the quark generations. The fields in Eq. (2.43) are the weak interaction eigenstates. By applying separate rotations to the left- and right-handed components of the quark fields, we can express Eq. (2.43) in terms of the mass eigenstates. If the left-handed (right-handed) components are rotated by the unitary matrix L (R) we can obtain a diagonal mass matrix, $M' = LMR^\dagger$. We need two different rotation matrices for the up- and down-quarks, which we will denote by the subscripts u and d, respectively. This rotation of the quark fields has to be performed for the complete SM Lagrangian. However, the neutral-current parts of the electroweak and the QCD Lagrangians are flavor diagonal in terms of either their mass or weak interaction eigenstates[8]. The only parts of the Lagrangian which are not flavor diagonal are those which involve the coupling of the W boson to the quark fields. These terms involve the combination of fields

$$W\bar{U}_L D_L = W\bar{U}'_L L_u L_d^\dagger D'_L \equiv W\bar{U}'_L V D'_L, \qquad (2.44)$$

where $V = L_u L_d^\dagger$ is the *Cabibbo-Kobayashi-Maskawa* (CKM) matrix and $U'_L = L_u U_L$ ($D'_L = L_d D_L$) are the up-type (down-type) quark mass eigenstates. Hence, we can work in a physical, *i.e.* mass, basis for the quarks by simply including the relevant elements of the CKM matrix at the vertex which couples the W boson to the quarks. Conventionally[9], the rotation is only applied to either the up- or the down-type quark sector, leaving the other sector flavor-diagonal. The CKM matrix is given by three real mixing angles and one CP-violating complex phase.

2.7. Lepton- and Baryon-number conservation

In addition to the gauge and Lorentz symmetries, there are more symmetries in the Standard Model. These symmetries are consequences of the gauge and Lorentz symmetries, the particle content of the SM and the requirement of renormalizability. There are two global symmetries[10] of particular interest for this thesis:

- **Lepton Number**. The mixing between weak interaction eigenstates and mass eigenstates, which we observed in the quark sector in the previous section, does not appear in the lepton-sector of the Standard Model[11]. This is due to an additional symmetry called

---

[8] Hence, flavor-changing neutral currents (FCNCs) are forbidden at tree-level within the SM.

[9] In supersymmetric theories with R-parity violation, which will be discussed in the next chapter, the choice of the rotation basis can have phenomenological consequences, see Ref. [17].

[10] These symmetries are violated in the Standard Model by non-perturbative effects [49, 50].

[11] However, the observation of neutrino oscillations indicates the violation of lepton flavor [51]. The neutrino

Lepton Number. Here, the lepton number is a quantum number assigned to the SM fermions such that the lepton fields have lepton number $+1$, the antileptons have lepton number -1 and all the other fields have lepton number zero. This symmetry is respected by the electroweak Lagrangian, Eq. (2.28).

- **Baryon Number**. We assign the baryon number such that the quarks have baryon number $+1/3$, the antiquarks have baryon number $-1/3$ and all other fields have baryon number zero. This choice leads to the fact, that baryons have baryon number $+1$ and mesons and all other fields have baryon number zero. Both the QCD Lagrangian, Eq. (2.27), and the electroweak Lagrangian, Eq. (2.28), respect this symmetry.

We want to emphasize that we did not construct the Lagrangian to have these symmetries. It is impossible to write down a term in the Lagrangian which is renormalizable, Lorentz and gauge invariant, but violates one of these discrete symmetries given the particle content of the Standard Model. This is important as in a supersymmetric theory it is possible to have such terms in the Lagrangian.

---

mixing can then be parametrized by the *Pontecorvo-Maki-Nakagawa-Sakata* (PMNS) matrix. If we further assume neutrinos to be Majorana particles, lepton-number is also violated [52].

3. Supersymmetry

Despite its great success the Standard Model is not considered as a complete theory of the fundamental forces, if for no other reason than that it does not include gravity. It is rather accepted to be a low-energy effective theory of some larger theory which may be

- a grand unified theory (GUT) in which the gauge group of the SM is unified as a part of a larger gauge group, e.g. $SU(5)$ or $SO(10)$ [53, 54];
- a string theory, which would also include gravity. Here, we usually have more than four space-time dimensions [55, 56].

This larger theory is hoped to explain some of the open questions of the SM, for example, why there are three generations of fermions. Also it should predict some of the free parameters of the SM, e.g. the particle masses.

Besides these rather deep theoretical questions, there are also experimental observations which can not be explained by the SM, most importantly the observation of cold dark matter [9] and dark energy [57], neutrino oscillations [10], and the matter-antimatter asymmetry of the universe [11].

The theory of supersymmetry (SUSY) may provide an explanation for some of these phenomena. Furthermore, it may elegantly solve the *hierarchy problem*, which we will discuss in detail in the next section. Supersymmetry is considered as a promising intermediate theory on the way to the *Theory of Everything* (TOE). And in fact, the most promising string theories are based on supersymmetry.

A detailed introduction to supersymmetry is *e.g.* given in Ref. [58, 59, 60, 61, 55, 62, 63]. Here, we concentrate only on the main aspects relevant for this work.

3.1. Motivation for Supersymmetry

The hierarchy problem [8, 58, 64, 65, 66] is one of the most striking arguments that the SM is not the complete story and supersymmetry provides a very natural solution to this problem. Note, that other solutions exist for instance in technicolor models [67], little Higgs models [68] or models with extra dimensions [69, 70, 71].

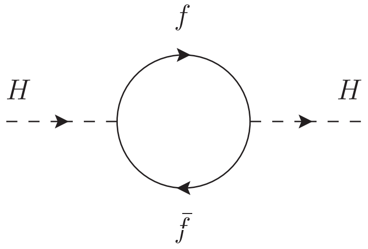

Figure 3.1.: Fermionic one-loop contribution to the Higgs mass.

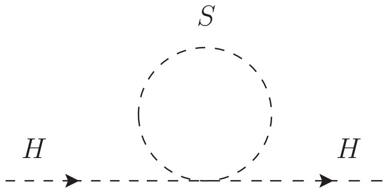

Figure 3.2.: One-loop contribution to the Higgs mass from an extra scalar field.

Consider the one-loop corrections from fermion loops to the Higgs mass[1] of the SM, shown in Fig. 3.1. From this diagram we get a contribution

$$\delta M_{H\,f}^2 = \Pi_H(M_H^2), \tag{3.1}$$

where

$$i\Pi_H(p^2) = -\frac{|\lambda_f|^2}{4}\int \frac{d^4k}{(2\pi)^4}\frac{\mathrm{tr}[(\not{k}+\not{p}+m_f)(\not{k}+m_f)]}{[(k+p)^2-m_f^2][k^2-m_f^2]} \tag{3.2}$$

and $\lambda_f = m_f/v$ is the coupling of the fermion f to the Higgs field H. Naïvely, from power counting, this diagram is quadratically divergent. The divergence can be regulated by imposing an ultraviolet momentum cut-off, Λ, yielding

$$\delta M_{H\,f}^2 = \frac{|\lambda_f|^2}{16\pi^2}\left[-2\Lambda^2 + 6M_f^2\ln(\Lambda/M_f)\right]. \tag{3.3}$$

Here, we neglected terms which are finite in the limit $\Lambda \to \infty$.

We see from Eq. (3.3), that the SM Higgs mass depends quadratically on the cut-off scale Λ, which is understood to be the energy scale at which new physics enters to alter the high-energy bahavior of the theory. Assuming the SM is valid up to typical GUT or string energy scales, i.e. $\Lambda \sim M_{\rm GUT} \simeq 2\cdot 10^{16}$ GeV or $\Lambda \sim M_{Pl} \simeq 10^{19}$ GeV, the natural[2] value of the Higgs mass is $10^{14} - 10^{17}$ GeV rather than the upper limit of around 170 GeV suggested by electroweak precision data [72, 73, 74, 75]. This huge discrepancy, which is directly related to the energy scale of new physics, is known as the hierarchy problem.

To solve this problem, one might want to pick a Λ that is not too large. In this case, new physics at the scale Λ still has to explain, why the loop integral cuts off at Λ. Moreover, new particles that couple directly or indirectly to the Higgs field will give contributions similar to Eq. (3.3) via virtual effects. Thus, the Higgs mass remains very sensitive to any new particles entering at higher energies.

We can see how this problem is solved in supersymmetry by considering an additional scalar field S which couples to the Higgs field via the Lagrangian term $-\lambda_S|H|^2|S|^2$. This gives an extra one-loop contribution, Fig. 3.2, to the Higgs mass

$$\delta M_{H\,S}^2 = \frac{|\lambda_S|^2}{16\pi^2}\left[\Lambda^2 - 2M_S^2\ln(\Lambda/M_S)\right], \tag{3.4}$$

---

[1] In fact, this argument counts for any scalar fields of a theory, which couple to fermions.

[2] Natural in the sense that the Higgs mass is not *fine-tuned*. Fine-tuning means, there is an accidental cancellation between large quantities (here, the bare mass and the mass correction), that does not rely on any known physical mechanism.

where we have again neglected terms which are finite in the limit $\Lambda \to \infty$. In supersymmetry, we have two complex scalar fields for each Dirac fermion and hence the quadratic dependencies on Λ in Eq. (3.3) and Eq. (3.4) will cancel provided that $\lambda_S = |\lambda_f|^2$. This is the case if supersymmetry is unbroken. In order to guarantee that supersymmetry breaking does not spoil this solution to the hierarchy problem, the relationships between the dimensionless couplings have to be maintained. This is the case if the supersymmetry breaking is "soft", i.e. the effective Lagrangian of the theory can be written in the form

$$\mathcal{L} = \mathcal{L}_{\mathrm{SUSY}} + \mathcal{L}_{\mathrm{soft}}, \tag{3.5}$$

where $\mathcal{L}_{\mathrm{SUSY}}$ preserves supersymmetry invariance and $\mathcal{L}_{\mathrm{soft}}$ violates supersymmetry but contains only mass terms and coupling parameters of *positive* mass dimension. However, the mass splittings between SM particles and their superpartners cannot be too large. The masses of the (lighter) superpartners should be at most of about 1 TeV in order to derive a Higgs vev resulting in M_W, $M_Z = 80.4$, 91.2 GeV without miraculous cancellations [58].

Apart from the solution of the hierarchy problem, there are further theoretical as well as experimental facts pointing to a supersymmetric extension of the Standard Model (SSM):

- Supersymmetry is the only possible way to extend the Lorentz- (or Poincaré-) space-time symmetry [76, 77]. This will be discussed in some detail in Sect. 3.2.
- We have seen in Sect. 2.3 that local gauge invariance requires the introduction of a gauge boson. Similarly, local supersymmetry requires the introduction of a massless spin-2 field, the graviton (and its spin-3/2 superpartner, the gravitino) which mediates gravitational interactions. Thus we have a connection to general relativity [78, 79, 80, 81, 82, 83, 84].
- Realistic string theories are based on supersymmetry. However, this does not necessarily imply weak-scale SUSY, see e.g. Ref [55, 56].
- In the Standard Model the gauge couplings do not unify. However, in the SSM the gauge couplings will meet at a scale of $\mathcal{O}(10^{16}$ GeV) as long as the SUSY particle masses are of $\mathcal{O}(100$ GeV $-$ 10 TeV) and there are no intermediate fields [85, 86, 87, 88, 89]. This gives a connection to GUTs.
- The SSM provides a natural explanation for the origin of electroweak symmetry breaking and the large difference between M_Z and M_{Pl}. A positive Higgs mass parameter squared of $\mathcal{O}(100^2\ \mathrm{GeV}^2)$ at a scale of $\mathcal{O}(10^{16}$ GeV) can run to a negative value at the electroweak scale, M_Z, which is needed for EWSB (see Sect. 2.3). This mechanism is called radiative electroweak symmetry breaking (REWSB) [90]. Again, the superpartners of the SM fields are required not to be heavier than a few TeV.
- The SSM contributions to the anomalous magnetic moment of the muon may explain the 3σ deviation between the SM prediction and the experimental observations [35, 36, 37, 38].
- In case both lepton-number and baryon-number are conserved, the SSM contains a good cold dark matter candidate, the neutralino [91]. However, there also exist possible candidates in case one of these symmetries is violated, *cf.* also Sect. 3.4.3.
- If lepton-number is violated, the SSM possesses an elegant mechanism to generate neutrino masses [92, 93, 94, 95, 96][3]. We briefly discuss this in Sect. 3.4.3.

Remarkably, there are several arguments for SUSY requiring that the masses of the superpartners of the SM fields are of $\mathcal{O}(\lesssim 1$ TeV). This is the reason for the optimism of particle

---

[3] We can also generate neutrino masses via the seesaw mechanism if we introduce right-handed neutrinos in the SSM [97, 98, 99, 100, 101]. However, this introduces an additional scale in the theory, namely the Majorana mass of the right-handed neutrinos.

physicists that supersymmetry will be discovered at the Large Hadron Collider (LHC) [102, 103] or even at Tevatron [104] if it is realized in nature.

3.2. Global Supersymmetry

A supersymmetry transformation turns a bosonic state into a fermionic state, and vice versa. The generator of the SUSY transformation, Q, must be an anticommuting spinor, with

$$Q \mid \text{boson}\rangle = \mid \text{fermion}\rangle, \qquad Q \mid \text{fermion}\rangle = \mid \text{boson}\rangle. \tag{3.6}$$

Because the SUSY generators are fermionic operators, they carry spin 1/2. This means that supersymmetry must be a space-time symmetry. For interacting quantum field theories the possible forms of such symmetries are highly restricted by the Haag-Łopuszanski-Sohnius extension of the Coleman-Mandula theorem [76, 77]. This theorem states, that the only possibility to extend the Poincaré algebra in a non-trivial way is to introduce N sets of fermionic generators $\{Q^i_\alpha, \bar{Q}^{\dot{\alpha}}_i\}_{i=1\ldots N}$ which transform as $(\frac{1}{2}, 0)$ and $(0, \frac{1}{2})$ representations of the proper orthochronous Lorentz group. In general there can be up to $N = 8$ of these sets, however for realistic theories that, like the Standard Model, have chiral fermions and thus allow for parity-violating interactions, only $N = 1$ supersymmetric quantum field theories are suitable. The SUSY generators have to satisfy the following algebra of anti-commutation and commutation relations[4]:

$$\{Q_\alpha, \bar{Q}_{\dot{\beta}}\} = 2\sigma^\mu_{\alpha\dot{\beta}} P_\mu, \tag{3.7}$$

$$\{Q_\alpha, Q_\beta\} = \{\bar{Q}_{\dot{\alpha}}, \bar{Q}_{\dot{\beta}}\} = 0, \tag{3.8}$$

$$[Q_\alpha, P^\mu] = [\bar{Q}_{\dot{\alpha}}, P^\mu] = 0, \tag{3.9}$$

where Q ($\bar{Q}$) is a left-handed (right-handed) two-component Weyl spinor with $\alpha, \beta\, (\dot{\alpha}, \dot{\beta}) = 1, 2$, and $\sigma^\mu = (\mathbb{1}, \vec{\sigma})$ with $\vec{\sigma}$ the Pauli matrices. P^μ is the momentum operator, i.e. the generator of space-time translations.

In $N = 1$ SUSY, each SM particle has a superpartner with its spin differing by 1/2. Together they form a supermultiplet, which is an irreducible representation of the SUSY algebra. One can show by use of Eq. (3.9) that each supermultiplet contains an equal number of fermionic and bosonic degrees of freedom [58]. The superpartners of the SM fields have the same gauge quantum numbers, since Q commutes with the generators of the gauge interactions. From Eq. (3.9) follows also that Q commutes with $P^2 = M^2$. Thus, all fields in a supermultiplet possess the same mass M. However, we have not observed any superpartners of SM particles yet, so SUSY must be a broken symmetry, if it really exists in nature.

For the construction of a supersymmetric extension of the SM there are two relevant kinds of supermultiplets: A *chiral* (or *matter*) supermultiplet, which contains a single two-component Weyl fermion (spin 1/2) and a complex scalar field (spin 0), and a *vector* (or *gauge*) superfield with a massless vector boson (spin 1) and a two-component Weyl fermion. In order to include gravity, we need an additional supermultiplet with the graviton (spin 2) and its fermionic superpartner the gravitino (spin 3/2).

Moreover, each supermultiplet contains an auxiliary field which allows the SUSY algebra to close off-shell, i.e. when the classical equations of motion are not satisfied. However, at the end

---

[4] We do not show the commutation relations involving rotation generators, because they are not important for the further discussion.

of the day, these fields can be eliminated and expressed in terms of the physical fields by use of their classical equations of motion.

It is most convenient to write the supermultiplets in a compact form using the so-called *superfield formalism.* A detailed description of this formalism can be found in the literature, see e.g. [59, 60, 61].

3.3. The Supersymmetric Extension of the Standard Model

3.3.1. Particle Content

The Supersymmetric Extension of the Standard Model with minimal particle content (SSM) is given by the chiral and gauge supermultiplets shown in Tab. 3.1 and 3.2, respectively.

To understand the allocation of the SM fields to the supermultiplets it is important to note that only chiral supermultiplets can accommodate fermions whose left-handed parts transform differently under the gauge group than their right-handed parts. Hence, the left- and right-handed SM fermions belong to different chiral supermultiplets and therefore have different superpartners called sfermions. We have three generations, $i = 1, 2, 3$, of left-handed (right-handed) squarks, $\tilde{u}_{Li}$, $\tilde{d}_{Li}$ ($\tilde{u}_{Ri}$, $\tilde{d}_{Ri}$), which are the spin-0 superpartners[5] of the left-handed (right-handed) up- and down-type quarks, respectively; the superpartners of the left-handed (right-handed) charged leptons, the left-handed (right-handed) charged sleptons, $\tilde{\ell}_{Li}$ ($\tilde{\ell}_{Ri}$); and the sneutrinos, $\tilde{\nu}_i$, which are the superpartners of the neutrinos. It is conventional that all SM fermions are described by left-handed Weyl spinors. Thus, we have given the conjugates of the right-handed quarks and leptons in Tab. 3.1, which are left-handed spinors.

In Tab. 3.1 we observe, that we need at least two Higgs doublets to construct the SSM. This is due to the fact, that the fermionic partner of a single Higgs doublet would lead to a gauge anomaly of the electroweak symmetry [105]. With two Higgs doublets of opposite $U(1)_Y$ charge, *cf.* Tab. 3.1, the contributions to this anomaly cancel. Moreover, SUSY requires the superpotential (see below) to be an analytic function of the chiral superfield. Thus we need two Higgs doublets to be able to give mass to both the up- and the down-type quarks via the Higgs mechanism.

The SM gauge bosons and their fermionic superpartners, the gauginos, reside in gauge supermultiplets, *cf.* Tab. 3.2. We have the bino, $\tilde{B}^0$, the superpartner of the $U(1)_Y$ gauge boson; the neutral and charged winos, $\tilde{W}^0$, $\tilde{W}^\pm$, the superpartners of the $SU(2)$ gauge bosons; and the gluinos, $\tilde{g}_a$, $a = 1, \ldots, 8$, the superpartners of the $SU(3)_C$ gauge bosons.

After electroweak symmetry breaking (EWSB), some of the fields in Tab. 3.1 and Tab. 3.2 will have the same quantum numbers and thus they can mix. In the case of lepton-number conservation, we will have the following mixings [63, 106]:

- The bino and the neutral winos and Higgsinos mix and their mass eigenstates are called neutralinos, $\tilde{\chi}^0_n$, with $n = 1, 2, 3, 4$ denoting an increasing mass hierarchy (i.e. $\tilde{\chi}^0_1$ is the lightest neutralino).
- From the mixing of the charged winos and higgsinos we get the charginos, $\tilde{\chi}^\pm_l$, with $l = 1, 2$. Again, $\tilde{\chi}^\pm_1$ is the lighter mass eigenstate.

---

[5] Note, that the R and L chirality indices on scalar fields only distinguish between independent fields corresponding to the superpartners of right- and left-handed fermion fields, respectively. In fact, since the sfermions are spin-0 particles, they have no “handedness”.

Field names	superfield	spin 0	spin 1/2	$SU(3)_C$, $SU(2)_L$, $U(1)_Y$
squarks, quarks (×3 families)	Q_i	$(\tilde{u}_{Li}\,\tilde{d}_{Li})$	$(u_{Li}\,d_{Li})$	$(\mathbf{3},\,\mathbf{2},\,+1/6)$
	$\bar{U}_i$	$\tilde{u}^*_{Ri}$	$u^\dagger_{Ri}$	$(\bar{\mathbf{3}},\,\mathbf{1},\,-2/3)$
	$\bar{D}_i$	$\tilde{d}^*_{Ri}$	$d^\dagger_{Ri}$	$(\bar{\mathbf{3}},\,\mathbf{1},\,+1/3)$
sleptons, leptons (×3 families)	L_i	$(\tilde{\nu}_i\,\tilde{\ell}_{Li})$	$(\nu_i\,\ell_{Li})$	$(\mathbf{1},\,\mathbf{2},\,-1/2)$
	$\bar{E}_i$	$\tilde{\ell}^*_{Ri}$	$\ell^\dagger_{Ri}$	$(\mathbf{1},\,\mathbf{1},\,+1)$
Higgs, higgsinos	H_1	$(H_1^0\,H_1^-)$	$(\tilde{H}_1^0\,\tilde{H}_1^-)$	$(\mathbf{1},\,\mathbf{2},\,-1/2)$
	H_2	$(H_2^+\,H_2^0)$	$(\tilde{H}_2^+\,\tilde{H}_2^0)$	$(\mathbf{1},\,\mathbf{2},\,+1/2)$

Table 3.1.: Chiral supermultiplets (with their gauge representation) of the SSM. $i = 1, 2, 3$ is the generation index.

Field names	superfield	spin 1/2	spin 1	$SU(3)_C$, $SU(2)_L$, $U(1)_Y$
bino, B boson	V_1	$\tilde{B}^0$	B^0	$(\mathbf{1},\,\mathbf{1},\,0)$
winos, W bosons	V_2	$\tilde{W}^\pm$, $\tilde{W}^0$	$W^\pm$, W^0	$(\mathbf{1},\,\mathbf{3},\,0)$
gluinos, gluons	V_3	$\tilde{g}_a$	g_a	$(\mathbf{8},\,\mathbf{1},\,0)$

Table 3.2.: Gauge supermultiplets (with their gauge representation) of the SSM.

- The squarks and sleptons in Tab. 3.1 are given in the flavor basis. These can mix between different generations and between the left- and right-handed fields, leading in general to 6×6 mass matrices for each the sleptons, the down-type and the up-type squarks. However, the mixing between different generations of squarks and sleptons is highly restricted by experimental bounds on flavor-changing-neutral-currents (FCNCs) [107, 108]. Moreover, the (squared) mass terms and trilinear scalar interactions[6] which lead to the mixing between the left- and right-handed states within one generation are usually assumed to be proportional to the respective SM fermion mass and Yukawa couplings, respectively, see also Sect. 3.4. Thus, we will only consider L-R mixing for the third generation squarks and sleptons. There, we will denote the mass eigenstates by $\tilde{t}_l$, $\tilde{b}_l$ and $\tilde{\tau}_l$, respectively, with $l = 1, 2$ denoting the mass hierarchy as above.

In the SM, lepton number is accidentally conserved, i.e. lepton-number conservation is only a consequence of gauge invariance and the SM particle content. However, as we will see in Sect. 3.3.2, lepton-number is not protected by gauge invariance in the SSM and in fact can be violated. In Tab. 3.1, we observe that the lepton and Higgs superfields have the same quantum numbers after EWSB. Thus, if lepton-number is violated, the lepton and Higgs superfields can mix. We will then have [17]

- Mixing between neutralinos and neutrinos given by a 7×7 mass matrix.
- Mixing between charginos and charged leptons. We will have a 5×5 mass matrix then.
- Mixing between charged sleptons and charged Higgs scalars by a 8×8 mass matrix. We have one zero mass eigenstate which corresponds to a Goldstone boson of EWSB.
- Mixing between sneutrinos and neutral Higgs scalars. Assuming CP conservation, there are two 5×5 mass matrices: One mixes the CP-even part of the sneutrino fields with

---

[6] These terms break supersymmetry explicitly. They will be discussed in Sect. 3.3.4.

the CP-even Higgs fields, and the other mixes the CP-odd part of the sneutrino fields with the CP-odd Higgs fields. The latter mass matrix possesses again a zero mass eigenstate, corresponding to a Goldstone boson. The CP-even sneutrinos can get non-zero vacuum-expectation-values (vevs) after EWSB. However, in order to avoid unphysically large neutrino masses, these vevs must be small [17].

3.3.2. Superpotential and Proton Decay

In a renormalizable supersymmetric field theory[7], the interactions and masses of all particles are determined just by their gauge transformation properties and by the superpotential W, which is a holomorphic function of the chiral superfields. With the field content given in Tab. 3.1, the most general gauge invariant and renormalizable superpotential of the SSM is [109, 110]

$$W_{\mathrm{SSM}} = W_{\mathrm{P}_6} + W_{\not{\mathrm{P}}_6}, \tag{3.10}$$

$$W_{\mathrm{P}_6} = \epsilon_{ab}\left[(\mathbf{Y}_E)_{ij} L_i^a H_1^b \bar{E}_j + (\mathbf{Y}_D)_{ij} Q_i^{ax} H_1^b \bar{D}_{jx} + (\mathbf{Y}_U)_{ij} Q_i^{ax} H_2^b \bar{U}_{jx} + \mu H_1^a H_2^b\right], \tag{3.11}$$

$$W_{\not{\mathrm{P}}_6} = \epsilon_{ab}\left[\frac{1}{2}\lambda_{ijk} L_i^a L_j^b \bar{E}_k + \lambda'_{ijk} L_i^a Q_j^{bx} \bar{D}_{kx} + \kappa_i L_i^a H_2^b\right] + \frac{1}{2}\epsilon_{xyz}\lambda''_{ijk} \bar{U}_i^x \bar{D}_j^y \bar{D}_k^z, \tag{3.12}$$

where $i, j, k = 1, 2, 3$ are generation indices, $a, b = 1, 2$ are $SU(2)$ indices and $x, y, z = 1, 2, 3$ are $SU(3)$ color indices. We follow the notation of [17].

We divided the superpotential, Eq. (3.10), into two parts[8]. The first part, W_{P_6}, involves the 3×3 Yukawa matrices for the leptons, $\mathbf{Y}_E$, down-quarks, $\mathbf{Y}_D$, and up-quarks, $\mathbf{Y}_U$. These give masses to the leptons and quarks after EWSB. μ is the Higgs mixing parameter, which contributes to the Higgs masses.

While these interactions conserve baryon- and lepton-number, the second part, $W_{\not{\mathrm{P}}_6}$, contains baryon-number-violating (BNV) and lepton-number-violating (LNV) operators. Expanded in standard four-component Dirac notation, the trilinear interaction terms associated with the λ, λ' and λ'' couplings read, respectively

$$\mathcal{L}_{L_i L_j \bar{E}_k} = -\frac{1}{2}\lambda_{ijk}\left(\tilde{\nu}_L^i \ell_L^j \bar{\ell}_R^k + \tilde{\ell}_L^j \bar{\ell}_R^k \nu_L^i + (\tilde{\ell}_R^k)^* (\bar{\nu}_L^i)^c \ell_L^j - (i \leftrightarrow j)\right) + \text{h.c.}, \tag{3.13}$$

$$\begin{aligned}\mathcal{L}_{L_i Q_j \bar{D}_k} = -\lambda'_{ijk}\Big(&\tilde{\nu}_L^i d_L^j \bar{d}_R^k + \tilde{d}_L^j \bar{d}_R^k \nu_L^i + (\tilde{d}_R^k)^* (\nu_L^i)^c d_L^j \\ &-\tilde{\ell}_L^i u_L^j \bar{d}_R^k - \tilde{u}_L^j \bar{d}_R^k \ell_L^i - (\tilde{d}_R^k)^* (\ell_L^i)^c u_L^j\Big) + \text{h.c.},\end{aligned} \tag{3.14}$$

$$\mathcal{L}_{\bar{U}_i \bar{D}_j \bar{D}_k} = -\frac{1}{2}\lambda''_{ijk}\left((\tilde{u}_R^i)^* \bar{d}_R^j (\bar{d}_R^k)^c + (\tilde{d}_R^k)^* \bar{u}_R^i (\bar{d}_R^j)^c + (\tilde{d}_R^j)^* \bar{u}_R^i (\bar{d}_R^k)^c\right) + \text{h.c.}. \tag{3.15}$$

Here, the superscript ^{c} denotes the charge conjugate of a spinor and the superscript * the complex conjugate of a scalar field. We suppressed the summation over gauge indices. The terms proportional to λ'', Eq. (3.15), violate baryon number, whereas the terms proportional to λ, λ' and κ, Eq. (3.13), Eq. (3.14) and the bilinear term in Eq. (3.12), violate lepton number. In Fig. 3.3, we give some example Feynman diagrams, which arise from these interactions.

However, BNV and LNV terms can not be simultaneously present in the theory, otherwise the proton will decay rapidly [111, 112, 113, 114, 115]. This is in contradiction with experiments

---

[7] Once we consider a broken supersymmetric field theory, the soft SUSY-breaking Lagrangian $\mathcal{L}_{\mathrm{soft}}$ must be taken into account (see Sec. 3.3.4).

[8] The terminology of P_6 and $\not{\mathrm{P}}_6$ will become clear in section 3.3.3.

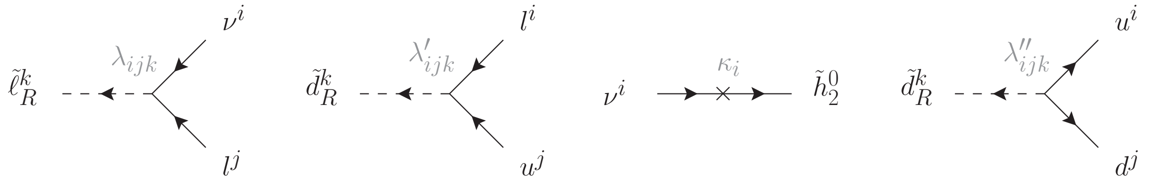

(a) (b) (c) (d)

Figure 3.3.: Lepton-number violating (a,b,c) and baryon-number violating (d) interactions. Diagram (a) corresponds to the third term in Eq. (3.13), (b) shows the sixth term in Eq. (3.14), and (d) gives the third term in Eq. (3.15). The bilinear interaction (c) is contained in the term $\kappa_i L^a_i H^b_2$ in Eq. (3.12).

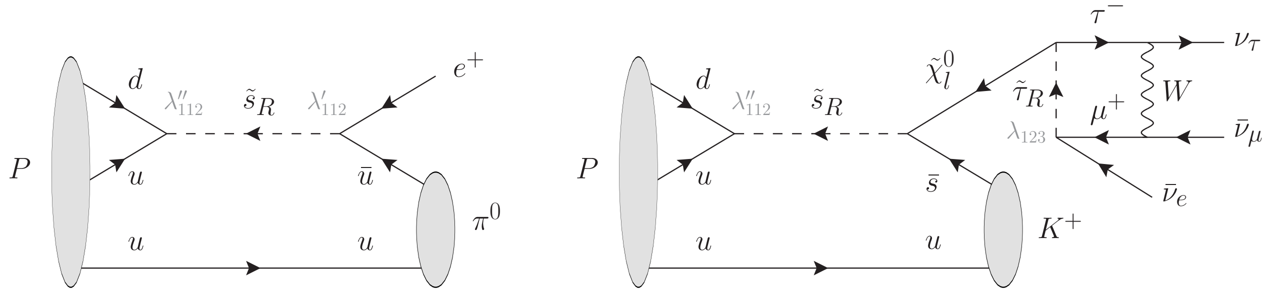

Figure 3.4.: Proton decay $P \to \pi^0 e^+$ via non-vanishing couplings $\lambda'_{112} \times \lambda''_{112}$ (*left figure*) and $P \to K^+ \nu_\tau \bar{\nu}_e \bar{\nu}_\mu$ via non-vanishing couplings $\lambda_{123} \times \lambda''_{112}$ (*right figure*).

[116, 117] and the proton lifetime [118] puts strict bounds on the products of BNV and LNV couplings. In Fig. 3.4 we give an example for the proton decays $P \to \pi^0 e^+$ (left figure) and $P \to K^+ \nu_\tau \bar{\nu}_e \bar{\nu}_\mu$ (right figure), mediated by a non-vanishing product $\lambda'_{112} \times \lambda''_{112}$ and $\lambda_{123} \times \lambda''_{112}$, respectively. Non-observation of proton decay yields the following bounds on these coupling products [115]:

$$|\lambda'_{112}\lambda''_{112}| \lesssim 2 \times 10^{-27} \left(\frac{M_{\tilde{s}_R}}{100 \text{ GeV}}\right)^2, \tag{3.16}$$

$$|\lambda_{123}\lambda''_{112}| \lesssim 10^{-14}. \tag{3.17}$$

In Eq. (3.17) a common sparticle mass of 1 TeV was assumed. Hence, even for loop-suppressed proton decays (*e.g.* right diagram in Fig. 3.4), the proton lifetime still puts a strict upper bound on (all) products of LNV and BNV couplings. Since the Yukawa couplings λ, λ' and λ'' are dimensionless parameters, it would be unnatural if they were extremely small but non-zero. Thus we need a symmetry to prohibit either BNV or LNV.

3.3.3. Discrete Symmetries

One way to prohibit LNV or BNV, and thus protect the proton from its supersymmetric death, is to introduce a discrete symmetry. The discrete symmetry has to be a remnant of a broken gauge symmetry[9], because otherwise, it will be broken by quantum gravity effects once gravity is included [119]. Requiring the discrete symmetry to be consistent with an underlying anomaly-

---

[9] Discrete symmetries of this kind are called *discrete gauge symmetries.*

free[10] $U(1)$ gauge symmetry and to allow a Majorana neutrino mass term[11] LLH_2H_2, only three possibilities are left [113, 122, 123, 124, 125]: R-parity (R_p), baryon-triality (B_3), and proton-hexality (P_6). The most popular choice is the $\mathbb{Z}_2$-symmetry R_p, usually defined as:

$$\mathrm{R}_p = (-1)^{2S+3B+L} = \begin{cases} +1 & \text{for SM particles} \\ -1 & \text{for SUSY particles} \end{cases} \tag{3.18}$$

Here, S, B and L denote the spin, baryon number and lepton number of a particle, respectively. Consequently, all SM (SUSY) particles are even (odd) under R-parity. An equivalent symmetry is matter-parity M_2

$$\begin{aligned} \{H_1, H_2\} &\to \{H_1, H_2\}, \\ \{L_i, \bar{E}_i, Q_i, \bar{U}_i, \bar{D}_i\} &\to e^{2\pi i/2}\{L_i, \bar{E}_i, Q_i, \bar{U}_i, \bar{D}_i\}. \end{aligned} \tag{3.19}$$

Both symmetries forbid all terms in $W_{\not{P}_6}$, Eq. (3.12). The minimal supersymmetric extension of the Standard Model (MSSM) is given by the particle content of Sec. 3.3.1 and the assumption of R_p (or M_2). In the MSSM, an important phenomenological feature is that SUSY particles can only be produced (and annihilated) pairwise. Once SUSY particles are produced, they will decay into the lightest supersymmetric particle (LSP), which cannot further decay due to the symmetry. Thus, it is a promising dark matter candidate. However, the latter requires the LSP to be charge-, flavor- and color-neutral. Therefore, SUSY models with R-parity conservation generally assume the lightest neutralino $\tilde{\chi}_1^0$ to be the LSP [91].

However, while these symmetries forbid all dimension-4 proton decay operators, the dimension-5 proton decay operators $QQQL$ and $\bar{U}\bar{U}\bar{D}\bar{E}$, both violating baryon- and lepton number, are still allowed [17]. These operators lead to suppressed proton decay.

The second possible discrete gauge symmetry, baryon triality B_3, is defined by the following $\mathbb{Z}_3$-transformation of the left-chiral superfields:

$$\begin{aligned} Q_i &\to Q_i, \\ \{H_2, \bar{D}_i\} &\to e^{2\pi i/3}\{H_2, \bar{D}_i\}, \\ \{H_1, \bar{U}_i, L_i, \bar{E}_i\} &\to e^{4\pi i/3}\{H_1, \bar{U}_i, L_i, \bar{E}_i\}. \end{aligned} \tag{3.20}$$

This symmetry prohibits the BNV operator $\bar{U}\bar{U}\bar{D}$ but allows the LNV terms in $W_{\not{P}_6}$, Eq. (3.12). In addition, the dangerous dimension-5 proton decay operators, which were allowed by R-parity, are forbidden by baryon triality.

Finally, we have the $\mathbb{Z}_6$-symmetry proton-hexality, which is isomorphic to the direct product of matter parity and baryon triality, $P_6 \cong \mathrm{M}_2 \times \mathrm{B}_3$:

$$\begin{aligned} Q_i &\to Q_i, \\ \{H_1, \bar{U}_i, \bar{E}_i\} &\to e^{2\pi i/6}\{H_1, \bar{U}_i, \bar{E}_i\}, \\ L_i &\to e^{8\pi i/6} L_i, \\ \{H_2, \bar{D}_i\} &\to e^{10\pi i/6}\{H_2, \bar{D}_i\} \end{aligned} \tag{3.21}$$

---

[10] Note, that anomalies can be cancelled by the introduction of new fields, see e.g. [120, 121]. We shall not consider this possibility here.

[11] The non-renormalizable five-dimensional operator LLH_2H_2 violates lepton-number by $\Delta L = 2$. It is necessary for the generation of neutrino masses in models, which prohibit lepton number violation at the renormalizable level.

Proton hexality has the same phenomenological consequences as R-parity, but forbids the dangerous dimension-5 proton decay operators.

In order to forbid proton decay, one might want to only forbid the LNV terms and allow the BNV term $\bar{U}\bar{D}\bar{D}$ in the superpotential via a discrete symmetry called lepton parity. However, it turned out that this discrete symmetry is not consistent with the requirement that it has to be a remnant of a broken anomaly-free gauge symmetry [17]. Thus, from this point of view, lepton number violation seems to be favored over baryon number violation.

Finally, we want to note that both B_3 and P_6 treat quark and lepton superfields differently. In grand unified theories (GUTs) this is unnatural[12]. However, there are string models which can successfully incorporate both lepton- and baryon-number violation [126]. Concerning proton decay, there is no preference between P_6 and B_3. However, lepton-number-violation will have some important phenomenological consequences, as discussed in Sec. 3.4.3.

3.3.4. Supersymmetry breaking

A realistic phenomenological model must contain supersymmetry breaking, since SUSY particles with equal mass as their SM partners are ruled out by experiment. We expect supersymmetry to be spontaneously broken. In this way, supersymmetry is hidden at low energies analogous to the electroweak symmetry in the SM. However, there is no consensus on exactly how the SUSY breaking should be done and many models of spontaneous symmetry breaking have been proposed. For phenomenological studies, it is very useful to parametrize our ignorance of these issues by adding extra interaction terms to the supersymmetrized SM Lagrangian, which break supersymmetry explicitly. The SUSY-breaking couplings should be *soft* (i.e. of positive mass dimension) in order not to reintroduce quadratic divergencies in quantum corrections to scalar masses, which would spoil the natural solution of the hierarchy problem. The most general form of explicit SUSY-breaking consistent with P_6 and the minimal particle content of the SSM is[13] [127, 128]

$$\begin{aligned} -\mathcal{L}_{\mathrm{soft}}^{\mathrm{P}_6} = & \left(\frac{1}{2}M_1\tilde{B}\tilde{B} + \frac{1}{2}M_2\tilde{W}\tilde{W} + \frac{1}{2}M_3\tilde{g}\tilde{g} + \mathrm{h.c.}\right) + m_{H_1}^2 H_1^\dagger H_1 + m_{H_2}^2 H_2^\dagger H_2 \\ & + \tilde{L}_i^\dagger (\mathbf{m}^{\mathbf{2}}_{\tilde{\mathbf{L}}})_{ij}\tilde{L}_j + \tilde{\bar{E}}_i^\dagger (\mathbf{m}^{\mathbf{2}}_{\tilde{\mathbf{E}}})_{ij}\tilde{\bar{E}}_j + \tilde{Q}_i^\dagger (\mathbf{m}^{\mathbf{2}}_{\tilde{\mathbf{Q}}})_{ij}\tilde{Q}_j + \tilde{\bar{U}}_i^\dagger (\mathbf{m}^{\mathbf{2}}_{\tilde{\mathbf{U}}})_{ij}\tilde{\bar{U}}_j + \tilde{\bar{D}}_i^\dagger (\mathbf{m}^{\mathbf{2}}_{\tilde{\mathbf{D}}})_{ij}\tilde{\bar{D}}_j \\ & \Big[-\tilde{B}H_1H_2 + (\mathbf{h}_E)_{ij}\tilde{L}_iH_1\tilde{\bar{E}}_j + (\mathbf{h}_D)_{ij}\tilde{Q}_iH_1\tilde{\bar{D}}_j + (\mathbf{h}_U)_{ij}\tilde{Q}_iH_2\tilde{\bar{U}}_j + \mathrm{h.c.}\Big] . \end{aligned} \tag{3.22}$$

Here, $\tilde{F} \in \{\tilde{Q}, \tilde{\bar{U}}, \tilde{\bar{D}}, \tilde{\bar{E}}, \tilde{L}\}$ denotes the scalar component of the corresponding chiral superfield, *cf.* Tab. 3.1. We sum over repeated (generation) indices while we have suppressed the summation over the gauge indices.

In the first row we have the mass terms for the gauginos and the Higgs scalars. M_1, M_2 and M_3 refer to the masses of the bino, the three winos and the eight gluinos, respectively. In the second row, we have the soft breaking scalar masses, $\mathbf{m}_{\tilde{\mathbf{F}}}{}^2$, of the corresponding scalar fields $\tilde{F}$. The last row contains the scalar interactions that correspond to the Yukawa couplings in the superpotential, Eq. (3.11). The first (bilinear) interaction contributes to the Higgs masses while the three trilinear scalar interaction terms contribute to the slepton and squark masses. After

---

[12] See e.g. Ref. [17] for a discussion of the GUT gauge groups $SU(5)$ and $SO(10)$.

[13] It is clear by looking at Eq. (3.22), that $\mathcal{L}_{\mathrm{soft}}^{\mathrm{P}_6}$ breaks supersymmetry, since it involves only fields without their superpartners.

EWSB, these terms mix the left- and right-handed sleptons and squarks. The soft-breaking scalar masses as well as the trilinear scalar interactions are 3 × 3 matrices in generation space.

With the supersymmetrization of the SM, there are (except for extending the Higgs sector) no additional parameters introduced. However, $\mathcal{L}_{\text{soft}}^{\mathrm{P}_6}$, Eq. (3.22), comes along with 105 new parameters, which have no counterpart in the SM. Thus, the P_6-SSM contains 124 independent parameters (including the SM parameters) [128]. In this extensive parameter space, phenomenological studies are very difficult. Thus we will need a guiding principle to reduce the amount of free parameters. We will address this issue in Sect. 3.4.

If the baryon- and lepton-number violating terms in Eq. (3.12) are allowed, we also need to add the following bilinear and trilinear interactions to the soft-breaking Lagrangian, Eq. (3.22), [17]:

$$\begin{aligned}-\mathcal{L}_{\text{soft}}^{\not{\mathrm{P}}_6} = &\Big[-\tilde{D}_i\tilde{L}_iH_2 + (\mathbf{h}_{E^k})_{ij}\tilde{L}_i\tilde{L}_j\tilde{\bar{E}}_k + (\mathbf{h}_{D^k})_{ij}\tilde{L}_i\tilde{Q}_j\tilde{\bar{D}}_k + (\mathbf{h}_{U^i})_{jk}\tilde{\bar{U}}_i\tilde{\bar{D}}_j\tilde{\bar{D}}_k + \text{h.c.}\Big]\\ &+\tilde{L}_i^\dagger(\mathbf{m}^2_{\tilde{L}_iH_1})H_1 + H_1^\dagger(\mathbf{m}^2_{H_1\tilde{L}_i})\tilde{L}_i \qquad (3.23)\end{aligned}$$

In the first row, we have the mass dimension two bilinear couplings $\tilde{D}_i$ and the mass dimension one trilinear couplings $(\mathbf{h}_{E^k})_{ij}$, $(\mathbf{h}_{D^k})_{ij}$ and $(\mathbf{h}_{U^i})_{jk}$, which are the soft-breaking analogue of the bilinear and trilinear couplings κ_i, λ_{ijk}, λ'_{ijk} and λ''_{ijk} of the superpotential, Eq. (3.12), respectively. The terms in the second row are mass terms, which contribute to the slepton-Higgs mass matrices.

If baryon- and lepton-number violation are allowed, we get 48 new parameters in the superpotential $W_{\not{\mathrm{P}}_6}$, Eq. (3.12), and again more than 100 new parameters from the soft-breaking terms in Eq. (3.23) in addition to those of the P_6-SSM.

3.4. Minimal Supergravity (mSUGRA)

3.4.1. Phenomenological motivation

Fortunately, there exists already experimental evidence for an underlying organizing principle that governs the soft SUSY breaking. Following this principle, the overwhelming amount of free parameters introduced in Eq. (3.22) can be significantly reduced.

In order to have a real Lagrangian, the slepton and squark mass matrices in Eq. (3.22) need to be hermitian. We might generically assume that the generational diagonal and off-diagonal matrix elements in Eq. (3.22) have the same order of magnitude. However, assuming that the SUSY breaking is $\lesssim \mathcal{O}(1\text{ TeV})$, the large generational off-diagonal matrix elements would lead to large flavor-changing-neutral-currents (FCNCs). These are in contradiction with experimental observations [107, 108], and thus, the low-scale SSM would be phenomenologically excluded. For instance, the matrix elements which couple the scalar electron (selectron) to the scalar muon (smuon) are strongly constrained by the non-observation of the process $\mu \to e\gamma$ [107, 129, 130]. In the squark sector, experimental constraints from meson-antimeson mixing like $K^0 - \bar{K}^0$, $D^0 - \bar{D}^0$ and $B^0 - \bar{B}^0$ mixing and rare processes like $b \to s\gamma$ strongly restrict the magnitude of the generational off-diagonal masses [107, 131, 132, 133, 134]. Note that bounds involving third-generation fields are in general less restrictive than those involving only fields of the first and second generation.

In principle, the P_6 SSM may also introduce 40 additional physical phases [135], which all introduce CP-violating effects. Again, these phases are strongly restricted by experimental observations, mainly from electric dipole moments (EDMs) [118, 107, 132, 134, 136, 137, 138, 139, 140, 141, 142].

All of these potentially dangerous flavor-changing and CP violating effects in the SSM can be avoided by assuming that supersymmetry breaking is *universal*, *i.e.* we assume that at the weak scale, M_Z, the squark and slepton squared-mass matrices are flavor-blind, each proportional to the 3×3 identity matrix in family space:

$$\mathbf{m}^2_{\tilde{\mathbf{L}}} = m^2_{\tilde{L}} \times \mathbb{1}, \ \mathbf{m}^2_{\tilde{\mathbf{E}}} = m^2_{\tilde{E}} \times \mathbb{1}, \ \mathbf{m}^2_{\tilde{\mathbf{Q}}} = m^2_{\tilde{Q}} \times \mathbb{1}, \ \mathbf{m}^2_{\tilde{\mathbf{U}}} = m^2_{\tilde{U}} \times \mathbb{1}, \ \mathbf{m}^2_{\tilde{\mathbf{D}}} = m^2_{\tilde{D}} \times \mathbb{1}. \tag{3.24}$$

Note that also other solutions exist [143, 144, 145, 146, 147, 148].

The trilinear scalar couplings $\mathbf{h}_E$, $\mathbf{h}_D$ and $\mathbf{h}_U$ in Eq. (3.22) couple left- and right-handed fields to each other. Thus, after EWSB, they will also contribute to the squark and slepton mass matrices and may induce large FCNCs. This can be avoided if we choose

$$\mathbf{h}_E = A_E \times \mathbf{Y}_E, \quad \mathbf{h}_D = A_D \times \mathbf{Y}_D, \quad \mathbf{h}_U = A_U \times \mathbf{Y}_U, \tag{3.25}$$

i.e. we assume that the trilinear couplings are proportional to the respective Yukawa coupling matrix at M_Z. In this way, their contributions are only significant for the third generation.

3.4.2. The P_6 mSUGRA model and its mass spectrum

As already mentioned in Sect. 3.1, a strong motivation for SUSY is the gauge coupling unification at a scale of $\mathcal{O}(10^{16}$ GeV). Assuming the SSM is embedded into a grand unification theory (GUT), the gauginos can naturally have equal masses at the GUT scale, M_{GUT}, *cf.* Eq. (3.22), because they are all in the same representation of the unified simple gauge group [54, 149, 150]. We thus have

$$M_1 = M_2 = M_3 \equiv M_{1/2} \qquad \text{at} \qquad M_{\mathrm{GUT}}. \tag{3.26}$$

In this context, it seems natural to rather assume the boundary conditions, Eq. (3.24) and Eq. (3.25), at M_{GUT}. Furthermore, we can simplify the model by assuming[14] an universal soft breaking scalar mass, M_0, for all the sfermions and Higgs fields and an universal trilinear interaction, A_0, *i.e.*

$$m^2_{\tilde{L}} = m^2_{\tilde{E}} = m^2_{\tilde{Q}} = m^2_{\tilde{D}} = m^2_{\tilde{U}} = m^2_{H_1} = m^2_{H_2} \equiv M_0 \qquad \text{at} \qquad M_{\mathrm{GUT}}, \tag{3.27}$$

$$A_E = A_D = A_U \equiv A_0 \qquad \text{at} \qquad M_{\mathrm{GUT}}. \tag{3.28}$$

The only missing ingredient for a complete model is the parametrization of the Higgs sector. A convenient choice are the parameters $\tan\beta$ and $\mathrm{sgn}(\mu)$, where $\tan\beta = \langle H_2 \rangle / \langle H_1 \rangle$ is the ratio of the vevs of the two Higgs doublets and $\mathrm{sgn}(\mu)$ is the sign of the Higgs mixing parameter μ, *cf.* Eq. (3.11). The magnitude of μ and the corresponding soft breaking coupling $\tilde{B}$, *cf.* Eq. (3.22), are derived from EWSB, *i.e.* from the minimization of the scalar potential [152].

With these simple assumptions at the GUT scale, we reduced the more than 100 parameters

---

[14] Note that, due to the RGE running, the scalar masses and trilinear interaction are in general not universal at M_Z, which can lead again to FCNCs. However, these are small and consistent with experimental observations as long as P_6 is conserved [151]. If P_6 is violated, we need to make sure that the FCNCs are not too large. This will be done throughout this thesis.

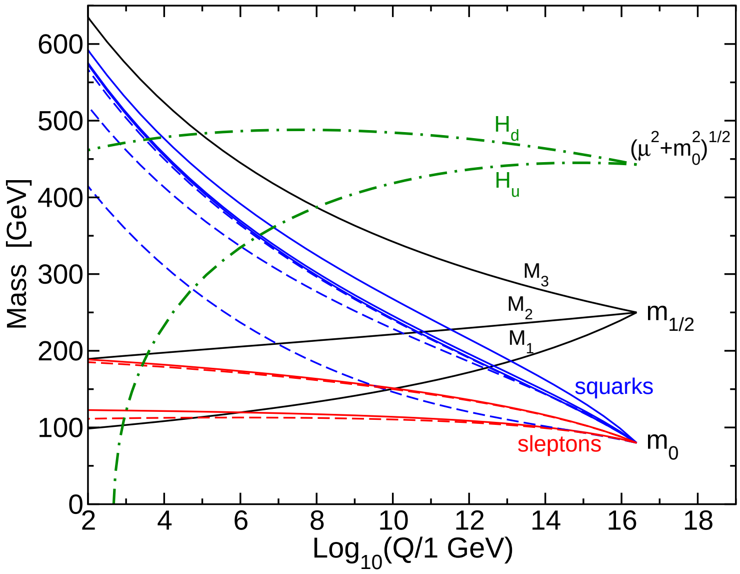

Figure 3.5.: RGE running of the slepton (red lines), squark (blue lines) and gaugino (black lines) soft-breaking masses from M_{GUT} to M_Z. Also shown is the running of the quantities $(\mu^2 + m^2_{H_1})^{1/2}$ and $(\mu^2 + m^2_{H_2})^{1/2}$. The latter runs negative, provoking electroweak symmetry breaking. This figure is taken from Ref. [58]. Note the slightly different notation, where $H_d \equiv H_1$ and $H_u \equiv H_2$.

of the P$_6$ SSM to only five:

$$M_0,\ M_{1/2},\ A_0,\ \tan\beta,\ \mathrm{sgn}(\mu). \tag{3.29}$$

This well-motivated and strongly restricted model for the SSM is known as the *minimal supergravity* (mSUGRA) model[15]. In the class of *supergravity* models [78, 79, 80, 81, 82, 83, 84], SUSY is a local symmetry and the theory can thus incorporate gravity. By imposing certain simplifying assumptions about the supergravity Lagrangian, we also obtain the minimal supergravity model [153, 154, 155, 156]. Thus, this model is also well motivated from a purely theoretical side.

We obtain the (experimentally accessible) particle mass spectrum at M_Z by evolution of the RGEs, *cf.* also Sect. 2.4. This is demonstrated in Fig. 3.5, where we show the running of the scalar and gaugino soft breaking masses from M_{GUT} to M_Z for a typical mSUGRA model. The input parameters at M_{GUT} are $M_0 = 80$ GeV, $M_{1/2} = 250$ GeV, $A_0 = -500$ GeV, $\tan\beta = 10$ and $\mathrm{sgn}(\mu) = +$. The running gaugino masses (black solid lines) are labeled by M_1, M_2 and M_3. For the squarks (blue lines) and sleptons (red lines), the dashed lines give the third family soft breaking masses while the solid lines correspond to those of the first and second family. Furthermore, the figure shows the running of the quantities $(\mu^2 + m^2_{H_1})^{1/2}$ and $(\mu^2 + m^2_{H_2})^{1/2}$, labeled by H_d and H_u, respectively, which appear in the Higgs potential. The figure is taken from Ref. [58].

We observe in Fig. 3.5, that the squarks and sleptons evolve very differently, *i.e.* although they have the same mass at M_{GUT}, the squarks are much heavier than the sleptons at M_Z. This can be understood, if we look at the dominant one-loop contributions to the RGEs for the

---

[15] This model is sometimes also denoted as the constrained minimal supersymmetric standard model (CMSSM), since the SUSY breaking does not necessarily have to be mediated by gravity.

squared slepton and squark soft breaking masses of the first two generations ($i = 1, 2$) [17]

$$16\pi^2 \frac{d(\mathbf{m}_{\tilde{\mathbf{E}}}{}^2)_{ii}}{dt} = -\left(\frac{24}{5} g_1^2 |M_1|^2 - \frac{6}{5} g_1^2 \mathcal{S}\right), \tag{3.30}$$

$$16\pi^2 \frac{d(\mathbf{m}_{\tilde{\mathbf{L}}}{}^2)_{ii}}{dt} = -\left(\frac{24}{5} g_1^2 |M_1|^2 + 6 g_2^2 |M_2|^2 + \frac{3}{5} g_1^2 \mathcal{S}\right), \tag{3.31}$$

$$16\pi^2 \frac{d(\mathbf{m}_{\tilde{\mathbf{U}}}{}^2)_{ii}}{dt} = -\left(\frac{32}{15} g_1^2 |M_1|^2 + \frac{32}{3} g_3^2 |M_3|^2 + \frac{4}{5} g_1^2 \mathcal{S}\right), \tag{3.32}$$

$$16\pi^2 \frac{d(\mathbf{m}_{\tilde{\mathbf{D}}}{}^2)_{ii}}{dt} = -\left(\frac{8}{15} g_1^2 |M_1|^2 + \frac{32}{3} g_3^2 |M_3|^2 - \frac{2}{5} g_1^2 \mathcal{S}\right), \tag{3.33}$$

$$16\pi^2 \frac{d(\mathbf{m}_{\tilde{\mathbf{Q}}}{}^2)_{ii}}{dt} = -\left(\frac{2}{15} g_1^2 |M_1|^2 + 6 g_2^2 |M_2|^2 + \frac{32}{3} g_3^2 |M_3|^2 - \frac{1}{5} g_1^2 \mathcal{S}\right), \tag{3.34}$$

with

$$\mathcal{S} = \mathrm{Tr}[\mathbf{m}_{\tilde{\mathbf{Q}}}{}^2 - \mathbf{m}_{\tilde{\mathbf{L}}}{}^2 - 2\mathbf{m}_{\tilde{\mathbf{U}}}{}^2 + \mathbf{m}_{\tilde{\mathbf{D}}}{}^2 + \mathbf{m}_{\tilde{\mathbf{E}}}{}^2] - m_{H_1}^2 + m_{H_2}^2. \tag{3.35}$$

Here, g_1, g_2 and g_3 are the $U(1)_Y$, $SU(2)$ and $SU(3)_C$ gauge couplings, respectively, and $t = \ln Q$ with Q the renormalization scale. For universal scalar masses, $\mathcal{S}$ is identical to zero at M_{GUT}. Furthermore, the coefficient of the $\mathcal{S}$ term is smaller compared to the M_1^2, M_2^2 and M_3^2 terms. Thus, the main contributions come from the terms proportional to the gaugino mass squared, M_1^2, M_2^2 and M_3^2, and the right hand side of Eqs. (3.30)-(3.34) is negative at every scale.

Evolving the RGEs from M_{GUT} down to M_Z, the negative slope in the RGEs increases the slepton and squark masses, as we can observe in Fig. 3.5. The proportionality to different gauge charges in Eqs. (3.30)-(3.34) leads to the various magnitudes of the slopes. They are largest for the strongly interacting sparticles and therefore, the squarks are much heavier then the sleptons. There is also a mass splitting between left- and right-handed sleptons, which can be explained in a similar way: The right-handed sleptons only couple via their $U(1)_Y$ gauge charges whereas the left-handed sleptons also couple via their $SU(2)$ gauge charges and thus get larger contributions from the gaugino masses. Therefore, the left-handed sleptons are heavier than the right-handed sleptons.

The third generation squarks and sleptons are generally lighter then the first and second generation masses. This has the following reason: The Higgs-Yukawa interactions for the third generation are roughly as strong as the gauge interactions. Therefore, they significantly contribute to the RGEs of the third generation sparticles. For instance, the dominant contribution to the RGE of the right-handed (soft breaking) stop mass squared is [17]

$$\begin{aligned} 16\pi^2 \frac{d(\mathbf{m}_{\tilde{\mathbf{U}}}{}^2)_{33}}{dt} = &-\left(\frac{32}{15} g_1^2 |M_1|^2 + \frac{32}{3} g_3^2 |M_3|^2 + \frac{4}{5} g_1^2 \mathcal{S}\right) \\ &+ (\mathbf{Y}_U)_{33}^2 \left[4(\mathbf{m}_{\tilde{\mathbf{U}}}{}^2)_{33} + 4(\mathbf{m}_{\tilde{\mathbf{Q}}}{}^2)_{33} + 4m_{H_2}^2\right] + 4(\mathbf{h}_U)_{33}^2, \end{aligned} \tag{3.36}$$

with $(\mathbf{h}_U)_{33} = (\mathbf{Y}_U)_{33} \times A_0$ at M_{GUT}. In contrast to Eq. (3.32), the large top-Yukawa coupling, $(\mathbf{Y}_U)_{33}$, and the corresponding trilinear scalar interaction, $(\mathbf{h}_U)_{33}$, additionally affect the running of the right-handed stop mass. These new terms in Eq. (3.36) are always positive and therefore tend to decrease the stop mass going from M_{GUT} to M_Z. Thus, the third generation sfermions are in general lighter than those of the first and second generation. Furthermore, we can have large mixing between left- and right-handed eigenstates for the third generation, which additionally decreases the mass of the lighter mass eigenstate.

The up-type Higgs doublet H_2 also couples directly to the top-Yukawa sector. This leads to a large decrease of the up-type Higgs mass parameter, m_{H_2}, going from M_{GUT} to M_Z, *cf.* Fig. 3.5. The quantity $(\mu^2 + m_{H_2}^2)$ even runs to negative values at the electroweak scale $\mathcal{O}(10^2\ \mathrm{GeV})$. This effect leads to radiative electroweak symmetry breaking [90]. Thus, the large top-Yukawa coupling induces a dynamical breakdown of the electroweak symmetry. By fixing $\tan\beta$, Eq. (3.29), the magnitude of the Higgs mixing parameter μ and the corresponding soft breaking coupling $\tilde{B}$ are obtained from the minimization of the scalar Higgs potential [152].

In Fig. 3.5 we observe the mass ordering of the gauginos, $M_1 < M_2 < M_3$ at M_Z. This is because the RGEs for the three gaugino mass parameters are determined by the same coefficients b_i, which describe the running of the gauge couplings [157]:

$$16\pi^2 \frac{dM_i}{dt} = 2 b_i g_i^2 M_i, \qquad \text{with} \qquad b_i = \{33/5, 1, -3\}, \tag{3.37}$$

for the gauge group index $i = 1, 2, 3$. As for the gauge coupling g_3, *cf.* Sect. 2.5, the mass of the $SU(3)_C$ gaugino, M_3, increases due to the negative coefficient b_3 when going from M_{GUT} to M_Z. In contrast, the masses of the bino, M_1, and winos, M_2, decrease. At every scale, the gaugino masses are related (up to small two-loop effects) by [157]

$$\frac{M_1}{g_1^2} = \frac{M_2}{g_2^2} = \frac{M_3}{g_3^2} = \frac{M_{1/2}}{g_{\mathrm{GUT}}^2}, \tag{3.38}$$

with the universal gauge coupling $g_{\mathrm{GUT}} \simeq 0.71$ at M_{GUT}. This relation directly implies $M_3 : M_2 : M_1 \simeq 7 : 2 : 1$ at M_Z.

From Fig. 3.5, we expect the LSP to be the lightest neutralino, $\tilde{\chi}_1^0$. For the mSUGRA parameters of Fig. 3.5, we obtain $M_1 = 95$ GeV, $M_2 = 190$ GeV and $\mu = 440$ GeV at M_Z. Thus, the mixing between the bino with the wino and the Higgsinos is small [106]. For many mSUGRA models we can approximate the gaugino masses in terms of the universal gaugino mass $M_{1/2}$ [158, 159],

$$m_{\tilde{\chi}_1^0} \simeq M_1 = 0.41 M_{1/2}, \tag{3.39}$$

$$m_{\tilde{\chi}_2^0} \simeq M_2 = 0.84 M_{1/2}, \tag{3.40}$$

i.e. the (second) lightest neutralino, $\tilde{\chi}_1^0$ ($\tilde{\chi}_2^0$), is bino-like (wino-like) and its mass is approximated by the bino (wino) mass parameter M_1 (M_2) at the weak scale.

The next-to-LSP (NLSP) is a slepton. This must be the lighter (mostly right-handed) scalar tau (stau), $\tilde{\tau}_1$, due to influence of the tau-Yukawa coupling and the L-R stau mixing. However, by increasing $M_{1/2}$, the mass of the (bino-like) $\tilde{\chi}_1^0$ increases faster than the (mostly right-handed) $\tilde{\tau}_1$ mass [158, 159]. Thus, at some point, the $\tilde{\tau}_1$ becomes the LSP instead of the $\tilde{\chi}_1^0$. Note, that increasing the value of $\tan\beta$ can also lead to a $\tilde{\tau}_1$ LSP, since it both increases the magnitude of the tau-Yukawa coupling and the L-R mixing [158, 21, 12, 20]. In P_6 conserving supersymmetric models, scenarios with a $\tilde{\tau}_1$ LSP are usually ignored, because the LSP is stable and thus needs to be charge and color neutral for cosmological reasons [91]. In this case, searches at the Large Electron-Positron Collider (LEP) at CERN restrict the LSP to be the lightest neutralino [160].

3.4.3. The P_6 violating mSUGRA model

In Sect. 3.4.1 and 3.4.2 we discussed the mSUGRA model and its sparticle mass spectrum at M_Z in the case of conserved P_6. We now want to extend our discussion to the P_6 violating mSUGRA model[16], which incorporates lepton or baryon number violating interactions, Eq. (3.12) and Eq. (3.23). This model was proposed in Ref. [17]. It contains the six parameters

$$M_0,\ M_{1/2},\ A_0,\ \tan\beta,\ \mathrm{sgn}(\mu),\ \mathbf{\Lambda}, \tag{3.41}$$

with

$$\mathbf{\Lambda} \in \{\lambda_{ijk},\ \lambda'_{ijk},\ \lambda''_{ijk}\} \qquad \text{at} \qquad M_{\mathrm{GUT}}, \tag{3.42}$$

i.e. we assume one additional (real) trilinear coupling at M_{GUT}. Analogous to Eq. (3.25) and Eq. (3.28), we also have one non-vanishing $\not{\mathrm{P}}_6$ term in the soft-breaking Lagrangian, Eq. (3.23), namely $\mathbf{h}_{\mathbf{\Lambda}} = A_0 \times \mathbf{\Lambda}$ at M_{GUT}. In this model, the more than 200 parameters of the $\not{\mathrm{P}}_6$ SSM are reduced to only six, which allows for detailed phenomenological studies.

In this model, the bilinear $\not{\mathrm{P}}_6$ operators, *cf.* Eq. (3.12), are naturally rotated away at M_{GUT} by a redefinition of the lepton doublet superfields L_i and the down-type Higgs doublet H_1 [17]. However, given a non-zero λ or λ' together with $\mu \neq 0$ at M_{GUT}, non-zero bilinear terms κ_i are generated at M_Z [161, 162, 163]. These terms lead to mixing between the neutrinos and neutralinos resulting in one non-zero neutrino mass at tree-level [92, 164, 165]. The other neutrino masses are generated at loop-level [94, 96, 166]. Note, that the upper cosmological bound on the sum of neutrino masses, *i.e.* $\sum m_{\nu_i} < 0.40$ eV at 99.9% confidence level (C.L.), determined by the Wilkinson Mircowave Anisotropy Probe (WMAP) [167] and Large Scale Structure (LSS) data [168], implies upper bounds on the λ and λ' couplings [17, 166].

In general, experimental bounds on products of two different $\not{\mathrm{P}}_6$ couplings are stronger than bounds on single couplings [115, 169, 170]. Therefore, a single dominating $\mathbf{\Lambda}$ coupling is phenomenologically well motivated[17]. However, through the coupled RGEs, one $\not{\mathrm{P}}_6$ coupling at M_{GUT} will generate additional $\not{\mathrm{P}}_6$ couplings at M_Z [17, 161, 162, 163, 171, 172, 173].

In contrast to the P_6 SSM, the additional LNV and BNV interactions in the $\not{\mathrm{P}}_6$ SSM, Eq. (3.12), generally allow for the single (resonant) production of sparticles at lepton colliders [174] as well as hadron colliders [15, 175, 176, 19]. Furthermore, the LSP decays into SM particles[18]. Thus, in principle, every sparticle is allowed to be the LSP, *i.e.* a $\tilde{\tau}_1$ LSP is equally well motivated as a $\tilde{\chi}_1^0$ LSP [17, 18]. In addition, the RGEs get new $\not{\mathrm{P}}_6$ contributions which can affect the running of the sparticle masses in a significant way [17, 21], *cf.* also Sect. 4.1. Thus, other LSP candidates exist besides the $\tilde{\tau}_1$ and the $\tilde{\chi}_1^0$. Restricting ourselves to the B_3 mSUGRA model, the possible LSP candidates are [12]

$$\tilde{\chi}_1^0,\ \tilde{e}_R,\ \tilde{\mu}_R,\ \tilde{\tau}_1,\ \tilde{\nu}_i, \tag{3.43}$$

where $\tilde{e}_R$ and $\tilde{\mu}_R$ denote the right-handed scalar electron (selectron) and scalar muon (smuon), respectively. At colliders, supersymmetric particles, once they are produced, will typically decay instantaneously on collider time scales down to the LSP. Therefore, the nature and possible decay

---

[16] If only lepton number is violated, we also denote the model as B_3 mSUGRA, *cf.* Sect. 3.3.3.

[17] Note, that the SM also has a strong hierarchy of the Higgs Yukawa couplings.

[18] Thus, the LSP is not a dark matter candidate in the P_6 violating SSM. In order to account for dark matter, other candidates, such as the axino [177, 178, 179, 180, 181], gravitino [182, 183] or the lightest U-parity particle [184, 185], have to be considered.

properties of the LSP are an essential ingredient for all SUSY signatures [17, 186, 187]. Scenarios with a neutralino LSP have been studied extensively, see *e.g.* Ref. [13, 14, 15, 16]. More recently, the stau LSP [17, 18, 19, 20] and the sneutrino LSP [21] have been considered. In this thesis, we investigate in detail the case of a $\tilde{e}_R$ or $\tilde{\mu}_R$ LSP.

4. Selectron and Smuon as the lightest supersymmetric particle (LSP)

In this chapter, we investigate the conditions which lead to a selectron or smuon LSP within the B_3 mSUGRA model. For this, we study the RGE running of the right-handed slepton mass of the first and second generation. We find a strong A_0 dependence in the running, which we study in detail. Then, we discuss the selectron and smuon LSP parameter space, the corresponding experimental constraints and possible mass hierarchies of the supersymmetric particles.

4.1. Renormalization group evolution of the right-handed slepton mass

In order to understand the dependence of the $\tilde{\ell}_R$ mass[1] at M_Z on the boundary conditions at M_{GUT}, we take a closer look at the relevant RGEs. As mentioned in Sect. 3.4.3, the RGEs in B_3 mSUGRA receive additional contributions from the LNV terms in Eq. (3.12). The dominant one-loop contributions to the running of the right-handed slepton mass are [17]

$$16\pi^2 \frac{d(m^2_{\tilde{\ell}^k_R})}{dt} = -\frac{24}{5} g_1^2 |M_1|^2 + \frac{6}{5} g_1^2 \mathcal{S} + 2\lambda^2_{ijk}\left[2(\mathbf{m}_{\tilde{\mathbf{L}}}{}^2)_{ii} + 2(\mathbf{m}_{\tilde{\mathbf{L}}}{}^2)_{jj} + (\mathbf{m}_{\tilde{\mathbf{E}}}{}^2)_{kk}\right] + 2(\mathbf{h}_{\mathbf{E}^{\mathbf{k}}})^2_{ij} \tag{4.1}$$

with

$$(\mathbf{h}_{\mathbf{E}^{\mathbf{k}}})_{ij} \equiv \lambda_{ijk} \times A_0 \qquad \text{at} \quad M_{\mathrm{GUT}}. \tag{4.2}$$

Here, $(\mathbf{h}_{\mathbf{E}^{\mathbf{k}}})_{ij}$ is the trilinear scalar soft breaking coupling corresponding to λ_{ijk}, *cf.* Eq. (3.23). We neglected the contributions from the Higg-Yukawa couplings, since these are only important for the third generation sfermions, *cf.* Sect. 3.4.2.

The first two terms on the right-hand side in Eq. (4.1) are also present in the P_6 conserving mSUGRA model, *cf.* Eq. (3.30). As discussed in Sect. 3.4.2, the sum of these two terms is negative at any scale and thus leads to an increase in $m_{\tilde{\ell}_R}$ while running from M_{GUT} to M_Z.

The remaining contributions are proportional to λ^2_{ijk} and $(\mathbf{h}_{\mathbf{E}^{\mathbf{k}}})_{ij}$; the latter implies also a proportionality to λ^2_{ijk} at M_{GUT}, *cf.* Eq. (4.2). These terms are positive and will therefore reduce $m_{\tilde{\ell}_R}$, when going from M_{GUT} to M_Z. They are new to the B_3 mSUGRA model compared to P_6 conserving mSUGRA. We can see from Eq. (4.1), that if the LNV coupling is roughly of the order of the gauge coupling g_1, *i.e.* $\lambda_{ijk} \gtrsim \mathcal{O}(10^{-2})$, these terms contribute substantially. Then, the $\tilde{\ell}_R$ mass may become lower than the $\tilde{\chi}_1^0$ and $\tilde{\tau}_1$ mass at M_Z, leading to a $\tilde{\ell}_R$ LSP scenario.

---

[1] We consider only the first two generations of sleptons, i.e. $\tilde{\ell}_R \in \{\tilde{e}_R, \tilde{\mu}_R\}$.

$L_iL_j\bar{E}_k$ coupling $\mathbf{\Lambda}$	LSP candidate	2σ bound (at M_Z)
λ_{121}	$\tilde{e}_R$	$0.03 \cdot (M_{\tilde{e}_R}/100\ \text{GeV})$
λ_{131}, λ_{231}	$\tilde{e}_R$	$0.05 \cdot (M_{\tilde{e}_R}/100\ \text{GeV})$
λ_{132}	$\tilde{\mu}_R$	$0.05 \cdot (M_{\tilde{\mu}_R}/100\ \text{GeV})$

Table 4.1.: List of $L_iL_j\bar{E}_k$ couplings needed to generate a $\tilde{e}_R$ or $\tilde{\mu}_R$ LSP. The third column gives the most recent experimental bounds (95% C.L.) on $\mathbf{\Lambda}$, taken from Ref. [170].

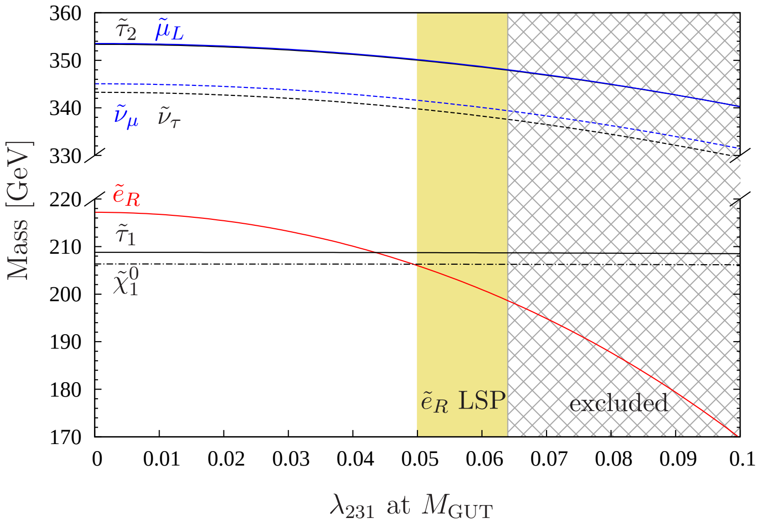

Figure 4.1.: Masses of $\tilde{e}_R$, $\tilde{\chi}_1^0$, $\tilde{\tau}_1$, $\tilde{\tau}_2$, $\tilde{\nu}_\tau$, $\tilde{\mu}_L$ and $\tilde{\nu}_\mu$ at M_Z as a function of λ_{231} at M_{GUT}. The other mSUGRA parameters are $M_0 = 150$ GeV, $M_{1/2} = 500$ GeV, $A_0 = -1000$ GeV, $\tan\beta = 5$ and $\mu > 0$. The yellow region corresponds to valid $\tilde{e}_R$ LSP scenarios. The gray patterned region is excluded by the experimental bound on λ_{231}, *cf.* Tab. 4.1.

The respective $L_iL_j\bar{E}_k$ couplings $\mathbf{\Lambda}$, which can lead[2] to a $\tilde{e}_R$ or a $\tilde{\mu}_R$ LSP, are given in Tab. 4.1 with their most recent experimental 2σ upper bounds [170]. These bounds scale with the mass of the respective right-handed slepton mass and apply at the weak scale, where the physical process occurs. Due to its RGE running, $\mathbf{\Lambda}$ at M_Z is roughly 1.5 times larger than $\mathbf{\Lambda}$ at M_{GUT} [161, 171].

In Fig. 4.1 we demonstrate the impact of a non-vanishing coupling $\lambda_{231}|_{\text{GUT}}$ on the running of the $\tilde{e}_R$ mass. We employ SOFTSUSY 3.0.13 [188, 189] for the evolution of the RGEs. We have chosen a fairly large value of $A_0 = -1000$ GeV. The other mSUGRA parameters are $M_0 = 150$ GeV, $M_{1/2} = 500$ GeV, $\tan\beta = 5$ and $\mu > 0$. In the R-parity conserving case, corresponding here to $\lambda_{231} = 0$, the $\tilde{\chi}_1^0$ is the LSP and the $\tilde{\tau}_1$ is the NLSP. The $\tilde{e}_R$ mass decreases for increasing λ_{231}, as described by Eq. (4.1). Furthermore, the masses of the left-handed[3] second and third generation sleptons, $\tilde{\mu}_L$, $\tilde{\tau}_2$, and sneutrinos, $\tilde{\nu}_\mu$, $\tilde{\nu}_\tau$, decrease, since

---

[2] In principle, λ_{212} and λ_{232} could also lead to a $\tilde{\mu}_R$ LSP. In general, these couplings generate tree-level neutrino masses that violate the neutrino mass bounds [167] in the case $\mathbf{\Lambda} \gtrsim \mathcal{O}(10^{-2})$. Note however, that at certain A_0 values, the corresponding tree-level neutrino mass can vanish [166], which reopens the possibility of a $\tilde{\mu}_R$ LSP generated via these couplings.

[3] In most mSUGRA scenarios, the heavier stau, $\tilde{\tau}_2$, contains a large left-handed component.

these SU(2) doublets couple directly via λ_{231}. Hence, λ_{231} contributes substantially[4] in their RGEs. In contrast, the mass of the $\tilde{\chi}_1^0$ is not changed, since it does not couple to the λ_{231} operator at one loop level. Also, the impact on the mass of the $\tilde{\tau}_1$, which is mostly right-handed, is small. We therefore obtain for this mSUGRA parameter set with $\lambda_{231}|_{\text{GUT}} \gtrsim 0.05$ a new LSP candidate, namely the right-handed selectron. Due to the experimental upper bound on λ_{231}, *cf.* Tab. 4.1, the gray pattered region with $\lambda_{231}|_{\text{GUT}} > 0.064$ is excluded at 95% C.L.. In Fig. 4.1, the allowed $\tilde{e}_R$ LSP region is marked in yellow. Note, that the valid parameter region with a $\tilde{e}_R$ LSP becomes larger once we consider scenarios with heavier sparticle masses. Moreover, once we go beyond the mSUGRA model and consider non-universal masses, a $\tilde{e}_R$ LSP can also be obtained without the RGE running effect discussed here. Then, $\tilde{e}_R$ LSP scenarios can exist with much smaller R-parity violating couplings. Basically, the collider study we present in this thesis, *cf.* Chapter 5, also applies to these more general $\tilde{\ell}_R$ LSP models, provided that we still have a dominant $L_i L_j \bar{E}_k$ coupling.

We can obtain a $\tilde{e}_R$ LSP ($\tilde{\mu}_R$ LSP) with a non-zero coupling λ_{121} or λ_{131} (λ_{132}) at M_{GUT} in a completely analogous way. We conclude this discussion by pointing out, that we need a $L_i L_j \bar{E}_k$ coupling $\mathbf{\Lambda} \gtrsim \mathcal{O}(10^{-2})$ to obtain a $\tilde{\ell}_R$ LSP (of flavor k). In the following, we investigate which other conditions at the GUT scale allow a $\tilde{\ell}_R$ LSP within B$_3$ mSUGRA. Therefore, we study in the next section in detail the A_0 dependence of the running $\tilde{\ell}_R$ mass. Then, we present two dimensional B$_3$ mSUGRA parameter scans with $\tilde{\ell}_R$ LSP regions in Sect. 4.3.

4.2. A_0 dependence

We now show that a large magnitude of a (negative) A_0 enhances the negative contribution to the $m_{\tilde{\ell}_R}$ mass, which originates from a non-vanishing $\lambda_{ijk}|_{\text{GUT}}$ coupling, as shown in the last section. The discussion is similar to the case of a sneutrino LSP, see Ref. [21].

According to Eqs. (4.1) and (4.2), A_0 enters the running of $m_{\tilde{\ell}_R}$ via the B$_3$ soft-breaking trilinear scalar coupling $(\mathbf{h}_{\mathbf{E}^k})_{ij}$. As t is decreased, the $(\mathbf{h}_{\mathbf{E}^k})_{ij}$-term gives a negative contribution to $m_{\tilde{\ell}_R}$. Its full contribution is proportional to the integral of $(\mathbf{h}_{\mathbf{E}^k})^2_{ij}$ over t, from $t_{\min} = \ln(M_Z)$ to $t_{\max} = \ln(M_{\text{GUT}})$.

In Fig. 4.2 we show the running of the trilinear coupling $(\mathbf{h}_{\mathbf{E}^k})_{ij}$ [Fig. 4.2(a)] and the resulting running for $(\mathbf{h}_{\mathbf{E}^k})^2_{ij}$ [Fig. 4.2(b)]. We assume a non-vanishing coupling $\lambda_{ijk}|_{\text{GUT}} = 0.1$ and a universal gaugino mass $M_{1/2} = 1000$ GeV. Different lines correspond to different values of A_0. The dominant contributions to the RGE of $(\mathbf{h}_{\mathbf{E}^k})_{ij}$ are given by [17]

$$16\pi^2 \frac{d(\mathbf{h}_{\mathbf{E}^k})_{ij}}{dt} = -(\mathbf{h}_{\mathbf{E}^k})_{ij} \left[\frac{9}{5} g_1^2 + 3 g_2^2\right] + \lambda_{ijk} \left[\frac{18}{5} g_1^2 M_1 + 6 g_2^2 M_2\right]. \tag{4.3}$$

The running is governed by two terms with opposite sign in Eq. (4.3), one proportional to $(\mathbf{h}_{\mathbf{E}^k})_{ij}$ and one proportional to λ_{ijk}. In contrast to the sneutrino LSP case, *cf.* Ref. [21], the running is independent of the strong coupling g_3 and the gluino mass M_3.

According to Eq. (4.2), the sign of the term proportional to $(\mathbf{h}_{\mathbf{E}^k})_{ij}$ in Eq. (4.3) depends on the sign of A_0. At M_{GUT}, this term is positive (negative) for negative (positive) A_0. Hence, for positive A_0, the term proportional to $(\mathbf{h}_{\mathbf{E}^k})_{ij}$ increases $(\mathbf{h}_{\mathbf{E}^k})_{ij}$ when we run from M_{GUT} to M_Z. Note, that the gauge couplings g_1 and g_2 decrease when going from M_{GUT} to M_Z.

---

[4] However, these contributions are always smaller than those to the right-handed slepton mass [17]. Thus, the left-handed sleptons and sneutrinos cannot become the LSP within B$_3$ mSUGRA with a non-zero λ_{ijk} coupling.

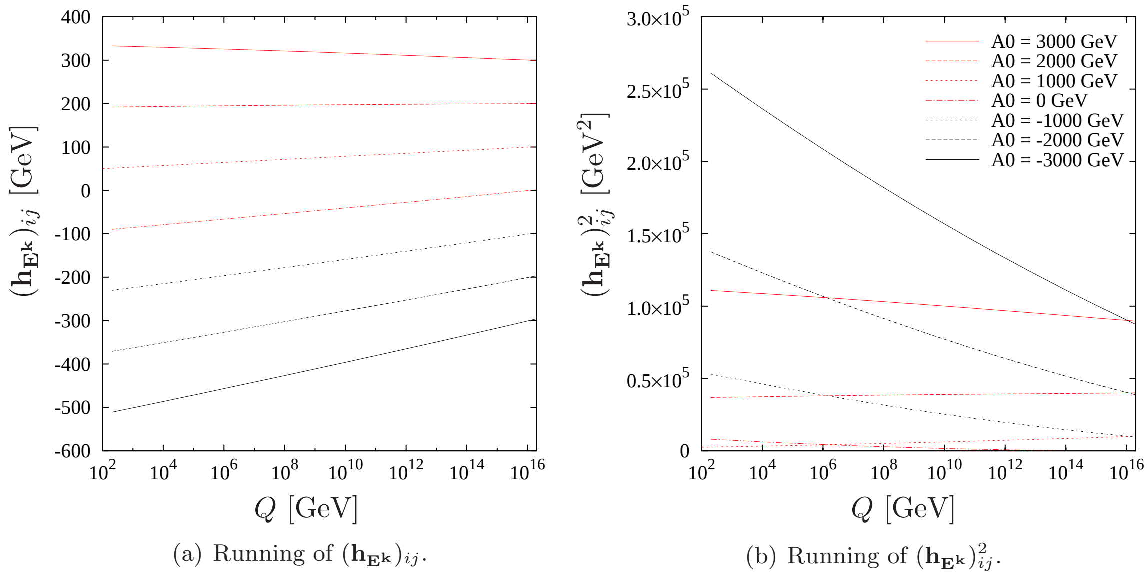

(a) Running of $(\mathbf{h}_{\mathbf{E}^k})_{ij}$.

(b) Running of $(\mathbf{h}_{\mathbf{E}^k})^2_{ij}$.

Figure 4.2.: Running of $(\mathbf{h}_{\mathbf{E}^k})_{ij}$ (left) and $(\mathbf{h}_{\mathbf{E}^k})^2_{ij}$ (right) from M_{GUT} to M_Z for different values of A_0, given by the legend in Fig. 4.2(b). At M_{GUT}, we choose $M_{1/2} = 1000$ GeV and $\lambda_{ijk} = 0.1$.

Assuming λ_{ijk} to be positive, the second term is always positive and thus decreases $(\mathbf{h}_{\mathbf{E}^k})_{ij}$ when running from M_{GUT} to M_Z. The λ_{ijk} coupling increases by roughly a factor of 1.5 when we run from M_{GUT} to M_Z. However, at the same time, the gaugino masses M_1 and M_2 as well as the gauge couplings g_1 and g_2 decrease. Therefore, this term gets relatively less important towards lower scales.

Now, we can understand the running of $(\mathbf{h}_{\mathbf{E}^k})_{ij}$ in Fig. 4.2(a). Given a positive A_0 (red lines), both terms in Eq. (4.3) have opposite signs and are thus competing with each other, leading only to a small change in $(\mathbf{h}_{\mathbf{E}^k})_{ij}$ during the running. Moreover, due to the running of the gauge couplings and gaugino masses[5] both terms decrease when we run from M_{GUT} to M_Z. In contrast, if we start with a negative A_0 (black lines), both terms give negative contributions to the running of $(\mathbf{h}_{\mathbf{E}^k})_{ij}$. Still, the contribution from the λ_{ijk} term in Eq. (4.3) decreases, however, the contribution from the term proportional to $(\mathbf{h}_{\mathbf{E}^k})_{ij}$ does not necessarily decrease when running from M_{GUT} to M_Z. Thus, for negative A_0, $(\mathbf{h}_{\mathbf{E}^k})_{ij}$ decreases with a large slope.

Recall from Eq. (4.1), that $m^2_{\tilde{\ell}_R}$ is reduced proportional to the integral of $(\mathbf{h}_{\mathbf{E}^k})^2_{ij}$ over t. Thus, according to Fig. 4.2(b), a negative value of A_0 leads to a smaller $m_{\tilde{\ell}_R}$ compared to a positive A_0 with the same magnitude.

4.3. Selectron and Smuon LSP parameter space

In this section, we present two dimensional B$_3$ mSUGRA parameter regions which exhibit a $\tilde{\ell}_R$ LSP. As we have seen in Sect. 4.1, the running of the $\tilde{\ell}_R$ mass is analogous for the first and second generation, *i.e.* the only difference in the running of the $\tilde{e}_R$ and $\tilde{\mu}_R$ mass is the dependence on the specific choice of the dominant $L_i L_j \bar{E}_k$ operator. Therefore, we only study here the case of

---

[5] In the term proportional to $(\mathbf{h}_{\mathbf{E}^k})_{ij}$, the factor including the gauge couplings generally decreases faster than $(\mathbf{h}_{\mathbf{E}^k})_{ij}$ can grow, assuming a physical parameter point with positive A_0.

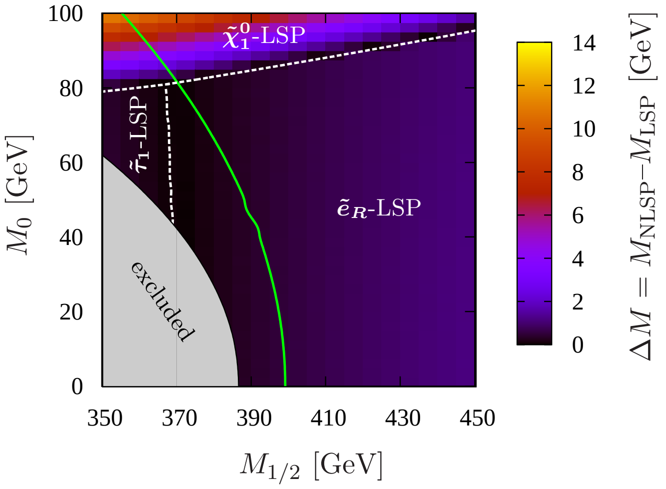

Figure 4.3.: Mass difference, ΔM, between the NLSP and LSP in the $M_{1/2} - M_0$ plane. The other B$_3$ mSUGRA parameters are $A_0 = -1250$ GeV, $\tan\beta = 5$, $\mathrm{sgn}(\mu) = +$ and $\lambda_{231}|_{\text{GUT}} = 0.045$. The LSP candidates are explicitly mentioned and their LSP regions are separated by the white dotted lines. The solid gray region on the bottom left corresponds to models which are excluded due to the bound on λ_{231}, *cf.* Tab. 4.1. The green contour line indicates the SUSY contribution to the anomalous magnetic moment of the muon, $\delta a_\mu^{\text{SUSY}}$. Models left of this contour line lie within the 2σ window for $\delta a_\mu^{\text{SUSY}}$, *cf.* Eq. (4.4).

a $\tilde{e}_R$ LSP with a dominant coupling λ_{231}. We can obtain the $\tilde{\mu}_R$ LSP region by the exchange of the couplings $\lambda_{231} \to \lambda_{132}$.

In Fig. 4.3 we show a typical B$_3$ mSUGRA parameter region with a $\tilde{e}_R$ LSP in the $M_{1/2} - M_0$ plane. We have chosen a negative value of A_0 with a fairly large magnitude, $A_0 = -1250$ GeV. The other parameters are $\tan\beta = 5$, $\mathrm{sgn}(\mu) = +$ as well as $\lambda_{231} = 0.045$ at the GUT scale. We observe that the $\tilde{e}_R$ LSP lives in an extended region in the B$_3$ mSUGRA parameter space. Competing LSP candidates are the lightest stau, $\tilde{\tau}_1$, and the lightest neutralino, $\tilde{\chi}_1^0$. The solid gray region at low values of $M_{1/2}$ and M_0 corresponds to scenarios with $\tilde{e}_R$ masses < 135 GeV. These models are excluded by the experimental upper bound on the λ_{231} coupling, *cf.* Tab. (4.1). The green contour line indicates the lower value of the 2σ window of the SUSY contribution to the anomalous magnetic moment of the muon [37, 38],

$$11.9 \times 10^{-10} < \delta a_\mu^{\text{SUSY}} < 47.1 \times 10^{-10}, \tag{4.4}$$

i.e. parameter points left to the green line lie within the 2σ window and thus may explain the discrepancy between the SM prediction and the observed value of a_μ.

Furthermore, the entire displayed region fulfills the 2σ constraint from the branching ratios of the flavor-changing-neutral-current (FCNC) decay $b \to s\gamma$ [190],

$$3.03 \times 10^{-4} < \mathcal{B}(b \to s\gamma) < 4.07 \times 10^{-4}, \tag{4.5}$$

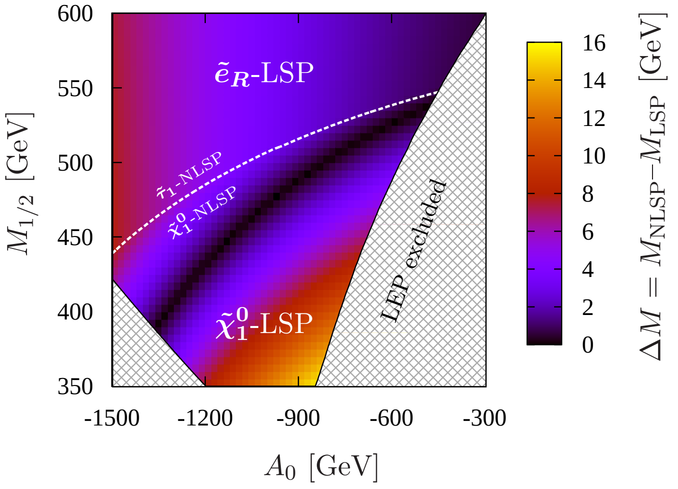

Figure 4.4.: Mass difference, ΔM, between the NLSP and LSP in the $A_0 - M_{1/2}$ plane with B_3 mSUGRA parameters $M_0 = 90$ GeV, $\tan\beta = 4$, $\mathrm{sgn}(\mu) = +$ and $\lambda_{231}|_{\mathrm{GUT}} = 0.045$. The patterned regions are excluded by the LEP Higgs bound, Eq. (4.7). The white dotted line separates $\tilde{e}_R$ LSP scenarios with different mass hierarchies $M_{\tilde{e}_R} < M_{\tilde{\tau}_1} < M_{\tilde{\chi}_1^0}$ (top) and $M_{\tilde{e}_R} < M_{\tilde{\chi}_1^0} < M_{\tilde{\tau}_1}$ (bottom).

and the 95% C.L. upper limit for the FCNC decay $B_s^0 \to \mu^+\mu^-$ [191],

$$\mathcal{B}(B_s^0 \to \mu^+\mu^-) < 3.6 \times 10^{-8}. \tag{4.6}$$

We employ micrOMEGAs2.2 [192] to calculate $\delta a_\mu^{\mathrm{SUSY}}$, $\mathcal{B}(b \to s\gamma)$ and $\mathcal{B}(B_s^0 \to \mu^+\mu^-)$. Also, we employ the 95% C.L. lower LEP exclusion bound on the light Higgs mass m_{h^0} [193],

$$m_{h^0} \geq 114.4 \text{ GeV}. \tag{4.7}$$

However, we reduce this bound by 3 GeV to account for numerical uncertainties of SOFTSUSY 3.0.13 [188, 189] which we use to calculate the SUSY and Higgs mass spectrum.

In Fig. 4.3 the $\tilde{e}_R$ is nearly mass degenerate with the $\tilde{\tau}_1$. However, the mass difference between the $\tilde{\tau}_1$ and the $\tilde{e}_R$ depends on $M_{1/2}$. We observe a $\tilde{\tau}_1$ LSP at small values $M_{1/2} \leq 370$ GeV, while the $\tilde{e}_R$ is the LSP for larger values of $M_{1/2}$. Increasing $M_{1/2}$ enhances the $(\mathbf{h}_{\mathbf{E}^k})^2_{ij}$ contribution in the running $\tilde{e}_R$ mass since the gaugino masses M_1 and M_2 enter the RGE of $(\mathbf{h}_{\mathbf{E}^k})_{ij}$, *cf.* Eq. (4.3). Furthermore, the $\tilde{\tau}_1$ mass receives larger contributions from $M_{1/2}$ due to its left-handed component, *cf.* Eq. (3.30)-(3.31). Thus, at larger values of $M_{1/2}$, the mass difference between the $\tilde{\tau}_1$ and the $\tilde{e}_R$ is larger[6]. The masses of the scalar particles strongly increase with M_0, while the mass of the (bino-like) neutralino is nearly unaffected by M_0. Thus, a large value of M_0 leads to a $\tilde{\chi}_1^0$ LSP.

The parameter region in Fig. 4.3 is particularly interesting, because it contains $\tilde{e}_R$ LSP models with a significant contribution to the anomalous magnetic moment of the muon, a_μ. These models have a light sparticle mass spectrum with $\tilde{e}_R$ masses of about $140 - 150$ GeV and can be already tested with existing data from the Tevatron experiments, as we will show in

---

[6] A larger mass difference between $\tilde{\tau}_1$ and the $\tilde{e}_R$ can also be obtained by increasing $\mathbf{\Lambda}$. However, larger values of $\mathbf{\Lambda}$ translate into a requirement of larger $\tilde{e}_R$ masses due to the experimental upper bound, *cf.* Tab. 4.1.

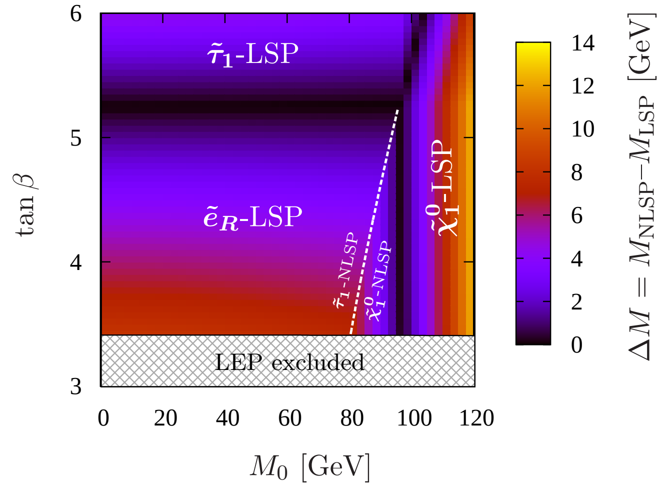

Figure 4.5.: Mass difference, ΔM, between the NLSP and LSP in the $M_0 - \tan\beta$ plane with B$_3$ mSUGRA parameters $M_{1/2} = 450$ GeV, $A_0 = -1250$ GeV, $\mathrm{sgn}(\mu) = +$ and $\lambda_{231}|_{\rm GUT} = 0.045$. The patterned regions are excluded by the LEP Higgs bound, Eq. (4.7). The white dotted line separates $\tilde{e}_R$ LSP scenarios with different mass hierarchies $M_{\tilde{e}_R} < M_{\tilde{\tau}_1} < M_{\tilde{\chi}_1^0}$ (left) and $M_{\tilde{e}_R} < M_{\tilde{\chi}_1^0} < M_{\tilde{\tau}_1}$ (right).

Sect. 5.2.

We give the mass difference, ΔM, between the NLSP and LSP in the $A_0 - M_{1/2}$ plane and $M_0 - \tan\beta$ plane in Fig. 4.4 and Fig. 4.5, respectively. Again, we choose the coupling $\lambda_{231} = 0.045$ at $M_{\rm GUT}$. The gray pattered regions correspond to models which are excluded by the LEP bound on the light Higgs mass, Eq. (4.7). The entire displayed region fulfills the constraints from $\mathcal{B}(b \to s\gamma)$ and $\mathcal{B}(B_s^0 \to \mu^+\mu^-)$. However, the sparticle mass spectra of these scenarios are too heavy to give a significant contribution to a_μ.

In the $A_0 - M_{1/2}$ plane [Fig. 4.4], we find a $\tilde{e}_R$ LSP for larger values of $M_{1/2}$, because $M_{1/2}$ increases the mass of the $\tilde{\chi}_1^0$ faster than the mass of the sleptons, *cf.* Sect. 3.4. As discussed in Sect. 4.2, the mass of the $\tilde{e}_R$ decreases for a large magnitude of a (negative) A_0, thus leading to an enhanced $\tilde{e}_R$ LSP region. Furthermore, the mass difference between the $\tilde{\tau}_1$ and the $\tilde{e}_R$ increases with $|A_0|$. In principle, there is also a $\tilde{e}_R$ region for large positive A_0, *cf.* Fig. 4.2(b), however, in this region the light Higgs mass is smaller as for negative A_0 [158]. Thus, this region is disfavored by the LEP Higgs mass constraint. Note, that at negative A_0 values with large magnitude, we also obtain a light top squark, $\tilde{t}_1$, since the top Yukawa coupling enters the RGE running of the $\tilde{t}_1$ mass in a similar way as the λ_{ijk} Yukawa coupling does for the $\tilde{\ell}_R$ mass.

In the $M_0 - \tan\beta$ plane [Fig. 4.5], we find a $\tilde{e}_R$ LSP for $\tan\beta \lesssim 5.2$ and $M_0 \lesssim 95$ GeV. As discussed at the end of Sect. 3.4, the mass of the $\tilde{\tau}_1$ decreases with increasing $\tan\beta$, while the mass of the $\tilde{e}_R$ is unaffected by $\tan\beta$. Thus, $\tan\beta$ is a handle for the mass difference of the $\tilde{\tau}_1$ and the $\tilde{e}_R$. As in Fig. 4.3, we obtain a $\tilde{\chi}_1^0$ LSP at large values of M_0.

We find basically two possible mass hierarchies for the $\tilde{e}_R$ LSP parameter space, indicated by the white dotted line in Fig. 4.4 and Fig. 4.5. Close to the $\tilde{\chi}_1^0$ LSP region, we observe a $\tilde{\chi}_1^0$ NLSP and a $\tilde{\tau}_1$ next-to-NLSP (NNLSP), *i.e.*

$$M_{\tilde{e}_R} < M_{\tilde{\chi}_1^0} < M_{\tilde{\tau}_1}. \tag{4.8}$$

However, for most of the parameter space, we have

$$M_{\tilde{e}_R} < M_{\tilde{\tau}_1} < M_{\tilde{\chi}_1^0}, \tag{4.9}$$

i.e. the $\tilde{\tau}_1$ is the NLSP and the $\tilde{\chi}_1^0$ is the NNLSP. These mass hierarchies lead to different collider phenomenology and will be our guideline in the selection of benchmark scenarios. For some regions with a large mass difference between the $\tilde{\chi}_1^0$ and the $\tilde{e}_R$, the $\tilde{\mu}_R$ can even be the next-to-NLSP (NNLSP), *i.e.* we have

$$M_{\tilde{e}_R} < M_{\tilde{\tau}_1} < M_{\tilde{\mu}_R} < M_{\tilde{\chi}_1^0}, \tag{4.10}$$

where the $\tilde{\chi}_1^0$ is the next-to-NNLSP (NNNLSP).

5. Probing Selectron and Smuon LSP models at hadron colliders

In this chapter we study B_3 mSUGRA models with a $\tilde{\ell}_R$ LSP at hadron colliders. We first discuss the characteristic collider signatures of these models. As we will see, $\tilde{\ell}_R$ LSP scenarios generally lead to multi-lepton final states. Therefore, we test these models in Sect. 5.2 in detail against a trilepton SUSY search, performed at the DØ experiment at the Tevatron. We present the $\tilde{\ell}_R$ LSP parameter region, which is excluded by the current results of the DØ analysis. We also show the regions of the parameter space, that can be probed with future Tevatron data.

In the main part of this chapter, Sect. 5.3, we discuss the prospects of a discovery of $\tilde{\ell}_R$ LSP models with early data at the LHC. Guided by the properties of three selected benchmark points with a $\tilde{e}_R$ LSP, we design an inclusive analysis with three final state leptons and perform a detailed Monte-Carlo (MC) study of the signal and SM backgrounds at both LHC center-of-mass energies of 7 TeV and 14 TeV. Finally, we apply the analysis to an extended supersymmetric parameter space and present the SUSY discovery potential in the $M_{1/2} - M_0$ plane.

5.1. Selectron and Smuon LSP signatures at hadron colliders

In this section, we classify the hadron collider signatures of $\tilde{e}_R$ and $\tilde{\mu}_R$ LSP models. We assume that the LSP decay is dominated[1] by only one P_6 violating operator $\mathbf{\Lambda}$, *cf.* Tab. 4.1. At the LHC the production of colored sparticles will be dominant for SUSY models with squark and gluino masses $\lesssim \mathcal{O}(1\text{ TeV})$ [194]. For simplicity we here focus on squark pair production with the following cascade process

$$qq/gg \to \tilde{q}\tilde{q} \to jj\tilde{\chi}_1^0\tilde{\chi}_1^0 \to jj\ell\ell\tilde{\ell}_R\tilde{\ell}_R, \tag{5.1}$$

where $\tilde{q}$ is a squark and j denotes a jet. Here, $\tilde{\ell}_R \in \{\tilde{e}_R, \tilde{\mu}_R\}$ is the LSP and the two leptons ℓ are of the same flavor as the LSP. The $\tilde{\ell}_R$ will promptly decay via the R-parity violating $L_iL_j\bar{E}_k$ operator $\mathbf{\Lambda}$ into a lepton and a neutrino. The collider signatures are classified in Tab. 5.1 according to the possible $\tilde{\ell}_R$ LSP decays. Here we assume that always only one $\mathbf{\Lambda}$ coupling is dominant. Assuming the SUSY cascade in Eq. (5.1), the resulting collider signatures involve two jets from the squark decays, two leptons of the same flavor as the LSP coming from the neutralino decay into the LSP, additional leptons from the LSP decay and missing transverse energy, $\not{E}_T$, due to the neutrinos. The p_T spectrum of the leptons from the decay $\tilde{\chi}_1^0 \to \ell\tilde{\ell}_R$ will depend on the mass difference between the $\tilde{\ell}_R$ LSP and the $\tilde{\chi}_1^0$. Note, that due to the Majorana nature of the $\tilde{\chi}_1^0$, every charge combination of the two $\tilde{\ell}_R$ LSPs is possible. Since $\mathbf{\Lambda}$ necessarily couples directly to the $\tilde{\ell}_R$ LSP, it will always decay via a 2-body decay.

In general, more complicated SUSY production and decay processes than Eq. (5.1) can occur. Fig. 5.1 gives an example, namely squark-gluino production followed by a lengthy decay cascade.

---

[1] In general, the $\not{P}_6$ couplings which are generated at M_Z by the coupled RGEs do not play a rôle. They lead to 2-body decays of the LSP with much smaller branching ratios (BRs).

$\mathbf{\Lambda}$ coupling	LSP decay	Hadron collider signature
λ_{121}	$\tilde{e}_R \to \left\{ \begin{array}{l} e\,\nu_\mu \\ \mu\,\nu_e \end{array} \right.$	$2j + 2e + \not{E}_T + \left\{ \begin{array}{c} 2e \\ e\mu \\ 2\mu \end{array} \right.$
λ_{131}	$\tilde{e}_R \to \left\{ \begin{array}{l} e\,\nu_\tau \\ \tau\,\nu_e \end{array} \right.$	$2j + 2e + \not{E}_T + \left\{ \begin{array}{c} 2e \\ e\tau \\ 2\tau \end{array} \right.$
λ_{231}	$\tilde{e}_R \to \left\{ \begin{array}{l} \mu\,\nu_\tau \\ \tau\,\nu_\mu \end{array} \right.$	$2j + 2e + \not{E}_T + \left\{ \begin{array}{c} 2\mu \\ \mu\tau \\ 2\tau \end{array} \right.$
λ_{132}	$\tilde{\mu}_R \to \left\{ \begin{array}{l} e\,\nu_\tau \\ \tau\,\nu_e \end{array} \right.$	$2j + 2\mu + \not{E}_T + \left\{ \begin{array}{c} 2e \\ e\tau \\ 2\tau \end{array} \right.$

Table 5.1.: Hadron collider signatures for selectron and smuon LSP scenarios assuming one dominant $L_i L_j \bar{E}_k$ operator $\mathbf{\Lambda}$ and the pair production of strongly interacting sparticles. The left column denotes the dominant $\mathbf{\Lambda}$ coupling, the middle column shows the possible LSP candidate and its decays and the right column gives the resulting collider signatures, assuming the SUSY cascade in Eq. (5.1).

Typically, these processes lead to additional final state particles, most notably

- additional jets from the production of gluinos and their subsequent decays into squarks and quarks,
- additional leptons from the decays of heavier neutralinos and charginos, which may come from the decay of left-handed squarks, and
- additional leptons from a $\tilde{\chi}_1^0$ decay into a non-LSP right-handed slepton $\tilde{\ell}_R$ (or lightest stau $\tilde{\tau}_1$), *i.e.* for example $\tilde{\chi}_1^0 \to \ell^- \tilde{\ell}_R^+$, followed by a three-body decay $\tilde{\ell}_R^+ \to \ell^+ \ell'^\pm \tilde{\ell}_R'^\mp$. Here, $\tilde{\ell}'_R$ denotes the LSP.

The three-body slepton decays in the last point are special to $\tilde{e}_R$ and $\tilde{\mu}_R$ LSP scenarios. The corresponding decay rates are calculated in the Appendix C and are taken into account for the following collider analysis. However, these decays play only a rôle in certain regions of the B_3 mSUGRA parameter space, *cf.* Fig. C.5.

As we discussed in Sect. 4.1, the $\mathbf{\Lambda}$ coupling is of similar size as the gauge couplings for $\tilde{\ell}_R$ LSP scenarios. This large coupling enables also P_6 violating decays of sparticles, which are not the LSP. Thus, not every SUSY decay cascade necessarily involves the LSP. Of particular importance are the P_6 violating decays of the $\tilde{\tau}_1$ [176], especially in the case when the $\tilde{\tau}_1$ NLSP is nearly mass degenerate with the $\tilde{\ell}_R$ LSP. Furthermore, the sneutrinos may decay into two leptons if they couple directly to $\mathbf{\Lambda}$. This leads to sharp sneutrino mass peaks in dilepton invariant mass distributions, as we will see in Sect. 6.3.1. However, all these P_6 violating decays of non-LSP sparticles also yield final state leptons. Thus, even though the LSP might not be involved in some decay cascades, a multi-lepton analysis is the best search strategy for $\tilde{\ell}_R$ LSP scenarios.

In most $\tilde{\ell}_R$ LSP scenarios within the B_3 mSUGRA model, the lightest top squark, $\tilde{t}_1$, is much lighter than the other squarks. Thus, $\tilde{t}_1$ pair production forms a sizable fraction of all SUSY production processes. The decay of each $\tilde{t}_1$ yields a b quark (either directly from the

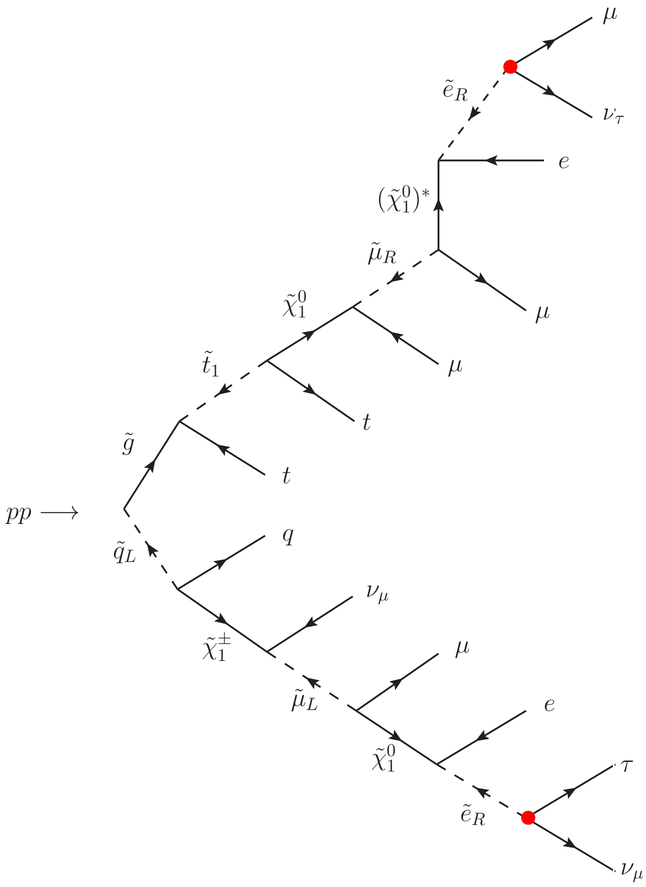

Figure 5.1.: Example for squark-gluino production with successive cascade decay into the two $\tilde{e}_R$ LSPs. Here, the LSP decays via the $\not{P}_6$ coupling λ_{231} (marked by red dots). In the upper decay chain, we get an additional t quark from the gluino decay into the $\tilde{t}_1$. Furthermore, the $\tilde{\mu}_R$ decays into the $\tilde{e}_R$ LSP via a virtual neutralino, yielding additional leptons. The lower decay cascade involves a chargino, $\tilde{\chi}_1^\pm$, and a left-handed smuon, $\tilde{\mu}_L$.

decay $\tilde{t}_1 \to \tilde{\chi}_1^+ b$ or from the top quark decay after $\tilde{t}_1 \to \tilde{\chi}_1^0 t$), thus we expect an enhanced b quark multiplicity for these scenarios. We will use the b quark multiplicity to discriminate signal events stemming from $\tilde{t}_1$ pair production in Sect. 6.

At the LHC, the multi charged lepton final states (especially electrons and muons) are the most promising signatures to be tested with early data. Electrons and muons in the detector can be efficiently identified and the SM background for high lepton multiplicities is very low [195]. In Sect. 5.3, we therefore investigate the discovery potential of $\tilde{\ell}_R$ LSP scenarios at the LHC with an inclusive three lepton search analysis.

Due to their striking multi-leptonic signatures, light $\tilde{\ell}_R$ LSP models might also be observable at the Tevatron. In the next section, we therefore study in detail how $\tilde{\ell}_R$ LSP models are constrained by the trilepton SUSY search analysis performed by the DØ experiment [196]. Due to the lower center-of-mass energy of the Tevatron compared to the LHC, the cross section for the production of (heavy) colored sparticles is not always dominant. Gaugino and slepton pair production usually comprise a sizable fraction of the total SUSY cross section, leading to events without hard jets, *cf.* Tab. 5.4.

5.2. Constraints from SUSY searches at the Tevatron

At the Tevatron at Fermilab both experiments DØ [196] and CDF [197, 198] have searched[2] for supersymmetry with final states containing three charged leptons, using the collected data of proton-antiproton ($p\overline{p}$) collisions at a center-of-mass energy $\sqrt{s} = 1.96$ TeV, corresponding to an integrated luminosity of 2.3 fb^{-1} and 3.2 fb^{-1}, respectively. These analyses were designed for the measurement of associated production of charginos and neutralinos [203] within P_6 conserving mSUGRA, using exclusive trilepton search channels [204, 205, 206, 207, 208]. Some of our lighter models could have led to an observable excess of events in these searches. Here we investigate quantitatively how these experimental analyses constrain the $\tilde{e}_R$ and $\tilde{\mu}_R$ LSP parameter space.

We follow the DØ analysis to test the exclusion of $\tilde{e}_R$ and $\tilde{\mu}_R$ LSP models. CDF uses a jet veto in the event selection, which is expected to lead to a reduced signal efficiency for many $\tilde{\ell}_R$ LSP models[3]. DØ distinguishes their search channels by the flavor of the final state leptons. Since the final state lepton flavor multiplicity depends on the choice of the $\mathbf{\Lambda}$ coupling, we expect different sensitivities of the DØ search channels for different choices of $\mathbf{\Lambda}$.

In the next section we describe how we emulate the DØ analysis and discuss the major changes to the original analysis. We test two benchmark points with a light $\tilde{e}_R$ LSP against our analysis in Sect. 5.2.2. Thereby we review the results of the DØ analysis. We show the excluded regions of the $\tilde{e}_R$ and $\tilde{\mu}_R$ LSP parameter space and an extrapolation to higher luminosities in Sect. 5.2.3.

5.2.1. The DØ trilepton analysis

The DØ search for associated production of charginos and neutralinos with final states containing three leptons is presented in Ref. [196]. The analysis is based on $p\overline{p}$ collision data at a center-of-mass energy of $\sqrt{s} = 1.96$ TeV corresponding to an integrated luminosity of $2.3\,\text{fb}^{-1}$, with the exception of the analysis using identified hadronic τ lepton decays, which is based on $1\,\text{fb}^{-1}$ of data. Four dedicated trilepton event selections were designed, distinguished by the lepton content in the final state, *i.e.* we have a $ee\ell$, $\mu\mu\ell$, $e\mu\ell$ and $\mu\tau$ selection without specification of the lepton charge. Here the third lepton ℓ corresponds to a reconstructed isolated track without using the DØ standard lepton identification criteria. The first three channels are separated into a low-p_T and a high-p_T selection, while the $\mu\tau$ channel contains a $\mu\tau\ell$ selection and a $\mu\tau\tau$ selection. In this study, we focus on the $ee\ell$, $\mu\mu\ell$ and $e\mu\ell$ selections. The $\mu\tau$ selection turned out to be insensitive to our models.

In our object reconstruction, we use cone isolation criteria for all leptons, where the cone radius $\Delta R = \sqrt{(\Delta\phi)^2 + (\Delta\eta)^2}$ is given by the distance in pseudorapidity η and azimuthal angle ϕ. Guided by the DØ object reconstruction, an electron (muon[4]) with pseudorapidity $|\eta| < 3.2$ ($|\eta| < 2.0$) is considered as isolated, if the scalar sum of the absolute value of the transverse momenta of all tracks in a cone of $\Delta\mathcal{R} = 0.4$ does not exceed 2.5 GeV. We do not loosen the reconstruction criteria for the third lepton ℓ but demand it to be an isolated electron or muon. Jets are reconstructed with FastJet 2.4.1 [209, 210] using the kt algorithm with cone radius

---

[2] Note, that also other SUSY searches using the tri-lepton or (like-sign) di-lepton signature have been performed at DØ and CDF [199, 200, 201, 202]. At the current status, these analyses use at most a dataset corresponding to 1.1 fb^{-1}. Thus, we do not expect these searches to be more restrictive than those presented here.

[3] In order to discriminate the $t\bar{t}$ background, CDF requires the scalar sum of the jet transverse energies $\sum E_t(\text{jets}) \leq 80$ GeV and the number of jets $N(\text{jets}) < 2$ [197]. We thus expect SUSY events from sparton (squark and/or gluino) pair production to be mostly rejected in the CDF analysis.

[4] This isolation criteria corresponds to *tight* muons in Ref. [196].

	Selection	$\mu\mu\ell$		$ee\ell$		$e\mu\ell$	
		low p_T	high p_T	low p_T	high p_T	low p_T	high p_T
I	$p_T^{\ell_1}, p_T^{\ell_2}$	$> 12, > 8$	$> 18, > 16$	$> 12, > 8$	$> 20, > 10$	$> 12, > 8$[a]	$> 15, > 15$
II	$m_{\ell_1\ell_2}$	$\in [20, 60]$	$\in [0, 75]$	$\in [18, 60]$	$\in [0, 75]$	-	-
	$\Delta\phi_{\ell_1\ell_2}$	< 2.9	< 2.9	< 2.9	< 2.9	-	-
III	$\not{E}_T$	> 20	> 20	> 22	> 20	> 20	> 20
	$\mathrm{Sig}(\not{E}_T)$	> 8	> 8	> 8	> 8	> 8	> 8
	m_T^{min}	> 20	> 20	> 20	> 14	> 20	> 15
	H_T	-	< 80	-	-	-	-
IV	$p_T^{\ell_3}$	> 5	> 4	> 4	> 12	> 6	> 6
V	$m_T^{\ell_3}$	> 10	> 10	> 10	> 10	> 10	> 8
	$m_{\ell_{1,2}\ell_3}$	$\notin [80, 110]$	-	-	-	< 70	< 70
VI	anti W	-	-	tight likelihood[b]	-	tight likelihood[c] hit in 2 inner layers[c] very tight muon isolation[d] $\sum_{0.05<\Delta R<0.4} p_T^{\ell_3} < 1$	
VII	$\not{E}_T \times p_T^{\ell_3}$	> 200	> 300	> 220	-	-	-
	p_T^{bal}	< 4	< 4	< 4	< 4	< 2	< 2

[a] $p_T^{\ell_1}$ and $p_T^{\ell_2}$ are electron and muon p_T, respectively.
[b] for $p_T^{\ell_3} < 15$ GeV
[c] for $m_T^{\mu} \in [40, 90]$ GeV
[d] for $m_T^{e} \in [40, 90]$ GeV

Table 5.2.: DØ selection criteria for the $\mu\mu l$, eel and $e\mu l$ analyses (all energies, masses and momenta in GeV, angles in radians) for the low-p_T selection and the high-p_T selection, see text and Ref. [196] for further details. We apply all cuts except the cut on $\mathrm{Sig}(\not{E}_T)$ in step III and the anti W requirements in step VI (both marked in gray).

$\Delta R = 0.4$ and must be within $|\eta| < 2.5$. In our Monte Carlo (MC) simulation, the missing transverse energy $\not{E}_T$ is calculated as the sum over the transverse momenta of all invisible particles[5].

In the following, we describe the general features of the various steps in the event selection. The details are given in Tab. 5.2 and the specific values should be taken from this table. For a detailed description and their effect on the Standard Model (SM) background we refer the reader again to Ref. [196].

First, each selection requires two identified leptons ($\ell = e$, μ) with a certain minimum transverse momenta $p_T^{\ell_1}$, $p_T^{\ell_2}$ (I). If more then two leptons are identified that satisfy the p_T criteria, the two leptons with the highest p_T are considered. Next, constraints on the invariant mass $m_{\ell_1\ell_2}$ and the opening angle $\Delta\phi_{\ell_1\ell_2}$ of the two leptons are imposed (II). This is followed in step

---

[5] Experimentally, we do not know the transverse momenta of the invisible particles. Here, we have to sum over the transverse momenta of all *visible* objects in the event. The missing transverse momentum can then be calculated using energy and momentum conservation, assuming that the initial state particles have zero transverse momentum.

(III) by requirements on $\not{E}_T$, the minimal transverse mass $m_T^{\min} = \min(m_T^{\ell_1}, m_T^{\ell_2})$, where

$$m_T^{\ell} = \sqrt{2p_T^{\ell}\not{E}_T[1-\cos\Delta\phi(\ell,\not{E}_T)]}, \tag{5.2}$$

and H_T, which is the scalar sum of the p_T of all jets with $p_T > 15$ GeV. In this step, a further requirement on $\mathrm{Sig}(\not{E}_T)$ is performed in the original DØ analysis, where $\mathrm{Sig}(\not{E}_T)$ is defined for events with at least one jet as

$$\mathrm{Sig}(\not{E}_T) \equiv \frac{\not{E}_T}{\sqrt{\sum_{\mathrm{jets}} \sigma^2(E_T^j || \not{E}_T)}}. \tag{5.3}$$

Here, $\sigma^2(E_T^j||\not{E}_T)$ is the jet energy resolution projected on the $\not{E}_T$ direction. This cut rejects events with $\not{E}_T$ faked by poorly measured jets. In our approach, we do not apply this cut on $\mathrm{Sig}(\not{E}_T)$, since we do not have a measure of the jet energy resolution. However, since the missing transverse energy is stemming mostly from the neutrinos coming from the leptonically decaying $\tilde{\ell}_R$ LSP, the effect of this cut is expected to be small.

In step IV, we demand an additional third lepton with a softer p_T requirement. Further cuts on its transverse mass $m_T^{\ell_3}$ and the invariant masses $m_{\ell_{1,2},\ell_3}$ of the third lepton with one of the preselected leptons are applied (V). For some channels in the original DØ analysis, step (VI) includes further lepton quality requirements using likelihood discriminants in order to reduce background from W boson production, where the second lepton is faked by jets or photons. This step is skipped in our approach, since the usage of these methods is beyond the scope of this work. In the last step (VII) a cut on the product of the third lepton p_T and $\not{E}_T$ and on the p_T balance

$$p_T^{\mathrm{bal}} = \frac{|\vec{p}_T^{\,\ell_1} + \vec{p}_T^{\,\ell_2} + \vec{\not{E}}_T|}{p_T^{\ell_3}} \tag{5.4}$$

is applied.

5.2.2. DØ results and a test of two benchmark scenarios

In this section, we select two benchmark scenarios which we test explicitly against the DØ analysis described in the last section. We focus on light $\tilde{\ell}_R$ LSP models with an LSP mass $M_{\mathrm{LSP}} \lesssim 200$ GeV. As discussed in Sect. 4.3, a general feature of these scenarios is a near mass degeneracy of the $\tilde{\ell}_R$ LSP with the $\tilde{\tau}_1$, which is the NLSP for most of the parameter space, *cf.* Fig. 4.3. The B_3 mSUGRA parameters for the two benchmark points, denoted SUSY1 and SUSY2, are given in Tab. 5.3. Both scenarios exhibit a $\tilde{e}_R$ LSP with a dominant $\not{P}_6$ coupling $\lambda_{231}|_{\mathrm{GUT}} = 0.045$.

The benchmark point SUSY1 represents a wide region of of the $\tilde{e}_R$ LSP parameter space, where the mass difference between the $\tilde{e}_R$ LSP and the lightest neutralino, $\tilde{\chi}_1^0$, is much larger than the mass difference between $\tilde{e}_R$ LSP and the $\tilde{\tau}_1$ NLSP. The masses of the $\tilde{e}_R$, $\tilde{\tau}_1$ and $\tilde{\chi}_1^0$ are given by 139.1 GeV, 139.6 GeV and 163.3 GeV, respectively. In fact, the NNLSP is the right-handed smuon, $\tilde{\mu}_R$, with mass $M_{\tilde{\mu}_R} = 156.2$ GeV. In contrast, SUSY2 lies in the boundary region to the $\tilde{\chi}_1^0$ LSP. Here, all three sparticles $\tilde{e}_R$, $\tilde{\tau}_1$ and $\tilde{\chi}_1^0$ have close to equal masses, with 151.5 GeV, 151.6 GeV and 152.8 GeV, respectively. Due to the low mass difference between the $\tilde{\chi}_1^0$ and the $\tilde{e}_R$, we expect the electrons from the decay $\tilde{\chi}_1^0 \to \tilde{e}_R e$ to be fairly soft, such that many do not fulfill the preselection criteria. Detailed tables containing all sparticle masses and decay modes for these benchmark models are given in Appendix A.1. Both SUSY1 and

B_3 mSUGRA parameter	SUSY1	SUSY2
M_0 [GeV]	0	80
$M_{1/2}$ [GeV]	400	375
A_0 [GeV]	-1250	-1250
$\tan\beta$	5	5
$\mathrm{sgn}(\mu)$	+	+
$\lambda_{231}\vert_{\mathrm{GUT}}$	0.045	0.045

Table 5.3.: B_3 mSUGRA parameter for the benchmark points SUSY1 and SUSY2.

Signal cross section (in fb) at the Tevatron	SUSY1	SUSY2
$\sigma(p\overline{p} \to \text{sparton pairs})$	1.5 ± 0.1	8.2 ± 0.2
$\sigma(p\overline{p} \to \text{slepton pairs})$	8.5 ± 0.2	6.4 ± 0.1
$\sigma\left(p\overline{p} \to \begin{array}{c}\text{gaugino pairs,}\\ \text{gaugino-sparton}\end{array}\right)$	3.8 ± 0.1	5.9 ± 0.1
$\sigma(p\overline{p} \to \text{sparticle pairs})$	13.8 ± 0.2	21.5 ± 0.2

Table 5.4.: Leading-order (LO) signal cross sections for $p\bar{p}$ collisions at a center-of-mass energy of $\sqrt{s} = 1.96$ TeV for the benchmark scenarios SUSY1 and SUSY2. We give the cross section of sparton (*i.e.* squark and gluino) pair, slepton pair and electroweak (EW) gaugino pair / EW gaugino-sparton production separately. The last row gives the total sparticle pair production cross section, which is the signal process. We employed HERWIG6.510 to derive the LO cross sections and for the event simulation. The uncertainties are due to statistical fluctuations from Herwig.

SUSY2 are chosen such that they are consistent with the 2σ lower value of $\delta a_\mu^{\mathrm{SUSY}}$ (green line in Fig. 4.3).

In order to test whether our benchmark models are excluded, we generate 2000 signal events scaled to an integrated luminosity of $2.3\mathrm{fb}^{-1}$ and apply the simplified DØ analysis described above. We employ the Feldman & Cousins method [211] to set 90% C.L. upper limits given the number of expected background events and the number of observed events, both taken from the DØ paper [196]. In those cases where the number of observed events is smaller than the expected background, we take as the upper limit the 90% C.L. *sensitivity*, defined as the average upper limit that would be obtained by an ensemble of experiments with the expected background and no true signal, and given in Tab. XII in Ref. [211][3]. We claim a 90% C.L. exclusion of the SUSY scenario, if the number of signal events exceeds this upper confidence limit in any step of the event selection. We do this comparison separately for all four[4] selection channels in order to gain some insights about their sensitivity on our models. Note that in this method, systematic uncertainties are not taken into account.

For the simulation, we use SOFTSUSY 3.0.13 [188, 189] to calculate the SUSY mass spectra. The SOFTSUSY output is fed into ISAWIG1.200 and ISAJET7.64 [212] in order to calculate

---

[3] For the number of expected background events > 15, we approximate the sensitivity by the Feldman & Cousins upper limit for $N_{\mathrm{obs}} = N_{\mathrm{bkg}}$.

[4] As mentioned before, the fourth channel including τ leptons is insensitive. Thus we do not present the results for this specific channel here.

Selection		$\mu\mu\ell$				$ee\ell$				$e\mu\ell$		
	Data	Backgrd.	SUSY1	SUSY2	Data	Backgrd.	SUSY1	SUSY2	Data	Backgrd.	SUSY1	SUSY2
I	194006	195557 ± 177	6.6	17.8	235474	232736 ± 202	19.8	11.7	16630	16884 ± 75	12.6	18.2
II	22766	26067 ± 88	1.4	4.2	31365	27184 ± 64	4.8	2.8				
III	178	181 ± 6.4	1.2	3.9	515	212 ± 12	4.3	2.6	1191	1177 ± 20	11.1	16.9
IV	7	2.9 ± 0.7	1.0	2.8	16	9.3 ± 2.0	3.0	1.3	22	18.0 ± 1.2	9.9	11.0
V	4	2.2 ± 0.5	0.6	2.4	9	5.9 ± 1.7	2.8	1.3	3	3.5 ± 0.5	3.8	3.9
VI					6	3.1 ± 0.4			2	1.6 ± 0.4		
VII	4	1.2 ± 0.2	0.5	1.8	2	1.8 ± 0.2	2.4	1.2	2	0.8 ± 0.2	1.2	1.0

Table 5.5.: Numbers of events observed in the data and expected for the background (taken from Ref. [196]) and numbers of signal (SUSY1 and SUSY2, see text) events at various stages of the analysis for the $\mu\mu\ell$, $ee\ell$ and $e\mu\ell$ channels and the low-p_T selection. Each row corresponds to a group of cuts, as detailed in Tab. 5.2.

Selection		$\mu\mu\ell$				$ee\ell$				$e\mu\ell$		
	Data	Backgrd.	SUSY1	SUSY2	Data	Backgrd.	SUSY1	SUSY2	Data	Backgrd.	SUSY1	SUSY2
I	140417	141781 ± 120	5.4	16.2	171001	170197 ± 175	19.0	11.1	4617	4709 ± 23	10.6	17.0
II	10349	10645 ± 51	1.9	5.6	8273	7937 ± 39	6.8	3.9				
III	173	176 ± 5.7	1.2	3.7	244	264 ± 10	6.4	3.8	727	738 ± 11	9.8	16.0
IV	7	3.8 ± 0.5	0.9	2.8	0	1.5 ± 0.3	3.9	1.8	11	12.7 ± 0.9	**8.8**	**10.3**
V	4	2.9 ± 0.4	0.9	2.8	0	1.1 ± 0.3	3.7	1.8	2	2.8 ± 0.5	3.3	3.6
VI									0	1.0 ± 0.2		
VII	4	2.0 ± 0.3	0.9	2.4	0	0.8 ± 0.1	**3.4**	1.7	0	0.5 ± 0.1	0.9	1.0

Table 5.6.: Numbers of events observed in the data and expected for the background (taken from Ref. [196]) and numbers of signal (SUSY1 and SUSY2, see text) events at various stages of the analysis for the $\mu\mu\ell$, $ee\ell$ and $e\mu\ell$ channels and the high-p_T selection. Each row corresponds to a group of cuts, as detailed in Tab. 5.2. Signal event yields that exceed the 90% C.L. upper exclusion bound are marked in boldfaced red.

the decay widths of the SUSY particles. The signal process, *i.e.* sparticle pair production, was simulated with HERWIG6.510 [213, 214, 215].

The leading-order (LO) cross section of this process and its subprocesses of sparton (*i.e.* squark and gluino) pair, slepton pair and electroweak (EW) gaugino pair / EW gaugino-sparton production for the two benchmark models is given in Tab. 5.4. For SUSY1, sparticle production is dominated by slepton and gaugino production. However, for SUSY2 the sparton production dominates due to the low mass of the lightest stop, $M_{\tilde{t}_1} = 304.9$ GeV, which decays exclusively to the lightest chargino and a bottom quark, *cf.* Tab. A.2. As a conservative approach, we only use the LO cross section for the signal, while the SM background in the DØ analysis [196] includes next-to-leading (NLO) and next-to-NLO corrections. For the calculation of the Feldman & Cousins confidence limits we employ ROOT [216].

In Tab. 5.5 and 5.6 we review the results from the DØ analysis and compare them with the results for the two B_3 mSUGRA models SUSY1 and SUSY2 for the low-p_T and the high-p_T selections, respectively.

In all selections, the signal event yield for both benchmark scenarios is $\lesssim 20$ events after the two lepton requirement (step I). Thus, the event yields in the first steps (I-III) of the analysis are dominated by the overwhelming SM background. The analysis becomes sensitive to the signal once we require the third lepton (step IV and beyond). Then, the SM background is reduced to $\mathcal{O}(1-20)$ expected events. We now discuss in detail the DØ results and the signal event yields of the different selections after step IV of the analysis was performed.

In the $\mu\mu\ell$ channel (in both the low-p_T and high-p_T selection), the number of observed events is larger than the number of expected events from the SM background for all steps beyond cut IV. Therefore, this channel has intrinsically a less restrictive impact on the SUSY models. We expect only $\mathcal{O}(1-3)$ signal events beyond step IV for both benchmark points. Hence, the $\mu\mu\ell$ channel cannot exclude these models.

Note, that SUSY2 yields roughly three times as many events in this selection as SUSY1. This is due to the enhanced $\tilde{t}_1$ pair production and their decay to the lightest chargino, as mentioned above. The chargino decays to the $\tilde{\nu}_\mu$ and a muon 21% of the time, leading to an enhanced number of muons in the signal. However, in the $\mu\mu\ell$ high-p_T selection, most of the signal events from sparton-pair production are rejected by the H_T cut in step III. This reduces in particular the SUSY2 event yield, since here the production of sparton-pairs comprises 38% of the signal cross section, *cf.* Tab. 5.4.

In the $ee\ell$ channel, the number of observed events is larger (lower) than the number of expected SM background events in the low-p_T (high-p_T) selection for all steps beyond cut IV. For both benchmark scenarios we expect $\mathcal{O}(1-4)$ signal events in these steps of the analysis. Furthermore, the expected signal events for SUSY1 are roughly two times more than for SUSY2. This is because in SUSY2 the mass difference between the $\tilde{\chi}_1^0$ and the $\tilde{e}_R$ LSP is small. Then, the electrons from the decay $\tilde{\chi}_1^0 \to \tilde{e}_R e$ tend to be soft and fail to pass the p_T criteria in step I of the *eel* selection. The SUSY1 event yield exceeds the 90% C.L. upper bound in step VII of the high-p_T $ee\ell$ selection and is therefore excluded by the DØtrilepton search.

For the low-p_T selection of the $e\mu\ell$ channel, the number of observed events tends to be larger than the number of expected SM background events, whereas in the high-p_T selection, the SM background is slightly overestimated. Both the SUSY1 and SUSY2 event yield exceed the 90% C.L. upper limit in step IV of the $e\mu\ell$ high-p_T selection. The following steps in the $e\mu\ell$ channel (step V and beyond) are not as sensitive to our models as step IV, because the cut on the dilepton invariant masses in step V significantly reduces the signal.

In general, the region close to a $\tilde{\chi}_1^0$ LSP is more difficult to exclude due to the soft electrons. For instance, in step IV of the $e\mu\ell$ low-p_T selection, the 90% C.L. upper limit is 13.0 events, while we expect 11.0 signal events for SUSY2. However, if we modify the M_0 value of SUSY2 from 80 GeV to 75 GeV, *i.e.* we basically change the mass difference between $\tilde{\chi}_1^0$ and $\tilde{e}_R$ from 1.3 GeV to 3.7 GeV, the number of expected signal events increases to 15.2 events and the model is excluded.

We conclude, that the DØ analysis using 2.3 fb^{-1} of data excludes both benchmark points SUSY1 and SUSY2 at 90% C.L.. The most restrictive channels for $\tilde{e}_R$ LSP models with a dominant λ_{231} coupling are the $ee\ell$ high-p_T selection (in step VII) and the $e\mu\ell$ high-p_T selection (in step IV). In the next section, we determine the excluded regions of the $\tilde{e}_R$ and $\tilde{\mu}_R$ LSP parameter space, considering also other dominant $\not{P}_6$ couplings.

5.2.3. Excluded selectron and smuon LSP parameter space with existing data

We now apply the DØ analysis to a more extensive parameter region with a $\tilde{\ell}_R$ LSP. For this, we perform a scan in the $M_{1/2} - M_0$ plane with $M_{1/2} \in [350\text{ GeV}, 500\text{ GeV}]$ in steps of $\Delta M_{1/2} = 5$ GeV and $M_0 \in [0\text{ GeV}, 120\text{ GeV}]$ in steps of $\Delta M_0 = 2.5$ GeV. We test both $\tilde{e}_R$ LSP and $\tilde{\mu}_R$ models with dominant $\not{P}_6$ couplings λ_{231}, λ_{131} and λ_{132}, respectively, with a value of 0.045 at M_{GUT}. The other B$_3$ mSUGRA parameter values are $A_0 = -1250$ GeV, $\tan\beta = 5$ and sgn$(\mu) = +$. The $\tilde{e}_R$ LSP parameter region with $\lambda_{231} \neq 0$ was already discussed in Sect. 4.3, *cf.* Fig. 4.3. For each parameter point with a $\tilde{\ell}_R$ LSP, 2000 events were generated and scaled to an integrated luminosity of $\int \mathcal{L}dt = 2.3 \text{ fb}^{-1}$ and the $ee\ell$, $\mu\mu\ell$ and $e\mu\ell$ low-p_T and high-p_T event selections were applied[5]. At each step of the event selection, the number of passed events is compared with the DØ results as described above. We make this comparison for all event selection steps once the third lepton is required, *i.e.* for step IV and beyond, *cf.* Tab. 5.2.

In the following figures, the patterned gray regions mark parameter points with either a neutralino or stau LSP (as indicated in the figures) which are not considered here. The solid gray region is ruled out by the bound on the $\not{P}_6$ coupling $\mathbf{\Lambda}$, *cf.* Tab. 4.1. The mass of the $\tilde{\ell}_R$ LSP (in GeV) is given by the gray contour lines.

In Fig. 5.2 we give the $\tilde{e}_R$ LSP parameter space for both a dominant $\not{P}_6$ coupling $\lambda_{231} = 0.045$ (upper figures) and $\lambda_{131} = 0.045$ (lower figures) at M_{GUT}. We show the parameter region that is excluded at 90% C.L. with 2.3 fb^{-1} of analyzed data for each channel and p_T selection separately. The figures on the left-hand-side (right-hand-side) show the low-p_T (high-p_T) selection of the $ee\ell$ and $e\mu\ell$ channel. The $\mu\mu\ell$ channel does not exclude any $\tilde{e}_R$ LSP parameter space with 2.3 fb^{-1} of data.

In $\tilde{e}_R$ LSP models with a dominant λ_{231} coupling (upper figures in Fig. 5.2), the LSP decays to 50% to a (hard) muon and a neutrino. Thus, the $e\mu\ell$ selection is very sensitive to these models and can exclude $\tilde{e}_R$ LSP scenarios with $\tilde{e}_R$ masses up to 150 GeV (155 GeV) and squark masses up to 850 GeV (880 GeV) with the low-p_T (high-p_T) selection, *cf.* Fig. 5.2(a) [Fig. 5.2(b)]. The sensitivity decreases for lower mass differences of the $\tilde{\chi}_1^0$ and the $\tilde{e}_R$ due to the softer electrons, as can be seen in all displayed channels in Fig. 5.2(a) and Fig. 5.2(b). Especially the $ee\ell$ becomes insensitive in this boundary region.

Considering $\tilde{e}_R$ LSP models with a dominant λ_{131} coupling (lower figures in Fig. 5.2), we would naïvely expect an enhanced sensitivity of the $ee\ell$ channel since the LSP decays to 50% to a (hard) electron and a neutrino. However, in the $ee\ell$ low-p_T selection in Fig. 5.2(c), the reach is actually worse than for $\tilde{e}_R$ LSP models with a dominant λ_{231} coupling at M_{GUT}, *cf.* Fig. 5.2(a). The reason is the following: If the two preselected electrons come from the same decay chain, *i.e.* one from the decay $\tilde{\chi}_1^0 \to \tilde{e}_R e$ and the other from $\tilde{e}_R \to e\nu_\tau$, they tend to point in the same direction as the neutrino. Thus, the p_T balance, Eq. (5.4), is large and these events are rejected in step VII of the event selection, *cf.* Tab. 5.2. Since the $ee\ell$ low-p_T selection is most sensitive in step VII, *cf.* Tab. 5.5, the exclusion reach of this channel is reduced[6]. In addition, this channel cannot exclude models with $M_{1/2} \lesssim 370$ GeV. Here, the average p_T of the third lepton is smaller, leading to a lower efficiency in step IV and even larger p_T balance, *cf.* Eq. (5.4). Due to the additional hard electrons from the LSP decay, the high-p_T selection of the $ee\ell$ channel in Fig. 5.2(d) has a slightly improved sensitivity for models near the $\tilde{\chi}_1^0$ LSP region, compared to the case with a coupling $\lambda_{231} \neq 0$, *cf.* Fig. 5.2(b). Supersymmetric decay chains with a $\tilde{e}_R$ LSP and a non-zero λ_{131} coupling usually do not involve muons. Thus, the sensitivity of the $e\mu\ell$ channels is lower than the sensitivity of the $ee\ell$ channels, except for parameter points close to the $\tilde{\chi}_1^0$ LSP region.

Comparing the excluded $\tilde{e}_R$ parameter regions in Fig. 5.2 with Fig. 4.3, we conclude that $\tilde{e}_R$ LSP scenarios with a significant contribution to the anomalous magnetic moment of the muon (green line in Fig. 4.3) are excluded at 90% C.L. by the DØ search with 2.3 fb^{-1} of analyzed data.

---

[5] We did the same for the $\mu\tau$ selections for an integrated luminosity of $\int \mathcal{L}dt = 1.0 \text{ fb}^{-1}$. However, this channel is not capable to exclude any $\tilde{\ell}_R$ LSP parameter space. Thus, we do not show any results for the $\mu\tau$ channels.

[6] The same effect also exists in the $e\mu\ell$ channel for scenarios with a dominant λ_{231} coupling. However, this channel is most sensitive in the steps IV and V, *i.e.* before the cut on the p_T balance is performed, *cf.* Tab. 5.5 and Tab. 5.6. Thus, the exclusion power of the $e\mu\ell$ channel does not significantly suffer from this effect.

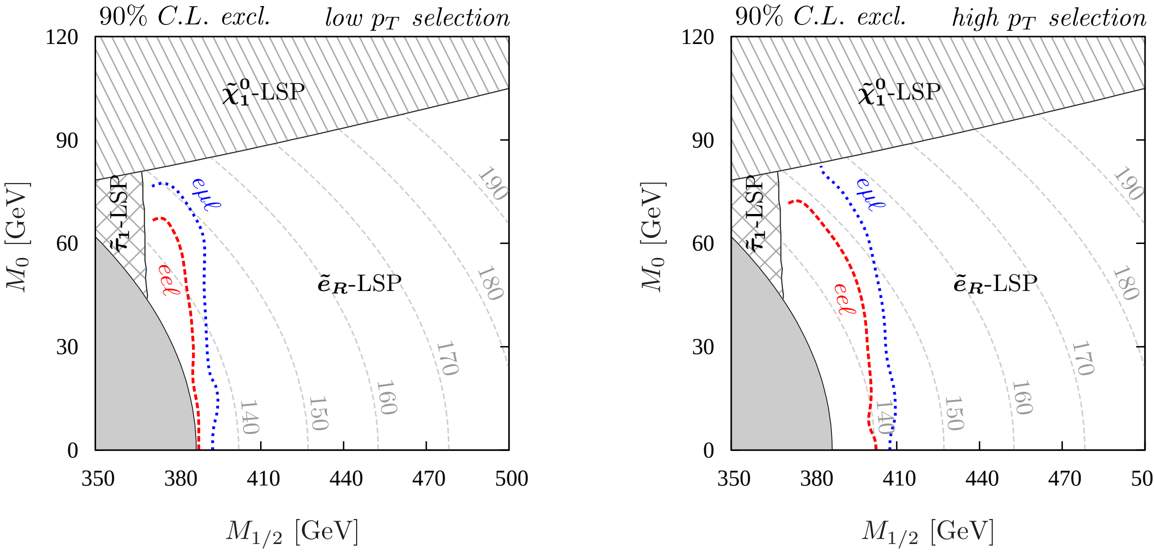

(a) Excluded $\tilde{e}_R$ LSP parameter space with a dominant λ_{231} coupling with the low-p_T selections.

(b) Excluded $\tilde{e}_R$ LSP parameter space with a dominant λ_{231} coupling with the high-p_T selections.

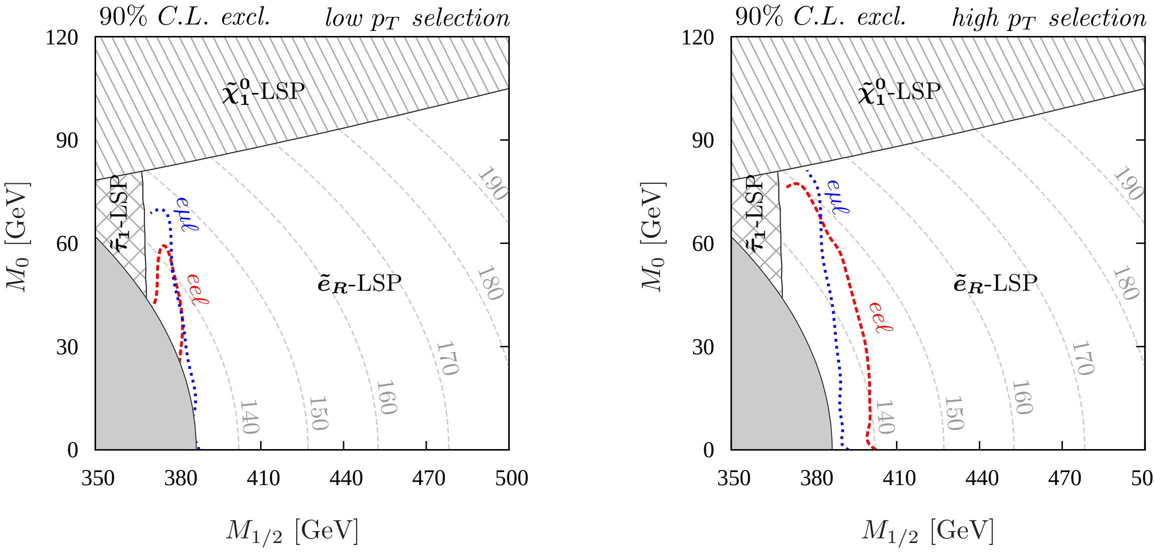

(c) Excluded $\tilde{e}_R$ LSP parameter space with a dominant λ_{131} coupling with the low-p_T selections.

(d) Excluded $\tilde{e}_R$ LSP parameter space with a dominant λ_{131} coupling with the high-p_T selections.

Figure 5.2.: Excluded regions (90% C.L.) of the $\tilde{e}_R$ LSP parameter space by the DØ trilepton analysis with 2.3 fb^{-1} of data. We show two different parameter regions with (a,b) $\lambda_{231} = 0.045$ and (c,d) $\lambda_{131} = 0.045$ as the dominant $\not{P}_6$ coupling at M_{GUT}. The other parameters are $A_0 = -1250$ GeV, $\tan\beta = 5$ and $\mathrm{sgn}(\mu) = +$. The colored contour lines give the excluded region by the different channels: In (a,c) they correspond to the *eel* (red, dashed) and $e\mu\ell$ (blue, dotted) low-p_T selections, while in (b,d) they are shown for the same channels in the high-p_T selection. The gray dotted contour lines give the LSP mass, $M_{\tilde{e}_R}$ in GeV, as indicated by the labels.

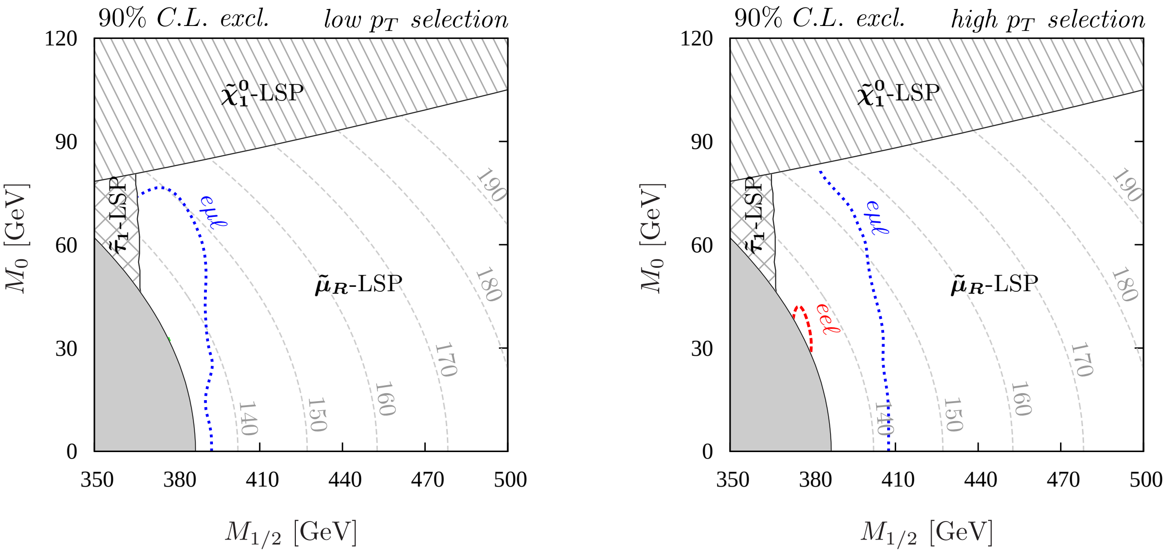

(a) Excluded $\tilde{\mu}_R$ LSP parameter space with a dominant λ_{132} coupling with the low-p_T selections.

(b) Excluded $\tilde{\mu}_R$ LSP parameter space with a dominant λ_{132} coupling with the high-p_T selections.

Figure 5.3.: Excluded regions (90% C.L.) of the $\tilde{\mu}_R$ LSP parameter space ($A_0 = -1250$ GeV, $\tan\beta = 5$, $\text{sgn}(\mu) = +$, $\lambda_{132}|_{\text{GUT}} = 0.045$) by the DØ trilepton analysis with 2.3 fb^{-1} of data. In (a) the blue dotted contour line corresponds to the $e\mu\ell$ low-p_T selection, while in (b) the red dashed and blue dotted contour lines indicate the $ee\ell$ and $e\mu\ell$ high-p_T selection, respectively. The gray dotted contour lines give the LSP mass, $M_{\tilde{\mu}_R}$ in GeV, as indicated by the labels.

The excluded $\tilde{\mu}_R$ LSP parameter space with a dominant $\not{P}_6$ coupling $\lambda_{132} = 0.045$ at M_{GUT} is shown in Fig. 5.3. In complete analogy to $\tilde{e}_R$ LSP models, we now have soft muons from the decay $\tilde{\chi}_1^0 \to \tilde{\mu}_R \mu$ in the region of low mass difference between the $\tilde{\chi}_1^0$ and the $\tilde{\mu}_R$ LSP. The $\tilde{\mu}_R$ LSP decays to 50% into a (hard) electron and a neutrino. Thus, the most sensitive channel is $e\mu\ell$, which has a similar reach for both the low-p_T and high-p_T selection as for the $\tilde{e}_R$ LSP models with a dominant λ_{231} coupling, *cf.* Fig. 5.2(a) and Fig. 5.2(b). The $ee\ell$ channel can only exclude a small fraction of the parameter space with its high-p_T selection, since the electron multiplicity is lower than in $\tilde{e}_R$ LSP models. Although these models exhibit an enhanced number of muons, the $\mu\mu\ell$ channel is still not as sensitive as the other channels due to its lower exclusion power, *cf.* Sect. 5.2.2.

We also compared the excluded $\tilde{\mu}_R$ LSP parameter space in Fig. 5.3 with those $\tilde{\mu}_R$ LSP regions[7], which give a significant contribution to a_μ. It turns out, that also these scenarios are excluded to 90% C.L. by the DØ analysis with 2.3 fb^{-1} of analyzed data.

In summary, the DØ trilepton SUSY search analysis using 2.3 fb^{-1} of data excludes $\tilde{e}_R$ and $\tilde{\mu}_R$ LSP scenarios with $M_{1/2} \lesssim (400 - 410)$ GeV at 90% C.L., roughly corresponding to LSP masses of $(140 - 150)$ GeV. Thus, the $\tilde{e}_R$ and $\tilde{\mu}_R$ LSP parameter regions with a significant contribution to the anomalous magnetic moment of the muon are ruled out. $\tilde{e}_R$ LSP scenarios with a dominant λ_{131} coupling are less constrained by the present analysis, since these models

---

[7] Note, that the $\tilde{\mu}_R$ mass enters in the SUSY contribution to the anomalous magnetic moment of the muon, $\delta a_\mu^{\text{SUSY}}$, via a neutralino-smuon-loop diagram [37]. Thus, $\delta a_\mu^{\text{SUSY}}$ is slightly larger in $\tilde{\mu}_R$ LSP models as in $\tilde{e}_R$ LSP models.

have a low muon multiplicity.

5.2.4. Sensitive selectron and smuon LSP parameter space with future data

Both Tevatron experiments DØ and CDF are expected to have acquired ~ 10 fb^{-1} of data at the end of this year (2010). Therefore, we extrapolate the current DØ results to study the prospects of an exclusion of $\tilde{\ell}_R$ LSP models, using data corresponding to an integrated luminosity of 10 fb^{-1}.

We assume that the events after each selection step in each channel are observed in the same rate as given by the results with integrated luminosity of 2.3 fb^{-1}, *cf.* Tab. 5.5 and Tab. 5.6. Then, we can extrapolate the data to the higher integrated luminosity of 10 fb^{-1}. By applying the same method as in the previous section, we determine the 90% C.L. sensitivity region, *i.e.* the supersymmetric parameter region which would lead to a significant deviation from the extrapolated data, assuming no discrepancies are observed.

In Fig. 5.4 we present the $\tilde{e}_R$ LSP parameter space, which can be excluded with a future integrated luminosity of 10 fb^{-1}. The parameter space is the same as in Fig. 5.2, *i.e.* the dominant $\not{P}_6$ operator is λ_{231} (λ_{131}) in the upper (lower) figures with a value of 0.045 at M_{GUT}. The 90% C.L. sensitivity regions for the channels $ee\ell$, $e\mu\ell$ and $\mu\mu\ell$ are given by the contour lines for the low-p_T (left figures) and high-p_T (right figures) selection.

For $\tilde{e}_R$ LSP models with a dominant λ_{231} coupling, the most sensitive channels are the $e\mu\ell$ and $ee\ell$ high-p_T selections, which may exclude scenarios with $M_{1/2} \lesssim 450$ GeV with future data. This corresponds to LSP masses $M_{\tilde{e}_R} \lesssim (160-170)$ GeV and squark masses $M_{\tilde{q}} \lesssim (900-950)$ GeV. As expected, the $e\mu\ell$ selections are more efficient than the $ee\ell$ channels for scenarios with low mass difference between the $\tilde{\chi}_1^0$ and the $\tilde{e}_R$. The $\mu\mu\ell$ channel may become sensitive for models with $M_{1/2} \approx (370-380)$ GeV, because then the $\tilde{t}_1$ decays dominantly via $\tilde{t}_1 \to \tilde{\chi}_1^+ b$, and the decay of the chargino leads to an enhanced muon multiplicity, *cf.* Tab. A.2. However, if the events are observed at the same rate as given by the current data, the $\mu\mu\ell$ channel will not play a major rôle in the exclusion of $\tilde{e}_R$ LSP scenarios.

For most of the $\tilde{e}_R$ LSP parameter space with a dominant λ_{131} coupling the high-p_T $ee\ell$ channel is the most sensitive and may exclude scenarios with $M_{1/2} \lesssim 440$ GeV with 10 fb^{-1}, *cf.* Fig. 5.4(d). This reach roughly corresponds to models with LSP masses $M_{\tilde{e}_R} \lesssim (155-165)$ GeV and squark masses $M_{\tilde{q}} \lesssim (870-940)$ GeV. As with 2.3 fb^{-1} of data, the $e\mu\ell$ selections perform slightly better than the $ee\ell$ selections for scenarios with a low mass difference between the $\tilde{\chi}_1^0$ and the $\tilde{e}_R$ LSP.

We present the sensitive $\tilde{\mu}_R$ LSP parameter space with a dominant $\not{P}_6$ coupling $\lambda_{132} = 0.045$ at M_{GUT} in Fig. 5.5. The parameter space is the same as in Fig. 5.3. With 10 fb^{-1}, the low-p_T (high-p_T) $e\mu\ell$ selection may exclude scenarios with $M_{1/2} \lesssim 430$ GeV (450 GeV), whereas the $ee\ell$ channel selection is only sensitive to scenarios with $M_{1/2} \lesssim 390$ GeV (420 GeV) in its low-p_T (high-p_T) selection. However, the $ee\ell$ channel sensitivity does not depend on the mass difference, between the $\tilde{\chi}_1^0$ and the $\tilde{\mu}_R$ LSP, while the sensitivity of the $e\mu\ell$ channel decreases to approximately the $ee\ell$ sensitivity. We observe in Fig. 5.5 that the $\mu\mu\ell$ channel may exclude $\tilde{\mu}_R$ LSP scenarios around $M_{1/2} \lesssim 390$ GeV.

We conclude this section by pointing out, that the DØ analysis may exclude an extended $\tilde{e}_R$ and $\tilde{\mu}_R$ parameter space with future data. Under the (strong) assumption, that we can linearly extrapolate the results given for an integrated luminosity of 2.3 fb^{-1} to a higher integrated luminosity, both $\tilde{e}_R$ LSP and $\tilde{\mu}_R$ LSP scenarios with $M_{1/2} \lesssim 450$ GeV may be excluded with 10 fb^{-1}.

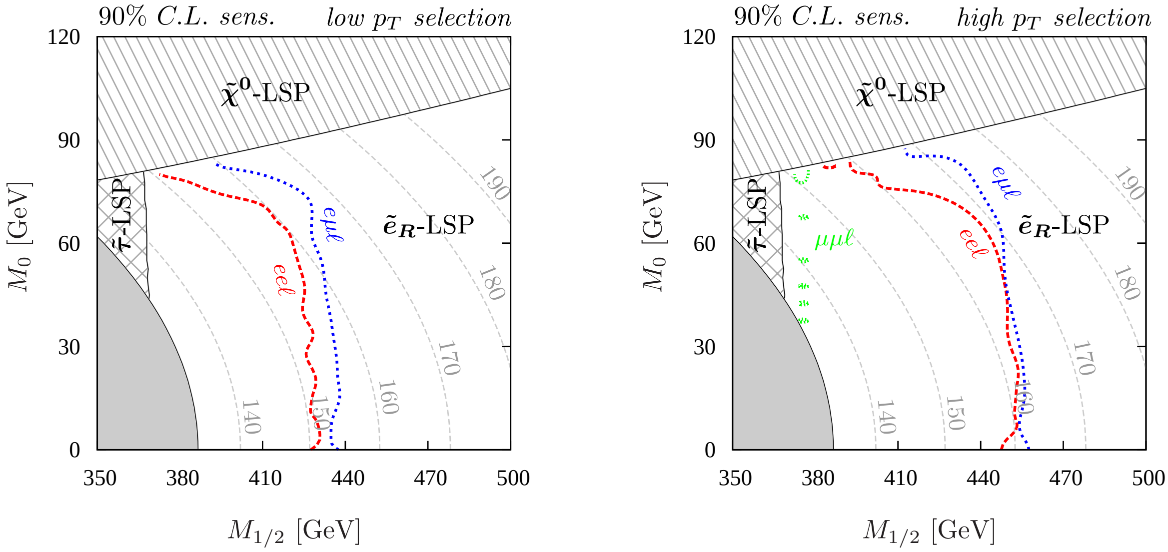

(a) $\tilde{e}_R$ LSP sensitivity region with a dominant λ_{231} coupling with the low-p_T selections.

(b) $\tilde{e}_R$ LSP sensitivity region with a dominant λ_{231} coupling with the high-p_T selections.

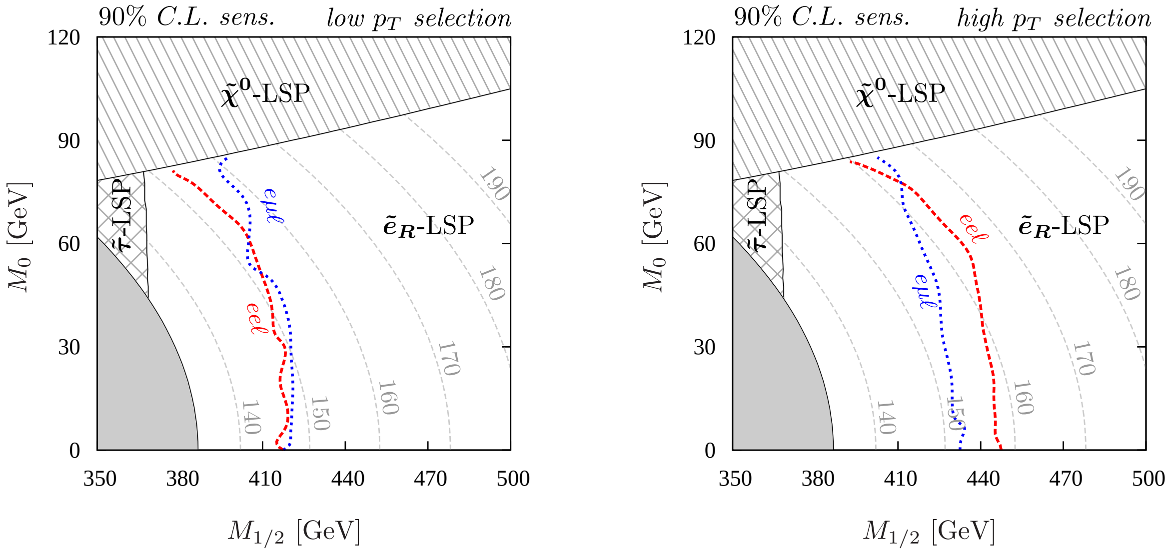

(c) $\tilde{e}_R$ LSP sensitivity region with a dominant λ_{131} coupling with the low-p_T selections.

(d) $\tilde{e}_R$ LSP sensitivity region with a dominant λ_{131} coupling with the high-p_T selections.

Figure 5.4.: Extrapolated sensitivity regions (90% C.L.) of the $\tilde{e}_R$ LSP parameter space for the DØ trilepton analysis with future data corresponding to an integrated luminosity of 10 fb^{-1}. The parameter regions are the same as in Fig. 5.2, *i.e.* we have (a,b) $\lambda_{231} = 0.045$ and (c,d) $\lambda_{131} = 0.045$ as the dominant $\not{P}_6$ coupling at M_{GUT}. The colored contour lines give the sensitivity of the different channels: In (a,c) they correspond to the *eel* (red, dashed) and $e\mu l$ (blue, dotted) low-p_T selections, while in (b,d) they are shown for the same channels in the high-p_T selection. In (b), the fine dotted, green contour gives the sensitivity of the $\mu\mu l$ high-p_T selection. The gray dotted contour lines give the LSP mass, $M_{\tilde{e}_R}$ in GeV, as indicated by the labels.

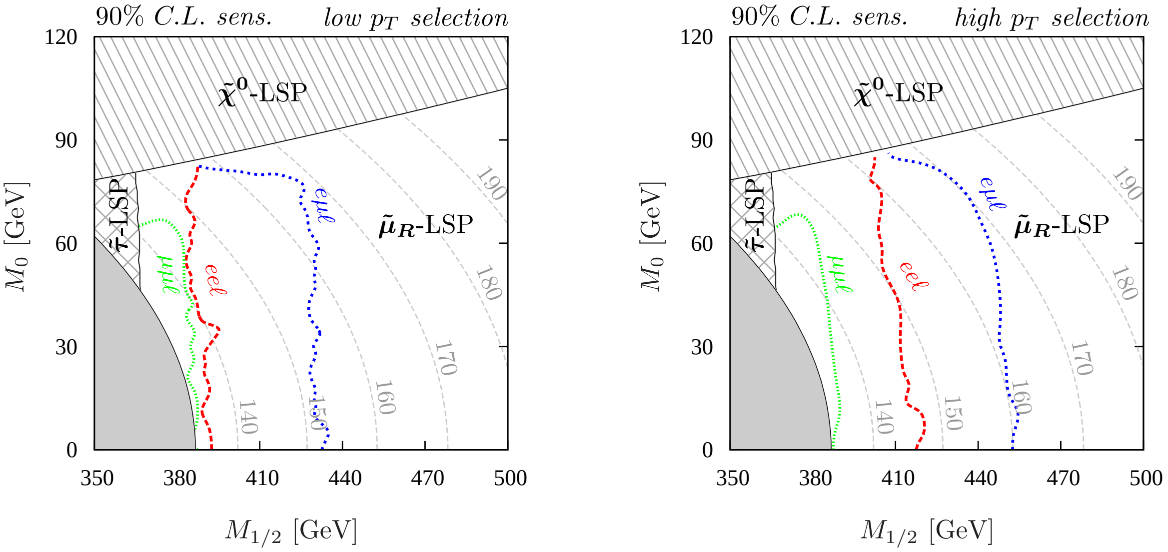

(a) $\tilde{\mu}_R$ LSP sensitivity region with a dominant λ_{132} coupling with the low-p_T selections.

(b) $\tilde{\mu}_R$ LSP sensitivity region with a dominant λ_{132} coupling with the high-p_T selections.

Figure 5.5.: Extrapolated sensitivity regions (90% C.L.) of the $\tilde{\mu}_R$ LSP parameter space for the DØ trilepton analysis with future data corresponding to an integrated luminosity of 10 fb^{-1}. The parameter regions are the same as in Fig. 5.3. The colored contour lines give the sensitivity of the different channels: In (a) they correspond to the $\mu\mu\ell$ (green, fine dotted), $ee\ell$ (red, dashed) and $e\mu\ell$ (blue, dotted) low-p_T selections, while in (b) they are shown for the same channels in the high-p_T selection. The gray dotted contour lines give the LSP mass, $M_{\tilde{\mu}_R}$ in GeV, as indicated by the labels.

5.3. Discovery potential at the LHC

In the beginning of this year (2010), the LHC at CERN started to take data for proton-proton (pp) collisions at a center-of-mass energy of $\sqrt{s} = 7$ TeV. The current plan schedules the collection of data corresponding to an integrated luminosity of $\int \mathcal{L}dt = 1\ \text{fb}^{-1}$ until the end of 2011. Then, the center-of-mass energy shall be increased to supposably $\sqrt{s} = 14$ TeV for a longer running period.

In this section, we study the discovery potential of $\tilde{e}_R$ and $\tilde{\mu}_R$ LSP models with an inclusive search analysis with three final state leptons at the LHC. Due to the striking multi-leptonic signatures of these models, *cf.* Sect. 5.1, these models may already be discovered with early LHC data. Thus, we study the prospects of a discovery with LHC data at both 7 TeV and 14 TeV center-of-mass energies.

In the next section, we select three benchmark scenarios as representatives of different regions in the $\tilde{\ell}_R$ LSP parameter space. The design of the search analysis is then guided by the properties of these signal benchmark points: We motivate the event selection by presenting the signal distributions of the transverse momentum, p_T, of the leptons and jets as well as event distributions in the various cut variables for the signal and SM background. Furthermore, we discuss in detail the impact of the analysis cuts on the signal and background and show, that the benchmark scenarios can be discovered with 1 fb^{-1} of LHC data at $\sqrt{s} = 7$ TeV. The discussion of the discovery potential is then extended to a larger B_3 mSUGRA parameter space. This will demonstrate, that our cuts work efficiently also beyond our benchmark points.

5.3.1. Benchmark Scenarios

In order to account for the different phenomenology of $\tilde{\ell}_R$ LSP models in the design of the three-lepton search analysis, we select one representative benchmark point for each mass hierarchy of the lightest sparticles, Eq. (4.8)-(4.10). The B_3 mSUGRA parameters and the masses of the lightest four sparticles of these benchmark points, denoted BE1, BE2 and BE3, are given in Tab. 5.7. All benchmark points exhibit a $\tilde{e}_R$ LSP via a dominant coupling $\lambda_{231} = 0.045$ at M_{GUT} and fulfill the experimental constraints from LEP Higgs searches, Eq. (4.7), and Tevatron trilepton SUSY searches, *cf.* Sect. 5.2, as well as the constraints on the $\not{P}_6$ coupling, *cf.* Tab. 4.1. The specific choice of the indices of the $\not{P}_6$ coupling $\mathbf{\Lambda}$, *cf.* Tab. 4.1, does not change the main structure of the mass spectrum[8] but only the lepton content in the final state at colliders, *cf.* Sect. 5.1. Since we want to design the search analysis as flavor-universal as possible, the selection of the benchmark models is somewhat independent of the choice of the $\mathbf{\Lambda}$ coupling indices. We therefore only study in detail the case of a $\tilde{e}_R$ LSP with a dominant λ_{231} coupling and argue, that these results also account for the other possible $\not{P}_6$ couplings and the case of a $\tilde{\mu}_R$ LSP.

We now discuss the main properties of the selected benchmark scenarios. The complete sparticle mass spectra and branching ratios are given in Appendix A.2.

The benchmark points BE1 and BE2 both feature a $\tilde{\tau}_1$ NLSP. In BE1, the $\tilde{\tau}_1$ is nearly mass degenerate with the $\tilde{e}_R$ and decays exclusively via the λ_{231} coupling into an electron and a muon neutrino. The NNLSP is the $\tilde{\mu}_R$ which decays via three-body decays into the $\tilde{e}_R$ or the $\tilde{\tau}_1$. There is a fairly large mass difference between the $\tilde{e}_R$ and the next-to-NNLSP (NNNLSP) $\tilde{\chi}_1^0$ of about 27 GeV. In contrast, in BE2 the $\tilde{\tau}_1$ mass is close to the mass of the $\tilde{\chi}_1^0$, which is the NNLSP. Thus, the $\tilde{\tau}_1$ dominantly decays into the $\tilde{e}_R$ via three-body decays. For this benchmark point, the mass difference between the $\tilde{e}_R$ and the $\tilde{\chi}_1^0$ is smaller, *i.e.* about 7 GeV. The NNNLSP is the $\tilde{\mu}_R$. Finally, the benchmark point BE3 features a $\tilde{\chi}_1^0$ NLSP with a mass difference to the $\tilde{e}_R$ of about 3 GeV. The $\tilde{\tau}_1$ NNLSP mostly decays into the $\tilde{\chi}_1^0$ and a τ (64.5%). The remaining decay is $\tilde{\tau}_1 \to e\nu_\mu$ via the λ_{231} coupling. Again, the $\tilde{\mu}_R$ is the NNNLSP.

5.3.2. Major Backgrounds

In the following Monte Carlo (MC) study, we consider the main SM backgrounds which can lead to three or more leptons ($\ell = e, \mu$) in the final state at particle level, *i.e.* after (heavy flavor) hadron and τ lepton decays. Moreover, we expect the SUSY signal events to contain additional energy from hard jets, which arise from decays of the heavier colored sparticles. We thus consider the following SM processes as the major backgrounds in our analysis:

- Top production. We consider top pair production ($t\bar{t}$), single-top production associated with a W boson (Wt) and top pairs associated with a gauge boson ($Wt\bar{t}$, $Zt\bar{t}$).
- $Z+$jets. The Z boson can decay into a pair of oppositely charged leptons. We consider Z production in association of one or two parton level jets. For these jets, we only consider c- and b-quarks. For the Zj background, we force the Z boson to decay into charged leptons.

---

[8] As discussed in Chapter 4, only the masses of those sparticles, which couple directly to the dominant $\mathbf{\Lambda}$ coupling, are significantly reduced compared to the P_6 conserving scenario. Changing the indices of the dominant $\mathbf{\Lambda}$ coupling interchanges the flavor of the mass reduced sparticles correspondingly, but preserves the main structure (*e.g.* mass hierarchy between LSP, NLSP, NNLSP, etc.) of the mass spectrum.

B_3-mSUGRA parameter	BE1	BE2	BE3
M_0 [GeV]	0	90	90
$M_{1/2}$ [GeV]	475	460	450
A_0 [GeV]	-1250	-1400	-1250
$\tan\beta$	5	4	4
$\mathrm{sgn}(\mu)$	$+$	$+$	$+$
$\lambda_{231}\|_{\mathrm{GUT}}$	0.045	0.045	0.045
lightest sparticles (mass/GeV)			
LSP	$\tilde{e}_R$ (168.7)	$\tilde{e}_R$ (182.3)	$\tilde{e}_R$ (182.0)
NLSP	$\tilde{\tau}_1$ (170.0)	$\tilde{\tau}_1$ (189.0)	$\tilde{\chi}_1^0$ (184.9)
NNLSP	$\tilde{\mu}_R$ (183.6)	$\tilde{\chi}_1^0$ (189.5)	$\tilde{\tau}_1$ (187.2)
NNNLSP	$\tilde{\chi}_1^0$ (195.7)	$\tilde{\mu}_R$ (199.0)	$\tilde{\mu}_R$ (195.9)

Table 5.7.: B_3 mSUGRA parameter and the mass hierarchies of the lightest four sparticles for the $\tilde{e}_R$ LSP benchmark points BE1, BE2 and BE3. The remaining spectrum and the branching ratios are given in Appendix A.

- $W +$ jets. The W boson can decay into a charged lepton and a neutrino. We demand two heavy flavor quarks (c, b) at parton level.
- Di-boson (WZ, ZZ) and Di-boson + jet (WWj, WZj, ZZj) production. For the di-boson background the gauge bosons are forced to decay leptonically. For WWj, we consider only the heavy flavor quarks c and b for the (parton level) jet, while for WZj and ZZj every quark flavor is taken into account.

In the backgrounds where we consider explicitly the production of heavy flavor quarks c and b at parton level, a cut on the minimal transverse momentum $p_T \geq 10$ GeV of the c or b quark is performed, because only then do these quarks have a fair probability to yield an additional isolated lepton [217]. Table 5.8 gives an overview of the background samples used in our analysis.

5.3.3. MC Simulation and object selection

The SM backgrounds $t\bar{t}$, $Zt\bar{t}$, $Zc\bar{c}$ and $Zb\bar{b}$ are simulated with Herwig6.510 [213, 214, 215]. For the other SM processes we employ MadGraph/MadEvent 4.4.30 [218] for the generation of the hard process which is then fed into Herwig6.510 for the hadronization process. The employed MC generators are listed in Tab. 5.8. We also give the leading-order (LO) cross section and the number of simulated events for each background sample for both 7 TeV and 14 TeV LHC collisions, derived with Herwig (for the backgrounds $t\bar{t}$, $Zt\bar{t}$, $Zc\bar{c}$ and $Zb\bar{b}$) and MadGraph (else). In order to be consistent, we only consider leading-order cross sections for signal and background samples. However, we want to note that next-to-leading-order (NLO) corrections can be large [219, 220]. These should be included in a more dedicated analysis. Furthermore, our simulation does not account for detector effects, *i.e.* we neglect backgrounds with leptons faked by jets or photons. It was shown in Ref. [195] that the QCD background can be efficiently suppressed in multi-lepton final states.

The SUSY mass spectra were calculated with SOFTSUSY 3.0.13 [188, 189]. The SOFTSUSY output was fed into ISAWIG1.200 and ISAJET7.64 [212] in order to calculate the decay widths of the SUSY particles. We added the three-body slepton decays $\tilde{\ell}_R \to \ell\ell'\tilde{\ell}'_R$ and $\tilde{\tau}_1 \to \tau\ell\tilde{\ell}_R$ to

Sample	sub-sample	cross section [pb]		simulated events		Generator
		7 TeV	14 TeV	7 TeV	14 TeV	
top	$t\bar{t}$	86.7	460.4	200 000	5 000 000	Herwig
	Wt	10.2	60.7	100 000	1 200 000	MadGraph + Herwig
	$Wt\bar{t}$	0.14	0.52	10 000	10 000	MadGraph + Herwig
	$Zt\bar{t}$	0.066	0.43	10 000	10 000	Herwig
$Z+$jets	$Zc\bar{c}$	49.5	187.2	100 000	2 000 000	Herwig
	$Zb\bar{b}$	44.6	170.5	100 000	2 000 000	Herwig
	$Z \to \ell^+\ell^- + j\,(j = c, b)$	59.6	202.5	180 000	3 700 000	MadGraph + Herwig
$W+$jets	$W \to \ell\nu + jj\,(j = c, b)$	38.2	95.2	135 000	1 400 000	MadGraph + Herwig
di-boson	$WZ \to$ charged leptons	0.20	0.40	100 000	100 000	MadGraph + Herwig
	$ZZ \to$ charged leptons	0.03	0.06	22 000	75 000	MadGraph + Herwig
	$WW + j\,(j = c, b)$	10.9	64.0	120 000	1 000 000	MadGraph + Herwig
	$WZ + j\,(j = \text{all})$	7.0	25.0	77 000	100 000	MadGraph + Herwig
	$ZZ + j\,(j = \text{all})$	3.2	10.2	16 000	280 000	MadGraph + Herwig

Table 5.8.: Monte Carlo (MC) samples of the SM background used for our analysis. The third and fourth (fifth and sixth) column give the leading-order cross section (number of simulated events) for *pp* collisions at a center-of-mass energy of $\sqrt{s} = 7$ TeV and $\sqrt{s} = 14$ TeV, respectively. For the event simulation we employ the MC generator listed in the last column. The cross section is obtained by the empoyed MC generator (MadGraph calculates the cross section in cases where we use both MadGraph and Herwig).

Cross section (in fb) at the LHC at $\sqrt{s} = 7$ TeV	BE1	BE2	BE3
$\sigma(pp \to \text{sparton pairs})$	86.7 ± 0.4	151.7 ± 0.7	138.6 ± 0.7
$\sigma(pp \to \text{slepton pairs})$	24.0 ± 0.1	19.9 ± 0.1	21.1 ± 0.1
$\sigma\left(pp \to \begin{matrix}\text{gaugino pairs,}\\ \text{gaugino-sparton}\end{matrix}\right)$	32.2 ± 0.2	38.6 ± 0.2	43.3 ± 0.2
$\sigma(pp \to \text{sparticle pairs})$	142.9 ± 0.5	210.2 ± 0.7	203.0 ± 0.7
Cross section (in fb) at the LHC at $\sqrt{s} = 14$ TeV	BE1	BE2	BE3
$\sigma(pp \to \text{sparton pairs})$	1968 ± 10	2771 ± 13	2759 ± 14
$\sigma(pp \to \text{slepton pairs})$	96.7 ± 0.5	83.9 ± 0.5	88.1 ± 0.5
$\sigma\left(pp \to \begin{matrix}\text{gaugino pairs,}\\ \text{gaugino-sparton}\end{matrix}\right)$	224 ± 1	259 ± 1	284 ± 1
$\sigma(pp \to \text{sparticle pairs})$	2288.7 ± 10.1	3113.9 ± 13.0	3131.1 ± 14.0

Table 5.9.: Leading-order signal cross section for *pp* collisions at center-of-mass energies $\sqrt{s} =$ 7 TeV and $\sqrt{s} = 14$ TeV for the benchmark scenarios BE1, BE2 and BE3. We give the cross section of sparton (*i.e.* squark and gluino) pair, slepton pair and electroweak (EW) gaugino pair / EW gaugino-sparton production separately. We further give the total sparticle pair production cross section, which is the signal process. We employ Herwig to determine the LO cross sections and to simulate ≈ 15 000 (≈ 250 000) events for the 7 TeV (14 TeV) MC signal samples. The uncertainties are due to statistical fluctuations from Herwig.

the ISAJET code, *cf.* Appendix C for the calculation and a discussion of these slepton decays. The signal processes, *i.e.* pair production of SUSY particles, were simulated with Herwig6.510.

In Tab. 5.9 we give the LO production cross section for all selected benchmark points at the LHC at center-of-mass energies of $\sqrt{s} = 7$ TeV and $\sqrt{s} = 14$ TeV. We present the cross sections the signal process, *i.e.* sparticle pair production, and three of its subprocesses: Firstly, the production of sparton pairs, where we consider squarks and gluinos as spartons; Secondly, slepton pair production and thirdly the production of electroweak (EW) gaugino pairs or an EW gaugino in association with a squark or gluino. For all benchmark points, sparton pair production is the dominant SUSY production process. Thus, the majority of SUSY events will fulfill our signature expectations including at least two hard jets, *cf.* Sect. 5.1. For the signal samples at 7 TeV (14 TeV), we generate approximately 15000 (250000) events.

The particle selection is inspired by the definitions used by the ATLAS collaboration for SUSY studies, *cf.* Ref. [195, pp. 1518]. We select leptons (*i.e.* electrons and muons) and jets with pseudorapidity $|\eta| < 2.5$ and minimum transverse momentum $p_T > 10$ GeV. We employ the following isolation criteria using the distance in pseudorapidity η and azimuthal angle ϕ, defined as $\Delta R = \sqrt{(\Delta\phi)^2 + (\Delta\eta)^2}$: Leptons are rejected, if the total transverse momentum of all particles within a cone of $\Delta R < 0.2$ around the lepton exceeds 1 GeV. Jets are reconstructed with FastJet 2.4.1 [209, 210] using the kt algorithm with cone radius $\Delta R = 0.4$. The missing transverse energy $\not{E}_T$ is given by the sum over the transverse momenta of the neutrinos.

5.3.4. Kinematic Distributions and Event Selection

In this section we discuss the kinematic event distributions for the benchmark points and motivate the event selection criteria. All figures are given for the simulated 7 TeV dataset and are either normalized or correspond to an integrated luminosity of $\int \mathcal{L}dt = 1\ \text{fb}^{-1}$. In Appendix B we discuss the performance of the analysis for the LHC at 14 TeV.

The normalized p_T distribution of the electrons (muons) after the object selection is shown in Fig. 5.6(a) (Fig. 5.6(b)) for the B_3 mSUGRA benchmark models. In all scenarios, the electrons mostly stem from the neutralino decay $\tilde{\chi}_1^0 \to \tilde{e}_R e$, while many of the muons come from the LSP decay $\tilde{e}_R \to \mu\nu_\tau$.

For BE1, the mass difference between the $\tilde{\mu}_R$ ($\tilde{\chi}_1^0$) and the $\tilde{e}_R$ LSP is about 15 (27) GeV and thus quite large. Furthermore, the $\tilde{\tau}_1$ NLSP exclusively decays via the P_6 violating decay $\tilde{\tau}_1 \to e\nu_\mu$. Thus, the electrons tend to have a hard p_T. For instance, 81% of all electrons have $p_T^{\text{el}} \gtrsim 25$ GeV. However, a large amount of the muons are soft, *cf.* Fig. 5.6(b). A sizable fraction of all muons do not fulfill the object selection requirement $p_T > 10$ GeV, such that 34% of all events do not contain any selected muon. These soft muons stem from the three body decays of the $\tilde{\mu}_R$ into the $\tilde{e}_R$ or the $\tilde{\tau}_1$.

The benchmark points BE2 and BE3 have similar lepton p_T spectra: Due to the smaller mass differences between the $\tilde{\chi}_1^0$ and the $\tilde{e}_R$ LSP compared to BE1, the electrons are softer. For instance the fraction of selected electrons with $p_T^{\text{el}} \lesssim 25$ GeV is 55% (34%) for BE2 (BE3). Because of the lepton p_T requirement in the object selection, the electron multiplicity is reduced in these scenarios: 30% (50%) of all events do not contain any selected electron in BE2 (BE3). In contrast, these two scenarios have a harder muon p_T spectrum than BE1, since the majority of the muons stem from the $\tilde{e}_R$ LSP decay.

We conclude, that the lepton p_T spectrum strongly depends on the sparticle mass spectrum. Thus, we desist from making further requirements on the lepton p_T since this would imply a strong model dependence in the event selection.

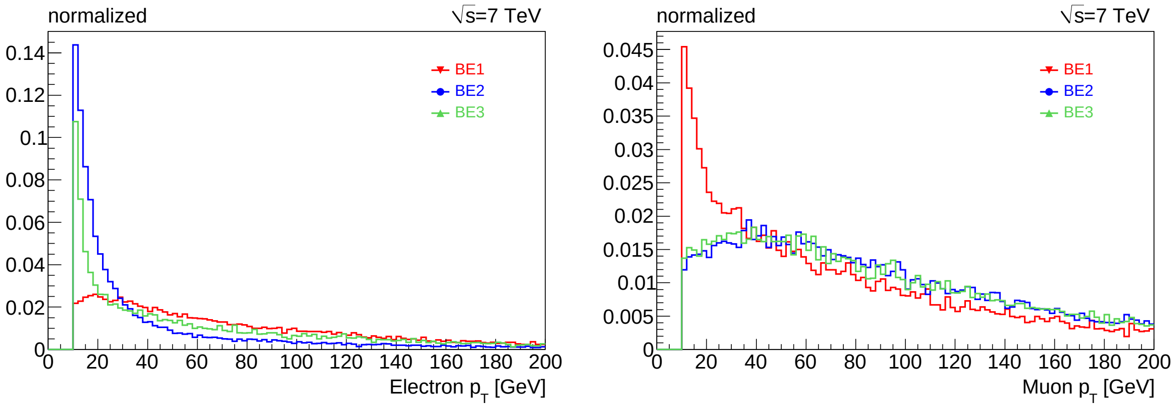

(a) Electron p_T distribution.

(b) Muon p_T distribution.

Figure 5.6.: Normalized lepton transverse momentum (p_T) distributions of SUSY benchmark models BE1 (red), BE2 (blue) and BE3 (green) for a center-of-mass energy of $\sqrt{s} = 7$ TeV and after object selection cuts. Note, that these distributions contain all selected leptons (of the given flavor) of the event.

In Fig. 5.7(a) [Fig. 5.7(b)] we present the normalized p_T distribution of the (second) hardest jet for the benchmark scenarios BE1, BE2 and BE3. For all signal models we observe a broad peak of the hardest jet p_T at around 400 GeV. These jets stem from the decays of the heavier squarks, whose masses are typically around $800 - 1000$ GeV, and from the gluino decays into the $\tilde{t}_1$ and a t quark. We find another peak of both the hardest and second hardest jet at around 100 GeV. These jets are formed by the t quark from the $\tilde{t}_1$ decay. The peak is most pronounced for BE2, since here we have a light $\tilde{t}_1$ mass, $M_{\tilde{t}_1} = 448$ GeV, and thus $\tilde{t}_1$ pair production is enhanced. In contrast, the $\tilde{t}_1$ mass is about 90 GeV heavier for BE1 and thus, the peak is hardly visible. For this benchmark point, the p_T distribution of both the hardest and second hardest jet rather peaks at low values, $p_T \lesssim 50$ GeV. These soft jets stem from initial and final state radiation of gluons and are selected as the hardest and second hardest jet in the case of EW gaugino and slepton pair production. These channels form a sizable fraction (39%) of the sparticle pair production for BE1, while they are less important for BE2 and BE3, *cf.* Tab. 5.9. However, this picture will change for a center-of-mass energy of $\sqrt{s} = 14$ TeV, where sparton pair production is much more dominant for all three benchmark points.

We now discuss the construction of our event selection. In order to motivate the selection steps, we show in Fig. 5.8 the event distribution as a function of the respective cut variable for the SM background, the three $\tilde{e}_R$ LSP benchmark models BE1, BE2, and BE3, as well as for comparison the P_6 conserving SUSY benchmark model SPS1a [221] before the corresponding cut. In Tab. 5.10 we give the number of background and signal events after each selection step of the analysis. Furthermore, we provide for each signal benchmark scenario the cut-flow of the significance estimator[9] $S/\sqrt{B}$, where S (B) is the number of signal (background) events. In general, the signal can be defined to be observable if [222, 223]

$$S \geq max\left[5\sqrt{B},\ 5,\ 0.2B\right]. \tag{5.5}$$

---

[9] Note that this widely used estimator is an approximation for large Poisson statistics with $S \ll B$. Thus, in particular in the case of low SM background and larger number of signal events, this significance estimator should not be taken too seriously.

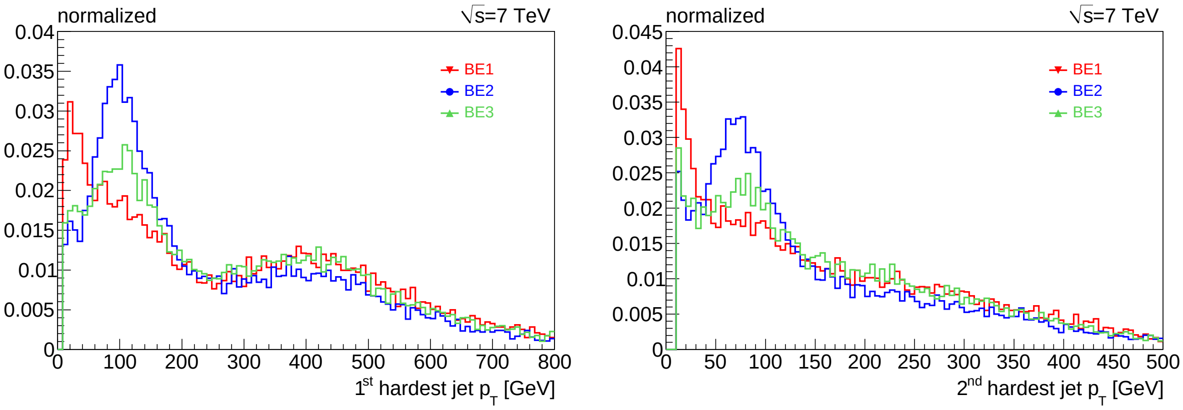

(a) p_T distribution of the hardest jet.

(b) p_T distribution of the 2nd hardest jet.

Figure 5.7.: Normalized jet transverse momentum (p_T) distributions for the SUSY benchmark models BE1 (red), BE2 (blue) and BE3 (green) for a center-of-mass energy of $\sqrt{s} = 7$ TeV and after object selection cuts.

The requirement $S \geq 0.2B$ avoids the possibility that a small signal on top of a large background could otherwise be regarded as statistically significant, although this would require the background level to be known to an excellent precision. In the case of a very low background expectation, $B \leq 1$, we still require 5 signal events for a discovery.

As we have seen in Sect. 5.1, we expect an extensive number of leptons in the final state. However, the lepton flavor multiplicity depends on the LSP flavor as well as on the $\mathbf{\Lambda}$ coupling, *cf.* Tab. 5.1. Also, the p_T spectrum of the leptons depends on the mass hierarchy. To be as model independent as possible, we simply demand three leptons (e or μ) without further p_T requirements in step I of our event selection.

In Fig. 5.8(a) we show the lepton multiplicity. We clearly observe more leptons in the B_3 mSUGRA models than for SPS1a. All SM backgrounds can be highly reduced by demanding three (or more) leptons. We also see, that in demanding five leptons, we could already get a background free signal. However, this would also significantly reduce the signal. Furthermore, we do not take into account detector effects and leptons, which may be faked by jets or photons. These effects could also lead to background events with more than five leptons. After step I the main SM background comes from di-boson events ($\approx 68\%$). No $W +$jets events survived this cut, indicated by $\lesssim 1.0$ events in Tab. 5.10. The number of signal events is reduced to 63% (44%) for BE1 (BE2). Even more signal events are rejected in the benchmark scenario BE3 (30% of the events survive the cut), because due to the low mass difference between the $\tilde{\chi}_1^0$ and the $\tilde{e}_R$ LSP, the lepton multiplicity is reduced. According to Eq. (5.5), BE1 and BE2 are already observable after this cut.

We show the jet multiplicity in Fig. 5.8(b) after demanding three leptons. Due to the weak object selection criteria that we chose for the jets, we observe a high jet multiplicity. As discussed in Sect. 5.1, we expect at least two jets from squark and gluino decays. Thus we demand in step II of our event selection the number of jets to be $N_{\text{jet}} \geq 2$. This cut reduces most of the di-boson backgrounds WZ and ZZ as well as about 70% of the $Z +$jets background. After this cut, the dominant SM background is $WZ + j$ ($\approx 39\%$). The number of signal events is reduced to 88% (83%) for BE1 and BE2 (BE3). After this requirement, also BE3 is observable.

In order to further reduce the SM backgrounds involving Z bosons, we construct the invariant

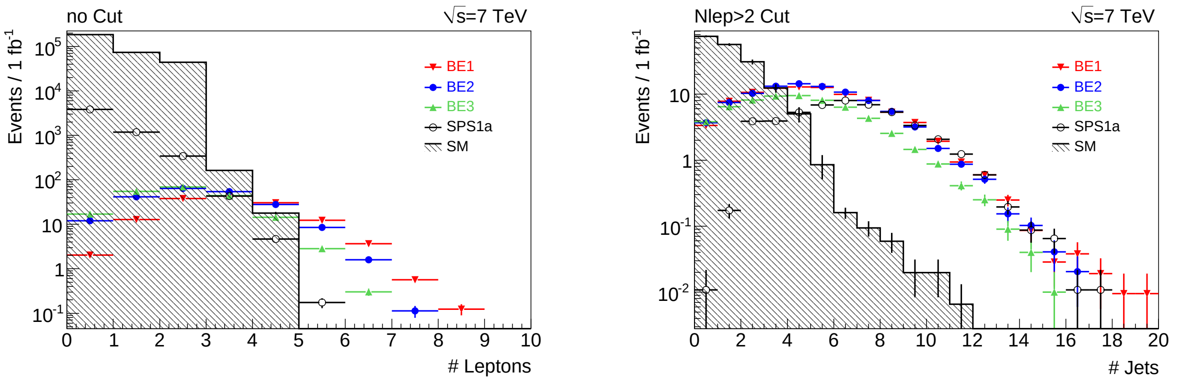

(a) Lepton (e, μ) multiplicity with no cut applied.

(b) Jet multiplicity with the trilepton cut applied.

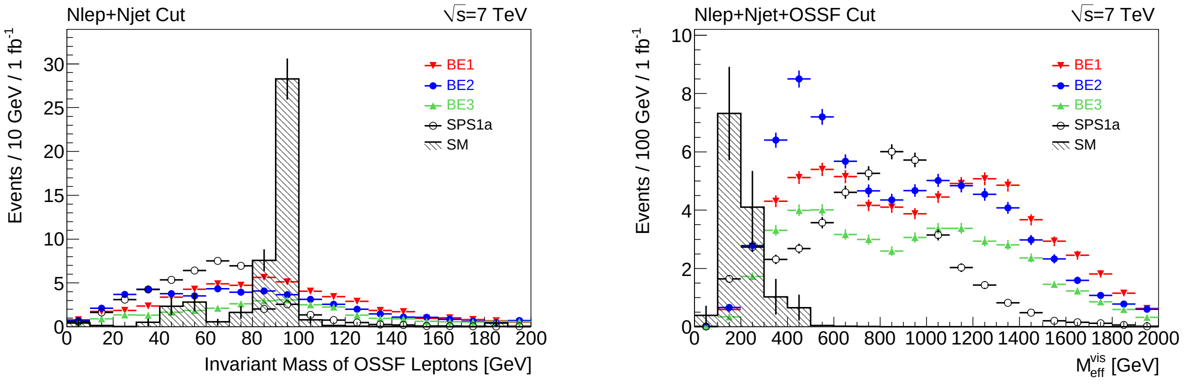

(c) Invariant mass distribution of the opposite sign same flavor lepton pairs with trilepton and jet multiplicity cut applied.

(d) Effective mass distribution with trilepton, jet multiplicity and OSSF mass cut applied.

Figure 5.8.: Event distributions of several cut variables: (a) lepton multiplicity, (b) jet multiplicity, (c) OSSF lepton invariant mass and (d) visible effective mass for the SM background (gray patterned) and the SUSY models BE1 (red), BE2 (blue), BE3 (green) and SPS1a (white). Note that Fig. 5.8(a) and 5.8(b) are given on a logarithmic scale. The distributions show events after the object selection and follow the event selection, *i.e.* they are presented before the cut on the respective variable is applied (see text). They correspond to an integrated luminosity of 1 fb^{-1} at a center-of-mass energy of 7 TeV.

mass of opposite-sign-same-flavor (OSSF) leptons, shown in Fig. 5.8(c). As expected, the SM background has a large peak at the Z boson mass $M_Z = 91.2$ GeV, while the signal distribution is mostly flat in that region. Thus, in step III of our event selection, we reject all events where the invariant mass of the OSSF leptons lies within a 10 GeV window around the Z boson mass, *i.e.* we demand

$$M_{\mathrm{OSSF}} \notin [81.2\ \mathrm{GeV}, 101.2\ \mathrm{GeV}]\,. \tag{5.6}$$

This cut strongly reduces the $Z+$jets and di-boson backgrounds, leaving $t\bar{t}$ as the dominant SM background. Roughly 85% – 90% of the signal events (all benchmark scenarios) survive this cut.

Sample	before cuts	$N_{\text{lep}} \geq 3$	$N_{\text{jet}} \geq 2$	M_{OSSF}	$M_{\text{eff}}^{\text{vis}} \geq 300$ GeV
top	97111 ± 197	14.9 ± 2.2	13.8 ± 2.1	12.0 ± 2.1	2.1 ± 0.8
$Z +$ jets	153591 ± 254	51.9 ± 4.3	16.6 ± 2.4	1.0 ± 0.6	$\lesssim 1.0$
$W +$ jets	38219 ± 103	$\lesssim 1.0$	$\lesssim 1.0$	$\lesssim 1.0$	$\lesssim 1.0$
di-boson	21331 ± 48	179.2 ± 3.0	53.5 ± 2.0	2.6 ± 0.4	0.7 ± 0.2
all SM	310252 ± 341	264.0 ± 5.7	83.9 ± 3.8	15.6 ± 2.2	2.8 ± 0.8
BE1	143.1 ± 1.2	90.5 ± 0.9	79.4 ± 0.9	68.8 ± 0.8	65.5 ± 0.8
$S/\sqrt{B}$	-	5.6	8.7	17.4	39.1
BE2	210.4 ± 1.5	92.6 ± 1.0	81.4 ± 0.9	73.8 ± 0.9	70.4 ± 0.8
$S/\sqrt{B}$	-	5.7	8.9	18.7	42.1
BE3	202.7 ± 1.4	61.6 ± 0.8	51.3 ± 0.7	45.2 ± 0.7	43.2 ± 0.7
$S/\sqrt{B}$	-	3.8	5.6	11.4	25.8

Table 5.10.: Number of SM background and signal events after each step in the event selection at $\sqrt{s} = 7$ TeV, scaled to an integrated luminosity of 1 fb^{-1}. We provide the results for the three signal benchmark scenarios BE1, BE2 and BE3. For each signal model, we give $S/\sqrt{B}$ as significance estimator. The uncertainties include statistical errors only.

SUSY events are expected to contain a large amount of energy in the form of high transverse momenta of the jets and leptons. Thus, we construct the visible[10] effective mass as the scalar sum of the absolute value of the transverse momenta of the four hardest jets and all selected leptons in the event,

$$M_{\text{eff}}^{\text{vis}} \equiv \sum_{i=1}^{4} p_T^{\text{jet},i} + \sum_{\text{all}} p_T^{\text{lep}}. \tag{5.7}$$

The visible effective mass distribution is shown in Fig. 5.8(d). The SM background dominates for $M_{\text{eff}}^{\text{vis}} < 300$ GeV, while most of the signal events exhibit a visible effective mass beyond 300 GeV. This threshold value is slightly higher for the 14 TeV dataset. Thus, we demand in step IV of our event selection

$$M_{\text{eff}}^{\text{vis}} > \begin{cases} 300 \text{ GeV}, & \text{if } \sqrt{s} = 7 \text{ TeV}, \\ 400 \text{ GeV}, & \text{if } \sqrt{s} = 14 \text{ TeV}. \end{cases} \tag{5.8}$$

After this cut, only 2.8 ± 0.8 SM events remain, dominated by the $t\bar{t}$ background. The signal is mainly unaffected by this cut. More than 95% of the signal events (all benchmark scenarios) survive this selection step.

We observe two peaks in the visible effective mass distribution for our benchmark scenarios. The peak at lower values of $M_{\text{eff}}^{\text{vis}}$ contains mainly events from $\tilde{t}_1$ pair production, while events from heavier squark or gluino production build the second peak at higher $M_{\text{eff}}^{\text{vis}}$ values. Due to the large difference of the $\tilde{t}_1$ mass to the other squark masses of about 400 GeV – 500 GeV (depending on the model), these peaks are clearly separated in the visible effective mass. We

---

[10] We denote this variable as *visible* effective mass because it does not include the missing transverse energy as in other definitions of the effective mass [195].

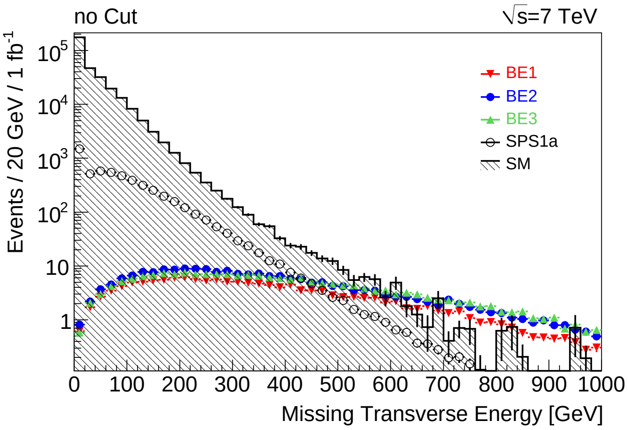

Figure 5.9.: Missing transverse energy, $\not{E}_T$, distribution for the B_3 benchmark points BE1, BE2 and BE3, the R-parity conserving benchmark scenario SPS1a and the SM background. The distributions show events before the event selection and correspond to an integrated luminosity of 1 fb^{-1} at $\sqrt{s} = 7$ TeV.

make use of this fact when we present a method to reconstruct the masses of both the $\tilde{t}_1$ and the right-handed first and second generation squarks, *cf.* Sect. 6.2.

In order to test the flavor sensitivity of this search, we applied the analysis to a modified version of the benchmark models presented in Tab. 5.7. Instead of λ_{231}, we chose λ_{131} (λ_{132}) as the dominant $\not{P}_6$ coupling to obtain the $\tilde{e}_R$ ($\tilde{\mu}_R$) as the LSP, while we left the other B_3 mSUGRA parameters unchanged. The results for the $\tilde{\mu}_R$ LSP scenario are in agreement with the original benchmark scenarios within $< 1\%$ deviations, which are due to statistical fluctuations of the MC estimate. However, for $\tilde{e}_R$ LSP scenarios with a dominant λ_{131} coupling, the cut on the invariant mass of OSSF leptons (step III) rejects more signal events than for scenarios with λ_{231} as the dominant $\not{P}_6$ coupling. For the modified scenario of BE1 (BE2), the number of signal events passing the M_{OSSF} cut is reduced by around 15% (3%) compared to the original results, *cf.* Tab. 5.10. This difference is strongest for BE1-like scenarios, because the endpoint of the di-electron invariant mass distribution, where one electron comes from the $\tilde{\chi}_1^0$ decay and the other from the $\tilde{e}_R$ LSP decay, *cf.* also Eq. (6.6a), coincides with the upper value of the Z boson mass window. We conclude that in most cases, our detailed study of $\tilde{e}_R$ LSP models with a dominant $\not{P}_6$ coupling λ_{231} as representative for a general B_3 mSUGRA model with a $\tilde{\ell}_R$ LSP is justified. However, for $\tilde{e}_R$ models with a dominant coupling λ_{1j1} ($j = 2,\ 3$), the signal efficiency and thus the discovery potential can be slightly reduced due to the M_{OSSF} cut.

In Fig. 5.9 we present the missing transverse energy event distribution for all signal scenarios and the SM background before the event selection criteria are applied. In P_6 conserving scenarios like SPS1a, the $\tilde{\chi}_1^0$ LSP is stable and escapes detection, leading to missing transverse energy $\not{E}_T$. However, even though the LSP decays within the detector in the B_3 scenarios BE1, BE2 and BE3, there is a significant amount of missing energy due to the neutrinos from the LSP decay. Moreover, the $\not{E}_T$ distribution for SPS1a falls off more rapidly than for the B_3 scenarios. Thus, B_3 scenarios can lead to even more missing transverse energy than P_6 conserving scenarios.

The performance of the event selection presented in this section on the signal and SM background samples for an integrated luminosity of 10 fb^{-1} at a center-of-mass energy of 14 TeV is discussed in Appendix B.

5.3.5. Discovery reach with early LHC data

The previous analysis is now extended to a more extensive supersymmetric parameter region. We provide the discovery potential of B_3 mSUGRA models with a $\tilde{e}_R$ LSP with early LHC data at $\sqrt{s} = 7$ TeV and $\sqrt{s} = 14$ TeV. For each center-of-mass energy, we perform a two dimensional parameter scan in the $M_{1/2} - M_0$ plane around the benchmark point BE1 ($A_0 = -1250$ GeV, $\tan\beta = 5$, $\mathrm{sgn}(\mu) = +$, $\lambda_{231}|_{\mathrm{GUT}} = 0.045$), *cf.* also Fig. 4.3. For each parameter point, we generate 1000 events and apply the analysis presented in the previous section. Thus, we do not optimize the cuts for each parameter point.

Due to the RGE running, all sparticle masses, especially those of the strongly interacting sparticles, increase with increasing $M_{1/2}$ [158]. Thus, by varying $M_{1/2}$, we can investigate the discovery potential as a function of the SUSY mass scale. As we have seen in the previous section, the discovery potential is also sensitive to the mass hierarchy of the lighter sparticles and, in particular, to the mass difference between the $\tilde{\chi}_1^0$ and the LSP. As with $M_{1/2}$, all sparticle masses also increase with increasing M_0, however, this mainly affects the scalar particles, while gauginos are nearly unaffected. Thus, M_0 provides a handle on the mass difference between the $\tilde{\chi}_1^0$ and the $\tilde{e}_R$ or $\tilde{\mu}_R$ LSP.

For the LHC at $\sqrt{s} = 7$ TeV, we give in Fig. 5.10 the signal cross section (in pb) [Fig. 5.10(a)] and the signal efficiency [Fig. 5.10(b)], *i.e.* the fraction of signal events that pass the analysis. The results are given only for B_3 mSUGRA models with a $\tilde{e}_R$ LSP, while models with a $\tilde{\chi}_1^0$ LSP ($\tilde{\tau}_1$ LSP) are indicated by the striped (checkered) region. The solid gray region is excluded by the experimental bound on the λ_{231} coupling.

The signal cross section, which is dominated by the production of colored sparticles, clearly decreases with increasing $M_{1/2}$, *i.e.* with an increasing SUSY mass scale. For instance, increasing $M_{1/2}$ from 400 GeV to 500 GeV reduces the cross section from 0.6 pb to 0.1 pb, while the right-handed squark (gluino) mass increases from around 820 GeV (930 GeV) to 1010 GeV (1150 GeV). In contrast, the M_0 dependence of the signal cross section is negligible.

For the benchmark scenario BE1 we obtained a signal efficiency of roughly 46%. Going beyond BE1, we observe in Fig. 5.10(b) that the signal efficiency lies between 30% and 50% for most of the $\tilde{e}_R$ LSP parameter space. Thus, the presented analysis works also quite well for a larger set of $\tilde{e}_R$ LSP models. However, the signal efficiency decreases dramatically for a decreasing mass difference, ΔM, between the $\tilde{\chi}_1^0$ and the $\tilde{e}_R$ LSP. For models with $\Delta M \lesssim 2.5$ GeV the signal efficiency is usually around 10% − 20%, because the electrons from the decay $\tilde{\chi}_1^0 \to \tilde{e}_R e$ are very soft and tend to fail the minimum p_T requirement. For models with $\Delta M > 10$ GeV, the signal efficiency becomes more or less insensitive of ΔM. Note that, if we choose a stronger minimum lepton p_T requirement in our analysis, this band of low signal efficiency will become wider.

The signal efficiency depends also slightly on $M_{1/2}$. At low values, $M_{1/2} \lesssim 400$ GeV, *i.e.* for models with a light sparticle mass spectrum, more events are rejected by the cut on the visible effective mass. Moreover, the SM particles from cascade decays and LSP decays then have on average smaller momenta than for scenarios with a heavier mass spectrum, and thus may fail to pass the object selection[11]. The signal efficiency is highest for values of $M_{1/2}$ between 450 GeV and 550 GeV and reaches up to 50%. However, when going to very large $M_{1/2}$, the signal efficiency again decreases. Here, the production of sparton pairs is suppressed due to their large masses. For instance, by varying $M_{1/2}$ from 500 GeV to 700 GeV, the fraction of sparton

---

[11] However, due to our rather weak p_T requirements for jets and leptons, this effect does not play a major rôle in this analysis.

pair production of the signal cross section decreases from 58% to 24% at a center-of-mass energy of $\sqrt{s} = 7$ TeV. Since our analysis is optimized for sparton pair production, the signal efficiency decreases with very large values of $M_{1/2}$.

In Fig. 5.11 we present the discovery potential for the LHC at $\sqrt{s} = 7$ TeV. The discovery reach for the integrated luminosities 100 pb^{-1}, 500 pb^{-1} and 1 fb^{-1} is given in Fig. 5.11(a). We use Eq. (5.5) as criteria for a discovery. Furthermore, we present the signal to background ratio, S/B, in Fig. 5.11(b). As shown in the previous section, the SM background can be reduced to 2.8 ± 0.8 events at $\sqrt{s} = 7$ TeV.

Fig. 5.11(a) suggests that $\tilde{e}_R$ LSP scenarios up to $M_{1/2} \lesssim 620$ GeV can be discovered with an integrated luminosity of 1 fb^{-1}. This corresponds to squark masses of 1.2 TeV and $\tilde{e}_R$ LSP masses of around 230 GeV. For these models, we have a signal over background ratio of $S/B \approx 3$ and thus, systematic uncertainties are not significant for a discovery. Furthermore, we see that BE1 can already be discovered with $\lesssim$ 100 pb^{-1} of data. We clearly see in Fig. 5.11 that scenarios with a small mass difference between the $\tilde{\chi}_1^0$ and the $\tilde{e}_R$ LSP are more difficult to discover.

We now discuss the prospects of a discovery at the LHC at $\sqrt{s} = 14$ TeV. In Fig. 5.12 we give the signal cross section [Fig. 5.12(a)] and the signal efficiency [Fig. 5.12(b)].

Due to the higher center-of-mass energy, the cross section is $\mathcal{O}(10)$ times larger than for $\sqrt{s} = 7$ TeV, *cf.* Fig. 5.10(a). For instance, at $M_{1/2} = 400$ GeV (500 GeV) the signal cross section at $\sqrt{s} = 14$ TeV is 7.2 pb^{-1} (1.7 pb^{-1}). Furthermore, the signal production is strongly dominated by sparton pair production, *cf.* also Tab. 5.9.

The signal efficiency at $\sqrt{s} = 14$ TeV is slightly improved compared to the results for $\sqrt{s} =$ 7 TeV. This is because due to the enhanced sparton pair production, more signal events pass the cut on the jet multiplicity, $N_{\text{jet}} \geq 2$, *cf.* also Appendix B. For the benchmark point BE1, we now obtain a signal efficiency of about 51%. Most of the parameter points in Fig. 5.12(b) exhibit a signal efficiency in the range of 40% to 60%. For the scenarios with low mass difference between the $\tilde{\chi}_1^0$ and the $\tilde{e}_R$ LSP, $\Delta M \lesssim 2.5$ GeV, the signal efficiency is reduced to around 15% – 25%. As for $\sqrt{s} = 7$ TeV, the signal efficiency decreases at very large values of $M_{1/2}$ because of the increasing sparton mass. Here, this effect slowly sets in at values $M_{1/2} \gtrsim 1100$ GeV, *i.e.* for scenarios with very heavy squark and gluino masses $\gtrsim$ 2 TeV. For instance, at $M_{1/2} = 1100$ GeV, sparton pair production still forms 52% of the signal cross section.

Applying the search analysis presented in Sect. 5.3.4 on the SM background samples at $\sqrt{s} = 14$ TeV with an integrated luminosity of 10 fb^{-1}, we obtain 64.7 ± 7.2 SM background events passing the full event selection, *cf.* Tab. B.1 in Appendix B. In Fig. 5.13 we give the discovery potential for the LHC at $\sqrt{s} = 14$ TeV. We give the discovery reach for the integrated luminosities 100 pb^{-1}, 1 fb^{-1} and 10 fb^{-1} in Fig. 5.13(a). The signal to background ratio S/B is shown in Fig. 5.13(b). We observe, that scenarios with $M_{1/2} \lesssim 1$ TeV (1.15 TeV) can be discovered with 1 fb^{-1} (10 fb^{-1}) with a signal over background ratio of 2 (0.6). This corresponds to squark masses of around 1.9 TeV (2.2 TeV) and LSP masses of roughly 370 GeV (450 GeV).

We conclude this section by pointing out that due to the striking multi-leptonic signature, the prospects of an early discovery of B_3 mSUGRA with a $\tilde{\ell}_R$ LSP are better than for P_6 conserving mSUGRA models [222, 223]. The discovery potential decreases significantly for scenarios with a low mass difference between the $\tilde{\chi}_1^0$ and $\tilde{\ell}_R$ LSP. Note, that the vast reach in $M_{1/2}$ is also due to the fact, that typically the $\tilde{t}_1$ mass is much smaller than those of the other squarks. For instance, at $M_{1/2} = 525$ GeV, the $\tilde{t}_1$ mass is around 630 GeV and thus can still be produced numerously at the LHC at $\sqrt{s} = 7$ TeV.

We want to remark that, for scenarios with low mass difference between the $\tilde{\chi}_1^0$ and the $\tilde{\ell}_R$ LSP, the search for like-sign di-lepton final states might be a more promising approach. Assuming both like-sign leptons originate from the LSP decay, a high lepton p_T requirement can be imposed, which may reduce the SM background dramatically [15, 224, 225, 226, 227]. However, a detailed analysis of these search channels is beyond the scope of this thesis.

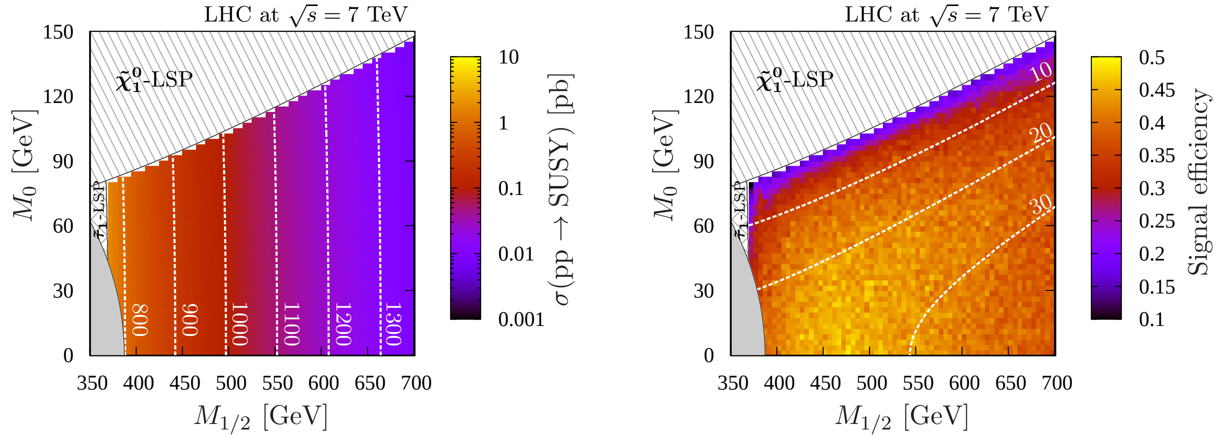

(a) Signal cross section in pb at the LHC at $\sqrt{s} = 7$ TeV. The white dotted contour lines give the $\tilde{q}_R$ mass in GeV.

(b) Selection efficiency for the signal events at the LHC at $\sqrt{s} = 7$ TeV. The white dotted contour lines give the mass difference, ΔM, between the $\tilde{\chi}_1^0$ and the $\tilde{e}_R$ LSP in GeV.

Figure 5.10.: Signal cross section (in pb) [Fig. 5.10(a)] and signal efficiency [Fig. 5.10(b)] at the LHC at $\sqrt{s} = 7$ TeV in the $M_{1/2} - M_0$ plane. The other parameters are those of BE1 ($A_0 = -1250$ GeV, $\tan\beta = 5$, $\text{sgn}(\mu) = +$, $\lambda_{231}|_{\text{GUT}} = 0.045$). The patterned regions correspond to scenarios with either a $\tilde{\tau}_1$ or $\tilde{\chi}_1^0$ LSP. The solid gray region is excluded by the bound on λ_{231}.

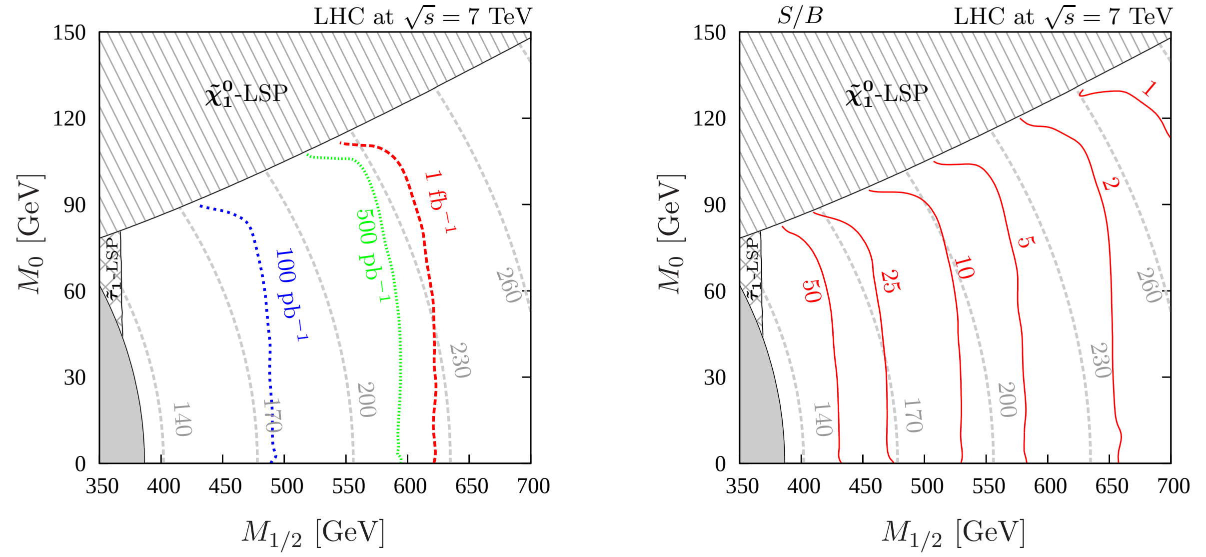

(a) Estimated contours of minimal required integrated luminosity to obtain an observable signal, *cf.* Eq. (5.5).

(b) Contours for the signal over background ratio, S/B, as given by the red labels.

Figure 5.11.: Discovery reach at the LHC at $\sqrt{s} = 7$ TeV. We give the minimal required integrated luminosity for a discovery in Fig. 5.11(a) and the signal to background ratio, S/B in Fig. 5.11(b). The $\tilde{e}_R$ LSP parameter region is shown for $A_0 = -1250$ GeV, $\tan\beta = 5$, $\text{sgn}(\mu) = +$ and $\lambda_{231}|_{\text{GUT}} = 0.045$. The patterned regions correspond to scenarios with either a $\tilde{\tau}_1$ or $\tilde{\chi}_1^0$ LSP. The solid gray region is excluded by the bound on λ_{231}. The grey dotted contour lines give the $\tilde{e}_R$ mass (in GeV) as indicated by the labels.

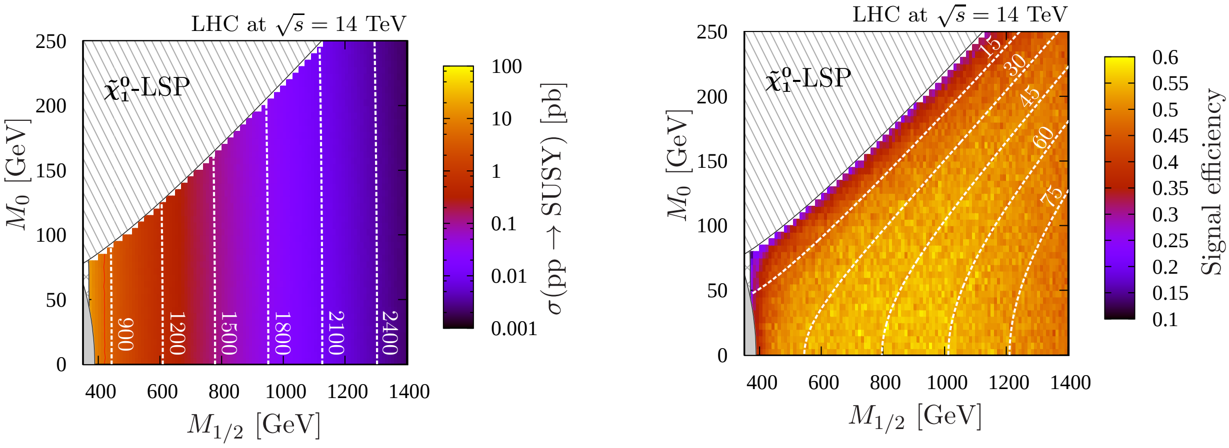

(a) Signal cross section in pb at LHC at $\sqrt{s} = 14$ TeV. The white dotted contour lines give the $\tilde{q}_R$ mass in GeV.

(b) Selection efficiency for the signal events at the LHC at $\sqrt{s} = 14$ TeV. The white dotted contour lines give the mass difference between the $\tilde{\chi}_1^0$ and the $\tilde{e}_R$ LSP in GeV.

Figure 5.12.: Signal cross section (in pb) [Fig. 5.12(a)] and signal efficiency [Fig. 5.12(b)] at the LHC at $\sqrt{s} = 14$ TeV in the $M_{1/2} - M_0$ plane. The other B_3 mSUGRA parameter are those of BE1, *i.e.* $A_0 = -1250$ GeV, $\tan\beta = 5$, $\mathrm{sgn}(\mu) = +$ and $\lambda_{231}|_{\mathrm{GUT}} = 0.045$.

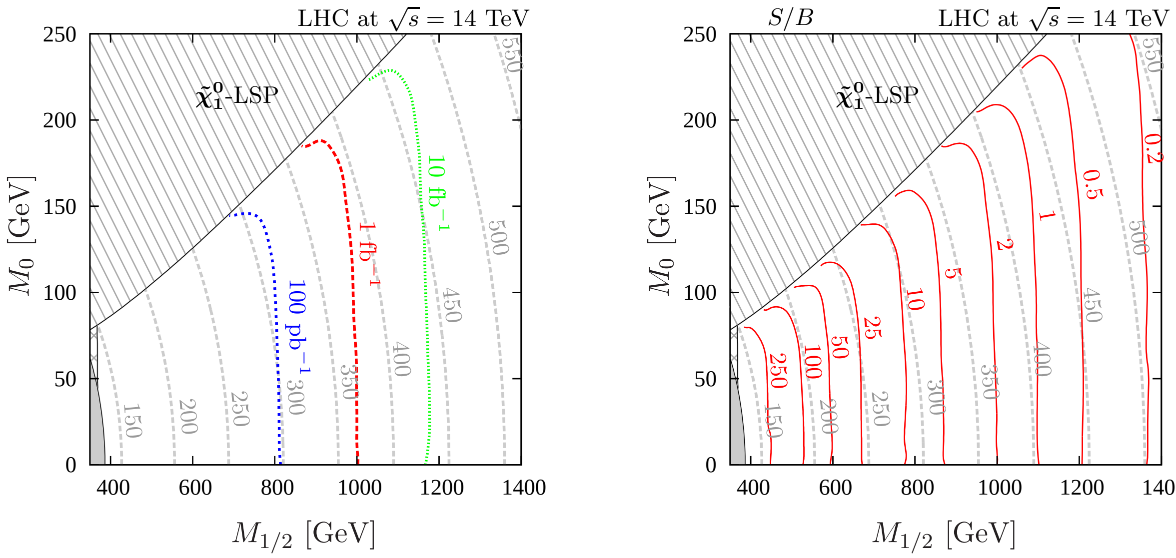

(a) Estimated contours of minimal required integrated luminosity to obtain an observable signal, *cf.* Eq. (5.5).

(b) Contours for the signal over background ratio, S/B, as given by the red labels.

Figure 5.13.: Discovery reach at the LHC at $\sqrt{s} = 14$ TeV. We give the minimal required integrated luminosity for a discovery in Fig. 5.13(a) and the signal to background ratio, S/B in Fig. 5.13(b). The $\tilde{e}_R$ LSP parameter region is shown for $A_0 = -1250$ GeV, $\tan\beta = 5$, $\mathrm{sgn}(\mu) = +$ and $\lambda_{231}|_{\mathrm{GUT}} = 0.045$. The patterned regions correspond to scenarios with either a $\tilde{\tau}_1$ or $\tilde{\chi}_1^0$ LSP. The solid gray region is excluded by the bound on λ_{231}. The grey dotted contour lines give the $\tilde{e}_R$ mass (in GeV) as indicated by the labels.

6. Mass reconstruction at the LHC

In the last section we have shown that B_3 mSUGRA scenarios with a $\tilde{\ell}_R$ LSP can already be tested quite stringently with early LHC data. If a discovery has been made, the next step would be to try to determine the sparticle mass spectrum. Here, we present an idea how some sparticle masses can be reconstructed, using the benchmark point BE2 as an example.

As in P_6 conserving scenarios, the decay chain of sparticles cannot be completely reconstructed, as the $\tilde{e}_R$ LSPs decay into neutrinos that cannot be detected. Thus, we focus on the measurement of edges and thresholds of invariant mass distributions formed from certain decay chains [228]. This method has been studied in detail for SPS1a [229, 230], at ATLAS [195] and at CMS [103, 231] as well as for baryon number violating scenarios [232].

6.1. The Basic Idea

We first discuss the general idea of the method. We assume the decay chain

$$D \to Cc \to Bbc \to Aabc, \tag{6.1}$$

illustrated in Fig. 6.1, where the particles D, C, B, and A are massive[1] and their masses satisfy

$$m_D > m_C > m_B > m_A. \tag{6.2}$$

The particles a, b and c are observed SM particles.

With particle A invisible, we can form four invariant mass combinations of the 4-momenta of the decay products c, b and a: m_{ba}, m_{ca}, m_{cb} and m_{cba}. The shapes and endpoints of these distributions are functions of the (unknown) particle masses in Eq. (6.2) and are derived under rather general assumptions in Ref. [233]. The maximal values of the two- and three-particle

---

[1] Particle A does not necessarily need to be massive.

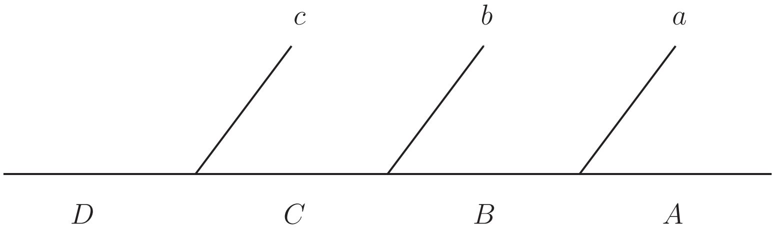

Figure 6.1.: Sequential decay chain used for the mass reconstruction.

invariant masses are given by

$$(m_{ba}^{\max})^2 = (m_C^2 - m_B^2)(m_B^2 - m_A^2)/m_B^2, \tag{6.3a}$$
$$(m_{ca}^{\max})^2 = (m_D^2 - m_C^2)(m_B^2 - m_A^2)/m_B^2, \tag{6.3b}$$
$$(m_{cb}^{\max})^2 = (m_D^2 - m_C^2)(m_C^2 - m_B^2)/m_C^2, \tag{6.3c}$$
$$(m_{cba}^{\max})^2 = \begin{cases} \max\Big[\frac{(m_D^2 - m_C^2)(m_C^2 - m_A^2)}{m_C^2}, \frac{(m_D^2 - m_B^2)(m_B^2 - m_A^2)}{m_B^2}, \frac{(m_D^2 m_B^2 - m_C^2 m_A^2)(m_C^2 - m_B^2)}{m_C^2 m_B^2}\Big], \\ \text{except for the special case in which } m_B^2 < m_A m_D < m_C^2 \text{ and } m_A m_C^2 < m_B^2 m_D, \\ \text{where we must use } (m_D - m_A)^2. \end{cases} \tag{6.3d}$$

In principle, these four equations are sufficient to determine the unknown masses m_D, m_C, m_B and m_A, once the endpoints are determined. In addition, the three-particle invariant mass, m_{cba}, has a non-zero threshold value given by

$$\begin{aligned}(m_{cba}^{\min})^2 = &\big[2m_B^2(m_D^2 - m_C^2)(m_C^2 - m_A^2) + (m_D^2 + m_C^2)(m_C^2 - m_B^2)(m_B^2 - m_A^2) \\ &- (m_D^2 - m_C^2)\sqrt{(m_C^2 + m_B^2)^2(m_B^2 + m_A^2)^2 - 16 m_C^2 m_B^4 m_A^2}\,\big]/(4m_B^2 m_C^2).\end{aligned} \tag{6.3e}$$

This can be used to over-constrain the problem for a more precise determination of the involved particle masses[2].

The most prominent application of this method is in P_6 conserving SUSY, where one investigates the decay cascade of a left-handed squark,

$$\tilde{q}_L \to q\tilde{\chi}_2^0 \to q\ell_n^\pm \tilde{\ell}_R^\mp \to q\ell_n^\pm \ell_f^\mp \tilde{\chi}_1^0. \tag{6.4}$$

Here, the lightest neutralino, $\tilde{\chi}_1^0$, is stable and escapes the detector unseen. It is a general feature of P_6 conserving SUSY, that the near lepton, ℓ_n, and far lepton, ℓ_f, are of the same flavor and thus indistinguishable on an event-by-event basis [228, 236]. Thus, the invariant mass distributions $m_{\ell_n q}$ and $m_{\ell_f q}$, cannot be formed unambiguously and one usually defines the slightly modified variables $m_{\ell q(low)}$ and $m_{\ell q(high)}$ [228, 233].

We now apply this method to our P_6 violating scenarios. We investigate the decay chain of a right-handed squark

$$\tilde{q}_R \to q\tilde{\chi}_1^0 \to q\ell^\pm \tilde{\ell}_R^\mp \to q\ell^\pm \ell'^\mp \nu, \tag{6.5}$$

where $\tilde{\ell}_R$ is the LSP. It decays into a lepton ℓ' and a neutrino, where the flavor depends on the dominant $\boldsymbol{\Lambda}$ coupling, *cf.* Tab. 5.1. In contrast to the P_6 conserving scenarios, we can actually distinguish the near and far lepton if we have a dominant $\not{\mathrm{P}}_6$ coupling $\boldsymbol{\Lambda} \in \{\lambda_{231}, \lambda_{132}\}$. The $\tilde{\ell}_R$ LSP then decays into a lepton of different flavor than its own flavor.

Another difference to the P_6 conserving scenarios is that the decay chain is initiated by a right-handed squark. In most $\tilde{\ell}_R$ LSP models, the (mostly right-handed) $\tilde{t}_1$ is much lighter than the first and second generation $\tilde{q}_R$ scenarios. Thus, we typically have two distinct squark mass scales. This enables the measurement of both the $\tilde{t}_1$ mass and the mass of the right-handed first and second generation squarks, $\tilde{q}_R$, simultaneously, if we succeed in separating the events from $\tilde{q}_R$ and $\tilde{t}_1$ pair production.

For the following study, we focus on the $\tilde{e}_R$ LSP benchmark model BE2. We concentrate

---

[2] Another variable which can be used is the Stransverse mass, m_{T2} [234, 235].

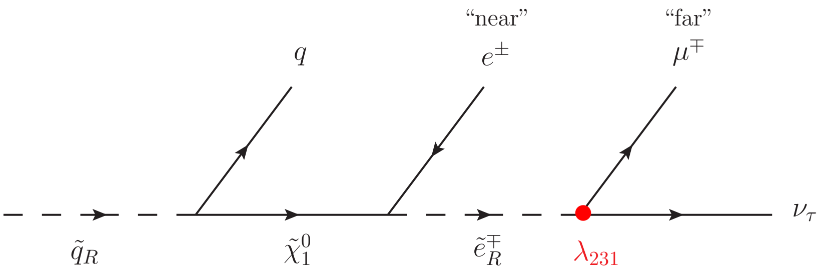

Figure 6.2.: Decay cascade of a right-handed squark, $\tilde{q}_R \to q\tilde{\chi}_1^0 \to qe^\pm\tilde{e}_R^\mp \to qe^\pm\mu^\mp\nu_\tau$, which is relevant for the mass reconstruction in $\tilde{e}_R$ LSP models with a non-zero λ_{231} coupling. The cascade leads to a jet, two distinguishable leptons and a neutrino. The P_6 violating decay of the $\tilde{e}_R$ LSP via the λ_{231} coupling is marked in red.

on the case, where the $\tilde{e}_R$ decays into a muon and a neutrino, because firstly, muons are much easier to reconstruct than τ leptons, and secondly, these events have a higher probability to pass the event selection which demands three leptons, *cf.* Sect. 5.3.4. The relevant decay cascade, Eq. (6.5), is shown in Fig. 6.2. This cascade yields a jet and two different flavor leptons of opposite charge, from which we can unambiguously form the invariant masses $m_{e\mu}$, $m_{e\mu q}$, m_{eq} and $m_{\mu q}$.

In the mass determination, one can leave the mass of the invisible particle, m_A, as a free parameter. However, once the P_6 violating decay chain, Eq. (6.5), is experimentally confirmed, the knowledge of $m_A = 0$ simplifies Eq. (6.3) and reduces the number of fit parameters by one. The endpoints of the invariant mass distributions are then given by

$$(m_{e\mu}^{\max})^2 = M_{\tilde{\chi}_1^0}^2 - M_{\tilde{e}_R}^2, \tag{6.6a}$$
$$(m_{\mu q}^{\max})^2 = M_{\tilde{q}_R}^2 - M_{\tilde{\chi}_1^0}^2, \tag{6.6b}$$
$$(m_{eq}^{\max})^2 = (M_{\tilde{q}_R}^2 - M_{\tilde{\chi}_1^0}^2)(M_{\tilde{\chi}_1^0}^2 - M_{\tilde{e}_R}^2)/M_{\tilde{\chi}_1^0}^2, \tag{6.6c}$$
$$(m_{e\mu q}^{\max})^2 = M_{\tilde{q}_R}^2 - M_{\tilde{e}_R}^2, \tag{6.6d}$$
$$(m_{e\mu q}^{\min})^2 = M_{\tilde{q}_R}^2(M_{\tilde{\chi}_1^0}^2 - M_{\tilde{e}_R}^2)/(2M_{\tilde{\chi}_1^0}^2). \tag{6.6e}$$

In BE2, $\tilde{t}_1$ pair production comprises approximately 30% of all sparton pair production, while right-handed first and second generation squarks are mainly produced in association with a gluino (16% of all sparton pair production) or in pairs (9% of all sparton pair production). Thus we have a similar number of events from $\tilde{t}_1$ pair production (denoted in the following as $\tilde{t}_1$ *events*) as from sparton pair production including a right-handed squark of the first or second generation (denoted as $\tilde{q}_R$ *events*). The approximate branching ratios of the subsequent cascade decays are

$$\tilde{q}_R \xrightarrow{100\%} q\tilde{\chi}_1^0 \xrightarrow{100\%} qe^\pm\tilde{e}_R^\mp \xrightarrow{50\%} qe^\pm\mu^\mp\nu_\tau, \tag{6.7}$$
$$\tilde{t}_1 \xrightarrow{71.9\%} t\tilde{\chi}_1^0 \xrightarrow{100\%} te^\pm\tilde{e}_R^\mp \xrightarrow{50\%} te^\pm\mu^\mp\nu_\tau, \tag{6.8}$$

respectively.

6.2. Event selection

In the following, we basically apply the same event selection as designed for a discovery at the LHC at $\sqrt{s} = 14$ TeV, *cf.* Sect. 5.3.4. Furthermore, for the construction of the invariant mass distributions, the event has to contain at least one electron and one muon with opposite charge. In order to enhance the probability of selecting the right muon, *i.e.* the μ from the $\tilde{e}_R$ decay, we require a minimal transverse momentum of the muon $p_T^\mu \geq 25$ GeV. At this stage we can construct the opposite-sign-different-flavor (OSDF) dilepton invariant mass distribution, $m_{e\mu}$. In order to reduce combinatorial background, we subtract the dilepton invariant mass distribution of same-sign-different-flavor (SSDF) leptons[3]. Note that this method also suppresses SUSY background processes, where the charges of the selected leptons are uncorrelated because of an intermediate Majorana particle (*i.e.* a neutralino), for instance SUSY decay chains involving the cascade $\tilde{\mu}_L^- \to \mu^- \tilde{\chi}_1^0 \to \mu^- e^\pm \tilde{e}_R^\mp$.

For the invariant mass distributions containing the jet, we design further selection cuts to discriminate between $\tilde{t}_1$ events and $\tilde{q}_R$ events. We expect at least two b jets in the $\tilde{t}_1$ events from the top quark decays. Thus, we introduce a simple b-tagging algorithm in our simulation, assuming a p_T independent b-tagging efficiency of 60%. See Ref. [195, pp. 397] and [237, pp. 461] for b-tagging studies of ATLAS and CMS, respectively. We demand 2 b-tagged jets for the $\tilde{t}_1$ event candidates while no b-tagged jet must be present for the $\tilde{q}_R$ event candidates. Moreover, we use the visible effective mass, $M_{\text{eff}}^{\text{vis}}$, as a handle to discriminate between $\tilde{t}_1$ and $\tilde{q}_R$ events, *i.e.* we impose the cuts

$$\begin{aligned} &400\text{ GeV} \leq M_{\text{eff}}^{\text{vis}} \leq 900\text{ GeV}, &&\text{for } \tilde{t}_1 \text{ events,} \\ &900\text{ GeV} \leq M_{\text{eff}}^{\text{vis}}, &&\text{for } \tilde{q}_R \text{ events,} \end{aligned} \tag{6.9}$$

respectively. For the construction of invariant mass distributions involving the quark from the squark decay, we consider the hardest and second hardest jet, j_1 and j_2, respectively. Due to the lighter $\tilde{t}_1$ mass, the jets are expected to be somewhat softer in $\tilde{t}_1$ events than in $\tilde{q}_R$ events. For BE2, we choose the following p_T selection criteria for the first and second hardest jet:

$$\begin{aligned} &\left.\begin{aligned} 50\text{ GeV} &\leq p_T^{j_1} \leq 250\text{ GeV} \\ 25\text{ GeV} &\leq p_T^{j_2} \end{aligned}\right\} &&\text{for } \tilde{t}_1 \text{ events,} \\ &\left.\begin{aligned} 250\text{ GeV} &\leq p_T^{j_1} \\ 100\text{ GeV} &\leq p_T^{j_2} \end{aligned}\right\} &&\text{for } \tilde{q}_R \text{ events.} \end{aligned} \tag{6.10}$$

Note that since we can not unambiguously determine the true jet of the cascade, we have combinatorial background from combinations with the wrong jet. After this event selection, the invariant mass distributions $m_{e\mu q}$, m_{eq}, and $m_{\mu q}$ are constructed as follows:

- $m_{e\mu q}$: We take the invariant masses of the selected two leptons together with the hardest and second hardest jet. The smaller (larger) value is taken for the edge (threshold) distribution. For the threshold distribution, we demand the dilepton invariant mass of the selected leptons to lie within $m_{e\mu}^{\max}/\sqrt{2} \leq m_{e\mu} \leq m_{e\mu}^{\max}$, corresponding to the subset

---

[3] In R-parity conserving scenarios, a technique called *flavor subtraction* is employed to reduce combinatorial background. There, the opposite-sign-different-flavor (OSDF) lepton invariant mass distribution is subtracted from the opposite-sign-same-flavor (OSSF) lepton distribution. This elegantly cancels the background, that arises from the combination of leptons coming from different decay chains. Our technique is based on the same idea. We refer to it as *charge subtraction.*

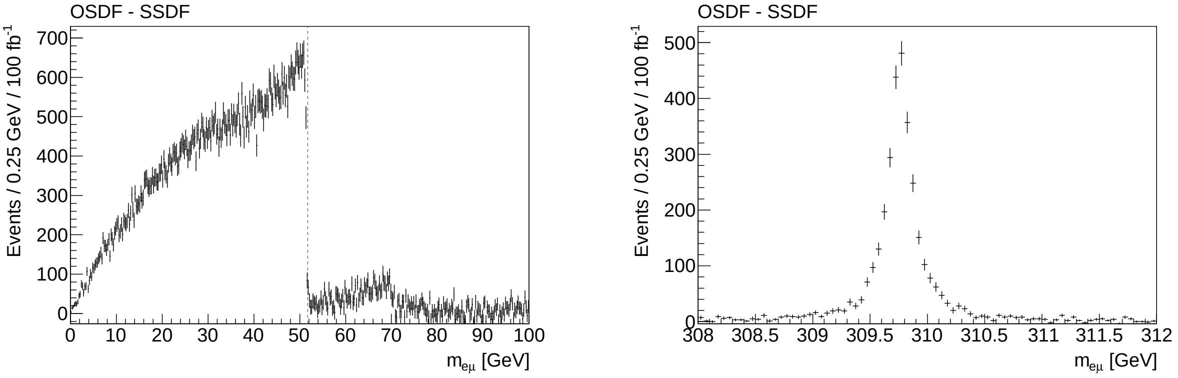

(a) Dilepton edge. The dashed line gives the expected value of 51.7 GeV, assuming the cascade decay in Eq. (6.5).

(b) Mass peak of the tau sneutrino, $\tilde{\nu}_\tau$, due to the P_6 violating decay $\tilde{\nu}_\tau \to e\mu$. The true mass value is $M_{\tilde{\nu}_\tau} = 309.76$ GeV.

Figure 6.3.: Dilepton invariant mass distribution. The dilepton edge, $m_{e\mu}^{\max}$, is shown in Fig. 6.3(a) and the mass peak of the tau sneutrino, $\tilde{\nu}_\tau$, is given in Fig. 6.3(b).

of events in which the angle between the two leptons (in the center of mass frame of the slepton) is greater than $\pi/2$ [228]. In the edge distribution, we require $m_{e\mu} \leq m_{e\mu}^{\max}$ and employ charge subtraction to reduce the combinatorial background.

- m_{eq} ($m_{\mu q}$): We construct[4] the invariant mass of a selected electron (muon) with the hardest and second hardest jet and take the lower value. Furthermore we require, that the selected electron (muon) forms a dilepton invariant mass $m_{e\mu} \leq m_{e\mu}^{\max}$ with a selected muon (electron).

For this construction, the dilepton invariant mass edge, $m_{e\mu}^{\max}$, must have already been fitted. In this study, we use the true value of the dilepton edge.

6.3. Results

We simulated BE2 signal events corresponding to an integrated luminosity of 100 fb^{-1} of LHC data at $\sqrt{s} = 14$ TeV. We assume, that the SM background can be reduced to a negligible amount with the given event selection and present only the invariant mass distributions for the signal sample. In the following figures, the gray dashed line indicates the nominal endpoint value given by Eq. (6.6), using the sparticle mass spectrum of BE2, *cf.* Tab. A.4.

We discuss the main contributions from various SUSY decay cascades to the invariant mass distributions. We give a rough estimate of how accurately the endpoints may be determined by a fit and investigate whether the result can be biased due to SUSY background processes or systematical effects of the event selection. The discussion presented here should be understood as a proof-of-principle of the feasibility of the method. A detailed reconstruction of the sparticle masses from the endpoints of the fitted invariant mass distributions will be investigated in the future.

---

[4] In this construction, we make use of the fact that we can distinguish the near and far lepton. However, we checked that the model-independent construction of the variables $m_{\ell q(near/far)}$ as proposed in Ref. [228] leads to similar results.

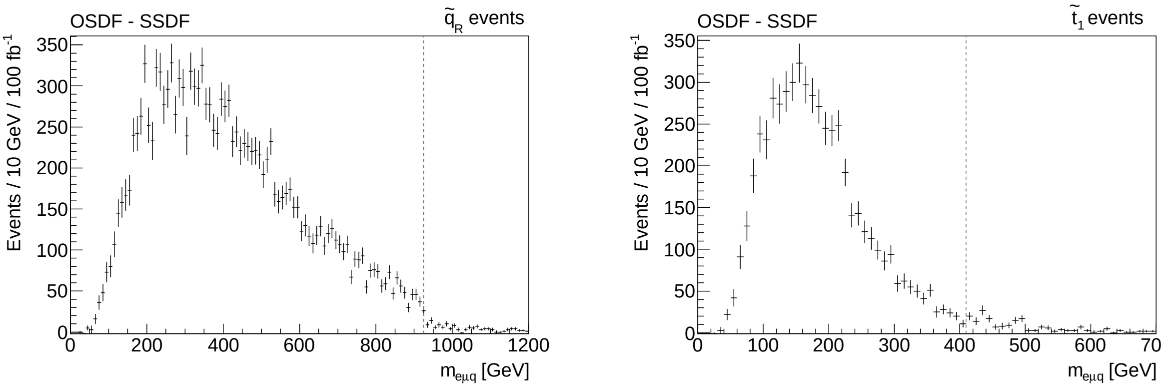

(a) $m_{e\mu q}$ distribution for the $\tilde{q}_R$ event selection. The dashed line gives the expected value of 925 GeV.

(b) $m_{e\mu q}$ distribution for the $\tilde{t}_1$ event selection. The dashed line gives the expected value of 410 GeV.

Figure 6.4.: Dilepton-jet invariant mass edge distribution for the $\tilde{q}_R$ event [Fig. 6.4(a)] and $\tilde{t}_1$ event [Fig. 6.4(b)] selection. The distributions are charge subtracted.

6.3.1. Dilepton invariant mass

In Fig. 6.3 we present the charge subtracted dilepton invariant mass distribution. We expect for the cascade decay in Eq. (6.5) a dilepton edge at 51.7 GeV, which we can clearly identify in Fig. 6.3(a). The observed edge matches quite accurately the nominal value and should be observable already with a few fb^{-1}.

For an invariant mass below the dilepton edge, the distribution shape slightly deviates from the (expected) triangular shape. This is because the LSP can decay into a neutrino and a τ lepton, which then decays into a muon and neutrinos. In this case, the muon only carries a fraction of the τ lepton p_T. We thus obtain a lower $m_{e\mu}$ value as in the case of the direct LSP decay $\tilde{e}_R \to \mu\nu_\tau$.

Beyond the endpoint at 51.7 GeV, we observe another small edge at about 70 GeV. These events come from the decay of the left-handed smuon, $\tilde{\mu}_L^\pm \to \mu^\pm\tilde{\chi}_1^0 \to \mu^\pm e^\mp \tilde{e}_R$. The true endpoint value for this cascade is 70.7 GeV.

Furthermore, we observe a sharp peak at 309.8 GeV in the di-lepton invariant mass distribution, shown in Fig. 6.3(b). Here, the mass of the tau sneutrino, $\tilde{\nu}_\tau$, is fully reconstructed due to the P_6 violating decay $\tilde{\nu}_\tau \to e^\mp\mu^\pm$. In addition, a similar peak can be seen in the $e\tau$ invariant mass at the muon sneutrino mass of 312.0 GeV, due to the P_6 violating decay $\tilde{\nu}_\mu \to e^\mp\tau^\pm$. This however requires the reconstruction of the τ lepton momentum. These sneutrino mass peaks should be observable with a few fb^{-1} of data and are thus a smoking gun for $\not{P}_6$ scenarios with a non-zero $L_iL_j\bar{E}_k$ coupling.

6.3.2. Dilepton-jet invariant mass

Now we turn to the invariant mass distributions formed by two leptons and a jet. In all invariant masses containing a jet, the endpoints (and thresholds) are “smeared”, since the contributing squarks in general have slightly different masses (except in the case of the $\tilde{t}_1$). In addition, the jet can lose some of its momentum due to final state radiation (FSR) of gluons, if the radiated gluons are not covered by the jet algorithm. This will slightly shift the distribution towards lower values of the invariant mass [233]. A detector simulation, which we do not include here,

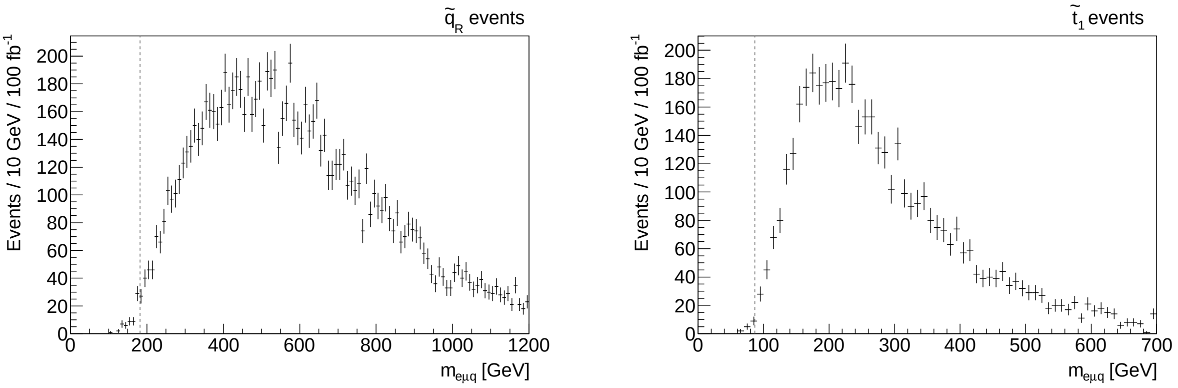

(a) $m_{e\mu q}$ threshold distribution for the $\tilde{q}_R$ event selection. The dashed line gives the expected value of 181 GeV.

(b) $m_{e\mu q}$ threshold distribution for the $\tilde{t}_1$ event selection. The dashed line gives the expected value of 86 GeV.

Figure 6.5.: Dilepton-jet invariant mass threshold distribution for the $\tilde{q}_R$ event [Fig. 6.5(a)] and $\tilde{t}_1$ event [Fig. 6.5(b)] selection.

would lead to additional smearing due to the energy (mis-)measurement. Thus, at the LHC, a precise determination of the endpoints in most cases will not be an easy task and will require a high luminosity and a good understanding of the detector effects.

In Fig. 6.4 we show the $m_{e\mu q}$ edge distribution for the $\tilde{q}_R$ event [Fig. 6.4(a)] and $\tilde{t}_1$ event [Fig. 6.4(b)] selection. In the $\tilde{q}_R$ event selection, the nominal value of 925 GeV, assuming the cascade decay in Eq. (6.7), can be identified fairly well. In contrast, in the $\tilde{t}_1$ event selection the identification of the endpoint at the nominal value of 410 GeV, assuming the $\tilde{t}_1$ decay chain in Eq. (6.8), is more difficult. The reasons are the following: Firstly, events with cascade decays of heavier squarks can leak into the $\tilde{t}_1$ event selection, in particular those with an initial bottom squark or a foregoing gluino, which decays into the $\tilde{t}_1$ and a t quark. If the selected jet stems from these heavy sparticle decays we can obtain $m_{e\mu q}$ values beyond 410 GeV. Secondly, the distribution flattens out as it approaches the nominal endpoint, because the jet p_T only carries a fraction of the t quark p_T. Moreover, the cut imposed on the jet transverse momentum, $p_T < 250$ GeV, tends to reject events at high $m_{e\mu q}$ values. Thus, the distribution does not linearly approach the endpoint.

Furthermore, the distribution in Fig. 6.4(b) contains events with the $\tilde{t}_1$ cascade decay

$$\tilde{t}_1 \overset{28.1\%}{\longrightarrow} b\tilde{\chi}_1^{\pm} \overset{19.9\%}{\longrightarrow} b\mu^{\pm}\tilde{\nu}_\mu \overset{14.2\%}{\longrightarrow} b\mu^{\pm}e^{\mp}\tau^{\pm}. \tag{6.11}$$

This cascade yields an $m_{e\mu q}$ endpoint at 322 GeV, which leads to the small abrupt change of the distribution slope observed in this region. One might suspect an edge around 220 GeV in Fig. 6.4(b), however, there is no SUSY cascade which yields an endpoint in this region. In fact, this strong decrease of the distribution is triggered by the jet-p_T requirements for the $\tilde{t}_1$ event selection, Eq. (6.10). By increasing the minimal and maximal jet-p_T limits, the “edge” at ≈ 220 GeV disappears and the distribution approaches the endpoint almost linearly. However, this also leads to more SUSY background events beyond the nominal endpoint.

In Fig. 6.5 we present the $m_{e\mu q}$ threshold distribution for the $\tilde{q}_R$ [Fig. 6.5(a)] and $\tilde{t}_1$ event [Fig. 6.5(b)] selection. In the $\tilde{q}_R$ event selection, we observe an edge slightly below the nominal threshold value of 181 GeV, assuming the $\tilde{q}_R$ cascade decay, Eq. (6.7). This shift towards lower

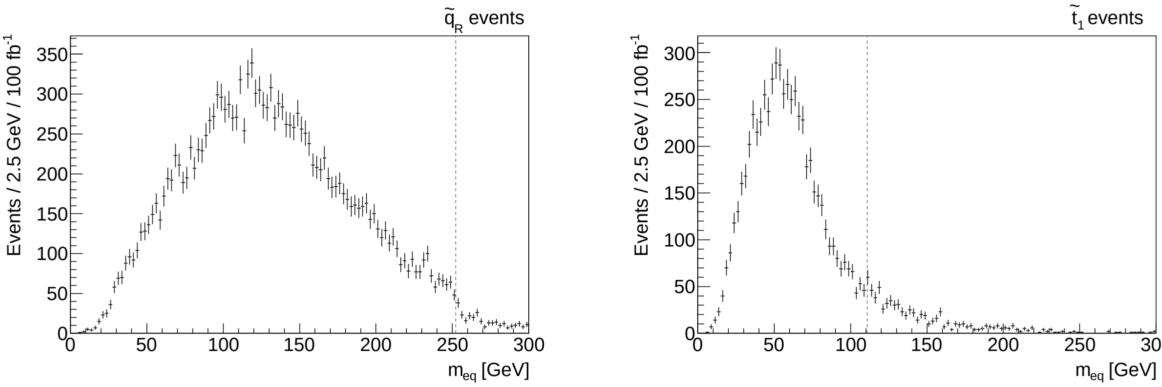

(a) m_{eq} distribution for the $\tilde{q}_R$ event selection. The dashed line gives the expected value of 251 GeV.

(b) m_{eq} distribution for the $\tilde{t}_1$ event selection. The dashed line gives the expected value, 111 GeV.

Figure 6.6.: Electron-jet invariant mass distribution for the $\tilde{q}_R$ event [Fig. 6.6(a)] and $\tilde{t}_1$ event [Fig. 6.6(b)] selection.

values of $m_{e\mu q}$ is due to gluon final state radiation (FSR) from the jet.

In general, the $m_{e\mu q}$ threshold value is set by the lightest squark. Thus, all events with values far below the endpoint at 181 GeV must contain third generation squarks. These events can leak into the $\tilde{q}_R$ event selection when the b quarks are not tagged. Events from $\tilde{t}_1$ pair production are efficiently rejected by the jet-p_T and $M_{\text{eff}}^{\text{vis}}$ requirement of the $\tilde{q}_R$ event selection. However, the $\tilde{t}_1$ decay chain in Eq. (6.8) can also be initiated by heavier squarks and gluinos, which decay into the $\tilde{t}_1$, leading to a hard jet and generally a high value of $M_{\text{eff}}^{\text{vis}}$.

The observed $m_{e\mu q}$ threshold in the $\tilde{t}_1$ event selection matches quite accurately the nominal value of 86 GeV, assuming the $\tilde{t}_1$ cascade decay in Eq. (6.8). The other cascade, Eq. (6.11), yields a $m_{e\mu q}$ threshold at 158 GeV which cannot be reliably identified since the slope of the distribution is very steep in this region.

6.3.3. Lepton-jet invariant masses

We now discuss the invariant mass distributions formed by one lepton and a jet. As described in Sect. 6.2, we consider only those electrons (muons), which form an dilepton invariant mass $m_{e\mu} < m_{e\mu}^{\text{max}} = 51.7$ GeV with the other selected muon (electron). For the lepton-jet invariant masses, we generally have more sources of SUSY background than in the dilepton and dilepton-jet invariant mass distributions, because we cannot employ the method of charge subtraction.

The electron-jet invariant mass distribution is presented in Fig. 6.6. In the $\tilde{q}_R$ event selection [Fig. 6.6(a)], we observe an edge near the nominal endpoint of 251 GeV. In contrast, the endpoint cannot be easily identified in the $\tilde{t}_1$ event selection [Fig. 6.6(b)]. As for the $m_{e\mu q}$ invariant mass, *cf.* Fig. 6.4(b), the distribution fades away as it approaches the nominal endpoint at 111 GeV, since the jet carries only a fraction of the t quark momentum. In addition, the $\tilde{t}_1$ decay cascade in Eq. (6.11) yields an endpoint at 266 GeV of the electron-jet invariant mass, leading to events beyond the nominal endpoint of the assumed $\tilde{t}_1$ cascade, Eq. (6.8). As a result, the distribution is almost smooth around 111 GeV, and thus, the determination of this endpoint will be a difficult task.

In Fig. 6.7 we show the far lepton-jet invariant mass distribution for the $\tilde{q}_R$ event [Fig. 6.7(a)] and $\tilde{t}_1$ event [Fig. 6.7(b)] selection.

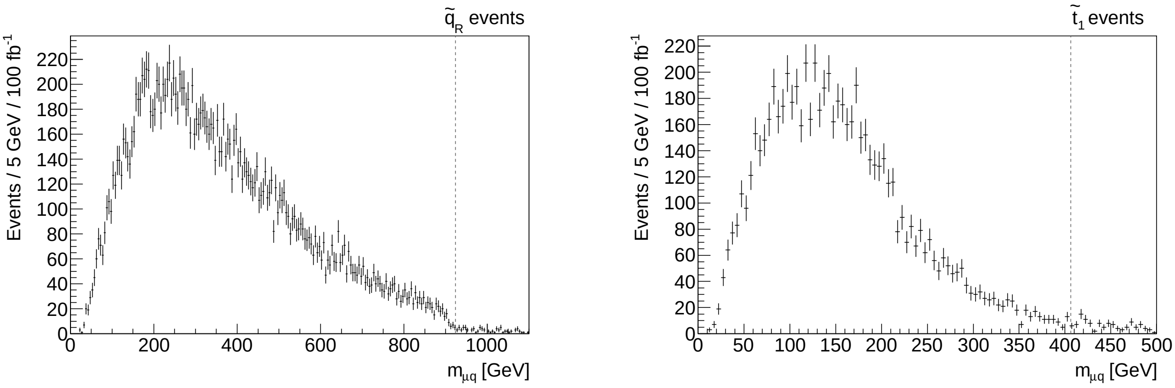

(a) $m_{\mu q}$ distribution for the $\tilde{q}_R$ event selection. The dashed line gives the expected value of 921 GeV.

(b) $m_{\mu q}$ distribution for the $\tilde{t}_1$ event selection. The dashed line gives the expected value, 406 GeV.

Figure 6.7.: Muon-jet invariant mass distribution for the $\tilde{q}_R$ event [Fig. 6.7(a)] and $\tilde{t}_1$ event [Fig. 6.7(b)] selection.

Assuming the $\tilde{q}_R$ decay cascade in Eq. (6.7), the $m_{\mu q}$ distribution has a nominal endpoint at 921 GeV. We can clearly observe an endpoint in Fig. 6.7(a), however, it might be underestimated by ≈ 20 GeV, due to the FSR of gluons from the jet.

In the $\tilde{t}_1$ event selection, the endpoint is again more difficult to observe. For values $m_{\mu q} \geq 300$ GeV, the distribution approaches the endpoint with a very flat linear slope. Thus, the determination of the endpoint requires high statistics. Moreover, we have background events beyond the endpoint from heavier squark cascade decays or combinations with a jet from a decaying gluino.

6.4. Prospects and future plans

In this chapter we presented a possible ansatz to determine the masses of the sparticles $\tilde{q}_R$, $\tilde{t}_1$, $\tilde{\nu}_\tau$, $\tilde{\chi}_1^0$ and $\tilde{e}_R$ for $\not{P}_6$ models with a $\tilde{e}_R$ LSP, using the endpoints of invariant mass distributions. In order to determine the $\tilde{q}_R$ mass (scale) and the $\tilde{t}_1$ mass simultaneously, we designed an event selection to discriminate between the two types of events. We studied this method for the benchmark scenario BE2. In general, the proposed cuts should be optimized to the model under investigation. For this specific example, the event discrimination seems to work fairly well.

In the $\tilde{q}_R$ event selection, we should be able to determine all endpoints quite accurately, however, a slight bias towards lower values is expected due to the final state radiation of gluons from the selected jet. The endpoint determination in the $\tilde{t}_1$ event selection is more problematic, for the following reasons: Both the requirement on the maximal jet-$p_T \leq 250$ GeV and the fact, that the jet carries only a fraction of the t quark p_T, flattens out the squark-related invariant mass distributions while approaching the endpoint. Furthermore, combinations of the leptons with a jet stemming from a decaying gluino can lead to values beyond the endpoint.

The observability of the endpoints in the $\tilde{t}_1$ related invariant masses may be improved by employing the reconstruction of the t quark momentum. Also, the choice of the jet-p_T and $M_{\rm eff}^{\rm vis}$ requirements may be optimized for a specific endpoint fit. For the future, we plan to fit the invariant mass distributions and determine the masses of the involved sparticles via a χ^2 minimization.

7. Summary and Conclusions

If the discrete symmetry P_6 (or R-parity) is violated, the lightest supersymmetric particle (LSP) is unstable. Then, cosmological constraints on the LSP do not apply and thus in principle any supersymmetric particle can be the LSP. In this thesis we presented the hadron collider phenomenology of supersymmetric models with a right-handed first or second generation charged slepton as the LSP. Hereby we restricted ourselves to the framework of minimal supergravity (mSUGRA) with conserved baryon triality (B_3). In this model, one non-vanishing lepton number violating (LNV) operator is present at the grand unification scale, M_{GUT}, in addition to the P_6 conserving mSUGRA parameters.

Due to these LNV interactions, the renormalization group equations (RGEs) of the sparticle masses receive new contributions, compared to the P_6 conserving case. We showed, that the mass of the right-handed slepton (of generation $k = 1, 2$), $\tilde{\ell}_R^k$, can be significantly reduced by the LNV interaction $\lambda_{ijk} L_i L_j \bar{E}_k$. For certain regions of the supersymmetric parameter space we obtain a $\tilde{\ell}_R^k$ LSP with a coupling $\lambda_{ijk} \gtrsim \mathcal{O}(10^{-2})$ at M_{GUT}. These parameter regions usually feature low values of $\tan\beta$ and M_0, a large value of $M_{1/2}$ and a large magnitude of a negative A_0. The latter enhances the impact of the LNV coupling, λ_{ijk}, in the renormalization group evolution of the $\tilde{\ell}_R^k$ mass.

Given a supersymmetric model with a selectron or smuon LSP, we classified its main hadron collider signatures, assuming the pair production of strongly interacting SUSY particles, see Tab. 5.1. In general, these models lead to striking multi-leptonic final state signatures and are thus interesting for early LHC studies.

Furthermore, we showed that selectron and smuon LSP models with $M_{1/2} \lesssim (400-410)$ GeV are already excluded at 90% C.L. by the trilepton search performed by the DØ experiment at the Tevatron. Therefore, the supersymmetric parameter regions, which might explain the discrepancy between the observed anomalous magnetic moment of the muon and its SM prediction, are ruled out. We further argued that this exclusion reach might be improved up to $M_{1/2} \lesssim 450$ GeV once the DØ search is applied to 10 fb^{-1} of data, which will be collected by the end of 2010.

In order to study the discovery potential at the LHC with early data, we performed a detailed Monte Carlo (MC) study for the SUSY signal and the main SM backgrounds. We selected three benchmark scenarios with a selectron LSP, representing different regions of the parameter space, and investigated their kinematic properties. Based on this, we designed an inclusive trilepton analysis to improve the signal to background ratio. We showed, that the SM background can be reduced to only a few events while our benchmark scenarios can clearly be discovered with $\mathcal{O}(50)$ selected events, using 1 fb^{-1} of LHC data at a center-of-mass energy of $\sqrt{s} = 7$ TeV.

We further showed that the proposed search works also quite well beyond our benchmark scenarios. For a wide region in the $M_{1/2} - M_0$ parameter space we achieve signal efficiencies in the range of $20\% - 50\%$ at $\sqrt{s} = 7$ TeV. The signal efficiency at $\sqrt{s} = 14$ TeV is even better, namely $40\% - 60\%$ for most of the parameter space. In the narrow region of low mass difference between the lightest neutralino and the selectron LSP the signal efficiency and thus the discovery potential decreases. This is due to the fact that the electrons from the neutralino decay into the LSP are very soft and thus tend to fail the minimum lepton p_T criteria. We presented the discovery reach for various integrated luminosities in the $M_{1/2} - M_0$ parameter plane for both 7 TeV and 14 TeV center-of-mass energies. With 1 fb^{-1} of data at a center-of-mass energy of 7 TeV (14 TeV) scenarios with squark masses of 1.2 TeV (1.9 TeV) and LSP masses of 230 GeV (370 GeV) can be discovered.

Besides the proposed inclusive trilepton seach, these models may also be discovered by narrow resonances in dilepton invariant mass distributions, since the sneutrinos may decay into two leptons via the present LNV interaction. We therefore advise the experiments to investigate dilepton invariant masses, where the leptons have different flavor.

In the case of a SUSY discovery, the masses of the supersymmetric particles have to be determined. We demonstrated that a widely used method, using the kinematic endpoints of invariant mass distributions, can also be applied in a slightly modified way in P_6 violating mSUGRA scenarios with a selectron or smuon LSP. Here, we investigate the decay chain of the right-handed squark and lightest top squark,

$$\tilde{q}_R/\tilde{t}_1 \to q\tilde{\chi}_1^0 \to q\ell^\pm\tilde{\ell}_R^\mp \to q\ell^\pm\ell'^\mp\nu.$$

In contrast to P_6 conserving scenarios, the number of unknown masses is reduced by one, due to the massless neutrino at the end of the decay cascade. Moreover, in scenarios with a dominant λ_{231} or λ_{132} coupling, we can distinguish between the near and far lepton on an event-by-event basis, since the leptons ℓ and ℓ' have different flavor. This is impossible in P_6 conserving scenarios.

Typically, we have a large mass splitting between the right-handed first and second generation squarks, $\tilde{q}_R$, and the lightest top squark, $\tilde{t}_1$. Therefore, we designed an event selection using the visible effective mass and the b jet multiplicity to discriminate between the decay cascades initiated by either the $\tilde{q}_R$ or the $\tilde{t}_1$. In this way, we may determine the mass (scale) of both squark types.

Using a large LHC dataset of 100 fb^{-1} at $\sqrt{s} = 14$ TeV, we presented several invariant mass distributions, which can be used for the mass reconstruction, exemplarily for one benchmark point and for both the $\tilde{q}_R$ and the $\tilde{t}_1$ event selection. In the $\tilde{q}_R$ event selection, the endpoints can be clearly identified, while the endpoint determination in the $\tilde{t}_1$ event selection is more problematic. The endpoint of the dilepton invariant mass is very clear and should already be observable with a few fb^{-1} of data.

The results presented here for the mass reconstruction method are to be understood as a proof-of-principle. In a future publication, we plan to fit the kinematic endpoints of the distributions in order to determine the $\tilde{q}_R$, $\tilde{t}_1$, $\tilde{\chi}_1^0$ and $\tilde{e}_R$ masses via a χ^2 minimization procedure. Then, we may quantitatively study how accurately these masses can be determined and whether the event selection between $\tilde{q}_R$ and $\tilde{t}_1$ events introduces a bias in the reconstructed sparticle mass. We will further investigate the impact of detector effects using a detector simulation.

We eagerly await the first results for new physics from the LHC experiments. These will shed new light on the possible new physics landscape at the TeV scale. As demonstrated, the supersymmetric models presented here are sensitive to early LHC data and might be discovered soon.

A. Properties of the benchmark models

In this appendix we discuss the mass spectrum of the supersymmetric particles and their decay properties for the selected Tevatron benchmark points SUSY1 and SUSY2 as well as the LHC benchmark points BE1, BE2 and BE3 in more detail. Sparticle masses, that are reduced by more than 5 GeV due to the impact of the λ_{231} coupling on the RGE running, and P_6 violating decays via the λ_{231} coupling are marked in bold-face in the following tables.

We remark, that only the masses of those sparticles, which couple directly via the $L_i L_j \bar{E}_k$ operator, are significantly reduced compared to the P_6 conserving case, *cf.* Sect. 4.1. Thus, since all benchmark models exhibit a dominant λ_{231} coupling, only the $\tilde{e}_R$, $\tilde{\mu}_L$, $\tilde{\nu}_\mu$, $\tilde{\tau}_2$ and $\tilde{\nu}_\tau$ are affected. These sparticles then also exhibit P_6 violating decays to SM particles via the λ_{231} coupling. Furthermore, the $\tilde{\tau}_1$ can also decay via the λ_{231} coupling due to its (small) left-handed component. This happens in particular in scenarios, where the $\tilde{\tau}_1$ is the NLSP and its mass is close to the LSP mass. Due to the λ_{231} coupling, the $\tilde{e}_R$ LSP decays undergo the 2-body decays $\tilde{e}_R \to \mu\nu_\tau$ and $\tilde{e}_R \to \tau\nu_\mu$.

Common to all benchmark points is a rather light $\tilde{t}_1$, compared to the other squarks. Due to the top Yukawa coupling, the RGE running of the stop mass receives large negative contributions for a large negative A_0, going from M_{GUT} to M_Z [158]. In all benchmark scenarios except SUSY2, the $\tilde{t}_1$ mostly decays into the $\tilde{\chi}_1^0$ and a t quark, while the decay $\tilde{t}_1 \to \tilde{\chi}_1^+ b$ is subdominant.

The $\tilde{e}_R$, $\tilde{\mu}_R$, $\tilde{\tau}_1$ and $\tilde{\chi}_1^0$ always form the lightest four sparticles in B_3 mSUGRA models with a $\tilde{e}_R$ or $\tilde{\mu}_R$ LSP. The next lightest sparticles are the sneutrinos with masses more than 100 GeV heavier as the right-handed sleptons. Those sneutrinos, which couple to the $L_i L_j \bar{E}_k$ operator, decay to roughly $10\% - 15\%$ into two SM leptons. Due to the $\tilde{\nu}$ mass, these leptons have a high p_T and in general allow for a mass reconstruction of the sneutrino, *cf.* Sect. 6.

The sneutrinos are followed by the (mostly) left-handed sleptons $\tilde{e}_L$, $\tilde{\mu}_L$ and $\tilde{\tau}_2$ in the mass hierarchy. Their masses are only slightly larger than those of the sneutrinos because they belong to the same $SU(2)$ doublet. We have P_6 violating decays into a lepton and a neutrino of those sleptons, which couple directly to the $L_i L_j \bar{E}_k$ operator. However, due to the neutrino, a mass reconstruction of the left-handed sleptons using these decays is difficult.

The remaining sparticle mass spectrum is nearly identical to that, which we would obtain in the P_6 conserving mSUGRA.

A.1. Benchmark scenarios for the Tevatron

The benchmark scenarios selected for the Tevatron possess a very light sparticle mass spectrum. The SUSY contribution to the anomalous magnetic moment of the muon, $\delta a_\mu^{\mathrm{SUSY}}$, agrees within 2σ with the discrepancy between the SM prediction and the observation, *cf.* Eq. 4.4. In both benchmark scenarios SUSY1 and SUSY2 the $\tilde{\tau}_1$ NLSP is nearly mass degenerate with the $\tilde{e}_R$ LSP and undergoes exclusively the $\not{\mathrm{P}}_6$ decay $\tilde{\tau}_1 \to e\tilde{\nu}_\mu$. The electrons from this decay usually have a high momentum.

In Tab. A.1 we give the sparticle mass spectrum and decay modes for SUSY1 ($M_0 = 0$ GeV, $M_{1/2} = 400$ GeV, $A_0 = -1250$ GeV, $\tan\beta = 5$, $\mathrm{sgn}(\mu) = +$, $\lambda_{231}|_{\mathrm{GUT}} = 0.045$). The $\tilde{e}_R$ LSP mass is about 139 GeV. Due to the low M_0 value, the mass difference between the $\tilde{\chi}_1^0$ NNNLSP and the $\tilde{e}_R$ LSP is about 24 GeV and thus fairly large. The right-handed smuon, $\tilde{\mu}_R$, is the NNLSP and undergoes three-body decays into the $\tilde{e}_R$ LSP and $\tilde{\tau}_1$ NLSP. These decays are discussed in detail in Appendix C and usually yield a low-p_T muon. The lightest stop, $\tilde{t}_1$, has a mass of 366 GeV and decays preferably into the $\tilde{\chi}_1^0$ and a t quark. The first generation squarks have masses around 820 − 860 GeV and the gluino mass is 934 GeV.

The sparticle mass spectrum and branching ratios of SUSY2 ($M_0 = 80$ GeV, $M_{1/2} = 375$ GeV, $A_0 = -1250$ GeV, $\tan\beta = 5$, $\text{sgn}(\mu) = +$, $\lambda_{231}|_{\text{GUT}} = 0.045$) are given in Tab. A.2. This scenario lies near the $\tilde{\chi}_1^0$ LSP region and thus, all three sparticle masses of the $\tilde{e}_R$ LSP, $\tilde{\tau}_1$ NLSP and $\tilde{\chi}_1^0$ NNLSP lie close together at around 152 GeV. We have a fairly light $\tilde{t}_1$ with a mass of 305 GeV. The $\tilde{t}_1$ decay into the $\tilde{\chi}_1^0$ and a t quark is kinematically forbidden and $\tilde{t}_1 \to \tilde{\chi}_1^{\pm} b$ is the only decay mode. The squarks of the first and second generation have masses around 780 − 820 GeV and the mass of the gluino is 881 GeV.

A.2. Benchmark scenarios for the LHC

The sparticle mass spectrum and the branching ratios for BE1 ($M_0 = 0$ GeV, $M_{1/2} = 475$ GeV, $A_0 = -1250$ GeV, $\tan\beta = 5$, $\text{sgn}(\mu) = +$, $\lambda_{231}|_{\text{GUT}} = 0.045$) are given in Tab. A.3. It has similar properties as the Tevatron benchmark point SUSY1 but a heavier mass spectrum, *e.g.* the $\tilde{e}_R$ mass is about 169 GeV and thus roughly 40 GeV heavier than in SUSY1. The $\tilde{\tau}_1$ is the NLSP and nearly mass degenerate with the $\tilde{e}_R$ LSP. It undergoes the P_6 violating decay $\tilde{\tau}_1 \to e\nu_\mu$, yielding high-$p_T$ electrons. The $\tilde{\mu}_R$ is the NNLSP and decays into the $\tilde{e}_R$ or the $\tilde{\tau}_1$ via three body decays. The $\tilde{\chi}_1^0$ is the NNNLSP. Besides the decay into the $\tilde{e}_R$ LSP and an electron (47.6%), it also decays to a sizable fraction (42.0%) into the $\tilde{\tau}_1$ NLSP and a τ lepton.

In Tab. A.4 we give the sparticle masses and decay properties for BE2 ($M_0 = 90$ GeV, $M_{1/2} = 460$ GeV, $A_0 = -1400$ GeV, $\tan\beta = 4$, $\text{sgn}(\mu) = +$, $\lambda_{231}|_{\text{GUT}} = 0.045$). Due to the lower value of $\tan\beta$, the mass difference between the $\tilde{\tau}_1$ NLSP and the $\tilde{e}_R$ LSP is slightly larger than in BE1, *i.e.* about 6.3 GeV. Furthermore, the $\tilde{\tau}_1$ NLSP is nearly mass degenerate with the $\tilde{\chi}_1^0$ NNLSP. Thus, it decays exclusively via 3-body decays into the $\tilde{e}_R$ LSP, yielding a low-p_T τ lepton and an electron. The $\tilde{\chi}_1^0$ NNLSP decays always into the $\tilde{e}_R$ LSP and an electron.

In Tab. A.5 we present the sparticle masses and branching ratios for BE3 ($M_0 = 90$ GeV, $M_{1/2} = 450$ GeV, $A_0 = -1250$ GeV, $\tan\beta = 4$, $\text{sgn}(\mu) = +$, $\lambda_{231}|_{\text{GUT}} = 0.045$). Here, the $\tilde{\chi}_1^0$ is the NLSP and the mass difference to the $\tilde{e}_R$ LSP is about 3 GeV. Therefore, the electrons from the $\tilde{\chi}_1^0$ decay are very soft. We have a $\tilde{\tau}_1$ NNLSP, which decays into the $\tilde{\chi}_1^0$ and a τ (64.5%) as well as via 2-body P_6 violating decays (35.5%). In both BE2 and BE3, the $\tilde{\mu}_R$ is the NNNLSP and decays exclusively into the $\tilde{\chi}_1^0$ and a muon.

In all LHC benchmark points, the $\tilde{t}_1$ mass is around 450 GeV − 550 GeV and the other squark masses are in the range of 800 GeV − 1 TeV. The heaviest sparticle is the gluino with a mass $\gtrsim 1$ TeV.

	mass [GeV]	channel	BR	channel	BR
$\tilde{e}_R^-$	**139.1**	$\mu^-\nu_\tau$	**50%**	$\tau^-\nu_\mu$	**50%**
$\tilde{\tau}_1^-$	139.6	$e^-\bar{\nu_\mu}$	**100%**		
$\tilde{\mu}_R^-$	156.2	$\tilde{e}_R^+e^-\mu^-$	30.2%	$\tilde{e}_R^-e^+\mu^-$	25.1%
		$\tilde{\tau}_1^+\tau^-\mu^-$	24.4%	$\tilde{\tau}_1^-\tau^+\mu^-$	20.3%
$\tilde{\chi}_1^0$	163.3	$\tilde{e}_R^-e^+$	24.7%	$\tilde{e}_R^+e^-$	24.7%
		$\tilde{\tau}_1^-\tau^+$	22.9%	$\tilde{\tau}_1^+\tau^-$	22.9%
		$\tilde{\mu}_R^-\mu^+$	2.4%	$\tilde{\mu}_R^+\mu^-$	2.4%
$\tilde{\nu}_\tau$	**254.9**	$\tilde{\chi}_1^0\nu_\tau$	63.9%	$W^+\tilde{\tau}_1^-$	24.1%
		$e^-\mu^+$	**12.1%**		
$\tilde{\nu}_\mu$	**258.1**	$\tilde{\chi}_1^0\nu_\mu$	84.5%	$e^-\tau^+$	**15.5%**
$\tilde{\nu}_e$	262.9	$\tilde{\chi}_1^0\nu_e$	100%		
$\tilde{\mu}_L^-$	**269.3**	$\tilde{\chi}_1^0\mu^-$	84.2%	$e^-\bar{\nu_\tau}$	**15.8%**
$\tilde{\tau}_2^-$	**269.6**	$\tilde{\chi}_1^0\tau^-$	63.7%	$H^0\tilde{\tau}_1^-$	13.1%
		$Z^0\tilde{\tau}_1^-$	12.8%	$e^-\bar{\nu_\mu}$	**10.5%**
$\tilde{e}_L^-$	273.9	$\tilde{\chi}_1^0e^-$	100%		
$\tilde{\chi}_2^0$	311.1	$\tilde{\nu}_\tau\nu_\tau$	10.8%	$\tilde{\nu}_\tau\bar{\nu_\tau}$	10.8%
		$\bar{\tilde{\nu}}_\mu\nu_\mu$	9.7%	$\tilde{\nu}_\mu\bar{\nu_\mu}$	9.7%
		$\bar{\tilde{\nu}}_e\nu_e$	8.1%	$\tilde{\nu}_e\bar{\nu_e}$	8.1%
		$\tilde{\mu}_L^-\mu^+$	6.6%	$\tilde{\mu}_L^+\mu^-$	6.6%
		$\tilde{\tau}_2^-\tau^+$	6.3%	$\tilde{\tau}_2^+\tau^-$	6.3%
		$\tilde{e}_L^-e^+$	5.4%	$\tilde{e}_L^+e^-$	5.4%
		$\tilde{\tau}_1^-\tau^+$	2.7%	$\tilde{\tau}_1^+\tau^-$	2.7%
$\tilde{\chi}_1^-$	311.2	$\bar{\tilde{\nu}}_\tau\tau^-$	22.3%	$\bar{\tilde{\nu}}_\mu\mu^-$	20.0%
		$\bar{\tilde{\nu}}_e e^-$	16.9%	$\tilde{\mu}_L^-\bar{\nu_\mu}$	12.7%
		$\tilde{\tau}_2^-\bar{\nu_\tau}$	12.1%	$\tilde{e}_L^-\bar{\nu_e}$	10.3%
		$\tilde{\tau}_1^-\bar{\nu_\tau}$	5.0%		
$\tilde{t}_1$	365.8	$\tilde{\chi}_1^0t$	69.1%	$\tilde{\chi}_1^+b$	30.9%
$\tilde{b}_1$	706.3	$W^-\tilde{t}_1$	78.5%	$\tilde{\chi}_1^-t$	12.8%
		$\tilde{\chi}_2^0b$	8.2%		
$\tilde{t}_2$	790.6	$Z^0\tilde{t}_1$	55.3%	$H^0\tilde{t}_1$	22.9%
		$\tilde{\chi}_1^+b$	14.3%	$\tilde{\chi}_2^0t$	1.2%
$\tilde{\chi}_3^0$	819.8	$\tilde{t}_1\bar{t}$	26.5%	$\tilde{t}_1^*t$	26.5%
		$\tilde{\chi}_1^-W^+$	14.2%	$\tilde{\chi}_1^+W^-$	14.2%
		$\tilde{\chi}_2^0Z^0$	12.6%	$\tilde{\chi}_1^0Z^0$	3.7%
		$\tilde{\chi}_2^0H^0$	1.0%		
$\tilde{b}_2$	821.5	$\tilde{\chi}_1^0b$	59.3%	$W^-\tilde{t}_1$	36.8%
		$\tilde{\chi}_1^-t$	2.0%	$\tilde{\chi}_2^0b$	1.2%
$\tilde{d}_R$ $(\tilde{s}_R)$	824.2	$\tilde{\chi}_1^0d(s)$	100%		
$\tilde{u}_R$ $(\tilde{c}_R)$	826.3	$\tilde{\chi}_1^0u(c)$	100%		
$\tilde{\chi}_2^-$	828.0	$\tilde{t}_1^*b$	57.5%	$\tilde{\chi}_2^0W^-$	12.9%
		$\tilde{\chi}_1^-Z^0$	12.4%	$\tilde{\chi}_1^-H^0$	11.6%
		$\tilde{\chi}_1^0W^-$	3.3%		
$\tilde{\chi}_4^0$	828.3	$\tilde{t}_1\bar{t}$	34.7%	$\tilde{t}_1^*t$	34.7%
		$\tilde{\chi}_1^-W^+$	9.0%	$\tilde{\chi}_1^+W^-$	9.0%
		$\tilde{\chi}_2^0H^0$	7.5%	$\tilde{\chi}_1^0H^0$	2.2%
$\tilde{u}_L$ $(\tilde{c}_L)$	856.3	$\tilde{\chi}_1^+d(s)$	65.9%	$\tilde{\chi}_2^0u(c)$	32.9%
		$\tilde{\chi}_1^0u(c)$	1.2%		
$\tilde{d}_L$ $(\tilde{s}_L)$	859.8	$\tilde{\chi}_1^-u(c)$	65.5%	$\tilde{\chi}_2^0d(s)$	32.8%
		$\tilde{\chi}_1^0d(s)$	1.7%		
$\tilde{g}$	933.8	$\tilde{t}_1\bar{t}$	23.4%	$\tilde{t}_1^*t$	23.4%
		$\tilde{b}_1\bar{b}$	9.2%	$\tilde{b}_1^*b$	9.2%
		$\tilde{b}_2\bar{b}$	2.6%	$\tilde{b}_2^*b$	2.6%
		$\tilde{d}_R\bar{d}(\tilde{s}_R\bar{s})$	2.5%	$\tilde{d}_R^*d(\tilde{s}_R^*s)$	2.5%
		$\tilde{u}_R\bar{u}(\tilde{c}_R\bar{c})$	2.4%	$\tilde{u}_R^*u(\tilde{c}_R^*c)$	2.4%
		$\tilde{u}_L\bar{u}(\tilde{c}_L\bar{c})$	1.3%	$\tilde{u}_L^*u(\tilde{c}_L^*c)$	1.3%
		$\tilde{d}_L\bar{d}(\tilde{s}_L\bar{s})$	1.2%	$\tilde{d}_L^*d(\tilde{s}_L^*s)$	1.2%

Table A.1.: Branching ratios (BRs) and sparticle masses for the benchmark scenario SUSY1. BRs smaller than 1% are neglected. $\not{P}_6$ decays are shown in bold-face. Masses which are reduced by more than 5 GeV (compared to the P_6 conserving spectrum) due to $\lambda_{231}|_{\mathrm{GUT}} = 0.045$ are also shown in bold-face.

	mass [GeV]	channel	BR	channel	BR
$\tilde{e}_R^-$	**151.5**	$\mu^-\nu_\tau$	**50%**	$\tau^-\nu_\mu$	**50%**
$\tilde{\tau}_1^-$	151.6	$e^-\bar{\nu_\mu}$	**100%**		
$\tilde{\chi}_1^0$	152.8	$\tilde{e}_R^- e^+$	50%%	$\tilde{e}_R^+ e^-$	50%
$\tilde{\mu}_R^-$	167.3	$\tilde{\chi}_1^0\mu^-$	100%		
$\tilde{\nu}_\tau$	**250.4**	$\tilde{\chi}_1^0\nu_\tau$	75.7%	$e^-\mu^+$	**12.6%**
		$W^+\tilde{\tau}_1^-$	11.7%		
$\tilde{\nu}_\mu$	**253.7**	$\tilde{\chi}_1^0\nu_\mu$	86.1%	$e^-\tau^+$	**13.9%**
$\tilde{\nu}_e$	258.5	$\tilde{\chi}_1^0\nu_e$	100%		
$\tilde{\mu}_L^-$	**265.0**	$\tilde{\chi}_1^0\mu^-$	85.5%	$e^-\bar{\nu_\tau}$	**14.5%**
$\tilde{\tau}_2^-$	**265.6**	$\tilde{\chi}_1^0\tau^-$	80.6%	$e^-\bar{\nu_\mu}$	**11.6%**
		$Z^0\tilde{\tau}_1^-$	7.7%		
$\tilde{e}_L^-$	269.6	$\tilde{\chi}_1^0 e^-$	100%		
$\tilde{\chi}_2^0$	291.0	$\bar{\tilde{\nu}}_\tau\nu_\tau$	12.0%	$\tilde{\nu}_\tau\bar{\nu_\tau}$	12.0%
		$\bar{\tilde{\nu}}_\mu\nu_\mu$	10.3%	$\tilde{\nu}_\mu\bar{\nu_\mu}$	10.3%
		$\bar{\tilde{\nu}}_e\nu_e$	7.9%	$\tilde{\nu}_e\bar{\nu_e}$	7.9%
		$\tilde{\mu}_L^-\mu^+$	5.5%	$\tilde{\mu}_L^+\mu^-$	5.5%
		$\tilde{\tau}_2^-\tau^+$	5.0%	$\tilde{\tau}_2^+\tau^-$	5.0%
		$\tilde{\tau}_1^-\tau^+$	4.7%	$\tilde{\tau}_1^+\tau^-$	4.7%
		$\tilde{e}_L^- e^+$	3.8%	$\tilde{e}_L^+ e^-$	3.8%
		$\tilde{\chi}_1^0 H^0$	1.0%		
$\tilde{\chi}_1^-$	291.0	$\bar{\tilde{\nu}}_\tau\tau^-$	24.8%	$\bar{\tilde{\nu}}_\mu\mu^-$	21.3%
		$\bar{\tilde{\nu}}_e e^-$	16.4%	$\tilde{\mu}_L^-\bar{\nu_\mu}$	10.5%
		$\tilde{\tau}_2^-\bar{\nu_\tau}$	9.6%	$\tilde{\tau}_1^-\bar{\nu_\tau}$	8.9%
		$\tilde{e}_L^-\bar{\nu_e}$	7.2%	$\tilde{\chi}_1^0 W^-$	1.0%
$\tilde{t}_1$	304.9	$\tilde{\chi}_1^+ b$	100%		
$\tilde{b}_1$	661.6	$W^-\tilde{t}_1$	80.9%	$\tilde{\chi}_1^- t$	11.2%
		$\tilde{\chi}_2^0 b$	7.5%		
$\tilde{t}_2$	750.2	$Z^0\tilde{t}_1$	57.1%	$H^0\tilde{t}_1$	22.2%
		$\tilde{\chi}_1^+ b$	13.2%	$\tilde{\chi}_2^0 t$	5.4%
		$\tilde{\chi}_1^0 t$	1.2%		
$\tilde{b}_2$	779.1	$\tilde{\chi}_1^0 b$	56.7%	$W^-\tilde{t}_1$	39.3%
		$\tilde{\chi}_1^- t$	1.9%	$\tilde{\chi}_2^0 b$	1.2%
$\tilde{d}_R$ $(\tilde{s}_R)$	781.9	$\tilde{\chi}_1^0 d(s)$	100%		
$\tilde{u}_R$ $(\tilde{c}_R)$	783.7	$\tilde{\chi}_1^0 u(c)$	100%		
$\tilde{\chi}_3^0$	793.9	$\tilde{t}_1\bar{t}$	28.5%	$\tilde{t}_1^* t$	28.5%
		$\tilde{\chi}_1^- W^+$	13.0%	$\tilde{\chi}_1^+ W^-$	13.0%
		$\tilde{\chi}_2^0 Z^0$	11.4%	$\tilde{\chi}_1^0 Z^0$	3.3%
		$\tilde{\chi}_2^0 H^0$	1.0%		
$\tilde{\chi}_2^-$	802.1	$\tilde{t}_1^* b$	60.4%	$\tilde{\chi}_2^0 W^-$	11.9%
		$\tilde{\chi}_1^- Z^0$	11.5%	$\tilde{\chi}_1^- H^0$	10.7%
		$\tilde{\chi}_1^0 W^-$	3.0%		
$\tilde{\chi}_4^0$	802.4	$\tilde{t}_1\bar{t}$	36.1%	$\tilde{t}_1^* t$	36.1%
		$\tilde{\chi}_1^- W^+$	8.2%	$\tilde{\chi}_1^+ W^-$	8.2%
		$\tilde{\chi}_2^0 H^0$	6.7%	$\tilde{\chi}_1^0 H^0$	2.0%
$\tilde{u}_L$ $(\tilde{c}_L)$	811.4	$\tilde{\chi}_1^+ d(s)$	66.0%	$\tilde{\chi}_2^0 u(c)$	33.0%
		$\tilde{\chi}_1^0 u(c)$	1.0%		
$\tilde{d}_L$ $(\tilde{s}_L)$	815.0	$\tilde{\chi}_1^- u(c)$	65.5%	$\tilde{\chi}_2^0 d(s)$	32.8%
		$\tilde{\chi}_1^0 d(s)$	1.7%		
$\tilde{g}$	881.0	$\tilde{t}_1\bar{t}$	24.7%	$\tilde{t}_1^* t$	24.7%
		$\tilde{b}_1\bar{b}$	9.5%	$\tilde{b}_1^* b$	9.5%
		$\tilde{b}_2\bar{b}$	2.4%	$\tilde{b}_2^* b$	2.4%
		$\tilde{d}_R\bar{d}(\tilde{s}_R\bar{s})$	2.3%	$\tilde{d}_R^* d(\tilde{s}_R^* s)$	2.3%
		$\tilde{u}_R\bar{u}(\tilde{c}_R\bar{c})$	2.2%	$\tilde{u}_R^* u(\tilde{c}_R^* c)$	2.2%
		$\tilde{u}_L\bar{u}(\tilde{c}_L\bar{c})$	1.2%	$\tilde{u}_L^* u(\tilde{c}_L^* c)$	1.2%
		$\tilde{d}_L\bar{d}(\tilde{s}_L\bar{s})$	1.1%	$\tilde{d}_L^* d(\tilde{s}_L^* s)$	1.1%

Table A.2.: Branching ratios (BRs) and sparticle masses for the benchmark scenario SUSY2. BRs smaller than 1% are neglected. $\not{P}_6$ decays are shown in bold-face. Masses which are reduced by more than 5 GeV (compared to the P_6 conserving spectrum) due to $\lambda_{231}|_{\mathrm{GUT}} = 0.045$ are also shown in bold-face.

	mass [GeV]	channel	BR	channel	BR
$\tilde{e}_R^-$	**168.7**	$\mu^- \nu_\tau$	**50%**	$\tau^- \nu_\mu$	**50%**
$\tilde{\tau}_1^-$	170.0	$e^- \bar{\nu}_\mu$	**100%**		
$\tilde{\mu}_R^-$	183.6	$\tilde{e}_R^+ e^- \mu^-$	34.6%	$\tilde{e}_R^- e^+ \mu^-$	28.3%
		$\tilde{\tau}_1^+ \tau^- \mu^-$	20.4%	$\tilde{\tau}_1^- \tau^+ \mu^-$	16.7%
$\tilde{\chi}_1^0$	195.7	$\tilde{e}_R^- e^+$	23.8%	$\tilde{e}_R^+ e^-$	23.8%
		$\tilde{\tau}_1^- \tau^+$	21.0%	$\tilde{\tau}_1^+ \tau^-$	21.0%
		$\tilde{\mu}_R^- \mu^+$	5.1%	$\tilde{\mu}_R^+ \mu^-$	5.1%
$\tilde{\nu}_\tau$	**306.5**	$\tilde{\chi}_1^0 \nu_\tau$	60.2%	$W^+ \tilde{\tau}_1^-$	28.4%
		$e^- \mu^+$	**11.4%**		
$\tilde{\nu}_\mu$	**309.4**	$\tilde{\chi}_1^0 \nu_\mu$	84.4%	$e^- \tau^+$	**15.6%**
$\tilde{\nu}_e$	313.5	$\tilde{\chi}_1^0 \nu_e$	100%		
$\tilde{\tau}_2^-$	**318.4**	$\tilde{\chi}_1^0 \tau^-$	59.0%	$H^0 \tilde{\tau}_1^-$	16.5%
		$Z^0 \tilde{\tau}_1^-$	14.1%	$e^- \bar{\nu}_\mu$	**10.4%**
$\tilde{\mu}_L^-$	**318.7**	$\tilde{\chi}_1^0 \mu^-$	84.1%	$e^- \bar{\nu}_\tau$	**15.9%**
$\tilde{e}_L^-$	322.8	$\tilde{\chi}_1^0 e^-$	100%		
$\tilde{\chi}_2^0$	372.0	$\tilde{\nu}_\tau \nu_\tau$	10.0%	$\tilde{\nu}_\tau \bar{\nu}_\tau$	10.0%
		$\tilde{\bar{\nu}}_\mu \nu_\mu$	9.2%	$\tilde{\nu}_\mu \bar{\nu}_\mu$	9.2%
		$\tilde{\bar{\nu}}_e \nu_e$	8.1%	$\tilde{\nu}_e \bar{\nu}_e$	8.1%
		$\tilde{\mu}_L^- \mu^+$	7.2%	$\tilde{\mu}_L^+ \mu^-$	7.2%
		$\tilde{\tau}_2^- \tau^+$	7.1%	$\tilde{\tau}_2^+ \tau^-$	7.1%
		$\tilde{e}_L^- e^+$	6.2%	$\tilde{e}_L^+ e^-$	6.2%
		$\tilde{\tau}_1^- \tau^+$	1.6%	$\tilde{\tau}_1^+ \tau^-$	1.6%
$\tilde{\chi}_1^-$	372.0	$\tilde{\bar{\nu}}_\tau \tau^-$	20.6%	$\tilde{\bar{\nu}}_\mu \mu^-$	19.0%
		$\tilde{\bar{\nu}}_e e^-$	16.8%	$\tilde{\mu}_L^- \bar{\nu}_\mu$	13.9%
		$\tilde{\tau}_2^- \bar{\nu}_\tau$	13.7%	$\tilde{e}_L^- \bar{\nu}_e$	12.0%
		$\tilde{\tau}_1^- \bar{\nu}_\tau$	3.1%		
$\tilde{t}_1$	531.1	$\tilde{\chi}_1^0 t$	62.2%	$\tilde{\chi}_1^+ b$	37.8%
$\tilde{b}_1$	847.3	$W^- \tilde{t}_1$	71.5%	$\tilde{\chi}_1^- t$	17.5%
		$\tilde{\chi}_2^0 b$	10.4%		
$\tilde{\chi}_3^0$	898.0	$\tilde{t}_1 \bar{t}$	19.7%	$\tilde{t}_1^* t$	19.7%
		$\tilde{\chi}_1^- W^+$	18.4%	$\tilde{\chi}_1^+ W^-$	18.4%
		$\tilde{\chi}_2^0 Z^0$	16.5%	$\tilde{\chi}_1^0 Z^0$	4.8%
		$\tilde{\chi}_2^0 H^0$	1.2%		
$\tilde{\chi}_2^-$	906.0	$\tilde{t}_1^* b$	47.6%	$\tilde{\chi}_2^0 W^-$	15.9%
		$\tilde{\chi}_1^- Z^0$	15.4%	$\tilde{\chi}_1^- H^0$	14.6%
		$\tilde{\chi}_1^0 W^-$	4.2%		
$\tilde{\chi}_4^0$	906.4	$\tilde{t}_1 \bar{t}$	29.6%	$\tilde{t}_1^* t$	29.6%
		$\tilde{\chi}_1^- W^+$	12.1%	$\tilde{\chi}_1^+ W^-$	12.1%
		$\tilde{\chi}_2^0 H^0$	10.3%	$\tilde{\chi}_1^0 H^0$	2.9%
$\tilde{t}_2$	919.4	$Z^0 \tilde{t}_1$	49.1%	$H^0 \tilde{t}_1$	24.6%
		$\tilde{\chi}_1^+ b$	17.3%	$\tilde{\chi}_2^0 t$	7.6%
		$\tilde{\chi}_1^0 t$	1.5%		
$\tilde{b}_2$	959.5	$\tilde{\chi}_1^0 b$	67.0%	$W^- \tilde{t}_1$	28.9%
		$\tilde{\chi}_1^- t$	2.1%	$\tilde{\chi}_2^0 b$	1.2%
$\tilde{d}_R$ $(\tilde{s}_R)$	962.3	$\tilde{\chi}_1^0 d(s)$	100%		
$\tilde{u}_R$ $(\tilde{c}_R)$	965	$\tilde{\chi}_1^0 u(c)$	100%		
$\tilde{u}_L$ $(\tilde{c}_L)$	1001.8	$\tilde{\chi}_1^+ d(s)$	65.9%	$\tilde{\chi}_2^0 u(c)$	32.9%
		$\tilde{\chi}_1^0 u(c)$	1.2%		
$\tilde{d}_L$ $(\tilde{s}_L)$	1004.7	$\tilde{\chi}_1^- u(c)$	65.5%	$\tilde{\chi}_2^0 d(s)$	32.8%
		$\tilde{\chi}_1^0 d(s)$	1.7%		
$\tilde{g}$	1093.7	$\tilde{t}_1 \bar{t}$	20.9%	$\tilde{t}_1^* t$	20.9%
		$\tilde{b}_1 \bar{b}$	8.5%	$\tilde{b}_1^* b$	8.5%
		$\tilde{b}_2 \bar{b}$	2.9%	$\tilde{b}_2^* b$	2.9%
		$\tilde{d}_R \bar{d}(\tilde{s}_R \bar{s})$	2.7%	$\tilde{d}_R^* d(\tilde{s}_R^* s)$	2.7%
		$\tilde{u}_R \bar{u}(\tilde{c}_R \bar{c})$	2.6%	$\tilde{u}_R^* u(\tilde{c}_R^* c)$	2.6%
		$\tilde{t}_2 \bar{t}$	1.6%	$\tilde{t}_2^* t$	1.6%
		$\tilde{u}_L \bar{u}(\tilde{c}_L \bar{c})$	1.4%	$\tilde{u}_L^* u(\tilde{c}_L^* c)$	1.4%
		$\tilde{d}_L \bar{d}(\tilde{s}_L \bar{s})$	1.3%	$\tilde{d}_L^* d(\tilde{s}_L^* s)$	1.3%

Table A.3.: Branching ratios (BRs) and sparticle masses for the benchmark scenario BE1. BRs smaller than 1% are neglected. $\not{P}_6$ decays are shown in bold-face. Masses which are reduced by more than 5 GeV (compared to the P_6 conserving spectrum) due to $\lambda_{231}|_{\mathrm{GUT}} = 0.045$ are also shown in bold-face.

	mass [GeV]	channel	BR	channel	BR
$\tilde{e}_R^-$	**182.3**	$\mu^-\nu_\tau$	**50%**	$\tau^-\nu_\mu$	**50%**
$\tilde{\tau}_1^-$	189.0	$\tilde{e}_R^+e^-\tau^-$	50.2%	$\tilde{e}_R^-e^+\tau^-$	49.5%
$\tilde{\chi}_1^0$	189.5	$\tilde{e}_R^-e^+$	50%	$\tilde{e}_R^+e^-$	50%
$\tilde{\mu}_R^-$	199.0	$\tilde{\chi}_1^0\mu^-$	100%		
$\tilde{\nu}_\tau$	**309.8**	$\tilde{\chi}_1^0\nu_\tau$	71.0%	$W^+\tilde{\tau}_1^-$	17.0%
		$e^-\mu^+$	**12.0%**		
$\tilde{\nu}_\mu$	**312.0**	$\tilde{\chi}_1^0\nu_\mu$	85.8%	$e^-\tau^+$	**14.2%**
$\tilde{\nu}_e$	317.0	$\tilde{\chi}_1^0\nu_e$	100%		
$\tilde{\tau}_2^-$	**320.8**	$\tilde{\chi}_1^0\tau^-$	69.9%	$e^-\bar{\nu}_\mu$	**11.3%**
		$H^0\tilde{\tau}_1^-$	10.2%	$Z^0\tilde{\tau}_1^-$	8.6%
$\tilde{\mu}_L^-$	**320.8**	$\tilde{\chi}_1^0\mu^-$	85.2%	$e^-\bar{\nu}_\tau$	**14.8%**
$\tilde{e}_L^-$	325.7	$\tilde{\chi}_1^0e^-$	100%		
$\tilde{\chi}_2^0$	360.1	$\bar{\tilde{\nu}}_\tau\nu_\tau$	10.5%	$\tilde{\nu}_\tau\bar{\nu}_\tau$	10.5%
		$\bar{\tilde{\nu}}_\mu\nu_\mu$	9.7%	$\tilde{\nu}_\mu\bar{\nu}_\mu$	9.7%
		$\bar{\tilde{\nu}}_e\nu_e$	7.9%	$\tilde{\nu}_e\bar{\nu}_e$	7.9%
		$\tilde{\mu}_L^-\mu^+$	7.0%	$\tilde{\mu}_L^+\mu^-$	7.0%
		$\tilde{\tau}_2^-\tau^+$	6.8%	$\tilde{\tau}_2^+\tau^-$	6.8%
		$\tilde{e}_L^-e^+$	5.4%	$\tilde{e}_L^+e^-$	5.4%
		$\tilde{\tau}_1^-\tau^+$	2.0%	$\tilde{\tau}_1^+\tau^-$	2.0%
		$\tilde{\chi}_1^0H^0$	1.3%		
$\tilde{\chi}_1^-$	360.2	$\bar{\tilde{\nu}}_\tau\tau^-$	21.7%	$\bar{\tilde{\nu}}_\mu\mu^-$	19.9%
		$\bar{\tilde{\nu}}_ee^-$	16.3%	$\tilde{\mu}_L^-\bar{\nu}_\mu$	13.4%
		$\tilde{\tau}_2^-\bar{\nu}_\tau$	13.2%	$\tilde{e}_L^-\bar{\nu}_e$	10.5%
		$\tilde{\tau}_1^-\bar{\nu}_\tau$	3.8%	$\tilde{\chi}_1^0W^-$	1.3%
$\tilde{t}_1$	448.3	$\tilde{\chi}_1^0t$	71.9%	$\tilde{\chi}_1^+b$	28.1%
$\tilde{b}_1$	809.1	$W^-\tilde{t}_1$	78.1%	$\tilde{\chi}_1^-t$	13.3%
		$\tilde{\chi}_2^0b$	8.1%		
$\tilde{t}_2$	887.0	$Z^0\tilde{t}_1$	52.7%	$H^0\tilde{t}_1$	25.9%
		$\tilde{\chi}_1^+b$	14.1%	$\tilde{\chi}_2^0t$	6.1%
		$\tilde{\chi}_1^0t$	1.2%		
$\tilde{\chi}_3^0$	936.7	$\tilde{t}_1\bar{t}$	26.0%	$\tilde{t}_1^*t$	26.0%
		$\tilde{\chi}_1^-W^+$	14.6%	$\tilde{\chi}_1^+W^-$	14.6%
		$\tilde{\chi}_2^0Z^0$	13.3%	$\tilde{\chi}_1^0Z^0$	3.8%
$\tilde{b}_2$	937.7	$\tilde{\chi}_1^0b$	67.9%	$W^-\tilde{t}_1$	26.0%
		$\tilde{\chi}_1^-t$	2.7%	$\tilde{\chi}_2^0b$	1.5%
$\tilde{d}_R$ ($\tilde{s}_R$)	939.8	$\tilde{\chi}_1^0d(s)$	100%		
$\tilde{u}_R$ ($\tilde{c}_R$)	942.9	$\tilde{\chi}_1^0u(c)$	100%		
$\tilde{\chi}_2^-$	944.5	$\tilde{t}_1^*b$	55.6%	$\tilde{\chi}_2^0W^-$	13.5%
		$\tilde{\chi}_1^-Z^0$	13.1%	$\tilde{\chi}_1^-H^0$	12.4%
		$\tilde{\chi}_1^0W^-$	3.4%		
$\tilde{\chi}_4^0$	945.1	$\tilde{t}_1\bar{t}$	33.3%	$\tilde{t}_1^*t$	33.3%
		$\tilde{\chi}_1^-W^+$	10.0%	$\tilde{\chi}_1^+W^-$	10.0%
		$\tilde{\chi}_2^0H^0$	8.5%	$\tilde{\chi}_1^0H^0$	2.4%
$\tilde{u}_L$ ($\tilde{c}_L$)	977.6	$\tilde{\chi}_1^+d(s)$	65.9%	$\tilde{\chi}_2^0u(c)$	32.9%
		$\tilde{\chi}_1^0u(c)$	1.2%		
$\tilde{d}_L$ ($\tilde{s}_L$)	980.4	$\tilde{\chi}_1^-u(c)$	65.6%	$\tilde{\chi}_2^0d(s)$	32.8%
		$\tilde{\chi}_1^0d(s)$	1.6%		
$\tilde{g}$	1063.1	$\tilde{t}_1\bar{t}$	23.0%	$\tilde{t}_1^*t$	23.0%
		$\tilde{b}_1\bar{b}$	8.7%	$\tilde{b}_1^*b$	8.7%
		$\tilde{b}_2\bar{b}$	2.4%	$\tilde{b}_2^*b$	2.4%
		$\tilde{d}_R\bar{d}(\tilde{s}_R\bar{s})$	2.4%	$\tilde{d}_R^*d(\tilde{s}_R^*s)$	2.4%
		$\tilde{u}_R\bar{u}(\tilde{c}_R\bar{c})$	2.3%	$\tilde{u}_R^*u(\tilde{c}_R^*c)$	2.3%
		$\tilde{t}_2\bar{t}$	2.0%	$\tilde{t}_2^*t$	2.0%
		$\tilde{u}_L\bar{u}(\tilde{c}_L\bar{c})$	1.2%	$\tilde{u}_L^*u(\tilde{c}_L^*c)$	1.2%
		$\tilde{d}_L\bar{d}(\tilde{s}_L\bar{s})$	1.1%	$\tilde{d}_L^*d(\tilde{s}_L^*s)$	1.1%

Table A.4.: Branching ratios (BRs) and sparticle masses for the benchmark scenario BE2. BRs smaller than 1% are neglected. $\not{P}_6$ decays are shown in bold-face. Masses which are reduced by more than 5 GeV (compared to the P_6 conserving spectrum) due to $\lambda_{231}|_{\mathrm{GUT}} = 0.045$ are also shown in bold-face.

	mass [GeV]	channel	BR	channel	BR
$\tilde{e}_R^-$	**182.0**	$\mu^-\nu_\tau$	**50%**	$\tau^-\nu_\mu$	**50%**
$\tilde{\chi}_1^0$	184.9	$\tilde{e}_R^-e^+$	50%	$\tilde{e}_R^+e^-$	50%
$\tilde{\tau}_1^-$	187.2	$\tilde{\chi}_1^0\tau^-$	64.5%	$e^-\bar{\nu}_\mu$	**35.5%**
$\tilde{\mu}_R^-$	195.9	$\tilde{\chi}_1^0\mu^-$	100%		
$\tilde{\nu}_\tau$	**304.3**	$\tilde{\chi}_1^0\nu_\tau$	73.6%	$W^+\tilde{\tau}_1^-$	14.2%
		$e^-\mu^+$	**12.2%**		
$\tilde{\nu}_\mu$	**306.2**	$\tilde{\chi}_1^0\nu_\mu$	86.0%	$e^-\tau^+$	**14.0%**
$\tilde{\nu}_e$	310.4	$\tilde{\chi}_1^0\nu_e$	100%		
$\tilde{\mu}_L^-$	**315.2**	$\tilde{\chi}_1^0\mu^-$	85.2%	$e^-\bar{\nu}_\tau$	**14.8%**
$\tilde{\tau}_2^-$	**315.3**	$\tilde{\chi}_1^0\tau^-$	72.5%	$e^-\bar{\nu}_\mu$	**11.7%**
		$H^0\tilde{\tau}_1^-$	8.5%	$Z^0\tilde{\tau}_1^-$	7.3%
$\tilde{e}_L^-$	319.3	$\tilde{\chi}_1^0e^-$	100%		
$\tilde{\chi}_2^0$	351.2	$\bar{\tilde{\nu}}_\tau\nu_\tau$	10.5%	$\tilde{\nu}_\tau\bar{\nu}_\tau$	10.5%
		$\bar{\tilde{\nu}}_\mu\nu_\mu$	9.7%	$\tilde{\nu}_\mu\bar{\nu}_\mu$	9.7%
		$\bar{\tilde{\nu}}_e\nu_e$	8.1%	$\tilde{\nu}_e\bar{\nu}_e$	8.1%
		$\tilde{\mu}_L^-\mu^+$	6.8%	$\tilde{\mu}_L^+\mu^-$	6.8%
		$\tilde{\tau}_2^-\tau^+$	6.6%	$\tilde{\tau}_2^+\tau^-$	6.6%
		$\tilde{e}_L^-e^+$	5.4%	$\tilde{e}_L^+e^-$	5.4%
		$\tilde{\tau}_1^-\tau^+$	2.0%	$\tilde{\tau}_1^+\tau^-$	2.0%
		$\tilde{\chi}_1^0H^0$	1.6%		
$\tilde{\chi}_1^-$	351.2	$\bar{\tilde{\nu}}_\tau\tau^-$	21.7%	$\bar{\tilde{\nu}}_\mu\mu^-$	20.1%
		$\bar{\tilde{\nu}}_e e^-$	16.8%	$\tilde{\mu}_L^-\bar{\nu}_\mu$	13.0%
		$\tilde{\tau}_2^-\bar{\nu}_\tau$	12.7%	$\tilde{e}_L^-\bar{\nu}_e$	10.4%
		$\tilde{\tau}_1^-\bar{\nu}_\tau$	3.8%	$\tilde{\chi}_1^0W^-$	1.6%
$\tilde{t}_1$	481.7	$\tilde{\chi}_1^0t$	62.1%	$\tilde{\chi}_1^+b$	37.9%
$\tilde{b}_1$	805.4	$W^-\tilde{t}_1$	73.9%	$\tilde{\chi}_1^-t$	15.9%
		$\tilde{\chi}_2^0b$	9.7%		
$\tilde{t}_2$	881.7	$Z^0\tilde{t}_1$	51.3%	$H^0\tilde{t}_1$	24.2%
		$\tilde{\chi}_1^+b$	16.1%	$\tilde{\chi}_2^0t$	7.0%
		$\tilde{\chi}_1^0t$	1.4%		
$\tilde{\chi}_3^0$	884.0	$\tilde{t}_1\bar{t}$	22.1%	$\tilde{t}_1^*t$	22.1%
		$\tilde{\chi}_1^-W^+$	17.0%	$\tilde{\chi}_1^+W^-$	17.0%
		$\tilde{\chi}_2^0Z^0$	15.4%	$\tilde{\chi}_1^0Z^0$	4.5%
		$\tilde{\chi}_2^0H^0$	1.0%		
$\tilde{\chi}_2^-$	892.4	$\tilde{t}_1^*b$	50.8%	$\tilde{\chi}_2^0W^-$	15.1%
		$\tilde{\chi}_1^-Z^0$	14.6%	$\tilde{\chi}_1^-H^0$	13.7%
		$\tilde{\chi}_1^0W^-$	3.8%		
$\tilde{\chi}_4^0$	893.1	$\tilde{t}_1\bar{t}$	31.4%	$\tilde{t}_1^*t$	31.4%
		$\tilde{\chi}_1^-W^+$	11.1%	$\tilde{\chi}_1^+W^-$	11.1%
		$\tilde{\chi}_2^0H^0$	9.4%	$\tilde{\chi}_1^0H^0$	2.7%
$\tilde{b}_2$	919.3	$\tilde{\chi}_1^0b$	70.5%	$W^-\tilde{t}_1$	26.0%
		$\tilde{\chi}_1^-t$	1.8%	$\tilde{\chi}_2^0b$	1.1%
$\tilde{d}_R$ ($\tilde{s}_R$)	921.1	$\tilde{\chi}_1^0d(s)$	100%		
$\tilde{u}_R$ ($\tilde{c}_R$)	923.8	$\tilde{\chi}_1^0u(c)$	100%		
$\tilde{u}_L$ ($\tilde{c}_L$)	957.9	$\tilde{\chi}_1^+d(s)$	65.9%	$\tilde{\chi}_2^0u(c)$	33.0%
		$\tilde{\chi}_1^0u(c)$	1.1%		
$\tilde{d}_L$ ($\tilde{s}_L$)	961.0	$\tilde{\chi}_1^-u(c)$	65.5%	$\tilde{\chi}_2^0d(s)$	32.7%
		$\tilde{\chi}_1^0d(s)$	1.7%		
$\tilde{g}$	1041.8	$\tilde{t}_1\bar{t}$	22.6%	$\tilde{t}_1^*t$	22.6%
		$\tilde{b}_1\bar{b}$	8.9%	$\tilde{b}_1^*b$	8.9%
		$\tilde{b}_2\bar{b}$	2.7%	$\tilde{b}_2^*b$	2.7%
		$\tilde{d}_R\bar{d}(\tilde{s}_R\bar{s})$	2.6%	$\tilde{d}_R^*d(\tilde{s}_R^*s)$	2.6%
		$\tilde{u}_R\bar{u}(\tilde{c}_R\bar{c})$	2.5%	$\tilde{u}_R^*u(\tilde{c}_R^*c)$	2.5%
		$\tilde{u}_L\bar{u}(\tilde{c}_L\bar{c})$	1.3%	$\tilde{u}_L^*u(\tilde{c}_L^*c)$	1.3%
		$\tilde{d}_L\bar{d}(\tilde{s}_L\bar{s})$	1.2%	$\tilde{d}_L^*d(\tilde{s}_L^*s)$	1.2%

Table A.5.: Branching ratios (BRs) and sparticle masses for the benchmark scenario BE3. BRs smaller than 1% are neglected. $\not{P}_6$ decays are shown in bold-face. Masses which are reduced by more than 5 GeV (compared to the P_6 conserving spectrum) due to $\lambda_{231}|_{\mathrm{GUT}} = 0.045$ are also shown in bold-face.

B. Signal and Background at the LHC at $\sqrt{s} = 14$ TeV

We present the cut flow of the signal and SM background events for 10 fb^{-1} of simulated LHC data at $\sqrt{s} = 14$ TeV in Tab. B.1. Although the benchmark scenarios BE1, BE2 and BE3 are already observable with very early data at the LHC with $\sqrt{s} = 7$ TeV, we provide their expected event yields here as a reference in order to compare the signal efficiencies.

We applied the inclusive three-lepton analysis as presented in Sect. 5.3.4. After the three lepton requirement (step I), the expected SM background is reduced to 5110 ± 49 events. Already at this stage, the expected signal event yield of BE1, BE2 and BE3 is overwhelming. The signal efficiency for step I is the same as at LHC at 7 TeV.

The jet multiplicity requirement (step II) reduces the SM background to 1669 ± 32 expected events, which mainly stem from Zj (26%), $t\bar{t}$ (24%) and WZ (15%) production. Due to the dominating sparton pair production of the benchmark scenarios at 14 TeV, *cf.* Tab. 5.9, almost every event has at least two hard jets. Thus, the signal efficiency of this cut is enhanced: For BE1 and BE2 (BE3), roughly 97% (95%) of all signal events pass the jet multiplicity cut. Compared to LHC at 7 TeV, the signal efficiency of step II is about 10% larger.

The Z veto (step III) effectively reduces the $Z+$jets and di-boson backgrounds, leaving a total expected SM background of 503 ± 20 events, which is then dominated by the $t\bar{t}$ sample (71%). For the benchmark scenarios, the signal efficiencies are about the same as at LHC at 7 TeV.

After the requirement on the visible effective mass, $M_{\mathrm{eff}}^{\mathrm{vis}} \geq 400$ GeV, (step IV), the SM background is reduced to 64.7 ± 7.2 events. It is dominated by the $t\bar{t}$ background (78%). More than 95% of the signal events pass this last cut.

Sample	before cuts	$N_{\mathrm{lep}} \geq 3$	$N_{\mathrm{jet}} \geq 2$	M_{OSSF}	$M_{\mathrm{eff}}^{\mathrm{vis}} \geq 400$ GeV
top	$(5215 \pm 2) \cdot 10^3$	553 ± 21	491 ± 20	397 ± 19	55.9 ± 7.0
$Z+$jets	$(5601 \pm 2) \cdot 10^3$	1980 ± 41	571 ± 22	48.7 ± 6.4	2.6 ± 1.5
$W+$jets	$(9516 \pm 9) \cdot 10^2$	4.8 ± 2.0	1.6 ± 1.1	$\lesssim 1.0$	$\lesssim 1.0$
di-boson	$(7719 \pm 8) \cdot 10^2$	2573 ± 17	605 ± 11	56.7 ± 4.4	6.1 ± 1.1
all SM	$(12540 \pm 3) \cdot 10^3$	5110 ± 49	1669 ± 32	503 ± 20	64.7 ± 7.2
BE1	23040 ± 47	14412 ± 37	13925 ± 37	12204 ± 34	11854 ± 34
BE2	30980 ± 57	13910 ± 38	13442 ± 37	12227 ± 36	11569 ± 35
BE3	31160 ± 55	9118 ± 30	8700 ± 29	7807 ± 28	7533 ± 27

Table B.1.: Number of SM background and signal events after each step in the event selection at $\sqrt{s} = 14$ TeV, scaled to an integrated luminosity of 10 fb^{-1}. We provide the results for the three signal benchmark scenarios BE1, BE2 and BE3. The uncertainties include statistical errors only.

C. Three-body slepton decays

In the ISAJET7.64 code, three-body slepton decays that result in a right-handed slepton of the first or second generation are not implemented, since in most SUSY scenarios the $\tilde{\tau}_1$ is considered to be lighter than the other sleptons. However, this is clearly not the case for $\tilde{e}_R$ and $\tilde{\mu}_R$ LSP scenarios, and these decays may be of greater importance in certain regions of the parameter space. Here, we calculate the three-body slepton decays of the right-handed sleptons and the $\tilde{\tau}_1$ into a right-handed slepton of the first or second generation. We only present the calculation of the spin-summed matrix amplitude squared. The phase-space integration is straight-forward [118] and is partly performed numerically using adaptive Gaussian quadrature in ISAJET. We use the 2-component spinor techniques and notation from Ref. [238] for the calculation.

C.1. Three-body slepton decay $\tilde{\ell}_R^- \to \ell^- \ell'^{\pm} \tilde{\ell}_R'^{\mp}$

We calculate the 3-body slepton decays $\tilde{\ell}_R^- \to l^- \ell'^{\pm} \tilde{\ell}_R'^{\mp}$ via a virtual neutralino, where ℓ, ℓ' ($\tilde{\ell}_R, \tilde{\ell}'_R$) denote the (right-handed) (s)leptons of the first and the second generation and the mass of the $\tilde{\ell}'_R$ is less than the mass of the $\tilde{\ell}_R$. We neglect Yukawa couplings and slepton mixing, i.e. our sleptons are purely R-type.

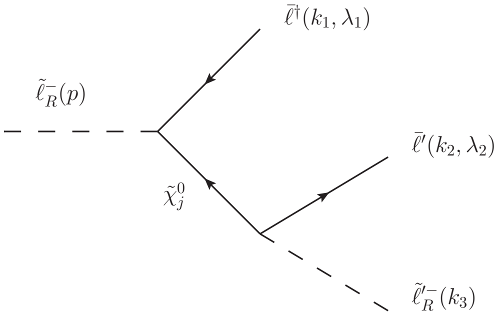

Figure C.1.: Feynman diagram for the three-body slepton decay $\tilde{\ell}_R^- \to \ell^- \ell'^+ \tilde{\ell}_R'^-$.

The Feynman diagram for the decay $\tilde{\ell}_R^- \to \ell^- \ell'^+ \tilde{\ell}_R'^-$ is shown in Fig. C.1. The momenta and polarizations of the particles are indicated on the diagram. The amplitude for this diagram, for each neutralino $\tilde{\chi}_j^0$ exchanged, is

$$i\mathcal{M} = (-ia_j^*)(-ia_j) x_2^\dagger \frac{i(p-k_1)\cdot\bar{\sigma}}{(p-k_1)^2 - m_{\tilde{\chi}_j^0}^2} y_1, \tag{C.1}$$

where $a_j \equiv \sqrt{2} g' N_{j1}$, and the spinor wave function factors are $y_1 = y(\vec{k_1}, \lambda_1)$ and $x_2^\dagger = x^\dagger(\vec{k_2}, \lambda_2)$. Squaring the total amplitude then yields

$$|\mathcal{M}|^2 = A\, x_2^\dagger (p-k_1)\cdot\bar{\sigma} y_1 y_1^\dagger (p-k_1)\cdot\bar{\sigma} x_2, \tag{C.2}$$

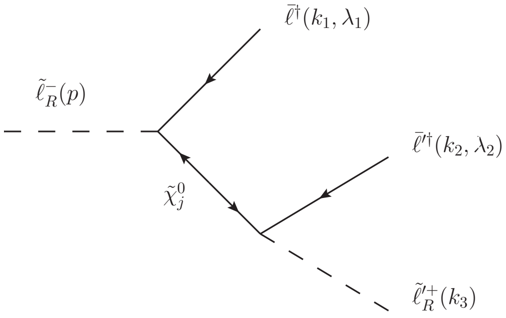

Figure C.2.: Feynman diagram for the three-body slepton decay $\tilde{l}_R^- \to l^- l'^- \tilde{l}_R'^+$.

with

$$A = \sum_{j,k=1}^{4} \frac{|a_j|^2}{(p-k_1)^2 - m_{\tilde{\chi}_j^0}^2} \cdot \frac{|a_k|^2}{(p-k_1)^2 - m_{\tilde{\chi}_k^0}^2}. \tag{C.3}$$

Summing over the spins leads to

$$\sum_{\lambda_1,\lambda_2} |\mathcal{M}|^2 = A \left[m_{13}^2 m_{23}^2 - p^2 k_3^2 \right], \tag{C.4}$$

where

$$m_{13}^2 \equiv (p-k_2)^2 = (k_1+k_3)^2, \tag{C.5}$$

$$m_{23}^2 \equiv (p-k_1)^2 = (k_2+k_3)^2. \tag{C.6}$$

We neglected the lepton masses ($k_1^2, k_2^2 \approx 0$) in Eq. (C.4).

Now we turn to the decay $\tilde{\ell}_R^- \to \ell^- \ell'^- \tilde{\ell}_R'^+$. Its Feynman diagram is given in Fig. C.2. The amplitude, for each neutralino $\tilde{\chi}_j^0$ exchanged, is given by

$$i\mathcal{M} = (-ia_j^*)(-ia_j) \frac{i m_{\tilde{\chi}_j^0}}{(p-k_1)^2 - m_{\tilde{\chi}_j^0}^2} y_1 y_2, \tag{C.7}$$

which leads to the following expression for the total amplitude squared:

$$|\mathcal{M}|^2 = B\, y_1 y_2 y_2^\dagger y_1^\dagger, \tag{C.8}$$

with

$$B = \sum_{j,k=1}^{4} \frac{|a_j|^2 m_{\tilde{\chi}_j^0}}{(p-k_1)^2 - m_{\tilde{\chi}_j^0}^2} \frac{|a_k|^2 m_{\tilde{\chi}_k^0}}{(p-k_1)^2 - m_{\tilde{\chi}_k^0}^2}. \tag{C.9}$$

Taking the spin sums and then the trace, we arrive at

$$\sum_{\lambda_1,\lambda_2} |\mathcal{M}|^2 = B(-m_{13}^2 - m_{23}^2 + p^2 + k_3^2). \tag{C.10}$$

Here, the proportionality to the neutralino mass, $m_{\tilde{\chi}_j^0}$, is due to the helicity flip of the neutralino, *cf.* Fig. C.2.

C.2. Three-body slepton decay $\tilde{\tau}_1^- \to \tau^- \ell^\pm \tilde{\ell}_R^\mp$

Now we calculate the more complicated decays $\tilde{\tau}_1^- \to \tau^- \ell^\pm \tilde{\ell}_R^\mp$. The $\tilde{\tau}_1$ is a mixture of L- and R-type eigenstates and, in addition, we cannot neglect the Yukawa couplings for the third generation.

The Feynman diagrams for the decay $\tilde{\tau}_1^- \to \tau^- \ell^+ \tilde{\ell}_R^-$ are shown in Fig. C.3. The amplitudes for these two diagrams are

$$i\mathcal{M}_{\mathrm{I}} = (-ia_j^{\tilde{\tau}})(-ia_j^{\tilde{\ell}*})\, x_2^\dagger \frac{i(p-k_1)\cdot\bar{\sigma}}{(p-k_1)^2 - m_{\tilde{\chi}_j^0}^2} y_1, \tag{C.11}$$

$$i\mathcal{M}_{\mathrm{II}} = (ib_j^{\tilde{\tau}})(-ia_j^{\tilde{\ell}*}) \frac{i m_{\tilde{\chi}_j^0}}{(p-k_1)^2 - m_{\tilde{\chi}_j^0}^2}\, x_2^\dagger x_1^\dagger, \tag{C.12}$$

where we used the following abbreviations:

$$a_j^{\tilde{\ell}} \equiv \sqrt{2} g' N_{j1}, \tag{C.13}$$

$$a_j^{\tilde{\tau}} \equiv Y_\tau N_{j3} L_{\tilde{\tau}_1}^* + \sqrt{2} g' N_{j1} R_{\tilde{\tau}_1}^*, \tag{C.14}$$

$$b_j^{\tilde{\tau}} \equiv Y_\tau N_{j3}^* R_{\tilde{\tau}_1}^* - \frac{1}{\sqrt{2}}(g N_{j2}^* + g' N_{j1}^*) L_{\tilde{\tau}_1}^*. \tag{C.15}$$

The total amplitude squared is

$$\begin{aligned} |\mathcal{M}|^2 = \sum_{j,k=1}^{4} C_{jk} \Big[& a_j^{\tilde{\tau}} a_k^{\tilde{\tau}*} x_2^\dagger (p-k_1)\cdot\bar{\sigma} y_1 y_1^\dagger (p-k_1)\cdot\bar{\sigma} x_2 \\ & - \big[a_j^{\tilde{\tau}} b_k^{\tilde{\tau}*} m_{\tilde{\chi}_k^0} + a_k^{\tilde{\tau}} b_j^{\tilde{\tau}*} m_{\tilde{\chi}_j^0}\big] x_2^\dagger (p-k_1)\cdot\bar{\sigma} y_1 x_1 x_2 \\ & + b_j^{\tilde{\tau}} b_k^{\tilde{\tau}*} m_{\tilde{\chi}_j^0} m_{\tilde{\chi}_k^0} x_2^\dagger x_1^\dagger x_1 x_2 \Big], \end{aligned} \tag{C.16}$$

where

$$C_{jk} = \frac{a_j^{\tilde{\ell}*}}{(p-k_1)^2 - m_{\tilde{\chi}_j^0}^2} \cdot \frac{a_k^{\tilde{\ell}}}{(p-k_1)^2 - m_{\tilde{\chi}_k^0}^2}. \tag{C.17}$$

Summing over the spins of the final state leptons, we derive

$$\begin{aligned} \sum_{\lambda_1,\lambda_2} |\mathcal{M}|^2 = \sum_{j,k=1}^{4} C_{jk} \Big[& a_j^{\tilde{\tau}} a_k^{\tilde{\tau}*} \left((-m_{23}^2 + p^2 - k_1^2)(-m_{13}^2 + p^2) - (p^2 + k_3^2 - m_{13}^2 - m_{23}^2)(p^2 - k_1^2) \right) \\ & - \big[a_j^{\tilde{\tau}} b_k^{\tilde{\tau}*} m_{\tilde{\chi}_k^0} + a_k^{\tilde{\tau}} b_j^{\tilde{\tau}*} m_{\tilde{\chi}_j^0}\big] m_\tau (m_{23}^2 - k_3^2) + b_j^{\tilde{\tau}} b_k^{\tilde{\tau}*} m_{\tilde{\chi}_j^0} m_{\tilde{\chi}_k^0} (p^2 + k_3^2 - m_{13}^2 - m_{23}^2) \Big], \end{aligned} \tag{C.18}$$

where we have neglected the mass of the lepton ($k_2^2 \approx 0$) in Eq. (C.18).

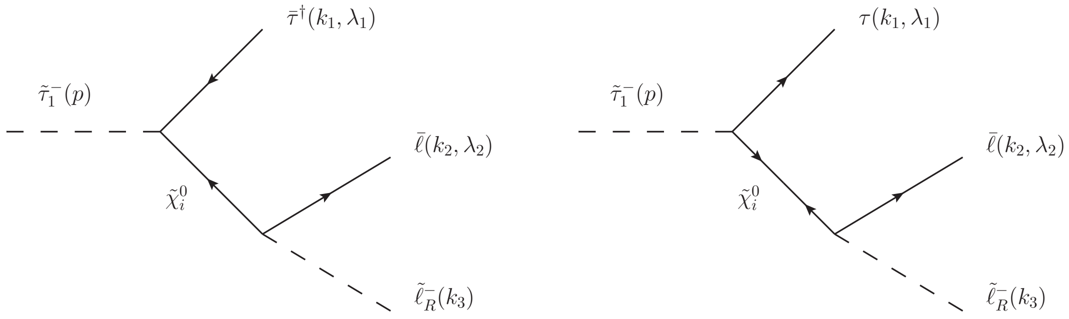

Figure C.3.: Feynman diagrams for the three-body slepton decay $\tilde{\tau}_1^- \to \tau^-\ell^+\tilde{\ell}_R^-$.

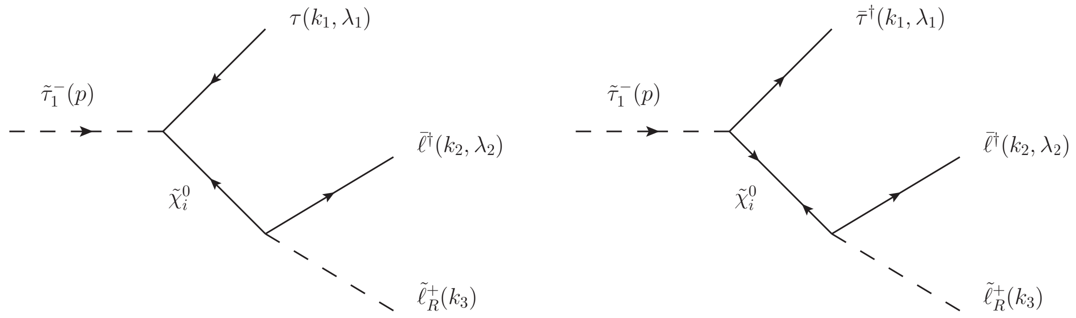

Figure C.4.: Feynman diagrams for the three-body slepton decay $\tilde{\tau}_1^- \to \tau^-\ell^-\tilde{\ell}_R^+$.

Now, we turn to the competing decay $\tilde{\tau}_1^- \to \tau^-\ell^-\tilde{\ell}_R^+$. The Feynman diagrams are shown in Fig. C.4. The amplitudes for these diagrams are

$$i\mathcal{M}_{\mathrm{I}} = (-ib_j^{\tilde{\tau}\,*})(-ia_j^{\tilde{\ell}\,*})\, x_2^\dagger \frac{i(p-k_1)\cdot\bar{\sigma}}{(p-k_1)^2 - m^2_{\tilde{\chi}^0_j}} y_1, \tag{C.19}$$

$$i\mathcal{M}_{\mathrm{II}} = (ia_j^{\tilde{\tau}\,*})(-ia_j^{\tilde{\ell}\,*}) \frac{im_{\tilde{\chi}^0_j}}{(p-k_1)^2 - m^2_{\tilde{\chi}^0_j}}\, x_2^\dagger x_1^\dagger. \tag{C.20}$$

This leads to an analogous calculation as for the decay $\tilde{\tau}_1^- \to \tau^-\ell^+\tilde{\ell}_R^-$ with interchanged coefficients $a_j^{\tilde{\tau}} \leftrightarrow b_j^{\tilde{\tau}\,*}$.

C.3. Resulting branching ratios in the $\tilde{\ell}_R$ LSP parameter space

In this section we study the previously calculated three-body slepton decays for the $\tilde{e}_R$ LSP parameter space in the $M_{1/2} - M_0$ plane. In Fig. C.5 we give the same parameter region as for the LHC discovery reach for $\sqrt{s} = 7$ TeV in Fig. 5.11, *i.e.* we chose the B$_3$ mSUGRA parameter $A_0 = -1250$ GeV, $\tan\beta = 5$, $\mathrm{sgn}(\mu) = +$ and $\lambda_{231}|_{\mathrm{GUT}} = 0.045$. Gray contour lines indicate sparticle mass differences that are relevant for the three-body slepton decay and are specified in the following for each subfigure. The values of the mass difference are indicated by the gray labels.

In Fig. C.5(a) we show the branching ratio for the right-handed smuon decay $\tilde{\mu}_R^- \to \mu^- e^- \tilde{e}_R^+$. The dashed (dotted) gray contour lines indicate the mass difference of the $\tilde{\mu}_R$ to the $\tilde{e}_R$ ($\tilde{\chi}_1^0$). In the shown $\tilde{e}_R$ LSP parameter region, the mass difference between $\tilde{\mu}_R$ and $\tilde{e}_R$ is more than 10 GeV, thus there is enough phase-space for the decays $\tilde{\mu}_R^- \to \mu^- e^\mp \tilde{e}_R^\pm$ to happen. In the white region, the $\tilde{\mu}_R$ is heavier than the $\tilde{\chi}_1^0$ and decays on-shell into the $\tilde{\chi}_1^0$. The branching ratio $\mathcal{B}(\tilde{\mu}_R^- \to \mu^- e^- \tilde{e}_R^+)$ increases with $M_{1/2}$ and is rather insensitive to M_0.

The decay $\tilde{\mu}_R^- \to \mu^- e^+ \tilde{e}_R^-$ behaves similarly to the decay $\tilde{\mu}_R^- \to \mu^- e^- \tilde{e}_R^+$. However, there is a asymmetry between these two decays, defined by

$$\mathcal{A}(\tilde{\mu}_R^- \to \mu^- e^\mp \tilde{e}_R^\pm) \equiv \frac{\mathcal{B}(\tilde{\mu}_R^- \to \mu^- e^- \tilde{e}_R^+) - \mathcal{B}(\tilde{\mu}_R^- \to \mu^- e^+ \tilde{e}_R^-)}{\mathcal{B}(\tilde{\mu}_R^- \to \mu^- e^- \tilde{e}_R^+) + \mathcal{B}(\tilde{\mu}_R^- \to \mu^- e^+ \tilde{e}_R^-)}, \tag{C.21}$$

due to the different results for the spin-summed squared matrix element, *cf.* Eq. (C.4) and (C.10). This asymmetry is shown in Fig. C.5(b). It is always positive and increases with increasing mass difference between the $\tilde{\chi}_1^0$ and the $\tilde{\mu}_R$.

The competing decay $\tilde{\mu}_R^- \to \mu^- \tau^- \tilde{\tau}_1^+$ is shown in Fig. C.5(c). Here, the dashed (dotted) gray contour lines give the mass difference of the $\tilde{\mu}_R$ to the $\tilde{\tau}_1$ ($\tilde{\chi}_1^0$). For light $\tilde{e}_R$ LSP scenarios, *i.e.* at $M_{1/2}$ values around 380 GeV, the $\tilde{\mu}_R$ decays in almost the same rate into the $\tilde{\tau}_1$ and the $\tilde{e}_R$ LSP. However, the branching ratios $\mathcal{B}(\tilde{\mu}_R^- \to \mu^- \tau^\mp \tilde{\tau}_1^\pm)$ decrease with increasing $M_{1/2}$, because then, the $\tilde{\tau}_1$ becomes more right-handed. Thus, at higher values of $M_{1/2}$ the $\tilde{\mu}_R$ prefers to decay into the $\tilde{e}_R$ LSP.

We give the asymmetry between the decays $\tilde{\mu}_R^- \to \mu^- \tau^- \tilde{\tau}_1^+$ and $\tilde{\mu}_R^- \to \mu^- \tau^+ \tilde{\tau}_1^-$, defined by

$$\mathcal{A}(\tilde{\mu}_R^- \to \mu^- \tau^\mp \tilde{\tau}_1^\pm) \equiv \frac{\mathcal{B}(\tilde{\mu}_R^- \to \mu^- \tau^- \tilde{\tau}_1^+) - \mathcal{B}(\tilde{\mu}_R^- \to \mu^- \tau^+ \tilde{\tau}_1^-)}{\mathcal{B}(\tilde{\mu}_R^- \to \mu^- \tau^- \tilde{\tau}_1^+) + \mathcal{B}(\tilde{\mu}_R^- \to \mu^- \tau^+ \tilde{\tau}_1^-)}, \tag{C.22}$$

in Fig. C.5(d). This asymmetry is positive for the shown $\tilde{e}_R$ LSP parameter space. As for $\mathcal{A}(\tilde{\mu}_R^- \to \mu^- e^\mp \tilde{e}_R^\pm)$, the asymmetry decreases with M_0, *i.e.* with decreasing mass difference between the $\tilde{\chi}_1^0$ and the $\tilde{\mu}_R$.

We present the branching ratio of the lightest stau decay $\tilde{\tau}_1^- \to \tau^- e^- \tilde{e}_R^+$ in Fig. C.5(e). The dashed (dotted) gray contour lines give the mass difference of the $\tilde{\tau}_1$ to the $\tilde{e}_R$ ($\tilde{\chi}_1^0$). Since the $\tilde{e}_R$ and $\tilde{\tau}_1$ are nearly mass degenerate for light $\tilde{e}_R$ scenarios, this decay becomes kinematically possible only for higher $M_{1/2}$ values. Here, the branching ratio severely depends on M_0. This is because there is also the competing R-parity violating decay $\tilde{\tau}_1 \to e \nu_\mu$ via the non-vanishing coupling λ_{231}. Thus, only for scenarios with a low mass difference between $\tilde{\chi}_1^0$ and $\tilde{\tau}_1$, the three-body decays $\tilde{\tau}_1^- \to \tau^- e^- \tilde{e}_R^+$ and $\tilde{\tau}_1^- \to \tau^- e^+ \tilde{e}_R^-$ become important. Again, we show the asymmetry of these two decays,

$$\mathcal{A}(\tilde{\tau}_1^- \to \tau^- e^\mp \tilde{e}_R^\pm) \equiv \frac{\mathcal{B}(\tilde{\tau}_1^- \to \tau^- e^- \tilde{e}_R^+) - \mathcal{B}(\tilde{\tau}_1^- \to \tau^- e^+ \tilde{e}_R^-)}{\mathcal{B}(\tilde{\tau}_1^- \to \tau^- e^- \tilde{e}_R^+) + \mathcal{B}(\tilde{\tau}_1^- \to \tau^- e^+ \tilde{e}_R^-)}, \tag{C.23}$$

in Fig. C.5(f). It behaves similar to the asymmetries for the $\tilde{\mu}_R$ decays, *i.e.* the asymmetry increases with increasing mass difference between the initial sparticle, $\tilde{\tau}_1$, and the intermediate sparticle, $\tilde{\chi}_1^0$. In Fig. C.5(f), the structure at low values of M_0 is due to numerical uncertainties, since the branching ratios $\mathcal{B}(\tilde{\tau}_1^- \to \tau^- e^\mp \tilde{e}_R^\pm)$ become very small.

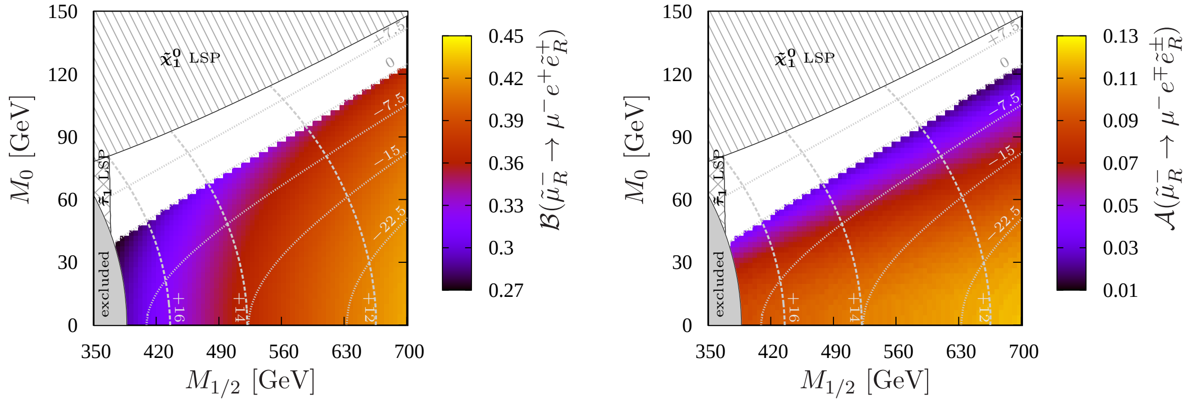

(a) Branching ratio $\mathcal{B}(\tilde{\mu}_R^- \to \mu^- e^+ \tilde{e}_R^+)$. The dotted and dashed contour lines give the mass difference $M_{\tilde{\mu}_R} - M_{\tilde{\chi}_1^0}$ and $M_{\tilde{\mu}_R} - M_{\tilde{e}_R}$, respectively.

(b) Asymmetry $\mathcal{A}(\tilde{\mu}_R^- \to \mu^- e^\mp \tilde{e}_R^\pm)$. The dotted and dashed contour lines give the mass difference $M_{\tilde{\mu}_R} - M_{\tilde{\chi}_1^0}$ and $M_{\tilde{\mu}_R} - M_{\tilde{e}_R}$, respectively.

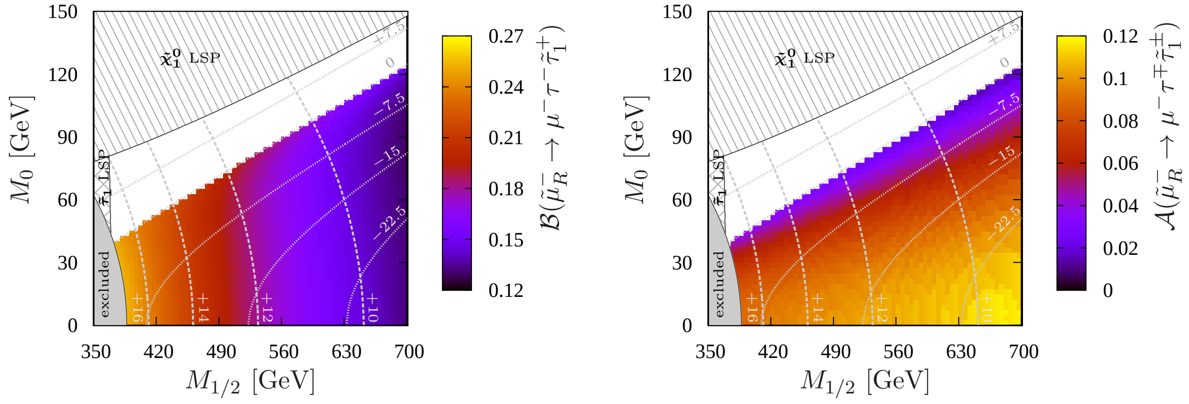

(c) Branching ratio $\mathcal{B}(\tilde{\mu}_R^- \to \mu^- \tau^- \tilde{\tau}_1^+)$. The dotted and dashed contour lines give the mass difference $M_{\tilde{\mu}_R} - M_{\tilde{\chi}_1^0}$ and $M_{\tilde{\mu}_R} - M_{\tilde{\tau}_1}$, respectively.

(d) Asymmetry $\mathcal{A}(\tilde{\mu}_R^- \to \mu^- \tau^\mp \tilde{\tau}_1^\pm)$. The dotted and dashed contour lines give the mass difference $M_{\tilde{\mu}_R} - M_{\tilde{\chi}_1^0}$ and $M_{\tilde{\mu}_R} - M_{\tilde{\tau}_1}$, respectively.

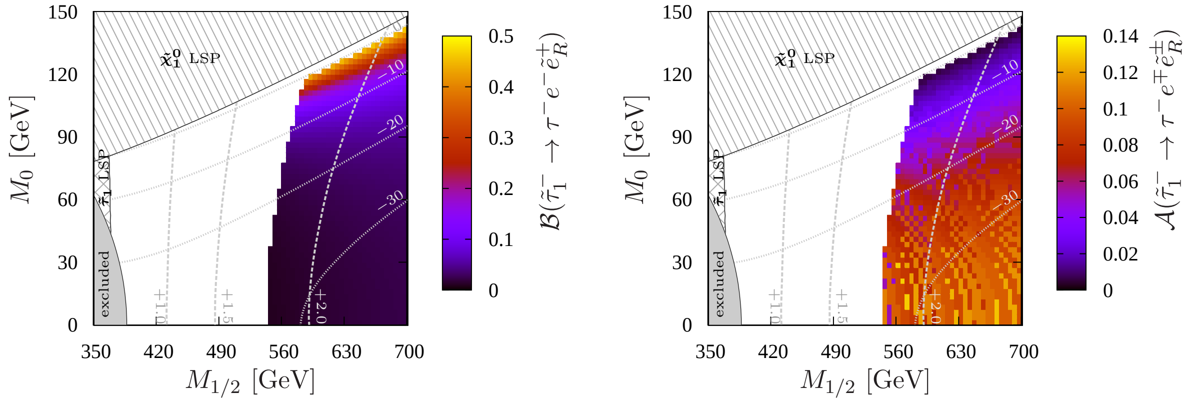

(e) Branching ratio $\mathcal{B}(\tilde{\tau}_1^- \to \tau^- e^- \tilde{e}_R^+)$. The dotted and dashed contour lines give the mass difference $M_{\tilde{\tau}_1} - M_{\tilde{\chi}_1^0}$ and $M_{\tilde{\tau}_1} - M_{\tilde{e}_R}$, respectively.

(f) Asymmetry $\mathcal{A}(\tilde{\tau}_1^- \to \tau^- e^\mp \tilde{e}_R^\pm)$. The dotted and dashed contour lines give the mass difference $M_{\tilde{\tau}_1} - M_{\tilde{\chi}_1^0}$ and $M_{\tilde{\tau}_1} - M_{\tilde{e}_R}$, respectively.

Figure C.5.: Branching ratios and asymmetries of three-body slepton decays, given in the $M_{1/2} - M_0$ plane for B$_3$ mSUGRA parameters $A_0 = -1250$ GeV, $\tan\beta = 5$, $\mathrm{sgn}(\mu) = +$ and $\lambda_{231}|_{\mathrm{GUT}} = 0.045$. Important mass differences between the involved sparticles are given by the gray contour lines.

Bibliography

[1] J. J. Thomson, *Cathode Rays*, Phil. Mag. **44** (1897) 293.

[2] A. Quadt, *Top quark physics at hadron colliders*, Eur. Phys. J. **C48** (2006) 835.

[3] The DONUT Collaboration, K. Kodama *et al.*, *Observation of tau-neutrino interactions*, Phys. Lett. **B504** (2001) 218, `hep-ex/0012035`.

[4] The DONuT Collaboration, K. Kodama *et al.*, *Final tau-neutrino results from the DONuT experiment*, Phys. Rev. **D78** (2008) 052002, `0711.0728`.

[5] A. Djouadi, *The Anatomy of electro-weak symmetry breaking. I: The Higgs boson in the standard model*, Phys. Rept. **457** (2008) 1, `hep-ph/0503172`.

[6] A. Djouadi, *The Anatomy of electro-weak symmetry breaking. II. The Higgs bosons in the minimal supersymmetric model*, Phys. Rept. **459** (2008) 1, `hep-ph/0503173`.

[7] H. E. Haber, *Present status and future prospects for a Higgs boson discovery at the Tevatron and LHC*, `1011.1038`.

[8] M. Drees, *An Introduction to supersymmetry*, `hep-ph/9611409`.

[9] G. Bertone, D. Hooper, and J. Silk, *Particle dark matter: Evidence, candidates and constraints*, Phys. Rept. **405** (2005) 279, `hep-ph/0404175`.

[10] R. N. Mohapatra *et al.*, *Theory of neutrinos: A white paper*, Rept. Prog. Phys. **70** (2007) 1757, `hep-ph/0510213`.

[11] M. Dine and A. Kusenko, *The Origin of the matter - antimatter asymmetry*, Rev.Mod.Phys. **76** (2004) 1, `hep-ph/0303065`.

[12] H. K. Dreiner and S. Grab, *All Possible Lightest Supersymmetric Particles in R-Parity Violating mSUGRA*, Phys. Lett. **B679** (2009) 45, `0811.0200`.

[13] R. M. Godbole, P. Roy, and X. Tata, *Tau signals of R-parity breaking at LEP-200*, Nucl. Phys. **B401** (1993) 67, `hep-ph/9209251`.

[14] H. K. Dreiner and G. G. Ross, *R-parity violation at hadron colliders*, Nucl. Phys. **B365** (1991) 597.

[15] H. K. Dreiner, P. Richardson, and M. H. Seymour, *Resonant slepton production in hadron hadron collisions*, Phys. Rev. **D63** (2001) 055008, `hep-ph/0007228`.

[16] A. Bartl, W. Porod, D. Restrepo, J. Romao, and J. W. F. Valle, *Neutralino phenomenology at LEP2 in supersymmetry with bilinear breaking of R-parity*, Nucl. Phys. **B600** (2001) 39, `hep-ph/0007157`.

[17] B. C. Allanach, A. Dedes, and H. K. Dreiner, *The R parity violating minimal supergravity model*, Phys. Rev. **D69** (2004) 115002, `hep-ph/0309196`.

[18] B. C. Allanach, M. A. Bernhardt, H. K. Dreiner, C. H. Kom, and P. Richardson, *Mass Spectrum in R-Parity Violating mSUGRA and Benchmark Points*, Phys. Rev. **D75** (2007) 035002, `hep-ph/0609263`.

[19] M. A. Bernhardt, H. K. Dreiner, S. Grab, and P. Richardson, *Single Slepton Production in association with a single Top Quark at the Tevatron and LHC*, Phys. Rev. **D78** (2008) 015016, `0802.1482`.

[20] K. Desch, S. Fleischmann, P. Wienemann, H. K. Dreiner, and S. Grab, *Stau as the Lightest Supersymmetric Particle in R-Parity Violating SUSY Models: Discovery Potential with Early LHC Data*, `1008.1580`.

[21] M. A. Bernhardt, S. P. Das, H. K. Dreiner, and S. Grab, *Sneutrino as Lightest Supersymmetric Particle in B_3 mSUGRA Models and Signals at the LHC*, Phys. Rev. **D79** (2009) 035003, `0810.3423`.

[22] S. L. Glashow, *Partial Symmetries of Weak Interactions*, Nucl. Phys. **22** (1961) 579.

[23] A. Salam and J. C. Ward, *Electromagnetic and weak interactions*, Phys. Lett. **13** (1964) 168.

[24] S. Weinberg, *A Model of Leptons*, Phys. Rev. Lett. **19** (1967) 1264.

[25] The UA1 Collaboration, G. Arnison *et al.*, *Experimental observation of isolated large transverse energy electrons with associated missing energy at s**(1/2) = 540-GeV*, Phys. Lett. **B122** (1983) 103.

[26] The UA1 Collaboration, G. Arnison *et al.*, *Experimental observation of lepton pairs of invariant mass around 95-GeV/c**2 at the CERN SPS collider*, Phys. Lett. **B126** (1983) 398.

[27] The Super-Kamiokande Collaboration, Y. Fukuda *et al.*, *Measurement of the flux and zenith-angle distribution of upward through-going muons by Super-Kamiokande*, Phys. Rev. Lett. **82** (1999) 2644, `hep-ex/9812014`.

[28] The Super-Kamiokande Collaboration, Y. Fukuda *et al.*, *Measurements of the solar neutrino flux from Super- Kamiokande's first 300 days*, Phys. Rev. Lett. **81** (1998) 1158, `hep-ex/9805021`.

[29] The SNO Collaboration, Q. R. Ahmad *et al.*, *Direct evidence for neutrino flavor transformation from neutral-current interactions in the Sudbury Neutrino Observatory*, Phys. Rev. Lett. **89** (2002) 011301, `nucl-ex/0204008`.

[30] The SNO Collaboration, B. Aharmim *et al.*, *Electron energy spectra, fluxes, and day-night asymmetries of B-8 solar neutrinos from the 391-day salt phase SNO data set*, Phys. Rev. **C72** (2005) 055502, `nucl-ex/0502021`.

[31] The CHOOZ Collaboration, M. Apollonio *et al.*, *Search for neutrino oscillations on a long base-line at the CHOOZ nuclear power station*, Eur. Phys. J. **C27** (2003) 331, `hep-ex/0301017`.

[32] B. T. Cleveland *et al.*, *Measurement of the solar electron neutrino flux with the Homestake chlorine detector*, Astrophys. J. **496** (1998) 505.

[33] M. C. Gonzalez-Garcia and M. Maltoni, *Phenomenology with Massive Neutrinos*, Phys. Rept. **460** (2008) 1, `0704.1800`.

[34] M. C. Gonzalez-Garcia, M. Maltoni, and J. Salvado, *Updated global fit to three neutrino mixing: status of the hints of theta13 > 0*, JHEP **04** (2010) 056, `1001.4524`.

[35] The Muon G-2 Collaboration, G. W. Bennett *et al.*, *Final report of the muon E821 anomalous magnetic moment measurement at BNL*, Phys. Rev. **D73** (2006) 072003, `hep-ex/0602035`.

[36] J. P. Miller, E. de Rafael, and B. L. Roberts, *Muon g-2: Review of Theory and Experiment*, Rept. Prog. Phys. **70** (2007) 795, `hep-ph/0703049`.

[37] D. Stockinger, *The muon magnetic moment and supersymmetry*, J. Phys. **G34** (2007) R45, `hep-ph/0609168`.

[38] D. Stockinger, $(g-2)_\mu$ *and supersymmetry: status and prospects*, `0710.2429`.

[39] M. E. Peskin and D. V. Schroeder, *An Introduction To Quantum Field Theory (Frontiers in Physics)*, Westview Press, (1995).

[40] P. W. Higgs, *Broken symmetries, massless particles and gauge fields*, Phys. Lett. **12** (1964) 132.

[41] P. W. Higgs, *BROKEN SYMMETRIES AND THE MASSES OF GAUGE BOSONS*, Phys. Rev. Lett. **13** (1964) 508.

[42] P. W. Higgs, *Spontaneous Symmetry Breakdown without Massless Bosons*, Phys. Rev. **145** (1966) 1156.

[43] F. Englert and R. Brout, *BROKEN SYMMETRY AND THE MASS OF GAUGE VECTOR MESONS*, Phys. Rev. Lett. **13** (1964) 321.

[44] T. W. B. Kibble, *Symmetry breaking in non-Abelian gauge theories*, Phys. Rev. **155** (1967) 1554.

[45] T.-P. Cheng and L.-F. Li, *Gauge theory of elementary particle physics*, Clarendon Press, Oxford, (1984).

[46] T. Kugo, *Eichtheorie*, Springer-Verlag, Berlin, (1997).

[47] S. Mele, *Measurements of the running of the electromagnetic coupling at LEP*, `hep-ex/0610037`.

[48] M. Girone and M. Neubert, *Measuring alpha(s) (Q**2) in tau decays*, `hep-ph/9605274`.

[49] G. 't Hooft, *Computation of the quantum effects due to a four- dimensional pseudoparticle*, Phys. Rev. **D14** (1976) 3432.

[50] G. 't Hooft, *Symmetry breaking through Bell-Jackiw anomalies*, Phys. Rev. Lett. **37** (1976) 8.

[51] S. King, *Neutrino mass*, Contemp.Phys. (2007), `0712.1750`.

[52] A. Zee, *A Theory of Lepton Number Violation, Neutrino Majorana Mass, and Oscillation*, Phys. Lett. **B93** (1980) 389.

[53] H. Georgi and S. L. Glashow, *Unity of All Elementary Particle Forces*, Phys. Rev. Lett. **32** (1974) 438.

[54] H. Fritzsch and P. Minkowski, *Unified Interactions of Leptons and Hadrons*, Ann. Phys. **93** (1975) 193.

[55] D. Bailin and A. Love, *Supersymmetric Gauge Field Theory and String Theory*, Taylor & Francis, (1994).

[56] M. Green, J. Schwarz, and E. Witten, *Superstring Theory: Volume 1, Introduction*, Cambridge University Press, (1988).

[57] P. J. E. Peebles and B. Ratra, *The cosmological constant and dark energy*, Rev. Mod. Phys. **75** (2003) 559, `astro-ph/0207347`.

[58] S. P. Martin, *A Supersymmetry Primer*, `hep-ph/9709356`.

[59] M. Drees, R. M. Godbole, and P. Roy, *Theory and Phenomenology of Sparticles*, World Scientific Publishing Co. Pte. Ltd., (2004).

[60] I. Aitchison, *Supersymmetry in Particle Physics, An Elementary Introduction*, Cambridge University Press, (2007).

[61] J. Wess and J. Bagger, *Supersymmetry and Supergravity*, Princeton University Press, (1992).

[62] H. P. Nilles, *Supersymmetry, Supergravity and Particle Physics*, Phys. Rept. **110** (1984) 1.

[63] H. E. Haber and G. L. Kane, *The Search for Supersymmetry: Probing Physics Beyond the Standard Model*, Phys. Rept. **117** (1985) 75.

[64] E. Gildener, *Gauge Symmetry Hierarchies*, Phys. Rev. **D14** (1976) 1667.

[65] M. J. G. Veltman, *The Infrared - Ultraviolet Connection*, Acta Phys. Polon. **B12** (1981) 437.

[66] E. Witten, *Dynamical Breaking of Supersymmetry*, Nucl. Phys. **B188** (1981) 513.

[67] C. T. Hill and E. H. Simmons, *Strong dynamics and electroweak symmetry breaking*, Phys. Rept. **381** (2003) 235, `hep-ph/0203079`.

[68] J. G. Wacker, *Little Higgs models: New approaches to the hierarchy problem*, `hep-ph/0208235`.

[69] N. Arkani-Hamed, S. Dimopoulos, and G. R. Dvali, *The hierarchy problem and new dimensions at a millimeter*, Phys. Lett. **B429** (1998) 263, `hep-ph/9803315`.

[70] N. Arkani-Hamed, S. Dimopoulos, and G. R. Dvali, *Phenomenology, astrophysics and cosmology of theories with sub-millimeter dimensions and TeV scale quantum gravity*, Phys. Rev. **D59** (1999) 086004, `hep-ph/9807344`.

[71] L. Randall and R. Sundrum, *A large mass hierarchy from a small extra dimension*, Phys. Rev. Lett. **83** (1999) 3370, `hep-ph/9905221`.

[72] G. Quast, *Global fit to electroweak precision data*, Eur. Phys. J. **C33** (2004) s641.

[73] H. Flacher *et al.*, *Gfitter - Revisiting the Global Electroweak Fit of the Standard Model and Beyond*, Eur. Phys. J. **C60** (2009) 543, `0811.0009`.

[74] The Gfitter Collaboration, J. Haller, *Fits of the Electroweak Standard Model and Beyond using Gfitter*, `0810.3664`.

[75] The Gfitter Collaboration, A. Hoecker, *Status of the global electroweak fit of the Standard Model*, PoS **EPS-HEP2009** (2009) 366, `0909.0961`.

[76] S. R. Coleman and J. Mandula, *ALL POSSIBLE SYMMETRIES OF THE S MATRIX*, Phys. Rev. **159** (1967) 1251.

[77] R. Haag, J. T. Lopuszanski, and M. Sohnius, *All Possible Generators of Supersymmetries of the s Matrix*, Nucl. Phys. **B88** (1975) 257.

[78] R. L. Arnowitt, P. Nath, and B. Zumino, *Superfield Densities and Action Principle in Curved Superspace*, Phys. Lett. **B56** (1975) 81.

[79] P. Nath and R. L. Arnowitt, *Generalized Supergauge Symmetry as a New Framework for Unified Gauge Theories*, Phys. Lett. **B56** (1975) 177.

[80] S. Deser and B. Zumino, *Consistent Supergravity*, Phys. Lett. **B62** (1976) 335.

[81] D. Z. Freedman, P. van Nieuwenhuizen, and S. Ferrara, *Progress Toward a Theory of Supergravity*, Phys. Rev. **D13** (1976) 3214.

[82] D. Z. Freedman and P. van Nieuwenhuizen, *Properties of Supergravity Theory*, Phys. Rev. **D14** (1976) 912.

[83] E. Cremmer *et al.*, *Spontaneous Symmetry Breaking and Higgs Effect in Supergravity Without Cosmological Constant*, Nucl. Phys. **B147** (1979) 105.

[84] E. Cremmer, S. Ferrara, L. Girardello, and A. Van Proeyen, *Yang-Mills Theories with Local Supersymmetry: Lagrangian, Transformation Laws and SuperHiggs Effect*, Nucl. Phys. **B212** (1983) 413.

[85] J. R. Ellis, S. Kelley, and D. V. Nanopoulos, *Probing the desert using gauge coupling unification*, Phys. Lett. **B260** (1991) 131.

[86] U. Amaldi, W. de Boer, and H. Furstenau, *Comparison of grand unified theories with electroweak and strong coupling constants measured at LEP*, Phys. Lett. **B260** (1991) 447.

[87] P. Langacker and M.-x. Luo, *Implications of precision electroweak experiments for M_t, ρ_0, $\sin^2\theta_W$ and grand unification*, Phys. Rev. **D44** (1991) 817.

[88] P. Langacker and N. Polonsky, *Uncertainties in coupling constant unification*, Phys. Rev. **D47** (1993) 4028, `hep-ph/9210235`.

[89] G. G. Ross and R. G. Roberts, *Minimal supersymmetric unification predictions*, Nucl. Phys. **B377** (1992) 571.

[90] L. E. Ibanez and G. G. Ross, *SU(2)-L x U(1) Symmetry Breaking as a Radiative Effect of Supersymmetry Breaking in Guts*, Phys. Lett. **B110** (1982) 215.

[91] J. R. Ellis, J. S. Hagelin, D. V. Nanopoulos, K. A. Olive, and M. Srednicki, *Supersymmetric relics from the big bang*, Nucl. Phys. **B238** (1984) 453.

[92] L. J. Hall and M. Suzuki, *Explicit R-Parity Breaking in Supersymmetric Models*, Nucl. Phys. **B231** (1984) 419.

[93] Y. Grossman and H. E. Haber, *(S)neutrino properties in R-parity violating supersymmetry. I: CP-conserving phenomena*, Phys. Rev. **D59** (1999) 093008, `hep-ph/9810536`.

[94] Y. Grossman and H. E. Haber, *Neutrino masses and sneutrino mixing in R-parity violating supersymmetry*, `hep-ph/9906310`.

[95] F. Borzumati, Y. Grossman, E. Nardi, and Y. Nir, *Neutrino masses and mixing in supersymmetric models without R parity*, Phys. Lett. **B384** (1996) 123, `hep-ph/9606251`.

[96] S. Davidson and M. Losada, *Basis independent neutrino masses in the R(p) violating MSSM*, Phys. Rev. **D65** (2002) 075025, `hep-ph/0010325`.

[97] P. Minkowski, *mu → e gamma at a Rate of One Out of 1-Billion Muon Decays?*, Phys. Lett. **B67** (1977) 421.

[98] T. Yanagida, *Horizontal gauge symmetry and masses of neutrinos*, In Proceedings of the Workshop on the Baryon Number of the Universe and Unified Theories, Tsukuba, Japan, 13-14 Feb 1979.

[99] R. N. Mohapatra and G. Senjanovic, *Neutrino mass and spontaneous parity nonconservation*, Phys. Rev. Lett. **44** (1980) 912.

[100] M. Gell-Mann, P. Ramond, and R. Slansky, *COMPLEX SPINORS AND UNIFIED THEORIES*, Print-80-0576 (CERN).

[101] R. N. Mohapatra and G. Senjanovic, *Neutrino Masses and Mixings in Gauge Models with Spontaneous Parity Violation*, Phys. Rev. **D23** (1981) 165.

[102] A. Collaboration, *ATLAS detector and physics performance. Technical design report. Vol. 2*, CERN-LHCC-99-15.

[103] The CMS Collaboration, G. L. Bayatian *et al.*, *CMS technical design report, volume II: Physics performance*, J. Phys. **G34** (2007) 995.

[104] The CDF Collaboration, T. Adams, *SUSY Searches at the Tevatron*, `0808.0728`.

[105] H. E. Haber, *Introductory low-energy supersymmetry*, `hep-ph/9306207`.

[106] J. F. Gunion and H. E. Haber, *Higgs Bosons in Supersymmetric Models. 1*, Nucl. Phys. **B272** (1986) 1.

[107] F. Gabbiani, E. Gabrielli, A. Masiero, and L. Silvestrini, *A complete analysis of FCNC and CP constraints in general SUSY extensions of the standard model*, Nucl. Phys. **B477** (1996) 321, `hep-ph/9604387`.

[108] S. Jager, *Supersymmetry beyond minimal flavour violation*, Eur. Phys. J. **C59** (2009) 497, `0808.2044`.

[109] S. Weinberg, *Supersymmetry at Ordinary Energies. 1. Masses and Conservation Laws*, Phys. Rev. **D26** (1982) 287.

[110] N. Sakai and T. Yanagida, *Proton Decay in a Class of Supersymmetric Grand Unified Models*, Nucl. Phys. **B197** (1982) 533.

[111] S. Dimopoulos, S. Raby, and F. Wilczek, *Proton Decay in Supersymmetric Models*, Phys. Lett. **B112** (1982) 133.

[112] A. Y. Smirnov and F. Vissani, *Large R-parity violating couplings and grand unification*, Nucl. Phys. **B460** (1996) 37, `hep-ph/9506416`.

[113] H. K. Dreiner, *An introduction to explicit R-parity violation*, `hep-ph/9707435`.

[114] G. Bhattacharyya and P. B. Pal, *Upper bounds on all R-parity-violating lambda lambda" combinations from proton stability*, Phys. Rev. **D59** (1999) 097701, `hep-ph/9809493`.

[115] R. Barbier *et al.*, *R-parity violating supersymmetry*, Phys. Rept. **420** (2005) 1, `hep-ph/0406039`.

[116] The Super-Kamiokande Collaboration, Y. Hayato *et al.*, *Search for proton decay through $p \to \bar{\nu} K^+$ in a large water Cherenkov detector*, Phys. Rev. Lett. **83** (1999) 1529, `hep-ex/9904020`.

[117] The Super-Kamiokande Collaboration, M. Shiozawa *et al.*, *Search for Proton Decay via $p \to e^+ \pi^0$ in a Large Water Cherenkov Detector*, Phys. Rev. Lett. **81** (1998) 3319, `hep-ex/9806014`.

[118] The Particle Data Group Collaboration, C. Amsler *et al.*, *Review of particle physics*, Phys. Lett. **B667** (2008) 1.

[119] L. M. Krauss and F. Wilczek, *Discrete Gauge Symmetry in Continuum Theories*, Phys. Rev. Lett. **62** (1989) 1221.

[120] S. Lola and G. G. Ross, *Baryon and lepton number (non)conservation in supersymmetric theories*, Phys. Lett. **B314** (1993) 336.

[121] D. J. Castano and S. P. Martin, *Discrete symmetries and isosinglet quarks in low-energy supersymmetry*, Phys. Lett. **B340** (1994) 67, `hep-ph/9408230`.

[122] L. E. Ibanez and G. G. Ross, *Discrete gauge symmetry anomalies*, Phys. Lett. **B260** (1991) 291.

[123] L. E. Ibanez and G. G. Ross, *Discrete gauge symmetries and the origin of baryon and lepton number conservation in supersymmetric versions of the standard model*, Nucl. Phys. **B368** (1992) 3.

[124] H. K. Dreiner, C. Luhn, and M. Thormeier, *What is the discrete gauge symmetry of the MSSM?*, Phys. Rev. **D73** (2006) 075007, `hep-ph/0512163`.

[125] H. K. Dreiner, C. Luhn, H. Murayama, and M. Thormeier, *Baryon Triality and Neutrino Masses from an Anomalous Flavor U(1)*, Nucl. Phys. **B774** (2007) 127, `hep-ph/0610026`.

[126] M. C. Bento, L. J. Hall, and G. G. Ross, *Generalized Matter Parities from the Superstring*, Nucl. Phys. **B292** (1987) 400.

[127] L. Girardello and M. T. Grisaru, *Soft Breaking of Supersymmetry*, Nucl. Phys. **B194** (1982) 65.

[128] H. E. Haber, *The status of the minimal supersymmetric standard model and beyond*, Nucl. Phys. Proc. Suppl. **62** (1998) 469, `hep-ph/9709450`.

[129] F. Gabbiani and A. Masiero, *FCNC in Generalized Supersymmetric Theories*, Nucl. Phys. **B322** (1989) 235.

[130] The MEGA Collaboration, M. L. Brooks *et al.*, *New Limit for the Family-Number Non-conserving Decay* $\mu^+ \to e^+\gamma$, Phys. Rev. Lett. **83** (1999) 1521, `hep-ex/9905013`.

[131] M. Ciuchini *et al.*, *Delta M(K) and epsilon(K) in SUSY at the next-to-leading order*, JHEP **10** (1998) 008, `hep-ph/9808328`.

[132] D. Becirevic *et al.*, $B_d - \bar{B}_d$ *mixing and the* $B_d \to J/\psi K_s$ *asymmetry in general SUSY models*, Nucl. Phys. **B634** (2002) 105, `hep-ph/0112303`.

[133] J. Foster, K.-i. Okumura, and L. Roszkowski, *New constraints on SUSY flavour mixing in light of recent measurements at the Tevatron*, Phys. Lett. **B641** (2006) 452, `hep-ph/0604121`.

[134] L. Silvestrini, *Searching for new physics in* $b \to s$ *hadronic penguin decays*, Ann. Rev. Nucl. Part. Sci. **57** (2007) 405, `0705.1624`.

[135] S. Dimopoulos and D. W. Sutter, *The Supersymmetric flavor problem*, Nucl. Phys. **B452** (1995) 496, `hep-ph/9504415`.

[136] J. R. Ellis, S. Ferrara, and D. V. Nanopoulos, *CP Violation and Supersymmetry*, Phys. Lett. **B114** (1982) 231.

[137] W. Buchmuller and D. Wyler, *CP Violation and R Invariance in Supersymmetric Models of Strong and Electroweak Interactions*, Phys. Lett. **B121** (1983) 321.

[138] J. Polchinski and M. B. Wise, *The Electric Dipole Moment of the Neutron in Low-Energy Supergravity*, Phys. Lett. **B125** (1983) 393.

[139] F. del Aguila, M. B. Gavela, J. A. Grifols, and A. Mendez, *Specifically Supersymmetric Contribution to Electric Dipole Moments*, Phys. Lett. **B126** (1983) 71.

[140] D. V. Nanopoulos and M. Srednicki, *THE DEMON OF LOCAL SUSY*, Phys. Lett. **B128** (1983) 61.

[141] T. Ibrahim and P. Nath, *CP violation from standard model to strings*, Rev. Mod. Phys. **80** (2008) 577, `0705.2008`.

[142] T. Falk, K. A. Olive, M. Pospelov, and R. Roiban, *MSSM predictions for the electric dipole moment of the Hg- 199 atom*, Nucl. Phys. **B560** (1999) 3, `hep-ph/9904393`.

[143] A. G. Cohen, D. B. Kaplan, and A. E. Nelson, *The more minimal supersymmetric standard model*, Phys. Lett. **B388** (1996) 588, `hep-ph/9607394`.

[144] J. D. Wells, *Implications of supersymmetry breaking with a little hierarchy between gauginos and scalars*, `hep-ph/0306127`.

[145] N. Arkani-Hamed and S. Dimopoulos, *Supersymmetric unification without low energy supersymmetry and signatures for fine-tuning at the LHC*, JHEP **06** (2005) 073, `hep-th/0405159`.

[146] Y. Nir and N. Seiberg, *Should squarks be degenerate?*, Phys. Lett. **B309** (1993) 337, `hep-ph/9304307`.

[147] G. D. Kribs, E. Poppitz, and N. Weiner, *Flavor in supersymmetry with an extended R-symmetry*, Phys. Rev. **D78** (2008) 055010, `0712.2039`.

[148] A. E. Blechman and S.-P. Ng, *QCD Corrections to K-Kbar Mixing in R-symmetric Supersymmetric Models*, JHEP **06** (2008) 043, `0803.3811`.

[149] S. Dimopoulos and H. Georgi, *Softly Broken Supersymmetry and SU(5)*, Nucl. Phys. **B193** (1981) 150.

[150] R. N. Mohapatra, *Unification and supersymmetry*, `hep-ph/9911272`.

[151] P. H. Chankowski, O. Lebedev, and S. Pokorski, *Flavour violation in general supergravity*, Nucl. Phys. **B717** (2005) 190, `hep-ph/0502076`.

[152] A. Dedes and P. Slavich, *Two-loop corrections to radiative electroweak symmetry breaking in the MSSM. ((U))*, Nucl. Phys. **B657** (2003) 333, `hep-ph/0212132`.

[153] A. H. Chamseddine, R. L. Arnowitt, and P. Nath, *Locally Supersymmetric Grand Unification*, Phys. Rev. Lett. **49** (1982) 970.

[154] R. Barbieri, S. Ferrara, and C. A. Savoy, *Gauge Models with Spontaneously Broken Local Supersymmetry*, Phys. Lett. **B119** (1982) 343.

[155] L. J. Hall, J. D. Lykken, and S. Weinberg, *Supergravity as the Messenger of Supersymmetry Breaking*, Phys. Rev. **D27** (1983) 2359.

[156] S. K. Soni and H. A. Weldon, *Analysis of the Supersymmetry Breaking Induced by N=1 Supergravity Theories*, Phys. Lett. **B126** (1983) 215.

[157] S. P. Martin and M. T. Vaughn, *Two loop renormalization group equations for soft supersymmetry breaking couplings*, Phys. Rev. **D50** (1994) 2282, `hep-ph/9311340`.

[158] M. Drees and S. P. Martin, *Implications of SUSY model building*, `hep-ph/9504324`.

[159] L. E. Ibanez, C. Lopez, and C. Munoz, *The Low-Energy Supersymmetric Spectrum According to N=1 Supergravity Guts*, Nucl. Phys. **B256** (1985) 218.

[160] T. Hebbeker, *Can the sneutrino be the lightest supersymmetric particle?*, Phys. Lett. **B470** (1999) 259, `hep-ph/9910326`.

[161] B. de Carlos and P. L. White, *R-parity Violation Effects through Soft Supersymmetry Breaking Terms and the Renormalisation Group*, Phys. Rev. **D54** (1996) 3427, `hep-ph/9602381`.

[162] H. K. Dreiner and H. Pois, *Two Loop supersymmetric renormalization group equations including R-parity violation and aspects of unification*, `hep-ph/9511444`.

[163] E. Nardi, *Renormalization group induced neutrino masses in supersymmetry without R-parity*, Phys. Rev. **D55** (1997) 5772, `hep-ph/9610540`.

[164] J. R. Ellis, G. Gelmini, C. Jarlskog, G. G. Ross, and J. W. F. Valle, *Phenomenology of Supersymmetry with Broken R-Parity*, Phys. Lett. **B150** (1985) 142.

[165] T. Banks, Y. Grossman, E. Nardi, and Y. Nir, *Supersymmetry without R-parity and without lepton number*, Phys. Rev. **D52** (1995) 5319, `hep-ph/9505248`.

[166] H. K. Dreiner, M. Hanussek, and S. Grab, *Bounds on R-parity Violating Couplings at the Grand Unification Scale from Neutrino Masses*, Phys. Rev. **D82** (2010) 055027, `1005.3309`.

[167] M. Cirelli and A. Strumia, *Cosmology of neutrinos and extra light particles after WMAP3*, JCAP **0612** (2006) 013, `astro-ph/0607086`.

[168] A. Goobar, S. Hannestad, E. Mortsell, and H. Tu, *A new bound on the neutrino mass from the SDSS baryon acoustic peak*, JCAP **0606** (2006) 019, `astro-ph/0602155`.

[169] M. Chemtob, *Phenomenological constraints on broken R parity symmetry in supersymmetry models*, Prog. Part. Nucl. Phys. **54** (2005) 71, `hep-ph/0406029`.

[170] Y. Kao and T. Takeuchi, *Single-Coupling Bounds on R-parity violating Supersymmetry, an update*, `0910.4980`.

[171] B. C. Allanach, A. Dedes, and H. K. Dreiner, *Bounds on R-parity violating couplings at the weak scale and at the GUT scale*, Phys. Rev. **D60** (1999) 075014, `hep-ph/9906209`.

[172] B. C. Allanach, A. Dedes, and H. K. Dreiner, *Two loop supersymmetric renormalization group equations including R-parity violation and aspects of unification*, Phys. Rev. **D60** (1999) 056002, `hep-ph/9902251`.

[173] V. D. Barger, M. S. Berger, R. J. N. Phillips, and T. Wohrmann, *Renormalization group evolution of R-parity violating Yukawa couplings*, Phys. Rev. **D53** (1996) 6407, `hep-ph/9511473`.

[174] The L3 Collaboration, M. Acciarri *et al.*, *Search for R-parity breaking sneutrino exchange at LEP*, Phys. Lett. **B414** (1997) 373.

[175] G. Moreau, E. Perez, and G. Polesello, *Resonant sneutrino production in supersymmetry with R- parity violation at the LHC*, Nucl. Phys. **B604** (2001) 3, `hep-ph/0003012`.

[176] H. K. Dreiner, S. Grab, and M. K. Trenkel, *Sτ LSP Phenomenology: Two versus Four-Body Decay Modes. Example: Resonant Single Slepton Production at the LHC*, Phys. Rev. **D79** (2009) 016002, `0808.3079`.

[177] E. J. Chun and H. B. Kim, *Nonthermal axino as cool dark matter in supersymmetric standard model without R-parity*, Phys. Rev. **D60** (1999) 095006, `hep-ph/9906392`.

[178] K. Choi, E. J. Chun, and K. Hwang, *Axino as a sterile neutrino and R parity violation*, Phys. Rev. **D64** (2001) 033006, `hep-ph/0101026`.

[179] H.-B. Kim and J. E. Kim, *Late decaying axino as CDM and its lifetime bound*, Phys. Lett. **B527** (2002) 18, `hep-ph/0108101`.

[180] E. J. Chun and H. B. Kim, *Axino Light Dark Matter and Neutrino Masses with R-parity Violation*, JHEP **10** (2006) 082, `hep-ph/0607076`.

[181] L. Covi and J. E. Kim, *Axinos as Dark Matter Particles*, New J. Phys. **11** (2009) 105003, `0902.0769`.

[182] W. Buchmuller, L. Covi, K. Hamaguchi, A. Ibarra, and T. Yanagida, *Gravitino dark matter in R-parity breaking vacua*, JHEP **03** (2007) 037, `hep-ph/0702184`.

[183] C. C. Jean-Louis and G. Moreau, *Dark matter and neutrino masses in the R-parity violating NMSSM*, J. Phys. **G37** (2010) 105015, `0911.3640`.

[184] H.-S. Lee, C. Luhn, and K. T. Matchev, *Discrete gauge symmetries and proton stability in the U(1)'-extended MSSM*, JHEP **07** (2008) 065, `0712.3505`.

[185] H.-S. Lee, K. T. Matchev, and T. T. Wang, *A U(1) -prime solution to the μ^- problem and the proton decay problem in supersymmetry without R-parity*, Phys. Rev. **D77** (2008) 015016, `0709.0763`.

[186] The R parity Working Group Collaboration, B. Allanach *et al.*, *Searching for R parity violation at Run II of the Tevatron*, `hep-ph/9906224`.

[187] H. K. Dreiner and S. Grab, *All Possible Lightest Supersymmetric Particles in R-Parity Violating mSUGRA Models and their Signals at the LHC*, AIP Conf. Proc. **1200** (2010) 358, `0909.5407`.

[188] B. C. Allanach, *SOFTSUSY: A C++ program for calculating supersymmetric spectra*, Comput. Phys. Commun. **143** (2002) 305, `hep-ph/0104145`.

[189] B. C. Allanach and M. A. Bernhardt, *Including R-parity violation in the numerical computation of the spectrum of the minimal supersymmetric standard model: SOFTSUSY3.0*, Comput. Phys. Commun. **181** (2010) 232, `0903.1805`.

[190] The Heavy Flavor Averaging Group *et al.*, *Averages of b-hadron, c-hadron, and tau-lepton Properties*, `1010.1589`.

[191] The CDF and D0 Collaboration, M. J. Morello, *Flavor Changing Neutral Current at the Tevatron*, PoS **BEAUTY2009** (2009) 048, `0912.2446`.

[192] G. Belanger, F. Boudjema, A. Pukhov, and A. Semenov, *Dark matter direct detection rate in a generic model with micrOMEGAs2.1*, Comput. Phys. Commun. **180** (2009) 747, `0803.2360`.

[193] The LEP Working Group for Higgs boson searches Collaboration, R. Barate *et al.*, *Search for the standard model Higgs boson at LEP*, Phys. Lett. **B565** (2003) 61, `hep-ex/0306033`.

[194] E. Eichten, I. Hinchliffe, K. D. Lane, and C. Quigg, *Super Collider Physics*, Rev. Mod. Phys. **56** (1984) 579.

[195] The ATLAS Collaboration, G. Aad *et al.*, *Expected Performance of the ATLAS Experiment - Detector, Trigger and Physics*, `0901.0512`.

[196] The D0 Collaboration, V. M. Abazov *et al.*, *Search for associated production of charginos and neutralinos in the trilepton final state using 2.3 fb-1 of data*, Phys. Lett. **B680** (2009) 34, `0901.0646`.

[197] The CDF Collaboration, T. Aaltonen *et al.*, *Search for Supersymmetry in* $p\bar{p}$ *Collisions at* $\sqrt{s} = 1.96$*-TeV Using the Trilepton Signature of Chargino-Neutralino Production*, Phys. Rev. Lett. **101** (2008) 251801, `0808.2446`.

[198] The CDF Collaboration, R. Forrest, *Search for Supersymmetry in* $p\overline{p}$ *Collisions at* $\sqrt{s} = 1.96$ *TeV Using the Trilepton Signature of Chargino-Neutralino Production*, `0910.1931`.

[199] The CDF Collaboration, A. Abulencia *et al.*, *Inclusive search for new physics with like-sign dilepton events in* $p\bar{p}$ *collisions at* $\sqrt{s} = 1.96$*- TeV*, Phys. Rev. Lett. **98** (2007) 221803, `hep-ex/0702051`.

[200] The CDF Collaboration, T. Aaltonen *et al.*, *Search for chargino-neutralino production in* $p\bar{p}$ *collisions at* $\sqrt{s} = 1.96$*-TeV*, Phys. Rev. Lett. **99** (2007) 191806, `0707.2362`.

[201] The D0 Collaboration, V. M. Abazov *et al.*, *Search for R-parity violating supersymmetry via the LL anti-E couplings* λ_{121}*,* λ_{122} *or* λ_{133} *in* $p\bar{p}$ *collisions at* $\sqrt{s} = 1.96$*-TeV*, Phys. Lett. **B638** (2006) 441, `hep-ex/0605005`.

[202] The D0 Collaboration, V. M. Abazov *et al.*, *Search for resonant second generation slepton production at the Tevatron*, Phys. Rev. Lett. **97** (2006) 111801, `hep-ex/0605010`.

[203] W. Beenakker *et al.*, *The Production of charginos / neutralinos and sleptons at hadron colliders*, Phys. Rev. Lett. **83** (1999) 3780, `hep-ph/9906298`.

[204] H. Baer, K. Hagiwara, and X. Tata, *CAN THE CERN p anti-p COLLIDER LIMIT GAUGINO MASSES?*, Phys. Rev. Lett. **57** (1986) 294.

[205] H. Baer, K. Hagiwara, and X. Tata, *Gauginos as a Signal for Supersymmetry at p anti-p Colliders*, Phys. Rev. **D35** (1987) 1598.

[206] V. D. Barger and C. Kao, *Trilepton signature of minimal supergravity at the upgraded Tevatron*, Phys. Rev. **D60** (1999) 115015, `hep-ph/9811489`.

[207] K. T. Matchev and D. M. Pierce, *Supersymmetry reach of the Tevatron via trilepton, like sign dilepton and dilepton plus* τ *jet signatures*, Phys. Rev. **D60** (1999) 075004, `hep-ph/9904282`.

[208] H. Baer, M. Drees, F. Paige, P. Quintana, and X. Tata, *Trilepton signal for supersymmetry at the Fermilab Tevatron revisited*, Phys. Rev. **D61** (2000) 095007, `hep-ph/9906233`.

[209] M. Cacciari and G. P. Salam, *Dispelling the N^3 myth for the k_t jet-finder*, Phys. Lett. **B641** (2006) 57, `hep-ph/0512210`.

[210] M. Cacciari, G. Salam, and G. Soyez, *FastJet Website*, `http://www.lpthe.jussieu.fr/~salam/fastjet/`.

[211] G. J. Feldman and R. D. Cousins, *A Unified Approach to the Classical Statistical Analysis of Small Signals*, Phys. Rev. **D57** (1998) 3873, `physics/9711021`.

[212] F. E. Paige, S. D. Protopopescu, H. Baer, and X. Tata, *ISAJET 7.69: A Monte Carlo event generator for p p, anti-p p, and e+ e- reactions*, `hep-ph/0312045`.

[213] G. Corcella *et al.*, *HERWIG 6.5: an event generator for Hadron Emission Reactions With Interfering Gluons (including supersymmetric processes)*, JHEP **01** (2001) 010, `hep-ph/0011363`.

[214] G. Corcella *et al.*, *HERWIG 6.5 release note*, `hep-ph/0210213`.

[215] S. Moretti, K. Odagiri, P. Richardson, M. H. Seymour, and B. R. Webber, *Implementation of supersymmetric processes in the HERWIG event generator*, JHEP **04** (2002) 028, `hep-ph/0204123`.

[216] R. Brun and F. Rademakers, *ROOT — An object oriented data analysis framework*, Nucl. Instr. & Meth. in Phys. Res. A **389(1-2)** (1997) 81 , See also `http://root.cern.ch/`.

[217] Z. Sullivan and E. L. Berger, *Isolated leptons from heavy flavor decays: Theory and data*, Phys. Rev. **D82** (2010) 014001, `1003.4997`.

[218] J. Alwall *et al.*, *MadGraph/MadEvent v4: The New Web Generation*, JHEP **09** (2007) 028, `0706.2334`.

[219] J. M. Campbell, J. W. Huston, and W. J. Stirling, *Hard Interactions of Quarks and Gluons: A Primer for LHC Physics*, Rept. Prog. Phys. **70** (2007) 89, `hep-ph/0611148`.

[220] The SM and NLO Multileg Working Group Collaboration, J. R. Andersen *et al.*, *The SM and NLO multileg working group: Summary report*, `1003.1241`.

[221] B. C. Allanach *et al.*, *The Snowmass points and slopes: Benchmarks for SUSY searches*, Eur. Phys. J. **C25** (2002) 113, `hep-ph/0202233`.

[222] H. Baer, V. Barger, A. Lessa, and X. Tata, *Supersymmetry discovery potential of the LHC at $\sqrt{s}$ =10 and 14 TeV without and with missing E_T*, JHEP **09** (2009) 063, `0907.1922`.

[223] H. Baer, V. Barger, A. Lessa, and X. Tata, *Capability of LHC to discover supersymmetry with $\sqrt{s} = 7$ TeV and* 1 fb^{-1}, JHEP **06** (2010) 102, `1004.3594`.

[224] H. Baer, X. Tata, and J. Woodside, *Multi - lepton signals from supersymmetry at hadron super colliders*, Phys. Rev. **D45** (1992) 142.

[225] H. Baer, M. Bisset, X. Tata, and J. Woodside, *Supercollider signals from gluino and squark decays to Higgs bosons*, Phys. Rev. **D46** (1992) 303.

[226] R. M. Barnett, J. F. Gunion, and H. E. Haber, *Discovering supersymmetry with like sign dileptons*, Phys. Lett. **B315** (1993) 349, `hep-ph/9306204`.

[227] H. K. Dreiner, M. Guchait, and D. P. Roy, *Like sign dilepton signature for gluino production at CERN LHC with or without R conservation*, Phys. Rev. **D49** (1994) 3270, `hep-ph/9310291`.

[228] B. C. Allanach, C. G. Lester, M. A. Parker, and B. R. Webber, *Measuring sparticle masses in non-universal string inspired models at the LHC*, JHEP **09** (2000) 004, `hep-ph/0007009`.

[229] B. K. Gjelsten, D. J. Miller, 2, and P. Osland, *Measurement of SUSY masses via cascade decays for SPS 1a*, JHEP **12** (2004) 003, `hep-ph/0410303`.

[230] B. K. Gjelsten, D. J. Miller, 2, and P. Osland, *Measurement of the gluino mass via cascade decays for SPS 1a*, JHEP **06** (2005) 015, `hep-ph/0501033`.

[231] M. Chiorboli and A. Tricomi, *Squark and gluino reconstruction in CMS*, CMS-NOTE-2004-029.

[232] B. C. Allanach *et al.*, *Measuring supersymmetric particle masses at the LHC in scenarios with baryon-number R-parity violating couplings*, JHEP **03** (2001) 048, `hep-ph/0102173`.

[233] D. J. Miller, P. Osland, and A. R. Raklev, *Invariant mass distributions in cascade decays*, JHEP **03** (2006) 034, `hep-ph/0510356`.

[234] C. G. Lester and D. J. Summers, *Measuring masses of semiinvisibly decaying particles pair produced at hadron colliders*, Phys. Lett. **B463** (1999) 99, `hep-ph/9906349`.

[235] A. Barr, C. Lester, and P. Stephens, *m(T2) : The Truth behind the glamour*, J. Phys. **G29** (2003) 2343, `hep-ph/0304226`.

[236] K. T. Matchev, F. Moortgat, L. Pape, and M. Park, *Precise reconstruction of sparticle masses without ambiguities*, JHEP **08** (2009) 104, `0906.2417`.

[237] The CMS Collaboration, G. L. Bayatian *et al.*, *CMS physics: Technical design report*, CERN-LHCC-2006-001.

[238] H. K. Dreiner, H. E. Haber, and S. P. Martin, *Two-component spinor techniques and Feynman rules for quantum field theory and supersymmetry*, `0812.1594`.

Acknowledgements

First of all, I would like to thank my supervisors Prof. Arnulf Quadt and Prof. Herbi Dreiner for giving me the opportunity to work in the field of high energy physics phenomenology, although this research field is generally not covered by the University of Göttingen, and for acting as referees for this diploma thesis. I also thank the University of Bonn for the nice hospitality during my stay in Bonn.

I especially thank Sebastian Grab for supervision, enlightening and encouraging discussions and for reading the manuscript. Furthermore, I would like to thank the people in my (and "the other") office, most notably Suchita Kulkarni, Moritz Meinecke and Branislav Poletanović, for helpful discussions and nice companionship.

I also thank Karina Williams, John Conley, Jamie Tattersall, Marja Hanussek and Jong Soo Kim for interesting discussions.

My special gratitude is dedicated to Annemarie for her love and support, and for her patience during the time of writing this thesis.

Last but certainly not least I would like to thank my family, especially my parents Werner and Ingelore and my brother Jan.